SPS consolidation of cubic boron nitride reinforced α-SiAlON ceramics

Jethro Christopher Garrett

A dissertation submitted to the Faculty of Engineering and the Built Environment, University of the Witwatersrand, in fulfillment of the requirements for the degree of Master of Science in Engineering.

Johannesburg, 2012

Declaration

I declare that this dissertation is my own unaided effort. It is being submitted for the degree of Master of Science in Engineering to the University of the Witwatersrand, Johannesburg. It has not been submitted before for any degree or examination to any other university.

_____

Jethro Christopher Garrett

_____ Day of _____ Year 2012

Abstract

Sialon ceramics have been recently investigated as cutting tools due to their higher hardness than that of silicon nitride ceramics. Improvements in properties such as hardness, fracture toughness and chemical resistance through cBN reinforcement will make a cutting insert much more suitable for cutting and wear applications than that of pure sialon ceramic. This would result in a material with a significantly wider range of applications than that of the corresponding unreinforced sialon matrix.

This work investigated the fabrication of α-sialon ceramics as well as their corresponding cBN containing composites by spark plasma sintering. Fully dense (> 97 % theoretical density) sialon ceramics with a cBN content of up to 30 vol. % could be produced at sintering temperatures of 1575°C, the same temperature required for the pure matrix. An increase in the sintering temperature promotes the α-sialon transformation in the presence of yttrium as the stabilizing cation and thus the Vickers hardness is improved for pure sialon where an increase in the sintering temperature from 1575 to 1625°C results in an increase from 18.2 ± 0.4 to 19.6 ± 0.5 GPa.

It was observed that additions of cBN grains to the sialon matrix negatively affect the primary densification mechanisms present in liquid phase sintering, those being particle rearrangement and solution-precipitation processes. The phase transformation of some cBN grains in the cBN containing sialon composites were only observed at temperatures of 1600°C (partial/surface) and 1625 °C (high). Furthermore, through this work it was found that an optimum addition of cBN grains to the sialon matrix was 10 vol.%. Improvements in the Vickers hardness and fracture toughness through the addition of cBN grains were obtained at all sintering temperatures carried out through this scope of work. The improvements of the Vickers hardness for the sialon composites containing 10 vol. % cBN as compared to the pure sialon ceramic are given as follows for the relevant sintering temperatures: 1575 (18.2 → 20.9 GPa), 1600 (19.1 → 21.3 GPa) and 1625°C (19.7 → 20.7 GPa). cBN containing sialon composites sintered at 1575°C maintain hardness greater than that of pure sialon with increasing cBN content up to 30 vol. %

cBN, however at higher sintering temperatures considerable deterioration of the cBN grains was observed due to hexagonalization of the dispersed cBN grains; this resulted in composites with lower hardness than that of the pure sialon ceramic. The fracture toughness was seen to improve significantly with 10 vol. % cBN addition to the sialon matrix (3.6 → 5.2 MPa.$m^{0.5}$) when sintered at 1575°C; however further addition of cBN does not result in a further improvement of the fracture toughness unless hexagonalization of the cBN grains takes place which is promoted further with increasing sintering temperature. Composites containing 30 vol. % cBN and sintered at 1625°C exhibit fracture toughness as high as 7.8 MPa.$m^{0.5}$, as a result of the excessive hexagonalization of the cBN grains. Lastly through this work it was revealed that cBN containing sialon composites sintered with α-sialon as the matrix have superior mechanical properties to those cBN composites prepared through the use of β-sialon.

Acknowledgements

I would like to acknowledge and thank the following individuals and groups for their assistance in the completion of this Master's degree (MSc (Eng)):

- **Prof. I. Sigalas** – For giving me the possibility to further my studies in the field of ceramics and above all supervision, financial aid and support.

- **Dr. habil. M. Herrmann** – For helping me get a glimpse of his knowledge in the field of SiAlON ceramics. Your guidance throughout the course of this project has been greatly appreciated and your constructive criticism has most improved my skills as a researcher immensely.

- **Element 6 (Pty.) Ltd** – For their financial assistance.

- **DST/NRF Centre of Excellence in Strong Materials** – For their financial assistance. I would especially like to thank all the administrative staff for their support and patience.

- **Office colleagues** – To the always entertaining Mr. R. Genga, Mr. P. Rokebrand, and Mr. V. Vythilingum, with you guys at Wits, no day is boring. Not only did we work hard, we played hard too.

- **Friends** – You all know who you are! You are all an important part of my life, we have shared many good times and I damn well know there are plenty more of them waiting for us out there.

- **Family** – Thank you for your support, particularly to the two beautiful woman who raised me to what I am today, my gran (Mrs. I. Garrett) and my mom (Ms. V. Garrett).

- **Ms. C. Gatonby** – To the love of life, thank you for all your support and understanding, especially for being so patient with all the long hours I've had to carry out at Wits, in order to complete this dissertation.

Table of Contents

DECLARATION

ABSTRACT ..... **I**

ACKNOWLEDGEMENTS ..... **III**

LIST OF FIGURES ..... **VIII**

LIST OF TABLES ..... **XIV**

1. INTRODUCTION **1**

2. LITERATURE REVIEW **3**

2.1. Background to silicon nitride **3**

2.2. Overview of silicon nitride ceramics **5**

2.2.1. Phase modifications of Si_3N_4 5
2.2.2. Densification methods of Si_3N_4 7
2.2.3. Properties of silicon nitride based ceramics 10

2.3. Sintering of sialon ceramics **11**

2.3.1. Modifications sialon phases 11
2.3.1.1. α-Sialon 12
2.3.1.2. β-Sialon 16
2.3.1.3. Grain morphology 16
2.3.2. Liquid phase 18
2.3.2.1. Particle rearrangement 20
2.3.2.2. Solution-precipitation 21
2.3.2.3. Ostwald ripening 22
2.3.2.4. Role of additives on the formation of α-sialon 23
2.3.2.5. Properties of α-sialon ceramics 27
2.3.2.5.1. Pressureless sintering 30
2.3.2.5.2. Hot isostatically pressed 33
2.3.2.5.3. Gas pressure sintered 34
2.3.2.5.4. Commercial sialon materials 36
2.3.3. FAST/SPS densification of sialon composites 37

2.4. Overview of the reinforcing superhard cBN agent **41**

2.4.1. cBN crystal structure 42
2.4.2. Sintering and properties of cBN materials 43

3. EXPERIMENTAL PROCEDURE 50

3.1. Starting powder characterisation 50

3.1.1. Particle size analysis 51
3.1.2. XRD analysis 52
3.1.3. Scanning electron microscopy of starting powders 52

3.2. Calculation of sialon matrices 52

3.3. Mixing of composite powders 54

3.3.1. Planetary ball mixing sialon constituents 55
3.3.2. Rotary evaporator 56
3.3.3. Sieving powder 56
3.3.4. Turbula mixing of cBN grains 56

3.4. Sintering of sialon based composites using the spark plasma technique 57

3.5. Characterization methods for sintered composites 58

3.5.1. Density measurements 58
3.5.2. Cutting the sintered composites 60
3.5.3. Mounting 60
3.5.4. Grinding and polishing techniques 61
3.5.5. XRD analysis 62
3.5.6. SEM of composites 62
3.5.7. Mechanical properties 62
3.5.7.1. Hardness 62
3.5.7.2. Indentation fracture toughness 64

4. EXPERIMENTAL RESULTS 66

4.1. Starting Powders 66

4.1.1. Particle size analysis 66
4.1.2. XRD Analysis 67
4.1.3. Scanning electron microscopy 69

4.2. Distribution of sialon constituents 72

4.3. Distribution of cBN grains in the sialon matrices 73

4.4. Densification of sintered sialon /cBN composites 74

4.4.1. Temperature measurements 75
4.4.2. Pure sialon 76
4.4.3. Sialon /cBN composites 79

4.5. Microstructure and phase evolution of sialon /cBN composites 84

4.5.1. M1/cBN composites 87
4.5.1.1. Sialon materials without cBN 87
4.5.1.2. M1 sialon containing cBN additive 90
4.5.2. M2 /cBN composites 93

4.5.3. M3 /cBN composites 96
4.5.4. M4 /cBN composites 99

4.6. Mechanical Properties 101

4.6.1. Pure sialon 101
4.6.2. Effects of cBN addition on the mechanical properties....102

5. DISCUSSION 106

5.1. Densification mechanism experienced in pure sialon ceramics 106

5.2. Effect of sintering temperature on the microstructure and mechanical properties of sialon ceramics 111

5.3. Effect on cBN addition on densification of sialon ceramics 114

5.4. Hexagonalization of cBN grains....119

5.5. Comparison of mechanical properties sialon/cBN composites 124

5.6. Fracture toughening mechanisms....129

6. CONCLUSION 134

7. FURTHER WORK.... 138

8. REFERENCE LIST 139

List of figures

Figure 2.1: Cross-sectional view of the combustion section of an internal combustion engine where the shaded parts are manufactured from silicon nitride. Taken from Heinmann, 2010 [10]. 4

Figure 2.2: Crystal structures of a) α-Si_3N_4, b) β-Si_3N_4 and c) γ-Si_3N_4adapted from Peng, 2004 [16]..... 6

Figure 2.3: Schematic of a two-stage multi-anvil press. Taken from Kroke, 2002 [20]..... 7

Figure 2.4: Structures of α-Si_3N_4 (a) and α-sialon (b) where M represents the stabilizing cation. Adapted from Petzow et al., 2002 [3]..... 13

Figure 2.5: The Y-Si-Al-O-N system illustrating the quasi-quaternary subsystem of Si_3N_4-AlN-Al_2O_3-SiO_2-Y_2O_3-YN (Jänecke Prism). Taken from Petzow et al., 2002 [3]. 14

Figure 2.6: Detailed depiction of the Jänecke Prism identifying possible phase formations. The α-sialon plane is highlighted. Adapted from A. Rosenflanz et al., 1999 [26]. 15

Figure 2.7: The effect of different stabilizing cations and the corresponding m and n values for stable α-sialon ranges used when designing α-sialon ceramics. Taken from Hermann et al., 2011 [2]..... 15

Figure 2.8: SEM micrograph showing the various α and β sialon phases identified..... 17

Figure 2.9: SEM micrographs of showing formation of the elongates Y-α-sialon (m=2.0 and n=1.5) compact with increasing temperature. Taken from Zhou et al., 2007 [12]. ... 18

Figure 2.10: Fracture toughness of α-Y-sialon as a function of the average aspect ratio of grains and the volume fraction of elongated grains. Taken from Zhou et al., 2007 [12]. 18

Figure 2.11: Densification curve for α-sialon sintered through the SPS technique. The inset in the top left shows the shrinkage rate as a function of the sintering temperature. The densification steps are highlighted by the denotation I, II and III as the particle rearrangement (I), solution-precipitation (II) and Ostwald ripening (III). 19

Figure 2.12: An example of the densification steps when forming Si_3N_4 ceramics through liquid phase sintering techniques. Taken from Carter et al. 2007 [7]..... 20

Figure 2.13.: HRTEM image of grain boundary glass film between grains and the triple point between two silicon nitride grains [1]. 22

Figure 2.14: Densification curves during hot pressing of Y-α-sialon (m=1.2 and n=1) with and without additional yttria (1.4 wt. %) [2]..... 24

Figure 2.15: The dissolution of the various starting powders and the effect on α-sialon with respect to sintering temperature and stabilizing cation. Adapted from Rosenflanz et al., 1999 [26]. 25
Figure 2.16: α-sialon plane represented by the Si_3N_4-4/3(AlN.Al_2O_3)-YN-3AlN subsystem in the Jänecke Prism. Taken from A. Rosenflanz et al., 1999 [26]..... 26
Figure 2.17: The range of possible m-values in α-sialon as a function of increasing ionic radii of the stabilizing cation. Taken from Petzow et al., 2002 [3]..... 26
Figure 2.18: The hot hardness of various cutting tool ceramics. Taken from Heinmann, 2010 [10]. 30
Figure 2.20: The effect of relative density on the hardness values obtained for Y-α-sialons. Taken from Zhou et al., 2007 [12]. 32
Figure 2.21: The effect of the average grain aspect ratio on the fracture toughness values of Y-α-sialons showing a linear relationship. Taken from Zhou et al., 2007 [12]..... 32
Figure 2.22: Indentation fracture toughness and the Vickers hardness (H_{v10}) of Y-α-sialons HIP-sintered at 1800°C for 1 hour with respect to the varying m value. Taken from Ye et al. , 2004 [50]. 34
Figure 2.23: Schematic of the tool assembly for the SPS consolidation technique showing the different graphite tooling. The optical pyrometer measurements are commonly taken at two positions a) 5mm above the top of the sample and b) on the outer-radial wall of the graphite die. Adapted from Langer et al., 2010 [54]. 37
Figure 2.25: The crystal lattices of the three BN-system allotropes a) h-BN b) c-BN c) w-BN, where (●) represents boron atoms and (○) represents nitrogen atoms [68]. 43
Figure 2.26: Bridgman-type HPHT sintering system, where 1 – Sample, 2 – shows plastic deformation of the gasket material, 3 – Pressure anvils, 4 – high power transformer supplying electrical heating and 5 – graphite resistive heater. Taken from Klimczyk et al., 2011 [72]. 44
Figure 2.27: Knoop hardness for the cBN-TiN-Al and cBN-Al systems where the sintering temperatures were varied from 1200 to 1400°C respectively [74]..... 45
Figure 2.28: Thermal diffusivities of WC-6Co and WC-6Co-25cBN composites. Taken from Yaman et al., 2009 [75]..... 46
Figure 2.29: Young's modulus and density of cBN-Si_3N_4 (I) composites sintered at different temperatures under high pressure. Taken from Klimczyk et al., 2011 [72]..... 47
Figure 2.30: Negative effect of cBN content on the densification of cBN / β-sialon composites sintered at 1500°C for a dwell time of 5 minutes. Taken from Ye et al., 2010 [55].. 48

Figure 2.31: Effects of cBN content on the mechanical properties of cBN/β-sialon. a) Vickers hardness and b) flexural strength and fracture toughness. Taken from Ye et al., 2010 [55]. 49
Figure 3.1: Location of sialon matrices on the sialon plane studied in this scope of work, showing the effect of compositional changes on the designing of sialon ceramics. 54
Figure 3.2: Milling action of the planetary ball mill [77] 55
Figure 3.3: Sintering profile of composites sintered at 1550°C showing the schedule of the sintering temperature and applied pressure. 58
Figure 3.4: Illustration of the measurement of the indentation diagonals required for Vickers hardness measurement. 63
Figure 3.5: Crack length measurement for determination of the fracture toughness 64
Figure 4.1: XRD pattern for UBE SNE-10 silicon nitride powder showing both phases α (■) and β (♦) are hexagonal. 68
Figure 4.2: XRD pattern for grade 1 cBN powder showing the cubic (■) and hexagonal (♦) phases 68
Figure 4.3: SEM imaging of alpha silicon nitride, SNE-10 starting powder from UBE Industries showing presence of beta silicon nitride whiskers (marked). 69
Figure 4.4: SEM imaging of Grade H aluminium nitride starting powder from Tokuyama Industries. 70
Figure 4.5: SEM imaging of AKP-50 alumina starting powder from Sumitomo 70
Figure 4.6: SEM imaging of fine grade yttria starting powder from H. C. Starck. 71
Figure 4.7: SEM imaging of Grade 1 cBN starting powder from Element 6 Pty Ltd. 71
Figure 4.8: SEM imaging of Grade 9 cBN starting powder from Element 6 Pty Ltd. 72
Figure 4.9: Back-scattered SEM imaging showing the distribution of the sialon constituents of M1-1550. 73
Figure 4.10: Secondary electron SEM imaging showing the grade 9 cBN grain distribution of M1 based composites sintered at 1600°C with varying cBN content: a) 0, b) 10, c) 20 and 30 vol, % cBN (d). 74
Figure 4.11: SEM images of the cross-sectional surface of pure M1 sialon sintered at: a) 1550°C showing porosity and b) 1575°C showing full densification. 77
Figure 4.12: Comparative densification curves for M1 sialon ceramics sintered at various temperatures 78
Figure 4.13: Optical microscopy of the dispersion of grade 1 cBN in the sialon matrix through the Turbula (a) and planetary ball milling (b and c) routes densified at 1575°C. ... 80

Figure 4.14: Influence of cBN content and sintering temperature on the percentage of the theoretical densities of M1 sialon ceramics. 82
Figure 4.15: Comparison of the X-Ray Diffractograms of pure sialon ceramics sintered at 1600°C. 86
Figure 4.16: Comparison of the X-Ray Diffractograms of pure M1- sialon sintered at different temperatures (1550-1625°C). 87
Figure 4.17: SEM micrographs of M1-sialon sintered at 1550°C showing porosity as well as poor grain growth in a) secondary electron and b) back-scattered detection modes. 89
Figure 4.18: SEM micrographs of M1-sialon showing that a fully dense sample can be obtained at 1575°C. 89
Figure 4.19: SEM micrographs of M1-sialon sintered at 1600°C in back-scattered detection mode. 89
Figure 4.20: SEM micrographs of M1-sialon sintered at 1625°C in back-scattered detection mode. 90
Figure 4.21: Comparison of the X-Ray Difftactograms of M1-sialon/cBN composites sintered at 1575°C with varying grade 9 cBN content (0-30 vol. %). 91
Figure 4.22: SEM micrographs of M1-Sialon/cBN composites sintered at 1600°C with varying cBN content: 10 (a, b), 20 (c, d) and 30 (e, f) vol. % cBN. 92
Figure 9.1: X-ray diffractograms of M2- sialon /cBN composites sintered with varying temperature (1575-1600°C) and cBN content (0 and 30 vol. %) 93
Figure 4.23: SEM micrographs comparing pure M2-sialon with M2-sialon sintered with 30 vol. % cBN at 1600°C: a, c and e) pure M2 and b, d and f) M2 with 30 vol. %cBN.... 95
Figure 4.25: X-ray diffractograms of M3- sialon /cBN composites sintered with varying temperature (1575-1600°C) and cBN content (0 and 30 vol. %) 96
Figure 4.24: SEM micrograph of M3-sialon sintered at 1550°C showing high yttria-rich glassy phase (YAG) and a considerable amount of the polytype phase. 97
Figure 4.25: SEM micrograph of M3-sialon sintered at 1625°C showing lower amount of glassy phase and smaller polytype clusters as compared than that sintered at 1550°C..... 98
Figure 4.26: SEM micrographs comparing pure M3-sialon with M3-sialon sintered with 30 vol. % cBN at 1600°C: a, b) pure M3 and c, d) M3 with 30 vol. % cBN. 99
Figure 4.27: X-ray diffractograms of M4 sialon /cBN composites sintered with at 1600°C with varying grade 9 cBN content (0 and 30 vol. %). 100

Figure 4.28: SEM micrograph showing the existence of the yttria rich pooling behaviour (a) and the α-sialon (equiaxed) and polytype (elongated clusters) phases that are present in M4 sialon sintered at 1600°C. 101
Figure 4.29: The effect of temperature and cBN content on the fracture toughness of M1/cBN composites. 104
Figure 5.1: Comparison of densification behaviour of M1, M2, M3 and M4 sialons sintered at 1600°C with 50 MPa uni-axial pressure constant throughout sintering……..107
Figure 5.2: Compositions of the various sialon matrices on the sialon plane..... 109
Figure 5.3: Graphical representation of the percentage of the theoretical densities for pure sialon ceramics sintered at various temperatures. 110
Figure 5.4: SEM micrographs showing the different grain morphologies of a) M1 sialon and b) M4 sialon sintered at 1600°C and analysed under back-scattered detection mode. 112
Figure 5.5: Effect of sintering temperature on the Vickers hardness of the varying sialon compositions. 113
Figure 5.6: Effect of sintering temperature on the fracture toughness of the varying sialon compositions. 113
Figure 5.8: Effect of grade 9 cBN on the percentage of the theoretical density of sialon matrices sintered at 1575°C. 116
Figure 5.9: Effect of grade 9 cBN on the percentage of the theoretical density of sialon matrices sintered at 1600°C. 117
Figure 5.10: Comparative densification curves for sialon ceramics sintered at 1600°C. 118
Figure 5.12 : SEM micrographs showing surface hexagonalization of some cBN grains in M1-sialon composite containing 30 vol. % cBN and sintered at 1600°C. Samples prepared by broad ion beam polishing courtesy of M. Herrmann of IKTS Fraunhofer. 119
Figure 5.13: SEM micrograph showing considerable degradation of random cBN grains of the M1-sialon composite containing 30 vol. %cBN and sintered at 1625°C. 120
Figure 5.14: SEM micrograph showing inhomogenous hexagonalization of cBN grains within the M1-sialon matrix when sintered at 1625°C. Samples prepared by broad ion beam polishing courtesy of M. Herrmann of IKTS Fraunhofer. 121
Figure 5.15: Comparison of the transformation of cBN grains with increasing sintering temperature, for pure cBN and β-sialon containing 20 vol. % cBN. Taken from Hotta et al., 2010 [87] 122

Figure 5.16: Effect of grade 9 cBN content on the mechanical properties of M1 sialon ceramics sintered with increasing temperature. 125
Figure 5.17: Effect of hardness with increasing secondary phase addition, a) SPS at 1500°C measured with 5 kg load Ye et al., 2010 [55], b) gas pressure sintered at 1930°C measured with a load of 10 kg. 127
Figure 5.18: Fracture mechanisms experienced in pure sialon ceramics, a) crack branching and b) crack deflection for M1-1600. 130
Figure 5.19: Typical back-scattered SEM image showing crack deflection in sialon M1-1600-10cBN. 130
Figure 5.20: Intergranular crack propagation of cBN grains reinforcing sialon by improving fracture toughness M1-30cBN-1600. 131
Figure 5.21: Intergranular (a) crack propagation around cBN grains and transgranular (b) crack propagation through cBN grains for M1-30cBN-1625. 132
Figure 5.22: Fracture surface of sialon/cBN composites showing cBN grain pull out as well as intergranular fracture of M1-30cBN (a) and M4-30cBN (b) sialon composites sintered at 1600°C. 133

List of tables

Table 2.1: Sintering processes used for silicon nitride based materials and the respective densification [3]. 10

Table 2.2: Sintering processes used for silicon nitride based materials and their respective properties [3]. 11

Table 2.3: Unit cell parameters, morphology and mechanical properties of both α and β phases of Si_3N_4 and Sialon. Taken from Peng, 2004 [19] 12

Table 2.4: Room temperature mechanical properties of Nd_2O_3-CaO doped α-sialons [35]. 27

Table 2.5: Mechanical properties of various sintered sialon ceramics and their respective retention (%) of room temperature modulus of rupture at elevated temperatures [50]. 29

Table 2.6: Showing the starting m and n values used in the study by Ye et al., 2004 [53], the composition of α and β-sialon and percentage of the theoretical density of the various Y- sialon composites sintered at 1800°C. 33

Table 2.7: Results obtained by Kurama et al., 2002 [40] for the various Y-α-sialon ceramics. 35

Table 2.8: Selected properties for commercial sialon ceramics with pure Si_3N_4 as comparison [13]. 36

Table 2.9: Sintering temperature for various α-sialon phases and their respective mechanical properties. Adapted from Peng, 2004 [19]. 39

Table 2.10: The characterization of α and β sialon composites sintered by Smirnov, 2009 [61] ... 40

Table 2.11: Properties of cBN and hBN [70]. 42

Table 2.12: Sintering condition, theoretical densities and mechanical properties of samples consolidated through SPS by Yama et al., 2009 [8]. 45

Table 2.13: A comparison of the density and mechanical properties of cBN-Si_3N_4 (3 vol. %) composites (I) and (II) sintered at 2240°C and 7.7 GPa pressure with BZN7000s as a reference material. Taken from Klimczyk et al., 2011 [75]. 47

Table 3.1: Details of the respective starting powders used in obtaining sialon based composites. 50

Table 3.2: Supplier information for other chemicals and consumables used in this scope of work. 51

Table 3.3: A summary of the composition, n and m values and cation ratio for the various sialon matrices. 53

Table 3.4: Pre-programmed grinding and polishing cycle with the respect to the different wheel, lubricant, duration and rotation speed. 61
Table 4.1: d_{50} of the respective starting powders obtained from the particle size distributions... 67
Table 4.2: XRD patterns used to identify the crystalline phases present in the starting powders. 67
Table 4.3: Density and open porosity results for pure M1 and M4 sialon ceramics sintered at 1500°C 75
Table 4.4: A summary of the composition, n and m values for the various sialon matrices. 76
Table 4.5: The density results of pure M1, M2, M3 and M4 sialon ceramics sintered at various temperatures. 77
Table 4.6: The densities obtained for the sialon composites sintered with and without grade 1 and grade 9 cBN. 81
Table 4.7: The density results of pure M1 and M1/cBN ceramics sintered at various temperatures. 82
Table 4.8: The density results of pure M2 and M2/cBN ceramics sintered at various temperatures. 83
Table 4.9: The density results of pure M3 and M3/cBN ceramics sintered at various temperatures. 83
Table 4.10: The density results of pure M4 and M4/cBN ceramics sintered at various temperatures. 84
Table 4.11: XRD pattern data used to analyse the x-ray diffractograms in this project. 85
Table 4.12: Intensities of the various formations of crystalline phases for pure sialon ceramics sintered at 1600°C. 86
Table 4.13: Identification of phases present and their respective trends for pure M1- sialon sintered at varying temperatures (x-phase present and ↑↓-trend). 88
Table 4.14: Hardness and fracture toughness results for pure M1, M2, M3 and M4 sialons sintered at various temperatures. 102
Table 4.15: The hardness and fracture toughness results pertaining to sintered M1/cBN composites. 103
Table 4.16: The hardness and fracture toughness results pertaining to sintered M2/cBN composites. 104
Table 4.17: The hardness and fracture toughness results relating to sintered M3/cBN composites. 105
Table 4.18: The hardness and fracture toughness results relating to sintered M4/cBN composites. 105

Table 5.1: Comparison of the onset temperature of eutectic liquid formation for the various sialon matrices..... 108
Table 5.2: Estimation of hBN content in the M1 sialon/cBN composites using 0, 10, 15 and 20 vol. % cBN to hBN formation. 123
Table 5.3: Comparison of the mechanical properties obtained for M4 sialon based composite with that sintered by Ye et al., 2010 [58]. 128

1. Introduction

Silicon nitride ceramics have been widely investigated due to their advantageous properties of high strength, fracture toughness, thermal shock resistance, chemical resistance and hardness at both room and elevated operating temperatures [1] [2]. The highly covalent bonds of silicon nitride (Si_3N_4) result in a low mass diffusivity. Therefore the material cannot be solid-state sintered; however, through the addition of various sintering aids and the application of external pressures, fully dense ceramics can be obtained [1]. Sialon ceramics are silicon nitride based alloys where the solid solutions of α and β sialon are isostructural with that of α-Si_3N_4 and β-Si_3N_4.The β-sialon phases are formed by the substitution of silicon by aluminium and of nitrogen by oxygen atoms in the Si_3N_4 crystal structure [3]. In addition to this substitution, α-sialon incorporates an interstitial cation into the α-sialon structure. Sialon ceramics are easier to fabricate than silicon nitride ceramics due to the increased amount of liquid phase present during consolidation which contributes to the particle rearrangement and the necessary transport required for solution-precipitation process during densification [3]. Furthermore, α-sialon ceramics have higher hardness when compared to that of β-silicon nitride ceramics, making them superior as cutting tool materials [4].

Ceramics in general are known to have low fracture toughness [5]; therefore, improvements in this key property are widely researched. High fracture toughness is one of the prerequisites for a material used in cutting tool applications, particularly in interrupted cutting [6]. There are several ways in which the fracture toughness of a ceramic can be increased. This work will investigate secondary reinforcement toughening, which can produce local internal stresses as well as offer crack deflection sites. The reinforcement of a ceramic for toughening purposes can be achieved in the form of particulates, whiskers and fibrous materials. Improving the fracture toughness of a ceramic for cutting applications is only an advantage when the hardness of the ceramic can be maintained or increased.

Thus the aim of this project is to investigate the reinforcement of sialon ceramics through the addition of superhard cubic boron nitride (cBN) particles in order to improve the hardness and

fracture toughness. Improvements in these key properties, through cBN reinforcement, will make a cutting insert much more suitable for interrupted cutting applications than the pure sialon ceramic [7]. Such a material is expected to have a significantly wider range of applications than the corresponding unreinforced sialon matrix.

The consolidation of the sialon ceramics and cBN containing sialon composites will be carried out through the use of spark plasma sintering (SPS) which is said to be an enhanced sintering technique due to its high heating and cooling rates with an applied pressure. It is also known that cBN has the tendency to transform into its more stable hexagonal phase when heated under low pressures [8]; the SPS consolidation technique is seen to be advantageous as compared to other common sintering techniques because the overall sintering time is significantly reduced, which in turn will lower this transformation. The effect of compositional changes to pure sialons will be investigated along with the influence of sintering temperatures on the respective microstructure, mechanical properties and phase formations. Furthermore the reinforcement of sialon ceramics through the addition of cBN grains will also be investigated in order to understand their effects on microstructure and mechanical properties.

2. Literature Review

2.1. Background to silicon nitride

Silicon nitride was first produced in 1857 [6]. Silicon nitride however was considered more of a compound of chemical interest and not yet as an engineering material [9]. During the period of 1948-1952 the Carborundum Company, New York applied for several patents on its manufacture and its potential uses as an engineering ceramic [10]. From 1958, Haynes (Union Carbide) produced silicon nitride commercially for applications such as thermocouple tubes, rocket nozzles as well as boats and crucibles for handling molten metal where its uses were primarily refractory in nature [10; 11]. Considerable investment also went into silicon nitride being made a material candidate for the use of high temperature structural applications such as ceramic gas turbines and small truck engines. However it was found that it would not be feasible to obtain reproducible complex shapes with the needed reliable combination of properties of high strength, oxidation resistance and creep resistance [10].

The high energy covalent chemical bonds of Si_3N_4 result in high hardness and strength. However these high energy bonds are a disadvantage during the sintering processes [1]. The self-diffusivity in silicon nitride is low and thus the mobility of atomic species required for densification only occurs above the temperature of 1850°C where Si_3N_4 begins to decompose. As a result of the difficulty experienced during the sintering of pure Si_3N_4, research during the 1960's explored the use of hot-pressing silicon nitride with various sintering additives in order to increase the density of the material closer to theoretical [12]. The term used to refer to this family of multi-component ceramic materials is known as silicon nitride ceramics.

The major application for silicon nitride ceramics today is as a cutting tool or ceramic ball bearings. This is due to its high hot hardness, good fracture toughness, thermal shock and chemical resistance [1] [2]. These properties make it a strong candidate when selecting tools for machining cast iron and nickel based alloys. The advantages of silicon nitride over conventional tungsten carbide tools are increased cutting speeds and longer tool life thus overall reduced costs.

Silicon nitride ceramics are also used in the automobile industry for applications such as diesel glow plugs, turbochargers and exhaust gas control valves [13] as seen in Figure 2.1.

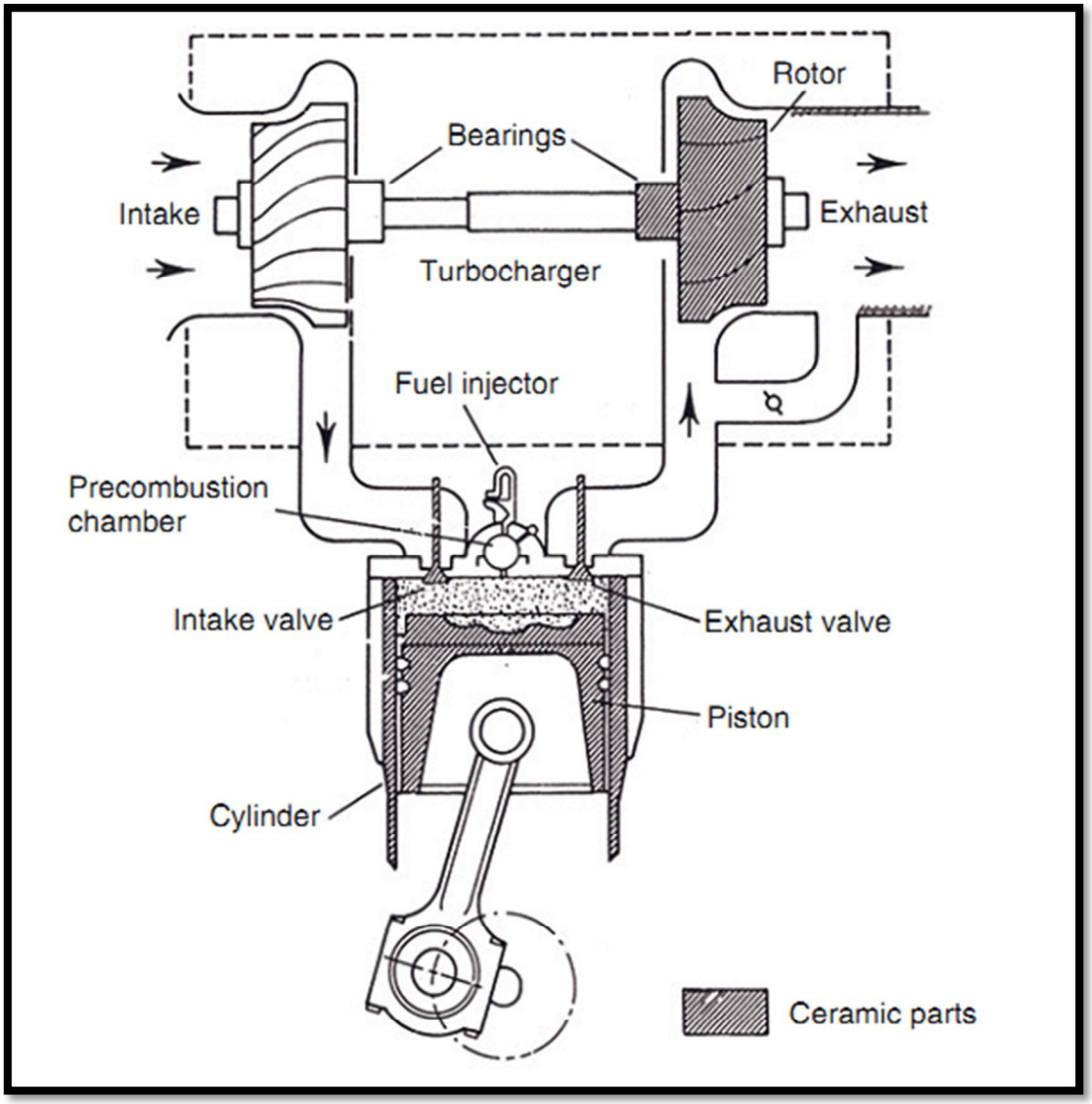


Figure 2.1: Cross-sectional view of the combustion section of an internal combustion engine where the shaded parts are manufactured from silicon nitride. Taken from Heinmann, 2010 [13].

Silicon nitride is used as the bearings in the main engine of the NASA space shuttle and is available in industry as a full ceramic bearing or ceramic hybrid (containing steel races) bearing. These silicon nitride ball-bearings are harder than metallic ones; this reduces the area of contact of the balls on the bearing track resulting in decreased friction, increased bearing life, operating temperature, corrosion resistance, lower density and the ability to operate without

lubricant. It must also be noted that some silicon nitride ceramics are still used as a refractories for kiln furniture, melting crucibles and ingot moulds [13] [14].

2.2. Overview of silicon nitride ceramics

The term silicon nitride ceramics refers to a wide range of multi-component mixtures of silicon nitride (Si_3N_4) [3], where the addition of other components is necessary in order to form the appropriate liquid phases which aid mass transport during sintering, thus achieving complete densification [15].

2.2.1. Phase modifications of Si_3N_4

Silicon nitride exists in three crystalline modifications namely α-Si_3N_4, β-Si_3N_4 and γ-Si_3N_4 which differ in atomic arrangements (see Figure 2.2) including an amorphous phase which is used extensively in the microelectronics industry in the form of thin films [16].

α-Si_3N_4 can be considered to be the low-temperature metastable modification of Si_3N_4 at normal pressures whereas β-Si_3N_4 is the more stable modification at higher temperatures [17]. Both α and β-Si_3N_4 structures have hexagonal symmetry; these structures consist of corner-sharing SiN_4 tetrahedra where the Si atom is situated in the center of the tetrahedron with four N atoms at its corners. The space groups for α-Si_3N_4 and β-Si_3N_4 are P31c and $P6_3$ respectively. The stacking sequence consists of alternate basal layers of silicon and nitrogen atoms in the 'ABCDABCDABCD…' sequence for α-Si_3N_4 and 'ABABAB…' for β-Si_3N_4 sequence, where the 'CD' layer is related to the 'AB' layer through a c-glide plane [1]. The c dimension of α-Si_3N_4 is approximately double that of β-Si_3N_4 [1]. The difference in the stacking sequences of the α-$Si_3N_4$and β-Si_3N_4 modifications results in the α-Si_3N_4 structure consisting of cavities and the β-Si_3N_4 structure consisting of continuous tunnels that run along the c-plane (Figure 2.2 a and b respectively). The lattice parameters for α-Si_3N_4 are subject to the oxygen content dissolved in the structure where an increase in the oxygen content results in a decrease in the *a*-lattice

parameter and an increase in the *c*-lattice parameter [3] and any deviations are a result of aluminium and oxygen impurities [3] where the oxygen content can be up to 0.258 wt. % [18].

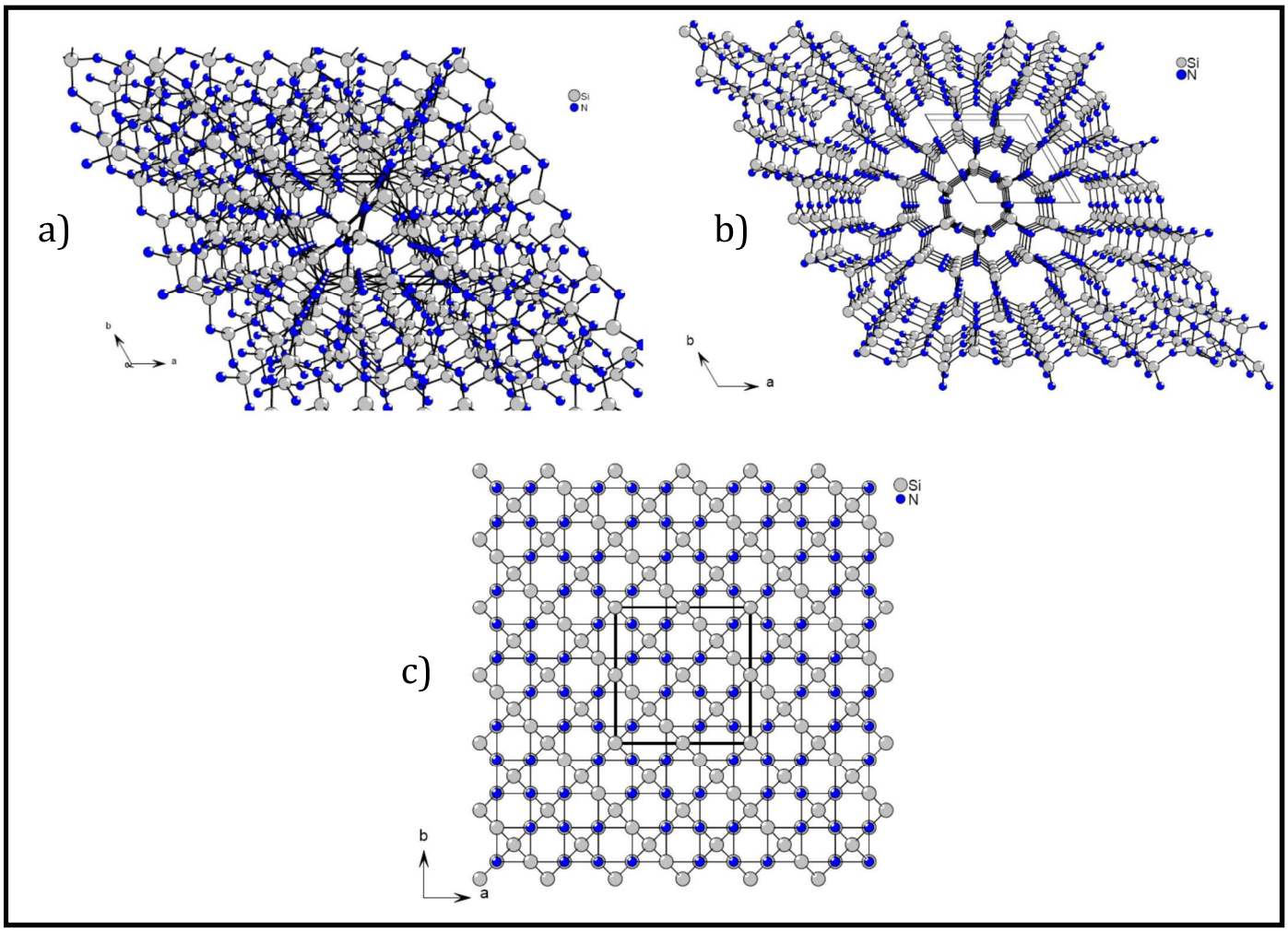


Figure 2.2: Crystal structures of a) α-Si_3N_4, b) β-Si_3N_4 and c) γ-Si_3N_4adapted from Peng, 2004 [19].

The transformation from α-Si_3N_4 to β-Si_3N_4 requires a lattice reconstruction; this can occur when the transforming material is in contact with a solvent. The higher solubility of the unstable α-Si_3N_4drives it into solution where it precipitates out as the less soluble and more stable form of β-Si_3N_4 [1].α-Si_3N_4 is unstable at temperatures above 1400°C [1] [3] and 1500°C [20]; when samples are sintered in excess of these temperatures the transformation to β-Si_3N_4 is irreversible. Pure α-Si_3N_4 powder was heat treated at 1900°C where slow phase transformation from α-Si_3N_4 to β-Si_3N_4 was observed due to the lack of transformation through the solution precipitation step coupled with impurities in the Si_3N_4 [3].

Due to the tunnel-like structure of the β-Si_3N_4 phase parallel to the c-axis, the diffusion of N atoms in β-Si_3N_4 (N-diffusion coefficient, $D_{N\beta} = 5.8x10^{6}$ $cm^2.s^{-1}$) is higher than that experienced in the α- Si_3N_4 phase ($D_{N\alpha} = 1.2x10^{-12}$ $cm^2.s^{-1}$) [21].

The more recently developed γ-Si_3N_4 has a cubic spinel structure where two Si atoms each co-ordinate six N atoms octahedrally and one Si atom co-ordinates four nitrogen atoms tetrahedrally [3] thus γ-Si_3N_4 can better be described as $Si[Si_2N_4]$. The symmetry of γ-Si_3N_4 is *Fd*-3*m* and requires high pressures and temperatures to be synthesized. Novel γ-Si_3N_4 was prepared at 15 GPa and temperatures exceeding 1920°C in a laser-heated diamond anvil cell [22]. However current practice employs a range of techniques to synthesize γ-Si_3N_4including the multianvil pressure apparatus (MAP) [23] and shock-wave synthesis [24].

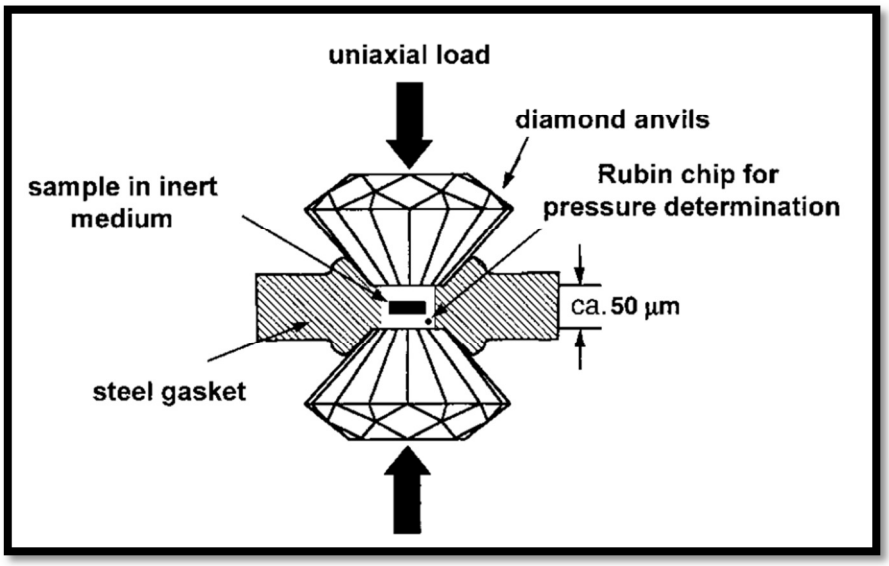


Figure 2.3: Schematic of a two-stage multi-anvil press. Taken from Kroke, 2002 [23].

2.2.2. Densification methods of Si_3N_4

Since silicon nitride is a material exhibiting highly covalent bonds with a very low diffusivity it cannot be sintered through the use of pressure less solid-state sintering. In order to obtain fully dense silicon nitride ceramics it is necessary to apply pressure during sintering and to introduce sintering aids.

For the last 40 years there has been a much better understanding of the role of sintering aids in the densification and microstructural development of silicon nitride based ceramics as well as the impact on the mechanical properties [25].

Through these investigations many forming techniques have been explored for silicon nitride ceramics such as sintered (SSN), gas pressure sintered (GPSN), reaction-bonded (RBSN), sintered reaction-bonded (SRBSN), hot-pressed (HPSN), hot isostatically pressed (HIPSN) and the more recently developed sintering technique, spark plasma sintered (SPS) silicon nitride.

Gas pressure sintering (GPSN) involves sintering the silicon nitride composite under a nitrogen pressured atmosphere (10 MPa) where a direct contact between the nitrogen gas and the sample prevents any decomposition of the Si_3N_4, thus allowing for higher sintering temperatures to be attained. The GPSN route allows for the production of complex shapes required for wear parts, cutting tools and ball bearings. The sintered silicon nitride method (SSN) also utilizes nitrogen as atmosphere however the gas pressure is somewhat lower (up to 0.3 MPa) than that of GPSN whilst sintering. The main advantages of SSN are the low sintering costs, fabrication of complex shapes and the possibility of a continuous sintering production process. However good sinterability is necessary and the composites produced have a lower strength then that of composites produced though the GPSN route. The GPSN is also advantageous over the SSN route due to the superior reproducibility, reliability and the lower additive content requirements [3] [14].

Hot pressed silicon nitride (HPSN) is a technique that is used to obtain densified silicon nitride ceramics. The specimen is placed in a graphite die where an axial pressure is applied by two punches (also graphite) coated with hexagonal boron nitride. This technique results in good densification with high reliability; however this method has low production rate and only simple shapes can be made due to the billet geometry and the fact that the billet will have to be diamond ground. Thus this method is only used in the evaluation of materials as cutting tool prototypes with simple geometries [3].

Hot isostatic pressing sintering (HIPSN) process involves sintering the silicon nitride composite under high isostatic pressure applied through a gaseous or liquid medium which in turn allows for larger and more complicated shapes to be produced in large quantities than the other methods. Particularly for the HIPSN method the compacted green body is coated with a glass that provides protection for the sample from the pressurized gaseous media in the form of a gas-tight membrane. There are two densification methods that are categorized under hot isostatic pressure sintering, the first being HIPSN and the other involves presintering (HIP-SSN). The HIP-SSN method is when the composite is sintered via SSN in order to close the porosity followed by HIPSN and the other method only utilizes a capsule and is known as HIPSN. Both the HIPSN and HIP-SSN techniques allow the production of complex shapes with high reliability however both methods are highly costly. HIP-SSN allows the sinterability of silicon nitride with no additives whereas HIP-SN allows the sinterability with low additives [3].

Reaction-bonded silicon nitride (RBSN) is made by carefully nitriding (N_2) a low cost silicon compact producing Si_3N_4 in the pores of the compact which results in little dimensional changes and a considerable increase in density. RBSN allows the production of parts to be made near net shape without the need of excessive grinding operations. However RBSN produces samples that have high porosity, low hardness and low strength; thus the materials sintered through RBSN are suitable for use mainly as refractory materials. An improvement of the porosity can be achieved by sintering the material obtained through RBSN using SSN, GPSN and HIP-SSN. This material is then classified as sintered RBSN (SRBSN). Low shrinkage and cost of raw materials favour this process; however the time consuming nitriding step required is a drawback [3]. A comparison of some of the various consolidation techniques can be seen in Table 2.1.

Table 2.1: Sintering processes used for silicon nitride based materials and the respective densification [3].

Sintering technique	Sintered Si_3n_4 based ceramics					Reaction bonded Si_3N_4 based ceramics	
	Low gas pressure sintering	Gas pressure sintering	Hot pressing	Hot isostatic pressing		Reaction bonding	Reaction bonding and post-sintering
				Pre-sintering	Capsule		
Acronym	SSN	GPSN	HPSN	HIP-SSN or HIPSN	HIPSN	RBSN	SRBSN or HIP-SRBSN
Starting silicon form	Si_3N_4	Si_3N_4	Si_3N_4	Si_3N_4	Si_3N_4	Si	Si
Additive content (vol. %)	7-20	3-15	2-15	2-15	0-8	0	3-15
Consolidation conditions	1600-1800°C with a nitrogen pressure up to 0.3 MPa	1750-2000°C with a nitrogen pressure up to 10 MPa	1500-1800°C uniaxial pressure in a graphite die	Presintered to closed porosity (SSN) then HPSN at 1750-2000°C with a gas pressure up to 200MPa	1750-2000°C with a gas pressure of 200 MPa	1200-1450°C in a nitrogen atmosphere for dwell times up to 100 hours	Nitridation via RBSN while using SSN, GPSN and HIP-SSN sintering technique
Linear shrinkage (%)	15-22	15-22	< 50	15-22	15-25	≈ 0	< 8-14
Relative density (%)	95-99	98-100	≈ 100	≈ 100	≈ 100	70-88	95-100

2.2.3. Properties of silicon nitride based ceramics

For cutting tool operations it is essential that materials with high hot hardness, fracture toughness and thermal shock resistance be selected. Sintered silicon nitride-based ceramics fall under this classification. However due to the various methods used to consolidate silicon nitride based ceramics different mechanical properties are attained:

Table 2.2: Sintering processes used for silicon nitride based materials and their respective properties [3].

Sintering technique	Sintered Si_3N_4 based ceramics					Reaction bonded Si_3N_4 based ceramics	
	Low gas pressure sintering	Gas pressure sintering	Hot pressing	Hot isostatic pressing		Reaction bonding	Reaction bonding and post-sintering
				Pre-sintering	Capsule		
Acronym	SSN	GPSN	HPSN	HIP-SSN or HIPSN	HIPSN	RBSN	SRBSN or HIP-SRBSN
Additive content (vol. %)	7-20	3-15	2-15	2-15	0-8	0	3-15
Linear shrinkage (%)	15-22	15-22	< 50	15-22	15-25	≈ 0	< 8-14
Relative density (%)	95-99	98-100	≈ 100	≈ 100	≈ 100	70-88	95-100
Strength at 20°C (MPa)	500-900	800-1500	800-1500	800-1500	500 (no additives) and 800- 1500 (with additives)	130-350	500-1000
Toughness ($MPa.m^{1/2}$)	5-8	5-11	5-8	5-11	3 (no additives) and 5-8 (with additives)	2-4	5-11

2.3. Sintering of sialon ceramics

Sialon ceramics are silicon nitride based alloys which are principally made up of the following elements: silicon (Si), aluminium (Al), oxygen (O) and nitrogen (N). Sialon ceramic materials have a large range of compositions and crystal structures due to their dependence on the composition of the material [26].

2.3.1. Modifications sialon phases

Sialons are solid solutions based on silicon nitride, where the α-sialon and β-sialon are isostructural with α- Si_3N_4 and β- Si_3N_4 respectively. The varying changes in properties for the various phases are given in Table 2.3.

Table 2.3: Unit cell parameters, morphology and mechanical properties of both α and β phases of Si_3N_4 and Sialon. Taken from Peng, 2004 [19].

	Unit cell parameter (Å)		Morphology of grains in sintered materials	Mechanical Properties	
	a	c		H_{v10} (GPa)	K_{1c} (MPa.$m^{1/2}$)
α-Si_3N_4	7.748	5.617	Equiaxed	≈20	≈3
β- Si_3N_4	7.617	2.911	Elongated	≈15	≈6
α-Sialon	7.801-7.864	5.679-5.720	Equiaxed Elongated	20-22 20-22	3-3.5 5-6.5
β-Sialon	7.610-7.716	2.911-3.007	Elongated	15-17	5-7

2.3.1.1. α-Sialon

The composition of the α-sialon phase can be described by the following formula [27]:

$$\mathbf{R_xSi_{12-(m+n)}Al_{(m+n)}O_nN_{16-n}} \qquad \textbf{Equation 2.1}$$

Where R represents stabilizing cation and x is the amount of the stabilizing cation with valency v^+. The stabilizing cations that are commonly used are Ca (Calcium), Mg (Magnesium), Li (Lithium), Y (Yttium) and other lanthanoid ions [1].

The m value expresses the amount of Si-N bonds (1.72-1.74Å) that are replaced by Al-N bonds (1.87Å) and is also dependent on the valency of (v^+) and amount (x) of the stabilizing cation (Equation 2.2).The addition of the stabilizing cations compensates for the valence discrepancy created through the replacement of Si-N by Al-N bonds.

$$\mathbf{m = v^+ . x} \qquad \textbf{Equation 2.2}$$

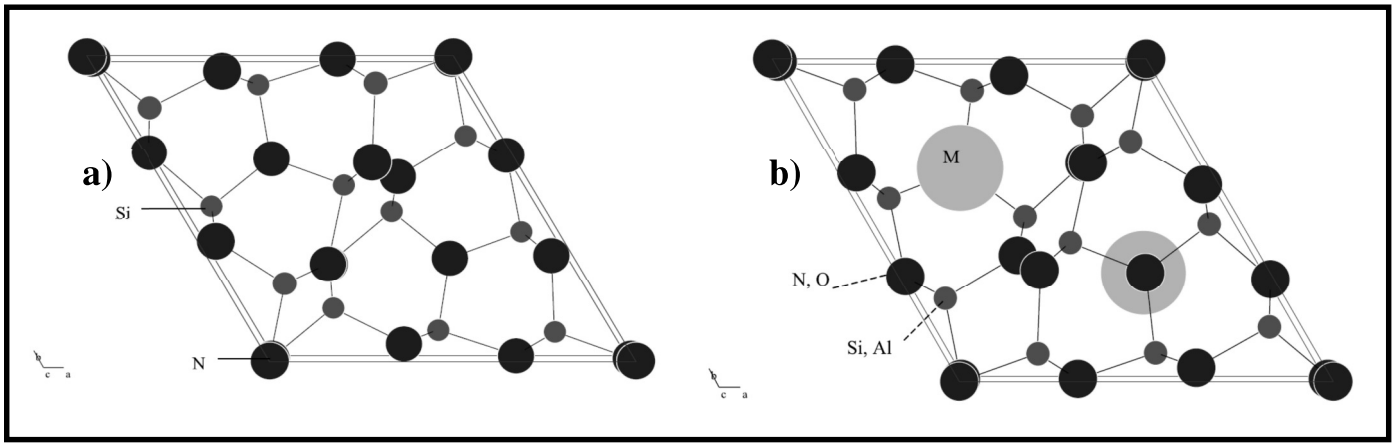


Figure 2.4: Structures of α-Si_3N_4 (a) and α-sialon (b) where M represents the stabilizing cation. Adapted from Petzow et al., 2002 [3].

The n-value on the other hand is related to the substitution of nitrogen (Si-N) by oxygen (Al-O) which can be achieved by replacing the silicon by the aluminum or through the presence of stabilizing cations. [27]. The n-value is also strongly dependent on the oxide solubility in the α-sialon and thus the maximum n-values strongly depend on the sintering temperature [28].

The large and complex phase diagram of the above five-component system, specifically R-Si-Al-O-N, where R=Y (Yttrium) is seen in Figure 2.5 and can be simplified into a quasi-quaternary phase diagram, named the Jänecke Prism and can be identified by the Si_3N_4-4(AlN)-2(Al_2O_3)-3(SiO_2)-2(Y_2O_3)-4(YN) system shown in Figure 2.6.

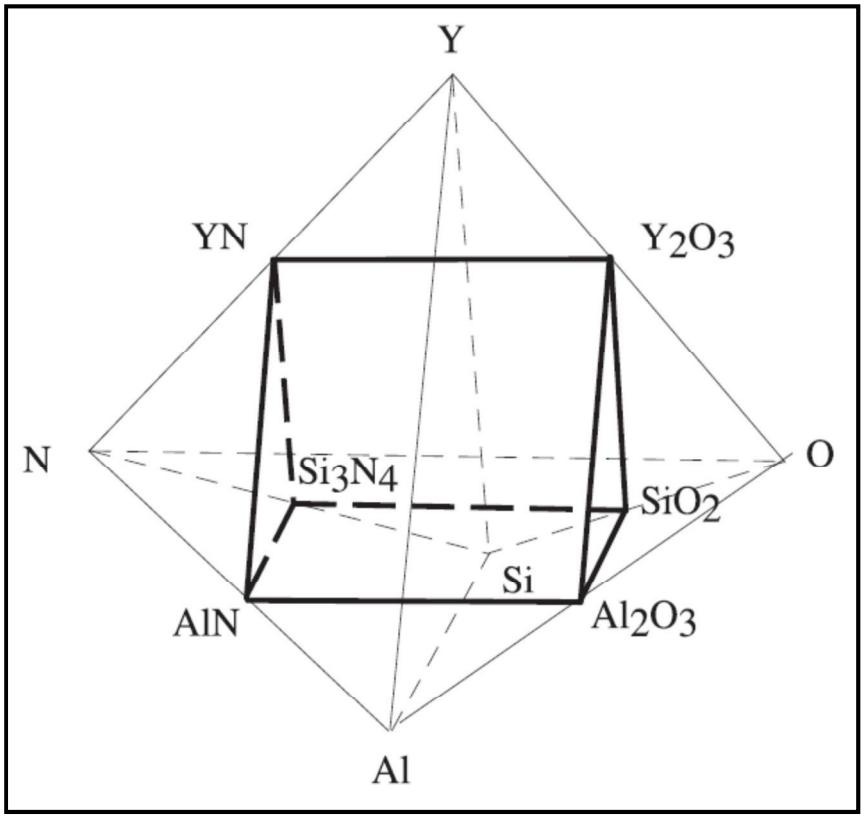


Figure 2.5: The Y-Si-Al-O-N system illustrating the quasi-quaternary subsystem of Si_3N_4-AlN-Al_2O_3-SiO_2-Y_2O_3-YN (Jänecke Prism). Taken from Petzow et al., 2002 [3].

The Jänecke Prism (Figure 2.6) is used to identify the formation of favourable phases in the Y-SiAlON system where examples of these phases are AlN polytypoids, YAG (yttrium aluminium garnet), β-sialon and α-sialon. A stable solid solution of α-Si_3N_4 (α-sialon) exists along the Si_3N_4-4/3(AlN.Al_2O_3)-YN.3AlN plane highlighted, furthermore when the α-sialon plane is enlarged (Figure 2.16) the variables 'm' and 'n' from Equation 2.1 can then be incorporated.

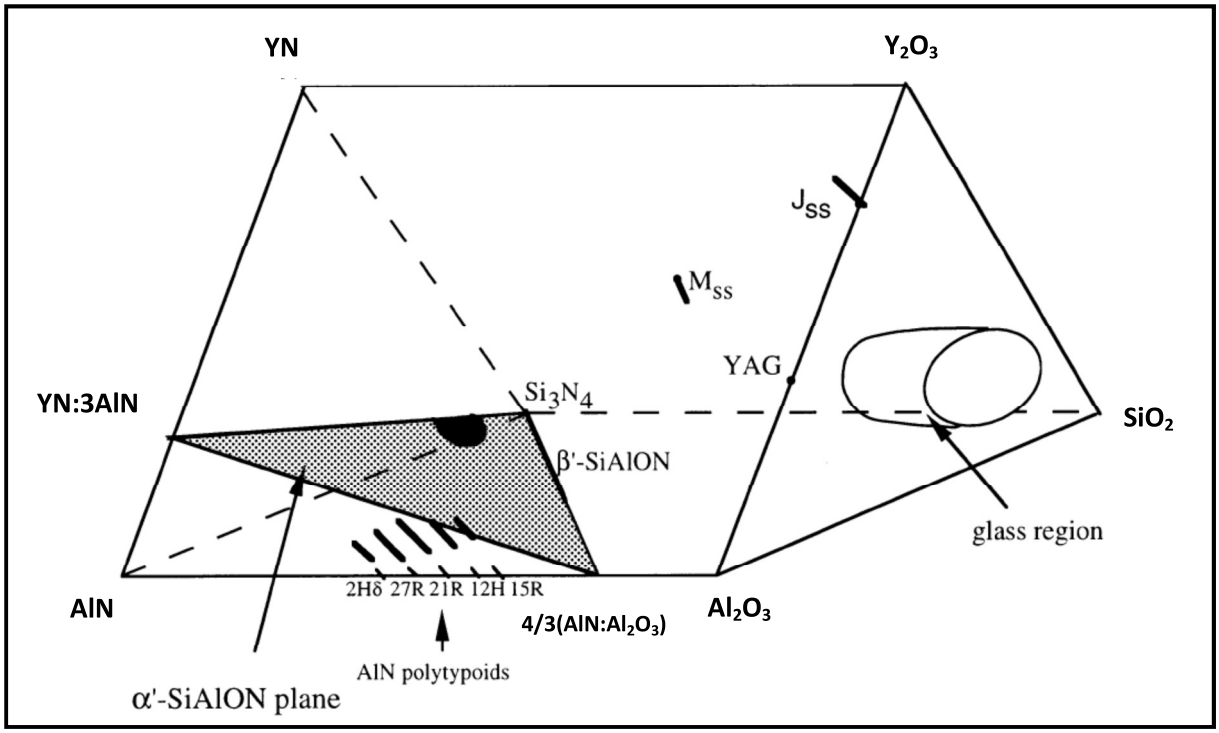


Figure 2.6: Detailed depiction of the Jänecke Prism identifying possible phase formations. The α-sialon plane is highlighted. Adapted from A. Rosenflanz et al., 1999 [29].

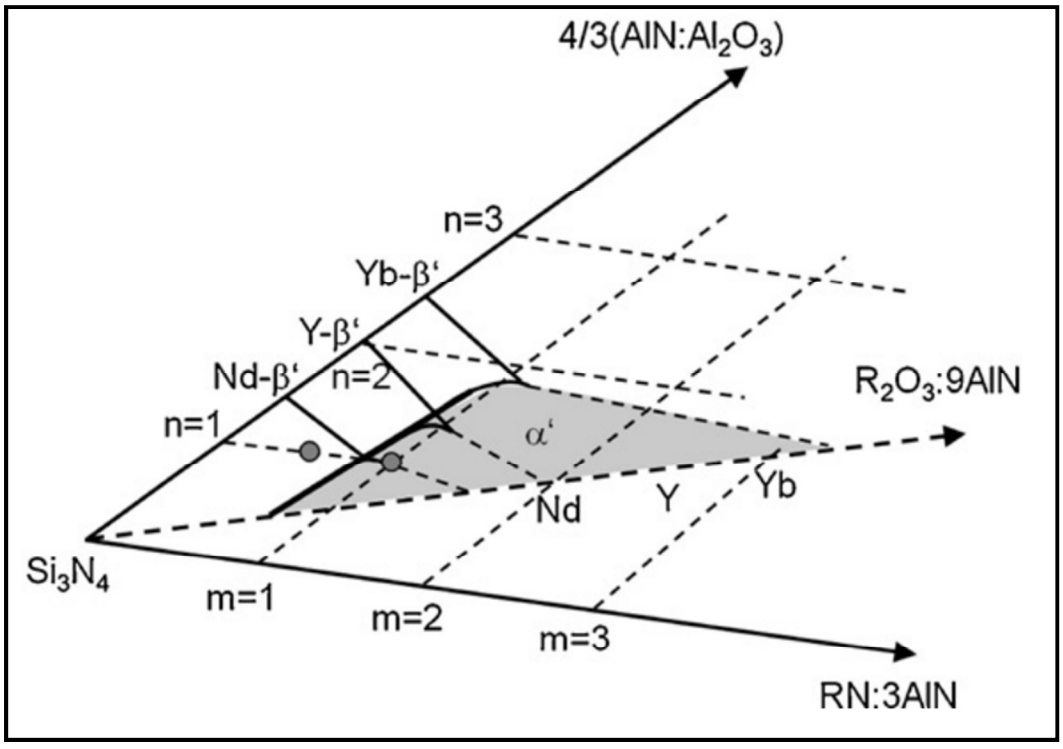


Figure 2.7: The effect of different stabilizing cations and the corresponding m and n values for stable α-sialon ranges used when designing α-sialon ceramics. Taken from Hermann et al., 2011 [2].

Through the use of simplified systems such as those depicted above in Figure 2.7 it is then possible to tailor-make the phases in a sialon ceramic by selecting the respective m and n values and calculating the starting composition required through the use of Equation 2.1. The tailoring of sialon phases can further be completed through the use of different stabilizing cations. It must be noted that the calculated compositions must include all additives as well as their respective oxide films present particularly for non-oxide ceramic powders.

2.3.1.2. β-Sialon

On the other hand, the composition of β-sialon can be represented by Equation 2.3,

$$Si_{6-z}Al_zO_zN_{8-z} \qquad \textbf{Equation 2.3}$$

Where the z value reperesents the number of replaced Si and N by Al and O ions and can vary between 0 - 4.2 depending on the sinering conditions whilst maintaining a metal (cation) to non-metal (anion) ratio of 3 : 4 [30] [31]. The single β-sialon phase is situated along the Si_3N_4-4/3($AlN.Al_2O_3$) line in Figure 2.6 and Figure 2.16.

2.3.1.3. Grain morphology

The β-sialon phase has elongated grain morphology (whisker-like) whereas the α-sialon phase is generally equiaxed; however an elongated morphology has been shown to have evolved [32] [33] [34]. More about this elongated α-sialon morphology will be discussed in Section 2.3.2.5. The AlN polytypoid microstructure appears to be clusters of elongated grains appearing similar to β-sialon however the structure is platelet-like when not cross-sectioned. The various α and β-sialon phases can be seen in Figure 2.8 where the α-sialon was prepared through the use of Nd_2O_3-CaO as a sintering aid [35].

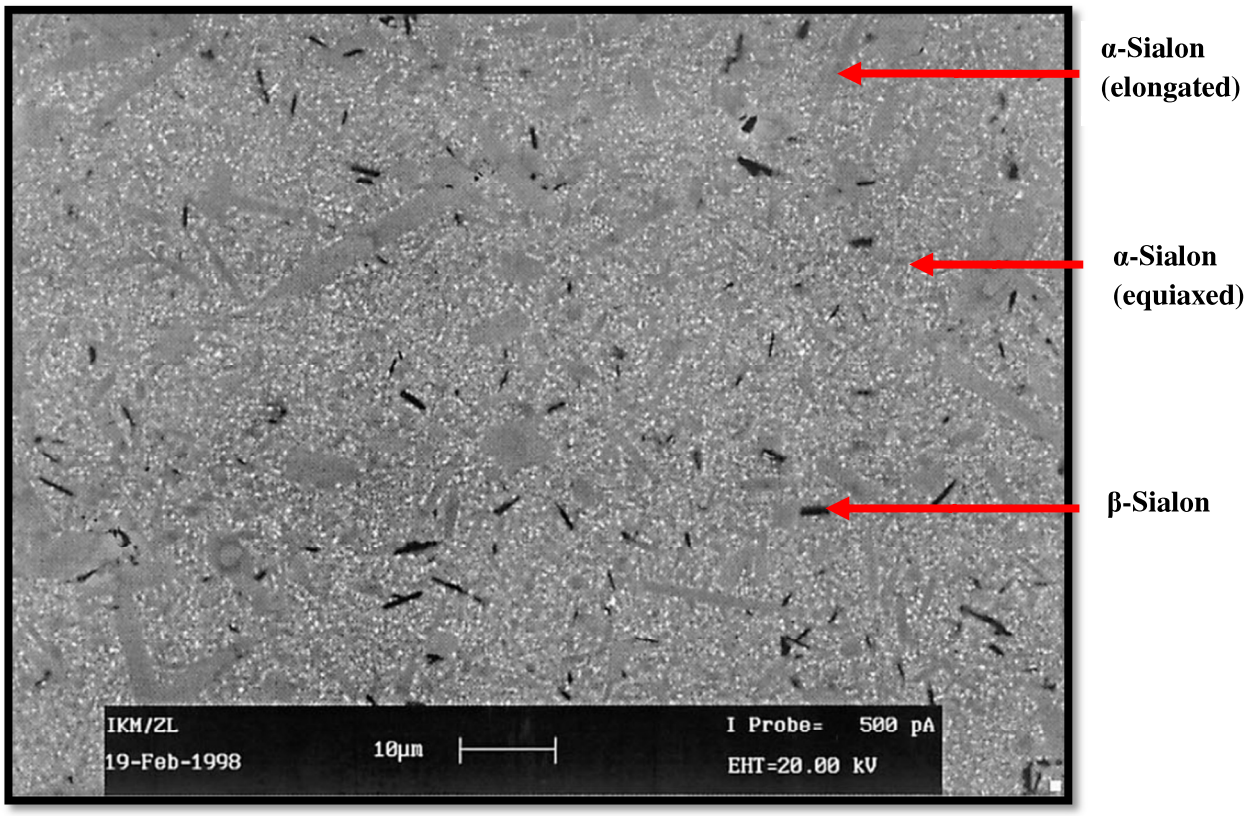


Figure 2.8: SEM micrograph showing the various α and β sialon phases identified.

The elongation of α-sialon grains is due to anisotropic growth; however in order to obtain this elongated morphology a sufficient quantity of rare-earth or alkaline rich liquid must still be present at relatively high temperatures. The decomposition temperature of 1900°C for Si_3N_4 must be accounted for, unless a pressured nitrogen gas atmosphere is experienced [19]. Adding too much extra liquid phase will also impact negatively on high-temperature properties of the sialon due to the softening of the more pronounced intergranular films.

The growth of the elongated α-sialon phase with increasing sintering temperature is shown in Figure 2.9. Furthermore the aspect ratio and volume of the elongated α-sialon phase is shown to increase linearly with the fracture toughness (Figure 2.10) due to the crack deflection and crack branching toughening mechanisms being increasingly present [15].

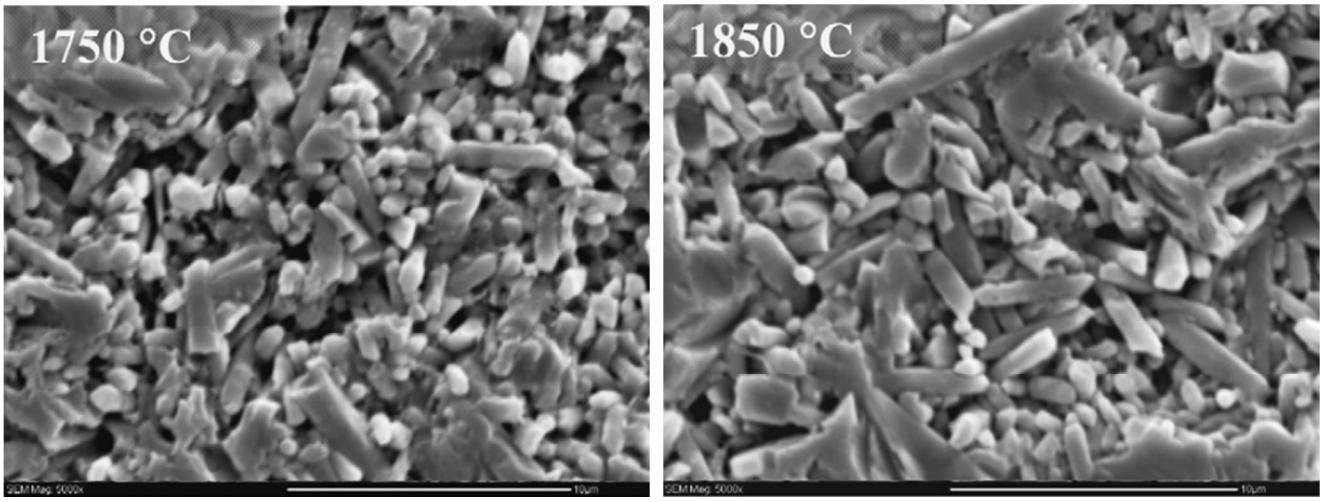


Figure 2.9: SEM micrographs of showing formation of the elongates Y-α-sialon (m=2.0 and n=1.5) compact with increasing temperature. Taken from Zhou et al., 2007 [15].

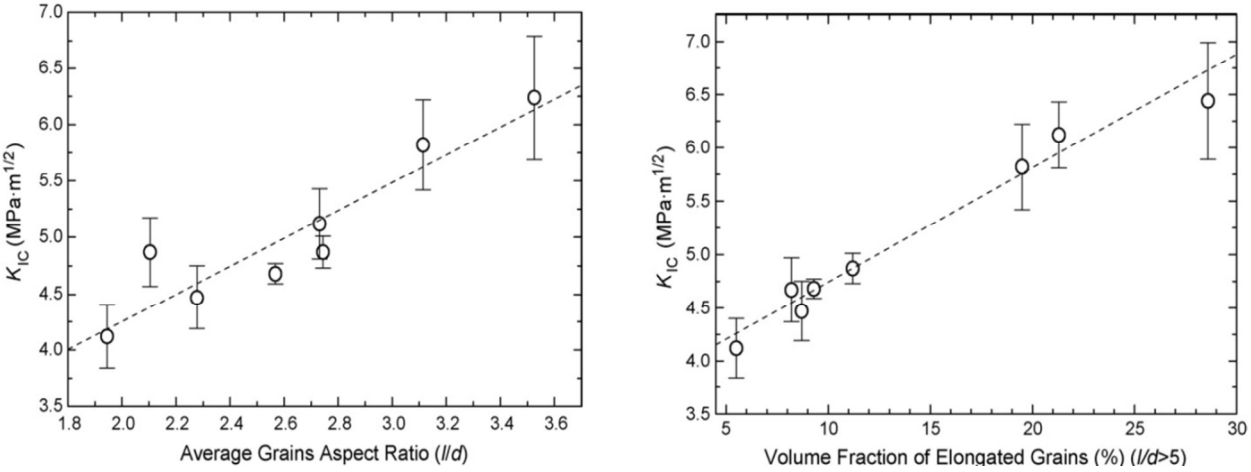


Figure 2.10: Fracture toughness of α-Y-sialon as a function of the average aspect ratio of grains and the volume fraction of elongated grains. Taken from Zhou et al., 2007 [15].

2.3.2. Liquid phase

It is known that silicon nitride is difficult to sinter without additives however through high cost techniques such as hot-isostatic pressure (HIP) methods, it is possible to obtain densified samples due to the adherent silica (SiO_2) on the surface of the Si_3N_4 particles (up to 3 vol. %) which would perform the role of the sintering aid [3]. Thus, through the use of sintering aids such as yttria (Y_2O_3), alumina (Al_2O_3), aluminium nitride (AlN) etc. and the SiO_2 on the surface of the starting powder it is possible to form a melt. The densification mechanism that is appropriate to silicon nitride based ceramics is founded on the Kingerey sintering model [36] [37] [38] [39]. Using α-

Si_3N_4 as a starting powder provides sites for the α-sialon nuclei to form and grow epitaxially; however the growth is strongly dependent on the amount and composition of the liquid phase [40]. There are three steps that lead to the consolidation of silicon nitride ceramics; these steps overlap one another and are referred to as particle rearrangement (I), solution-precipitation (II) and Ostwald ripening (III). These steps are illustrated in the densification curve of a sialon ceramic shown in Figure 2.11. However it must be noted that the particle rearrangement step is important in liquid-phase sintering especially when an external pressure is applied, resulting in rapid initial densification of the sialon composite [41].

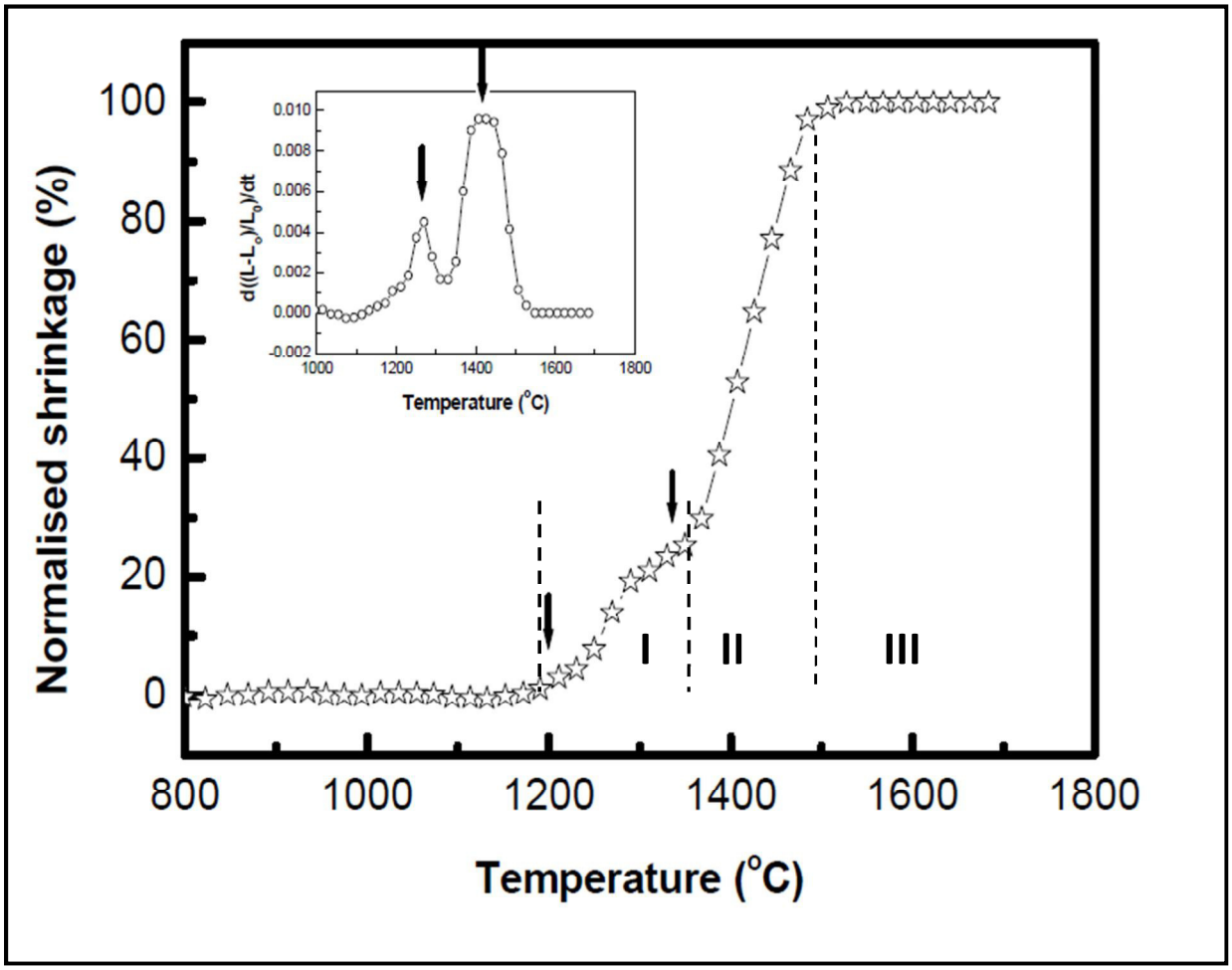


Figure 2.11: Densification curve for α-sialon sintered through the SPS technique. The inset in the top left shows the shrinkage rate as a function of the sintering temperature. The densification steps are highlighted by the denotation I, II and III as the particle rearrangement (I), solution-precipitation (II) and Ostwald ripening (III).

A schematic of the typical densification steps found in sintering β-sialon ceramics is given in Fig. 2.12, however it must be noted the same applies to α-sialon.

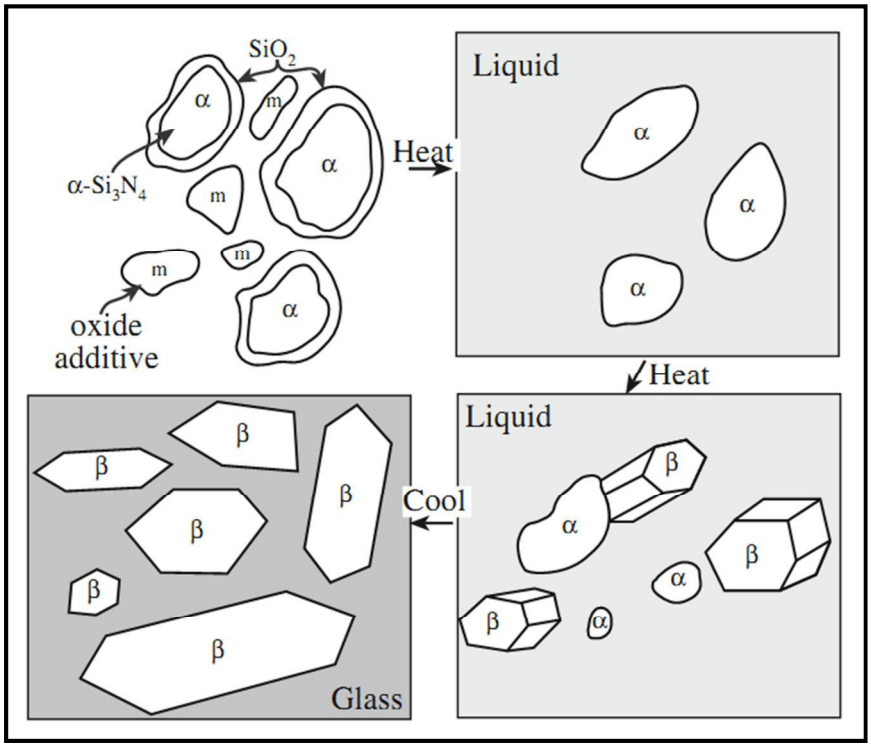


Figure 2.12: An example of the densification steps when forming Si_3N_4 ceramics through liquid phase sintering techniques. Taken from Carter et al. 2007 [10].

The glassy grain boundary phase contributes to the excellent properties such as high strength and fracture toughness in silicon nitride based ceramics; however softening of this phase at high temperatures has a negative effect on the properties of these materials at those conditions [42].

2.3.2.1. Particle rearrangement

The first step of densification occurs directly after any eutectic melt forms and it involves particle rearrangement resulting in the rapid densification where the lubricating wetting liquid penetrates between grains (aiding movement) and exerts an attractive force between them through capillary action which is coupled with the applied pressure during sintering [41]. The liquid eutectic phase eliminates porosity as the system minimizes its surface energy [41]. It is noted that the rearrangement is strongly enhanced by the application of an external pressure.

The formation of the ternary oxide eutectic melt can be seen through the reaction that takes place in the Y-Si-Al-O-N system at approximately ≈ 1340°C [43].

$SiO_2 + Al_2O_3 + Y_2O_3 \rightarrow (Si, Al, Y)O_y + YAG$ **Reaction 2.1**

The melt composition depends strongly on the composition of the starting powders and the eutectic melt would include Si_3N_4 and AlN which would result in the system not being in equilibrium due to the low solubility rate of the nitrides.

For successful liquid-phase sintering the solid phase must be soluble/slightly soluble in the liquid phase in order to aid mass transfer away from contact area; the liquid phase must wet the solid phase sufficiently and be present in amounts sufficient to wet the solid phase. It is also noted that capillary pressure is related to the particle size of the solid phase whereby the finer the particle size the higher the capillary pressure experienced; this in turn increases the densification particularly in the particle rearrangement stage [44]. It is possible however to obtain fully dense samples through only utilizing the particle rearrangement step provided that sufficient liquid phase is present.

2.3.2.2. Solution-precipitation

In the solution-precipitation step it must be noted that initially the predominant Si_3N_4 phase is α-Si_3N_4 as well as the α-sialon being stable in this region and as a result has lower solubility in comparison with β-Si_3N_4 and β-sialon. The β-sialon precipitates out as a prismatic hexagonal structure growing in the longitudinal direction (c-direction) [45]. Moreover smaller grains are more soluble than the larger sized ones and due to this difference in solubility an additional solubility gradient is created in the liquid; thus material is shifted from smaller grains through the action of diffusion in the liquid phase. The increase in the size of the larger grains is a process known as Ostwald ripening where the driving forces are the reduction of the interfacial energy and the capillary force [46]. Ostwald ripening is dependent on the dissolution of the solid into the liquid, the transport through the liquid as well as precipitation [17]. The two possible reactions that occur in the solution-precipitation step of the Y-SiAlON system can be seen below, whereby both reactions precipitate sialon phases [43] however since in this project the work takes place in the region where α-sialon is stable the predominant sialon phase produced will be α-sialon.

2.3.2.3. Ostwald ripening

The third step is the elimination of the closed porosity during which the liquid acts to form more rounded grain morphology; there is a reduction in the diffusion of constituents due to the amount of liquid present being decreased by the formation of α-sialon. Thus the densification slows down considerably. However microstructure coarsening is still experienced due to Ostwald ripening [45]. When sintering Si_3N_4 and sialon ceramics a thin liquid film exists around the grains. Thus no solid phase sintering is experienced. The glassy oxynitride film between grains can be identified through high resolution transmission electron microscopy (HRTEM) imaging, as shown in Figure 2.13.

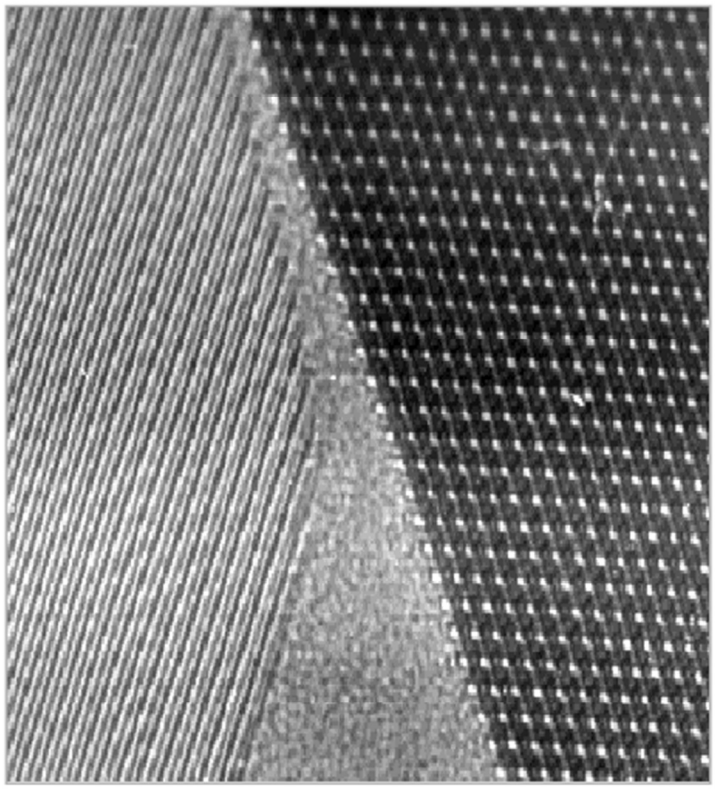


Figure 2.13.: HRTEM image of grain boundary glass film between grains and the triple point between two silicon nitride grains [1].

2.3.2.4. Role of additives on the formation of α-sialon

The value of m in the α-sialon region is dependent on the size of the stabilizing cation and is smallest for large rare earth ions (Er and Yb) and largest for small rare earth ions (Nd and Sm) [28] as shown in Figure 2.17. Thus the maximum stabilizing cation and the oxygen solubility in α-sialon increases with decreasing size of the lanthanides [3]. The α-sialon region is also dependent on temperature and is smaller at low temperatures [28].

A comparative study was completed by Rosenflanz et al., 1999 [29] on the use of various silicon nitride starting powders as well as different stabilizing cations in the preparation of α-sialon ceramics. The size of the stabilizing cations studied by these authors, in an increasing order is as follows: Nd, Sm, Gd, Dy, Y, Er and Yb. The sialon composites were sintered through hot pressing technique at a pressure of 30 MPa and varying temperatures. The effect of different cation type was initially observed through the use of β-Si_3N_4 (0.51 μm) powder followed by 0.5 and 1.25 μm α-sialon starting powders. The relationships are shown in Figure 2.15.

From Figure 2.15, a) the depletion of the β-Si_3N_4 starting powder can be seen to be directly correlated with the formation of the α-sialon phase, as expected. The formation of α-sialon is favoured for the larger cations namely Yb, Er and Y; the reason for this was considered to be the fact that the viscosity of the glassy phase decreases with increasing size of the stabilizing cation [47]. Intermediate phases were also formed when using rare-earth cation sialon systems and the amount of these intermediate phases increases with smaller sized rare-earth cations; the volume fraction of these phases however decreases with temperature.

A similar relationship for fine and coarse α-Si_3N_4 starting powders (Figure 2.15, b and c) was obtained to that of α-sialon sintered with β-Si_3N_4 as a precursor. Sintering sialon with α-Si_3N_4 starting powders is kinetically favourable over β-Si_3N_4 as they are less stable requiring a lower driving force. The α-sialon phase is favoured and formed at lower sintering temperatures. The formation of α-sialon is also affected by the size of the Si_3N_4 starting powders. This comparison is shown in Figure 2.15 b and c where it is revealed that the smaller sized starting powder compacts begin sintering ≈ 100°C lower than that of the coarser grained powder.

Herrmann et al., 2011 [2] reported that the absence of rare-earths in the melt, produced when sintering sialons, will result in the formation of polytypes and β-sialon rapidly reducing the liquid phase present. Furthermore this would result in reducing densification and grain growth as shown in Figure 2.14. A liquid phase with a high content of alkaline or rare-earth cations throughout sintering was also shown to promote the formation of elongated α-sialon grains by enabling anisotropic growth. When sintering α-sialons with excess stabilizing cations these cations are absorbed into the α-sialon and promote polytypoid formation. Through further heat treatment it is possible to dissolve the polytypes, but only slightly.

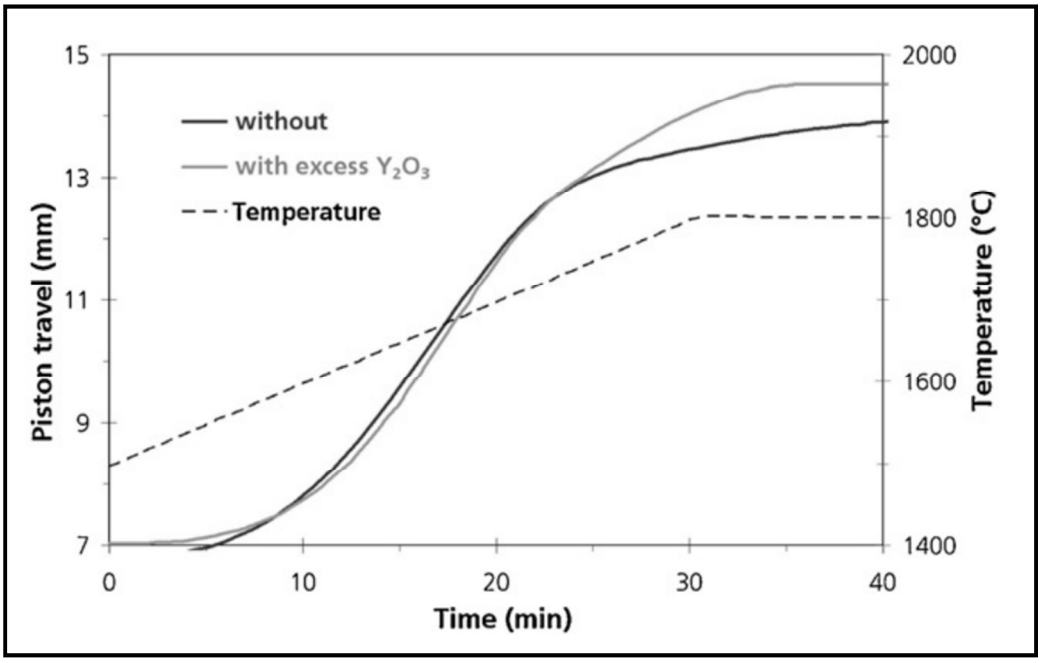


Figure 2.14: Densification curves during hot pressing of Y-α-sialon (m=1.2 and n=1) with and without additional yttria (1.4 wt. %) [2].

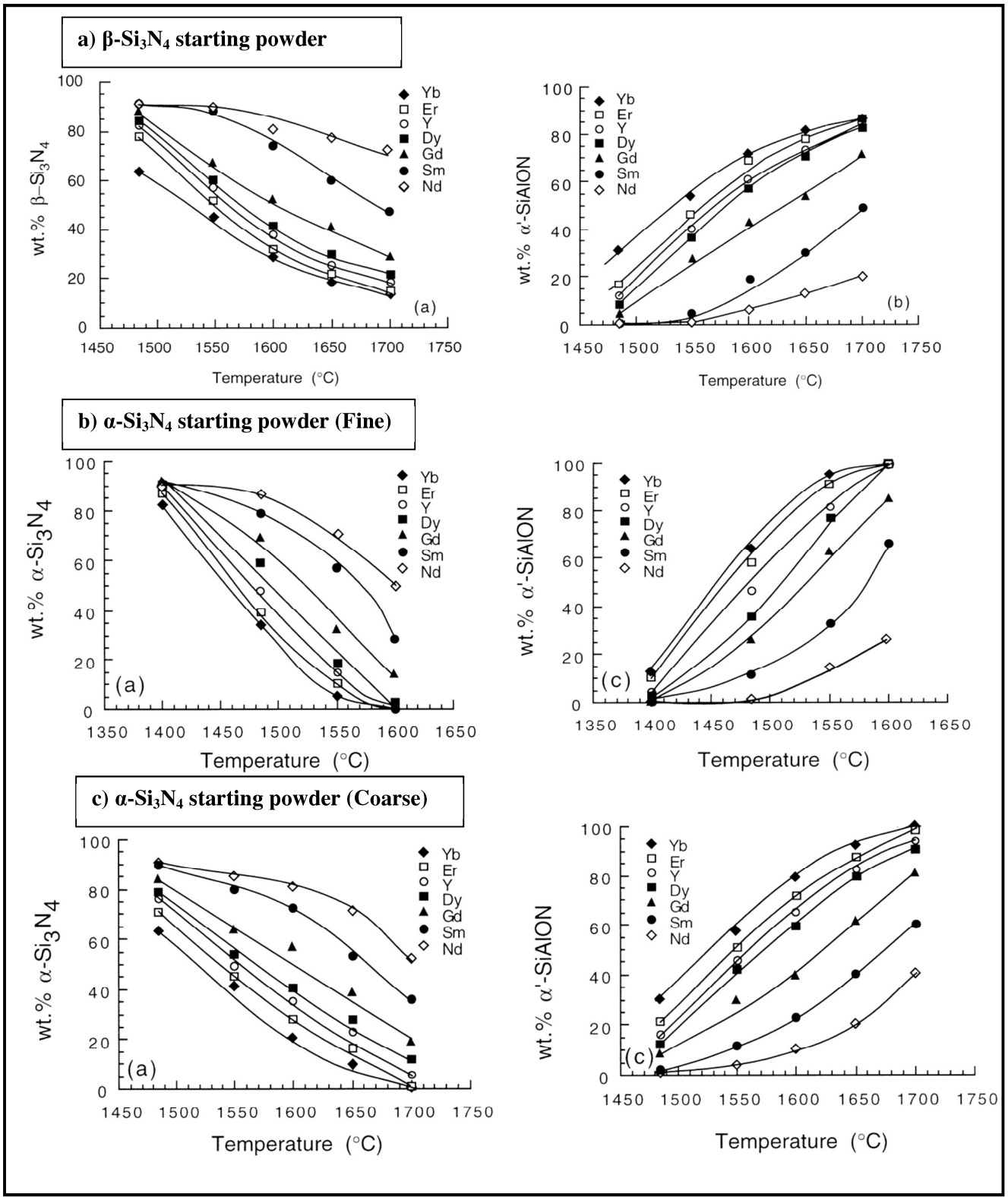


Figure 2.15: The dissolution of the various starting powders and the effect on α-sialon with respect to sintering temperature and stabilizing cation. Adapted from Rosenflanz et al., 1999 [29].

From Figure 2.16 it is further revealed that increasing cation size and sintering temperature promotes the formation of α-sialon however with increasing cation size the limit of m pertaining to the α-sialon solubility region is reduced, illustrated in Figure 2.17.

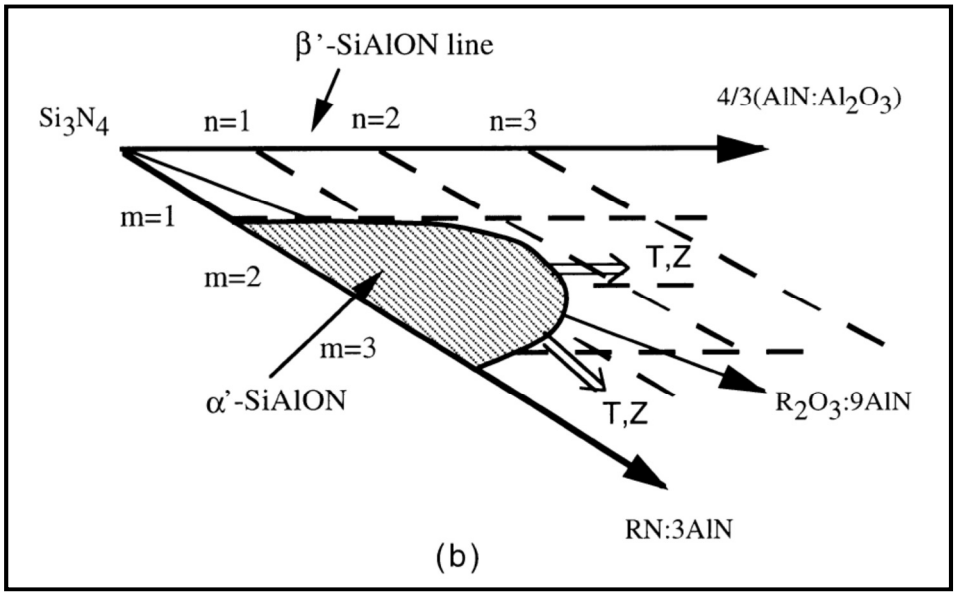


Figure 2.16: α-sialon plane represented by the Si_3N_4-4/3(AlN.Al_2O_3)-YN-3AlN subsystem in the Jänecke Prism. Taken from A. Rosenflanz et al., 1999 [29].

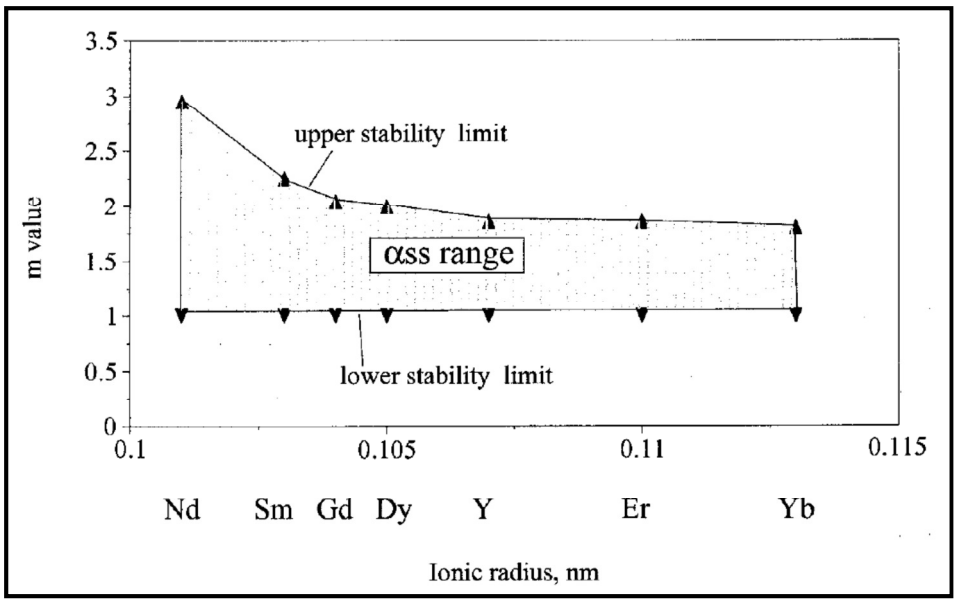


Figure 2.17: The range of possible m-values in α-sialon as a function of increasing ionic radii of the stabilizing cation. Taken from Petzow et al., 2002 [3].

2.3.2.5. Properties of α-sialon ceramics

The properties of the sialon ceramics are strongly dependent upon the composition of the α and β-sialon content and the residual glass phase due to their respective properties. Sialon ceramics are an attractive low-cost alternative to HPSN used in the machining of grey cast iron [13]. The advantages of sialon cutting tools over HPSN and other conventional cutting tools can be attributed to increases in the machining speed and tool life [13]. Sialons have replaced cemented carbide in the machining of nickel and titanium-based superalloys used in the aerospace industry as well as grey cast iron in the automotive industry [6].

α-Sialon is advantageous over β-sialon ceramics primarily due to the amount of the intergranular phase being reduced as the yttrium is absorbed into the α-sialon structure during sintering (See Figure 2.4). However the fracture toughness of β-sialon ceramics is superior to that of α-sialon based ceramics due to their elongated grains. Mandal, 1999 [35] further confirmed this when α-sialon ceramics doped with Nd_2O_3-CaO were sintered using a hot isostatic press at 1850°C for 1.5 hours under an argon gas pressure of 1 MPa, further sintering was carried out for an additional 1.5 hours under a gas pressure of 50 MPa. From Table 2.3 and Table 2.4 it is again seen that sialon ceramics made predominantly from elongated α-sialon grains have superior fracture toughness to that obtained for the equiaxed grains.

Table 2.4: Room temperature mechanical properties of Nd_2O_3-CaO doped α-sialons [35].

Morphology of α-sialon grains	H_{v10} (GPa)	K_{IC} (MPa.m$^{0.5}$)
Equiaxed	19.76	3,96
Elongated	19.30	6.31

From Table 2.3 the difference in properties between α and β-sialon phases are given, showing that the α-sialon phase (H_{v10} = 20-22 GPa) is harder than the β-sialon phase (15-17 GPa). Furthermore the fracture toughness of β-sialon (5-7 MPa.m$^{0.5}$) is superior to that of equiaxed α-sialon (3-3.5 MPa.m$^{0.5}$). However the elongated α-sialon phase maintains the high hardness while having increasing fracture toughness (from 3-3.5 to 5-6.5 MPa.m$^{0.5}$) due to the fact that

crystals with elongated rod-like grain structure possess better resistance to crack propagation [48]. Thus by having an interlocking structure of both α and β-sialon the fracture toughness can be increased at the expense of the hardness however this compromise can result in longer tool life by increasing damage tolerance [49].

Since α and β-sialon phases are completely compatible, composites consisting of a combination of α and β-sialon phases can be prepared by using the appropriate starting composition. These compacts exhibit an increase in the hardness as opposed to pure β-sialon however not as high as obtained in monolithic α-sialon [35]. Similarly for the fracture toughness of α-sialon phases with respect to monolithic β-sialon. High temperature operating conditions are limited by the softening of the intergranular film whereby service temperatures exceeding 1000°C results in significant deterioration of the important oxidation and creep resistance properties [35].

It was shown that different sialon phase compacts could be sintered at 1850°C for 2 hours by varying the phase composition and using a 1 MPa nitrogen gas atmosphere. Some samples were subsequently heat treated at 1400°C for 2 hours with a nitrogen gas pressure of 0.1 MPa. The modulus of rupture was then measured at elevated temperatures of 1200, 1300 and 1350°C and compared to that obtained at room temperature. The mechanical properties of these sialon compacts can be found in Table 2.5, together with the modulus of rupture and respective retention of the strength for the various sialon compacts [50].

From Table 2.5 it can be seen that the α-sialon compacts retain their strength at elevated temperatures as compared to α/β and β-sialons. However it must be noted that the room temperature strength is inferior as compared to these composites. The heat treated samples showed improved preservation of the room temperature strength as compared to those sintered without a heat treatment step. When comparing the fracture toughness and strength of monolithic α and β-sialon compacts it is seen that β-sialon has a lower fracture toughness and a considerably higher strength compared to α-sialon. Sialon ceramics maintain their strength at higher temperatures when compared with cemented carbides, alumina, and black ceramic (Al_2O_3/TiC) also their hot hardness is superior to these ceramics as shown in Figure 2.18. It must also be

noted that the hardness of sialon ceramics increases with increasing α-phase content at room and high temperatures [6] [51].

Table 2.5: Mechanical properties of various sintered sialon ceramics and their respective retention (%) of room temperature modulus of rupture at elevated temperatures [50].

Phases	Density (%TD)	Hardness (kg/mm^2)	Fracture toughness ($MPa.m^{0.5}$)	Modulus of rupture (MPa)			
				Room temperature	Retention of room temperature strength (%)		
					1200°C	1300°C	1350°C
α-sialon	98.13	2020	4.66	464 ± 54	70.7	-	40.7
Heat treated					92.7		77.8
α/β-sialon (2:3)	99.40	1760	5.59	763 ± 26	62.1	57.6	38.2
Heat treated					72.7	73.8	76
β-sialon	98.82	1640	4.72	745 ± 80	59.6		36.6

Thermal shock resistance is an important property when considering a material for cutting tool application. This is a result of the rapid changes in temperature experienced during cutting (through friction, the presence of cooling fluid and the process of interrupted cutting). Silicon nitride based ceramics exhibit superior thermal shock resistance where they are able to withstand quenching in cold water from 800 - 1000°C whereas zirconia and alumina ceramics can only tolerate 200 - 400°C [52].

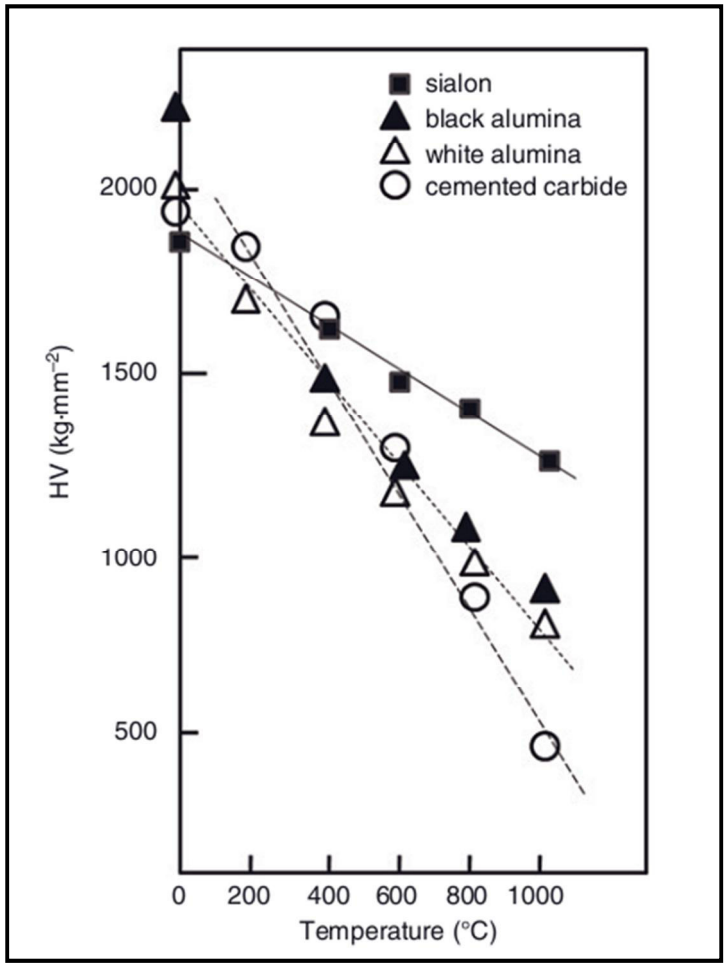


Figure 2.18: The hot hardness of various cutting tool ceramics. Taken from Heinmann, 2010 [13].

2.3.2.5.1. Pressureless sintering

Different compositions of Y-α-sialons were successfully sintered pressurelessly (> 98% theoretical density) between the temperatures of 1750 and 1920°C by Zhou et al., 2007 [15].The green compact was initially isostatically pressed at 225 MPa for two minutes and then placed in a vacuum graphite furnace heated under an atmosphere of nitrogen (~0.1 MPa) and held at the sintering temperature for a dwell time of two hours. The effects of two of the compositions sintered will be presented here; these are Y1515 and Y2015, where the first and last two numerical digits pertain to the value of m and n respectively. As an example, Y2015 would have an m value of 2.0 and an n value of 1.5.

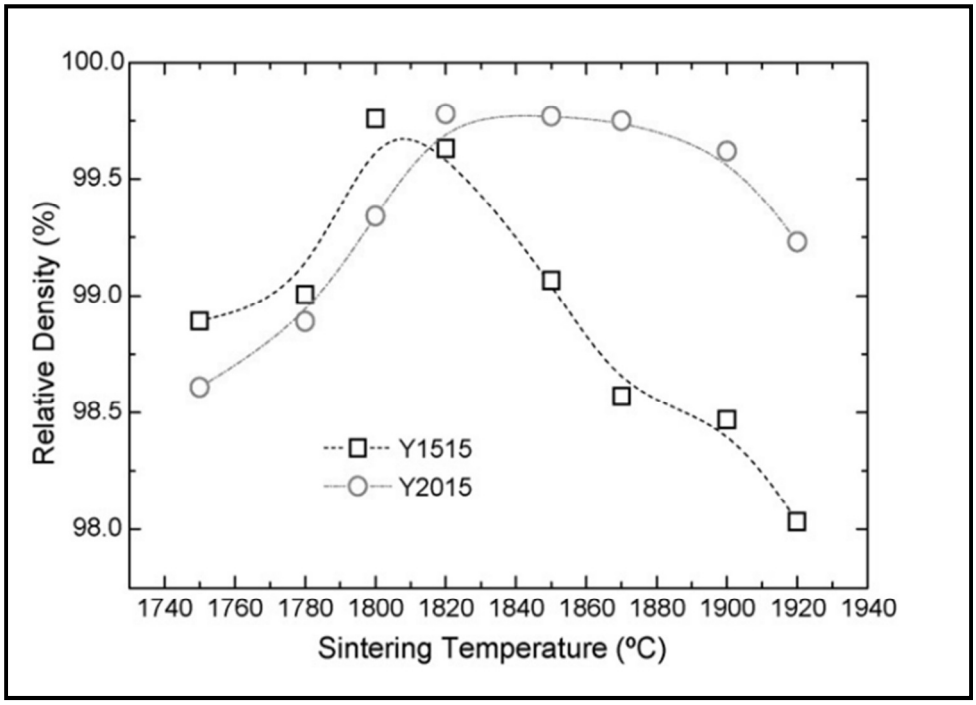


Figure 2.19: Relative densities for Yα-sialons pressurelessly sintered as a function of the sintering temperature. Taken from Zhou et al., 2007 [15].

From Figure 2.19 it could be seen that a maximum in density was achieved between the temperatures of 1800-1820°C. However a decrease in density was seen at temperatures exceeding 1820°C. This according to Zhou et al., 2007 is due to the decomposition of Si_3N_4 into silicon crystal and nitrogen. The effect of density on the Vickers hardness is shown in Figure 2.20, where an expected increase in the hardness with increasing relative density is observed.

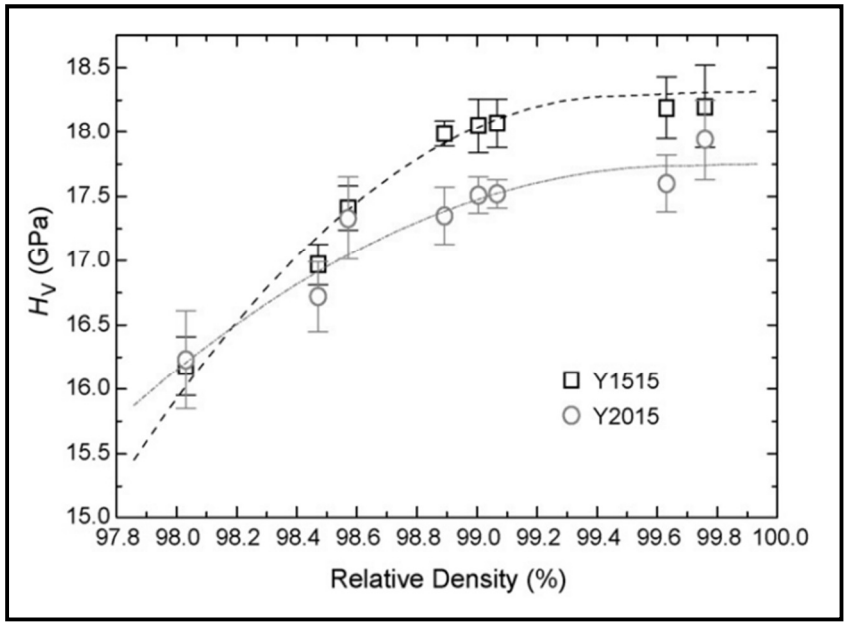


Figure 2.20: The effect of relative density on the hardness values obtained for Y-α-sialons. Taken from Zhou et al., 2007 [15].

The effect of the grain aspect ratio on the fracture toughness for samples sintered at different temperatures is shown in Figure 2.21, where a linear relationship is observed. It was found that the elongated α-sialon grains were uniformly distributed in a matrix of equiaxed grains and thus the interlocking microstructure allows for materials to have mechanical properties as high as 17.6 GPa and 6.2 MPa.m$^{0.5}$ for the Vickers hardness (H_{v10}) and fracture toughness respectively.

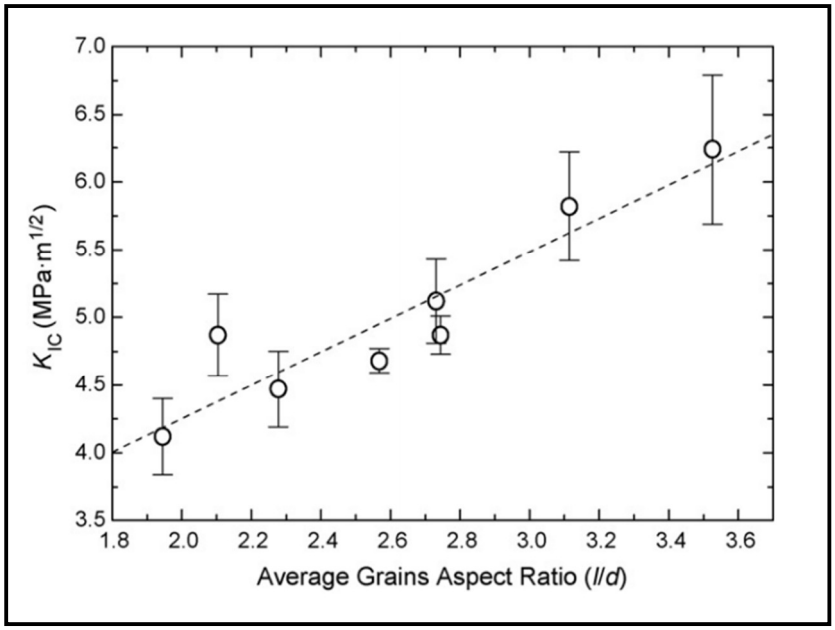


Figure 2.21: The effect of the average grain aspect ratio on the fracture toughness values of Y-α-sialons showing a linear relationship. Taken from Zhou et al., 2007 [15].

2.3.2.5.2. Hot isostatically pressed

Ye et al., 2004 [53] prepared dense Y-doped α and α/β-sialon composites from α-Si_3N_4 by hot isostatic pressing at 1800°C for 1 hour under an argon gas pressure of 1 MPa. The scope of research included using Equation 2.1 and varying the m value from 0.2 to 1.0 in increments of 0.2. The n value was taken to be constant however in each composition a 2 weight percent increase in yttria to aid full densification (denoted as E2). The α and β compositions and relative density for the composites sintered through HIPing is found in Table 2.6 and the effect of varying the m value on the mechanical properties is seen in Figure 2.22.

Table 2.6: Showing the starting m and n values used in the study by Ye et al., 2004 [53], the composition of α and β-sialon and percentage of the theoretical density of the various Y- sialon composites sintered at 1800°C.

Sample	m value	n value	Phase composition		Percentage theoretical density (%)
			α	β	
Y0210-E2	0.2	1.0	38	62	99.762
Y0410-E2	0.4	1.0	68	32	99.583
Y0610-E2	0.6	1.0	82	18	99.564
Y0810-E2	0.8	1.0	100	0	99.753
Y1010-E2	1.0	1.0	100	0	98.809

From Table 2.6 it can be seen that increasing the m-value results in the favourable formation of α-sialon at the expense of the β-sialon. This formation would result in a sialon composite with higher hardness but decreased fracture toughness due to the intrinsic properties of the α and β-sialon phases. This relationship is revealed in Figure 2.22.

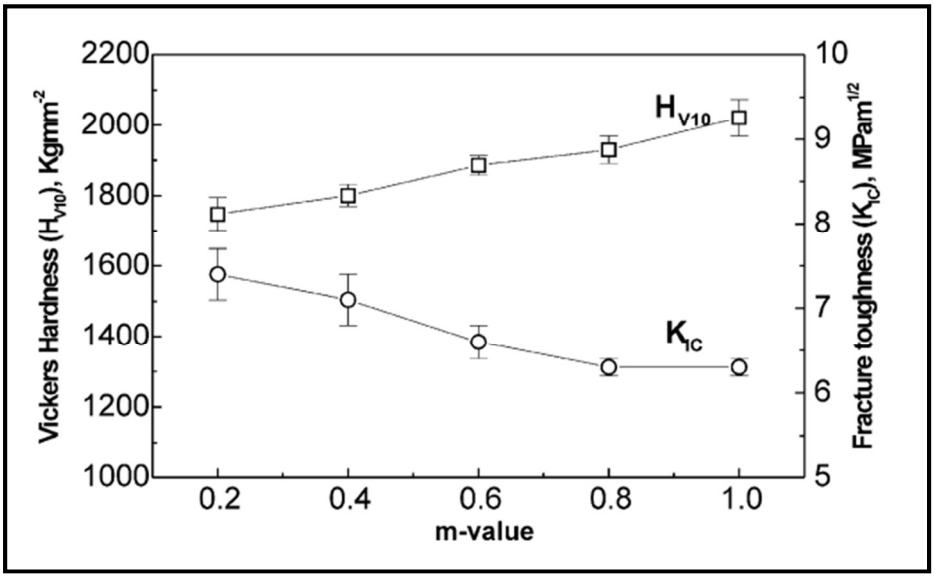


Figure 2.22: Indentation fracture toughness and the Vickers hardness (H_{v10}) of Y-α-sialons HIP-sintered at 1800°C for 1 hour with respect to the varying m value. Taken from Ye et al. , 2004 [53].

Olsson et al., 1990 [54] prepared β-sialon as well as mixed α/β-sialons through glass-encapsulated hot isostatic pressing technique using Y_2O_3 and La_2O_3 as sintering aids. The HIP-ing was carried out at two different sintering temperatures, 1550 and 1825°C with a dwell time of 2 hours. The compacts were placed under a 200MPa pressure of argon. It was found that sintering the various sialon composites at the temperature of 1550°C un-reacted α-Si_3N_4 was present as well as β-sialon and other secondary phases. Furthermore the samples sintered at 1825°C showed that the yttrium favoured the formation of α-sialon as compared to La_2O_3. The yttria also favours the formation of intergranular phase increasing the amount by as much as 50 % when La_2O_3 is replaced with Y_2O_3. Lastly it was observed that the fracture toughness of β-sialon doped with La is similar to that of Y-doped, however the hardness is inferior.

2.3.2.5.3. Gas pressure sintered

Kurama et al., 2002 [40] sintered a range of Y-α-sialon ceramics through the use of a gas pressure sintering furnace with a nitrogen atmosphere of 50 MPa . The sintering temperature used for the gas pressure sintering was 1825°C for 3 hours. There were variations in the sintering profile; specifically some samples were heated straight up to the dwell sintering temperature of 1825°C and others had a dwell period at 1500 and 1600°C for one hour each. The mechanical properties as well as the content of the α-sialon for some samples sintered in this project are shown in Table 2.7.

Table 2.7: Results obtained by Kurama et al., 2002 [40] for the various Y-α-sialon ceramics.

Sample name	Cation Ratio (m,n)	Sintering conditions	Density (g/cm^3)	α/(α+β) (%)	H_{v10} (GPa)	K_{1C} ($MPa.m^{0.5}$)	Strength (MPa)
ZY 1f	2.36 (0.44, 0.76)	1825°C/3 hours	3.274	81	1878 ± 26	4.4 ± 0.1	-
		1500°C/1 hours → 1825°C/3 hours	3.272		1824 ± 34	4.2 ± 0.1	638 ± 15
ZY 2c	1.61 (0.59, 0.98)	1825°C/3 hours	3.263	93.7	1976 ± 38	5.3 ± 0.1	-
		1500°C/1 hours → 1825°C/3 hours	3.245		1880 ± 23	5.6 ± 0.1	599 ± 75
ZY 2e	1.94 (0.59, 0.98)	1825°C/3 hours	3.276	96.3	1923 ± 50	5.4 ± 0.1	-
		1500°C/1 hours → 1825°C/3 hours	3.278		1962 ± 37	5.0 ± 0.1	676 ± 35
ZY 3b	1.43 (0.91, 0.98)	1825°C/3 hours	3.287	100	1808 ± 33	5.4 ± 0.1	-
		1500°C/1 hours → 1825°C/3 hours	3.307		1856 ± 50	4.4 ± 0.1	532 ± 50
ZY 3d	1.69 (0.91, 0.98)	1825°C/3 hours	3.314	100	1869 ± 26	3.9 ± 0.1	-
		1500°C/1 hours → 1825°C/3 hours	3.313		1864 ± 30	3.5 ± 0.1	491 ± 70
ZY 4a	1.20 (1.12, 1.17)	1825°C/3 hours	3.271	100	1823 ± 34	6.0 ± 0.1	-
ZY 4b	1.43 (1.12, 1.17)	1825°C/3 hours	3.314	100	1871 ± 25	4.3 ± 0.1	-
		1500°C/1 hours → 1825°C/3 hours	3.305		1817 ± 38	3.9 ± 0.1	-
		1600°C/1 hours → 1825°C/3 hours	3.298		1865 ± 28	4.8 ± 0.1	-
β-Si_3N_4 * (Comparison)				0	1480 ± 50	5.2 ± 0.1	920 ± 40

* β-Si_3N_4 material with 6 wt. % Y_2O_3 and 4 wt. % Al_2O_3.

The Y-α-sialon composites sintered with an additional holding period at 1500 or 1600°C showed a decrease in the final density. This was attributed to the formation of α-sialon at lower temperatures, thus significantly reducing the amount of liquid phase available for liquid phase sintering [40]. Furthermore the intermediate holding step led to a more uniform structure as opposed to that continually sintered at 1825°C. Some α-sialon composites have fracture

toughness comparable to, or even better than that of β-Si_3N_4 used for comparison. This is due to the formation of elongated α-sialon grains; the strength however is far superior for the β-Si_3N_4. This was attributed to higher defect sizes resulting from the inhomogeneous α-sialon formation [40].

2.3.2.5.4. Commercial sialon materials

The properties of a range of commercial sialon ceramics from Hitachi Metals America, Ltd and International Syalons Ltd. are shown in Table 2.8 where pure HPSN (no additives) was used as a benchmark showing significant improvements in the mechanical properties [13].

Table 2.8: Selected properties for commercial sialon ceramics with pure Si_3N_4 as comparison [13].

Property	Selected sialon specifications					Si_3N_4
	HCN-10 [a]	HCH-40 [a]	HSN-65 [a]	Syalon 101 [b]	Syalon 050 [b]	
Sialon phase	β	β	β	β	α/β	
Density (g/cm^3)	3.26	4.00	3.20	3.23	3.23	3.2
Flexural strength (MPa)	880	830	1050	-	-	600
Fracture toughness ($MPa.m^{1/2}$)	7.5	6	-	7.7	6.5	5.9
Hardness (GPa)	15.5	15.2	14	15	20	14.7
Modulus of elasticity (GPa)	290	330	-	288	300	300
Thermal shock resistance (ΔT)	710	400	-	900	600	> 800
Coefficient of thermal expansion ($x10^6 K^{-1}$)	3	3.1	3	3	3.2	3
Thermal conductivity ($W.m^{-1}.K^{-1}$)	17	25	65	21	20	> 80
Electrical resistivity (Ω.m)	$> 10^9$	10^7	10^{13}	10^{10}	10^{10}	$> 10^{13}$

[a] Hitachi Metals America, Ltd. [b] International Syalons Ltd., Newcastle, UK

From literature it is known that the properties of Si_3N_4 ceramics are dependent on sintering conditions and composition, therefore the values for this material given in Table 2.8 are not to be taken as set properties of Si_3N_4 but should be used merely for comparative purposes. Properties such as flexural strength have a range of values from 400 up to 1000 MPa for Si_3N_4, but are predominantly between 800-900°C when sintered with various additives and sintering conditions [55].

2.3.3. FAST/SPS densification of sialon composites

Similarly to hot pressing, the field-assisted sintering (FAST) and spark plasma sintering (SPS) techniques also utilize a graphite die with uniaxial pressure being applied by two rams coated with hexagonal boron nitride. However these sintering techniques utilize a pulsed direct current through the electrically conductive graphite die assembly to heat the compact. This enhances the densification [56].

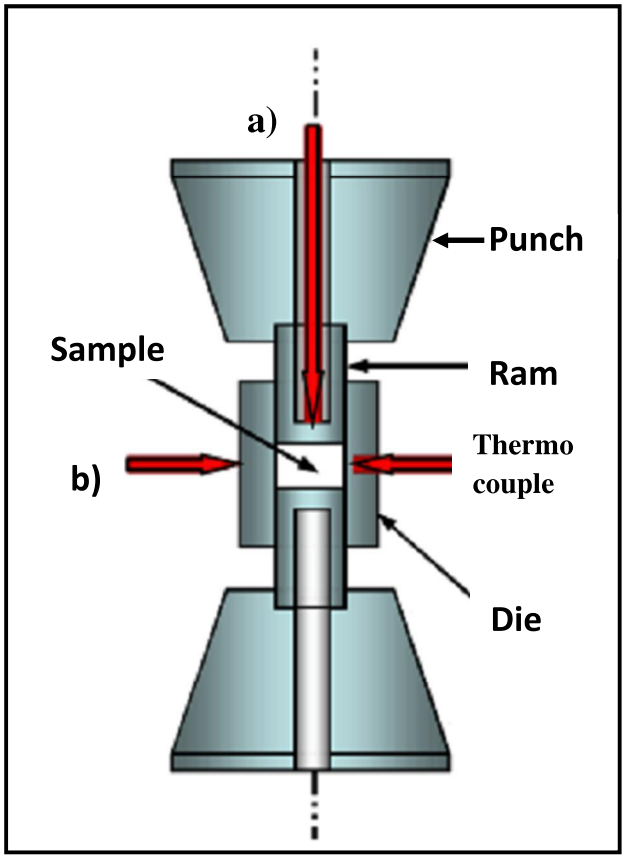


Figure 2.23: Schematic of the tool assembly for the SPS consolidation technique showing the different graphite tooling. The optical pyrometer measurements are commonly taken at two positions a) 5mm above the top of the sample and b) on the outer-radial wall of the graphite die. Adapted from Langer et al., 2010 [57].

The high heating rates are attributed to the resistance to the current passing through the die assembly and compact. The die assembly acts as an additional heating source to the compact. Enhanced densification of ceramic materials through SPS is attributed to the high-temperature or high-energy plasma that is generated between the voids of the powder particles. Full densification of the silicon nitride ceramic powder is possible at considerably lower temperatures (1400-1600°C) with shorter dwell times as compared with HPSN or other methods [58] [19]. Through SPS consolidation fast heating and cooling rates are achievable (up to 600 K/min) as well as good temperature distribution in electrically conducting materials; thus grain growth is greatly reduced as compared to other sintering methods. For electrically conductive materials sintered through SPS, the pulsing direct current is thought to increase densification through the generation of spark plasma, spark impact pressure, joule heating and an electrical field diffusion effect as the current passes through the sample [59]. However in non-conducting starting powders the current is not passed through the sample; instead the pulsing current is used to heat the die. The temperature and current density profiles that are present in configurations involving both non-conducting (Si_3N_4) and conducting (tungsten carbide) samples are shown in Figure 2.24.

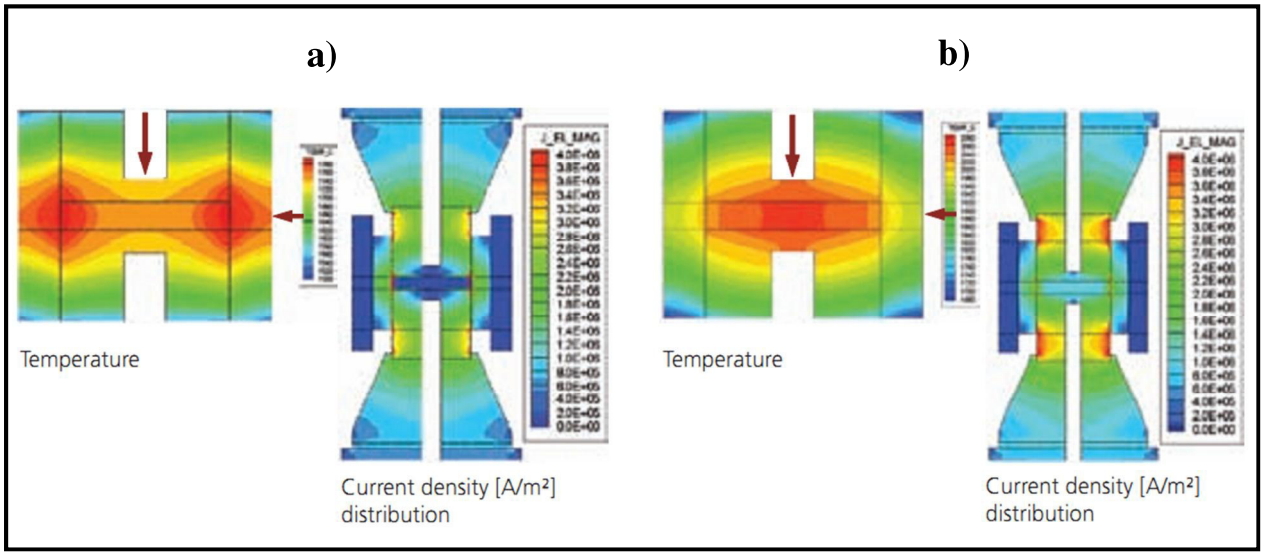


Figure 2.24: Calculated temperature and current density distributions during isothermal heating of a) silicon nitride at 1750°C (non-conductive) and b) tungsten carbide at 2000°C (conductive). Taken from Räthel et al., 2009 [60].

Figure 2.24 reveals that for non-conducting materials heated in the SPS the temperature on the walls of the die is higher than the internal temperature of the material. The opposite is found to occur in electrically conductive materials. When researching FAST/SPS consolidation of materials in literature it is very important to take note of where the optical pyrometer is used to

measure the temperature of the sample. The two most common areas used to estimate the temperature through the use of a focused optical pyrometer are on the outer die wall (FAST) and the other by focusing through the upper graphite punch (SPS), 5 mm from the top of the sample (See Figure 2.23). Thus sintering temperature deviations are produced when using the different temperature estimation techniques for systems set to the same conditions. The temperature is underestimated when measured radially with the optical pyrometer. Underestimation of the sintering temperature can be up to 100°C when calibrated copper melting experiments were conducted [57]. Even though SPS has proved to be an enhanced densification technique for sintering, high costs as well as the tool life being poor are the main disadvantages at present.

Table 2.9: Sintering temperature for various α-sialon phases and their respective mechanical properties. Adapted from Peng, 2004 [19].

Samples	Sintering Temperatures (°C)	Content of α –sialon (vol. %)*	H_{v10} (GPa)	K_{1c} (MPa.m$^{1/2}$)
Yb-SiAlON (oxygen content = 5 eq. %)	1550	76.4	20.2±0.2	3.9±0.2
	1600	90	20.4±0.2	3.6±0.2
	1650	100	20.6±0.2	3.8±0.2
	1700	100	19.7±0.2	4.2±0.1
	1750	100	19.9±0.2	5.2±0.3
	1830	100	19.6±0.2	5.3±0.2
Yb-SiAlON (oxygen content = 7 eq. %)	1500	72.7	19.9±0.2	3.5±0.2
	1600	92.0	19.8±0.2	3.7±0.1
	1650	100	20.2±0.2	3.9±0.2
	1700	100	20.1±0.2	4.4±0.1
	1750	100	19.6±0.2	6.3±0.2
	1800	100	20.0±0.2	6.2±0.3
(Y + Yb) - SiAlON (oxygen content = 7 eq. %)	1550	79.4	18.7±0.2	3.5±0.1
	1600	100	19.6±0.1	3.6±0.2
	1700	100	20.3±0.2	4.3±0.2
	1750	100	19.9±0.1	5.1±0.1
	1830	100	20.1±0.2	5.4±0.1

* Peng, 2004 [19] took the other crystalline phase to be made up of un-reacted Si_3N_4.

H. Peng, 2004 [19] investigated the effects of using yttrium, ytterbium and a mixture of the two on α-sialon composites sintered through the SPS technique with a heating rate of 200°C and an applied pressure of 50 MPa. The sintering was carried out through the use of the Dr. Sinter 2050 (Sumitomo Coal Mining Co. Ltd.). The sialon composites containing yttrium and ytterbium as the stabilizing cations have m and n values of 1.05 and 1.2 respectively. The stabilizing cation mixture of Y and Yb were added in an equimolar ratio. The mechanical properties of the sintered α-sialon compacts are shown in Table 2.9.

It was then noted that the sintered compacts containing elongated α-sialon grains exhibited the highest fracture toughness, where the increase in temperature promotes the anisotropic grain growth thus improving fracture toughness of the compacts, as revealed in Table 2.9. Furthermore the equiaxed α-sialon grains which are obtained at lower sintering temperatures have lower fracture toughness.

Table 2.10: The characterization of α and β sialon composites sintered by Smirnov, 2009 [61]

Sample	Sintering temperature (°C)	Phase composition*	Density (g/cm^3)	H_{V10} (GPa)
$Y_{0.5}Si_{9.75}Al_{2.25}O_{0.7}5N_{15.25}$	1650	α(s), α'(vw), β'(vw), M(vw)	3.13	13.2
	1700	α'(s), β'(s)	3.2	16
	1750	α'(s), β'(w)	3.22	19.2
	1800	α'(s), β'(vw)	3.15	19.5
$Nd_{0.5}Si_{9.75}Al_{2.25}O_{0.7}5N_{15.25}$	1650	α(s), M(w), β'(vw)	3.2	14.2
	1700	α'(s), β'(s), M(w)	3.35	18
	1750	α'(s), β'(w), M(w)	3.38	18.7
	1800	α'(s), β'(vw), M(vw)	3.35	18.7
$Ca_{0.5}Si_{11.5}Al_{1.5}O_{0.5}N1_{5.5}$	1650	α(s), α'(vw), β'(vw)	3.04	12.8
	1700	α'(s), α(vw), β'(vw)	3.11	19.1
	1750	α'(s), β'(vw)	3.13	19
	1800	α'(s), β'(vw)	3.13	19.1
$Si_{5.5}Al_{0.5}O_{0.5}N_{7.5}$	1650	α(s), β'(vw)	3.11	11.2
	1700	β'(s), α(vw)	3.22	14.2
	1750	β'(s)	3.21	15.2
	1800	β'(s)	3.18	15.6

*Where identified phases are denoted for simplicity where α: α-Si_3N_4, α': α-sialon, β': β –sialon, M: Mellilite. The intensities of the various identified phases were denoted by s: strong, w: weak and vw: very weak.

The effects of various sintering aids (CaO, Y_2O_3 and Nd_2O_3) on the formation of sialon phases were further investigated by Smirnov, 2009 [61]. Consolidation was obtained by using a uniaxial pressure of 50 MPa whilst using a heating rate of 100 K/min and a sintering dwell time 3-5 minutes depending on sample shrinkage rates. From Table 2.10 it was shown that sufficient densification was obtained for α and β-sialon samples sintered at a temperature of 1700°C with the maximum densities of α-sialons being obtained at 50°C higher. Y-α-sialons have the highest hardness with a maximum of 19.5 GPa when sintered at 1700°C, followed by Ca- and Nd-α-sialons respectively. Similarly, the highest hardness for β-sialons is obtained when sintering at 1800°C, giving a hardness of 15.6 GPa which is consistent with Table 2.3.

Furthermore, from the work completed by Smirnov, 2009 [61] the effect of adding an α-sialon precursor into the composite starting powder was investigated since it was expected that the α-sialon precursor addition would promote the formation of elongated α-sialon grains. However the opposite was found [61] . Excessive equiaxed α-sialon grain growth was experienced which resulted in the decrease of hardness when compared to sialon ceramics sintered without the α-sialon precursor.

2.4. Overview of the reinforcing superhard cBN agent

R. H. Wentorf was the first to synthesise cubic boron nitride (cBN) in 1957 from hexagonal boron nitride (hBN through high temperature and high pressure conditions similar to those used to synthesize diamond [62]. However cBN is produced commercially through the use of a mixture of hBN and a solvent-catalyst (alkaline metals and their nitrides) [63]. The synthesis is achieved by the dissolution of hBN in the solvent-catalyst, followed by the spontaneous nucleation of cBN. The synthesised cBN is then mixed with a reaction sintering aid and is sintered at 1200-1700°C and 4-6 GPa depending on the additive used and the starting size of the cBN crystals [64]. cBN has been classified as a superhard material where the term refers to materials which exhibit a Vickers hardness over 40 GPa [65]**.** Super hard materials are typically made up of light non-metallic based elements [66] [67] such as boron, carbon, nitrogen and oxygen since the strong covalent nature of the bonds that are present between these elements lead to extreme resistance to external shear.

Single crystals of synthesized diamond have a Vickers hardness ranging between 70 and 100 GPa [66] depending on the purity of the crystal, whereas cubic boron nitride has a hardness of 45 – 50 GPa [66]. The fracture toughness for a single crystal of diamond and cubic boron nitride are 5 and 2.8 MPa. $m^{1/2}$ [66] respectively.

These two materials are known to have great hardness, low mass density, high thermal conductivity, high chemical inertness and finally excellent wear resistance [66] [68] . Thus they are extensively used as cutting tools for materials such as rock, concrete, ceramics and other hard materials. However diamond is limited to its application as a cutting tool with iron-based alloys since the diamond chemically reacts with ferrous alloys at high temperatures resulting in degradation of the tool and its properties [65]. cBN on the other hand, being less reactive with ferrous alloys at high temperatures is widely used as a cutting tool in machining of iron-based materials. cBN also has thermal stability of up to 1000°C and is able to form passive oxide layers on its surface at high temperatures when in contact with oxygen [69].

2.4.1. cBN crystal structure

The boron nitride (BN) crystal structure is comparable to that of the modifications in the carbon system, where both systems have three phases. However in the BN system all three phases are synthetic unlike the carbon system. The three phases in the BN system are h-BN (hexagonal), c-BN (cubic) and w-BN (wurtzite) however the wurtzite phase is of little technological interest and very little information on it has been reported [70].

Table 2.11: Properties of cBN and hBN [70].

Property	**c-BN**	**h-BN**
Crystal structure	cubic, zinc-blende	hexagonal
Lattice constant	a = 3.61Å	a = 2.50Å, c = 6.60Å
Density	3.48 g/cm^3	2.2 g/cm^3
Thermal conductivity	0.02 - 0.09 $W.cm^{-1}.K^{-1}$	3.6 - 6.8x10^{-3} $W.cm^{-1}.K^{-1}$
Linear thermal expansion coefficient	4.8 x 10^{-6} K^{-1}	3.8 x 10^{-6} K^{-1}

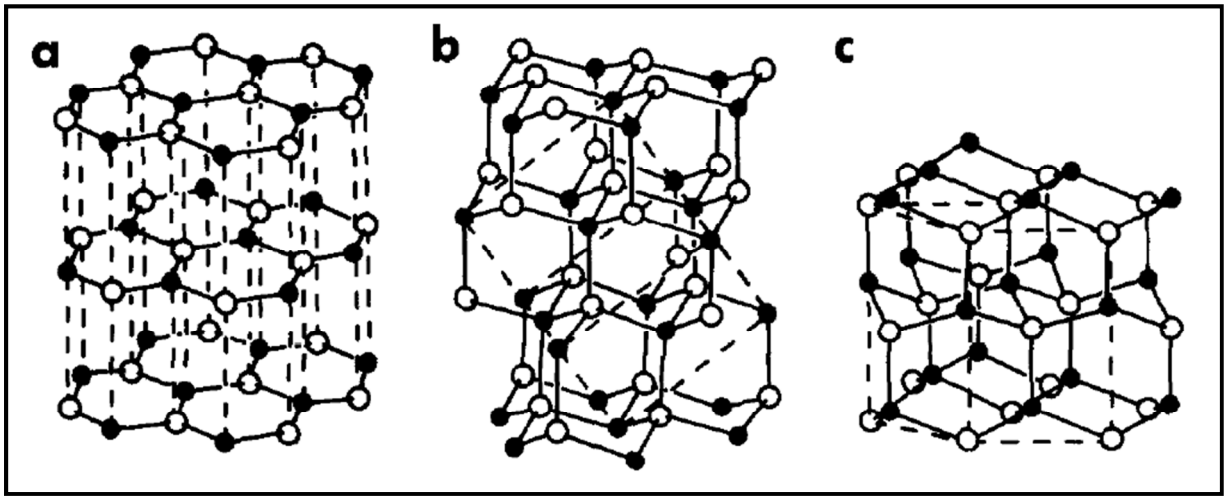


Figure 2.25: The crystal lattices of the three BN-system allotropes a) h-BN b) c-BN c) w-BN, where (●) represents boron atoms and (○) represents nitrogen atoms [71].

The equivalent phase of BN to diamond is the cubic phase where half the carbon atoms are replaced by nitrogen and the other half replaced by boron [72]. In some areas cBN surpasses diamond as an engineering material particularly in thermal stability and its effectiveness in machining of ferrous alloys [70] [72]. Both cBN and diamond have the 'zinc-blende' structure which is highly covalent, however they are only thermodynamically stable at ultra-high pressures. cBN cubic zinc-blende is of the face-centred cubic (FCC; $F\bar{4}3m$ space group) with a coordination number of 4 [73]. It must also be noted that there is a strong correlation with respect to the colour of cBN and its boron content where black indicates excessive boron and amber indicates boron deficiency [70].

2.4.2. Sintering and properties of cBN materials

Fully densified cBN is difficult to obtain unless high temperatures (1200-1500°C) and high pressures (4-6 GPa) are used [42]**.** Additives, either metallic (nickel, iron, cobalt, aluminium and titanium), or carbide (titanium carbide and tungsten carbide) or nitride (titanium nitride and tantalum nitride) in nature are used as reaction sintering agents or as fillers [63]. The difficulty of sintering cBN is attributable to the strongly covalent bonds which make it difficult to compress and sinter at low pressures [42] . Therefore the use of metal additives allows for reaction sintering taking place where a reaction between the cBN crystals and the additive results in the formation of metal borides and nitrides within the matrix. These ceramic phases act as binders for the

sintered ceramic, which is referred to as polycrystalline cubic boron nitride (PcBN) [74] although in reality it is a multiphase composite material. In order to avoid conversion of cBN to hBN during the sintering process, ultrahigh pressures (~5GPa) are required [74] . Commercial sintering of binderless cBN materials is completed by using high-pressure (7.7 GPa) and high-temperature (1880-2240°C) sintering method such as the Bridgman-type toroid apparatus (Figure 2.26) where the high-pressures are generated through compression and extrusion of the gasket material (lithographic stone) [75].

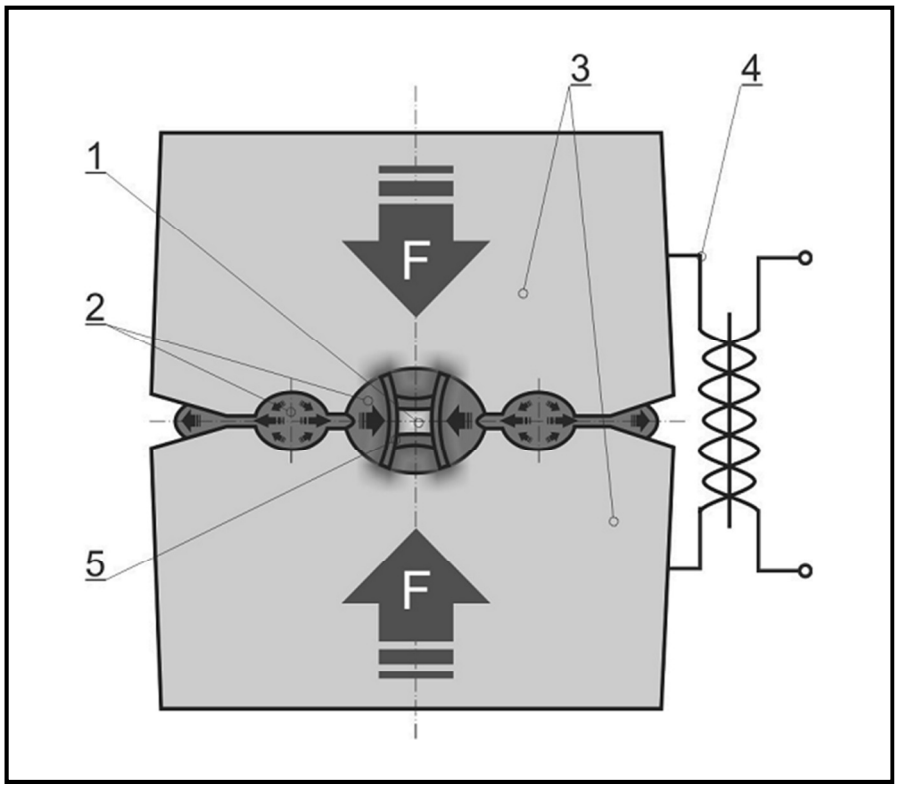


Figure 2.26: Bridgman-type HPHT sintering system, where 1 – Sample, 2 – shows plastic deformation of the gasket material, 3 – Pressure anvils, 4 – high power transformer supplying electrical heating and 5 – graphite resistive heater. Taken from Klimczyk et al., 2011 [75].

Walnsley et al. [76] reported that aluminum could be used as a reaction sintering aid for cBN whereby at high temperatures and pressures aluminum reacted with cBN to form aluminum nitride and aluminum diboride. These new phases contribute to the chemical inertness and thermal conductivity of the material [76]. However these binder phases exhibit excessive grain growth during sintering and to suppress this titanium nitride was added as an inert filler phase. This resulted in an increase in the hardness of the sintered compacts (cBN-TiN-Al as opposed to cBN-Al) [77] , as can be seen from Figure 2.27.

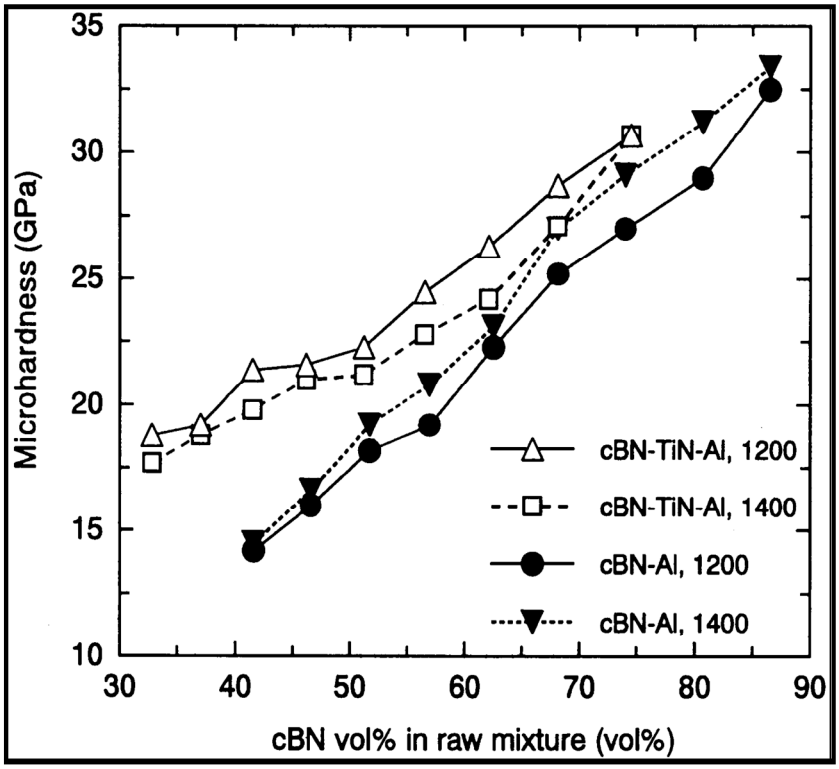


Figure 2.27: Knoop hardness for the cBN-TiN-Al and cBN-Al systems where the sintering temperatures were varied from 1200 to 1400°C respectively [77].

B. Yaman et al., 2009 [8] investigated the sintering behavior and mechanical properties of tungsten carbide cobalt as well as the effect of cBN addition to the composites consolidated through the SPS technique. The tungsten carbide cobalt material containing 6 wt. % cobalt (WC-6Co) and the composites containing cBN had 25 vol. % cBN. The sizes of the tungsten carbide cobalt powder and cBN starting powders were 0.8 and 5 μm respectively.

Table 2.12: Sintering condition, theoretical densities and mechanical properties of samples consolidated through SPS by Yama et al., 2009 [8].

Composition	Sintering Temperature (°C)	Pressure (MPa)	Theoretical density (%)	K_{1c} (MPa.m$^{1/2}$)	H_{v10} (GPa)
WC-6Co	1100	25	64.62		
WC-6Co	1150	50	86.47		
WC-6Co	1200	50	99.86	6.68 ± 0.5	18.59 ± 0.2
WC-6Co-25cBN	1250	75	99.40	10.90 ± 0.8	17.52 ± 0.6
WC-6Co-25cBN	1300	75	99.63	11.60 ± 0.7	20.59 ± 0.8

Through the addition of cBN into the WC-6Co matrix significant improvements in the fracture toughness is obtained with a small increase in the hardness. Tungsten carbide materials, in a great variety of microstructures and compositions are used in a wide range of machining tools. Due to the high temperatures that are generated during machining an improvement in the thermal properties of the cutting tool are required in order to efficiently remove heat away from the cutting zones.. The high temperatures attained can lead to chemical wear and tool failures if thermal conductivities are not satisfactory. Through the addition of cBN to the tungsten carbide matrix a further improvement in the thermal diffusivity is observed and can be seen in Figure 2.28.

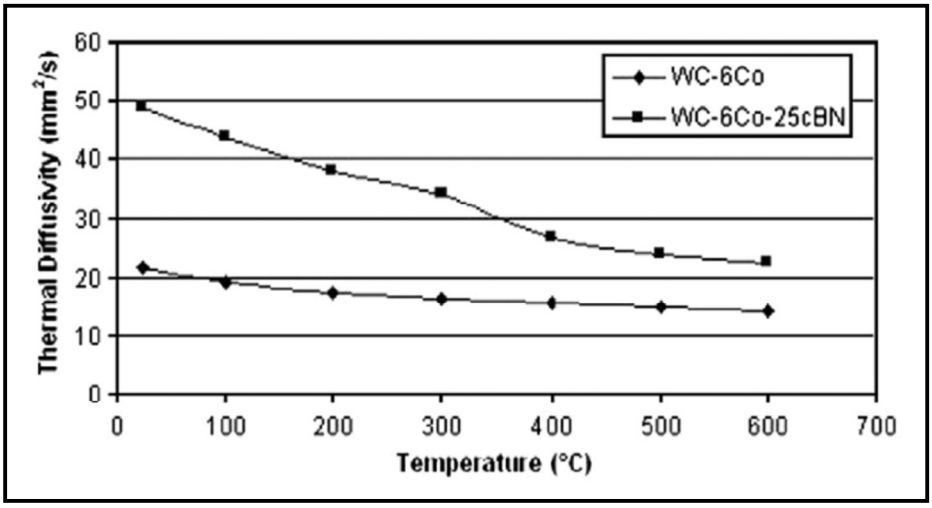


Figure 2.28: Thermal diffusivities of WC-6Co and WC-6Co-25cBN composites. Taken from Yaman et al., 2009 [8].

Klimczyk et al., 2011 [75] aimed to produce durable fine-grained cBN-Si_3N_4 composites with high hardness and fracture toughness through Bridgman-type HPHT synthesis (see Figure 2.26) where the Si_3N_4 (alpha nanosized powder 0.1 – 0.8 µm) was presumed to fill up the pores between the cBN grains resulting in increased fracture toughness through crack deflection. A low Si_3N_4 content (3 vol. %) was used as the sintering aid in order to maintain the Young's modulus and hardness attributed to pure PcBN. Two sample variations were produced using two different types of cBN starting powders. The first type had 3-5 µm cBN grains (I) and the second had having a mixture of cBN grain sizes. Specifically it was made up of 90 vol. % 3-5 µm and 10 vol. % 0-0.25µm cBN particles (II). The study involved sintering at a pressure of 7.7 GPa and utilizing a temperature range of 1880-2240°C. These composites exhibited an increase in the

density and Young's modulus with increasing sintering temperature (Figure 2.29). This could be done up to a maximum temperature after which the sample cracked.

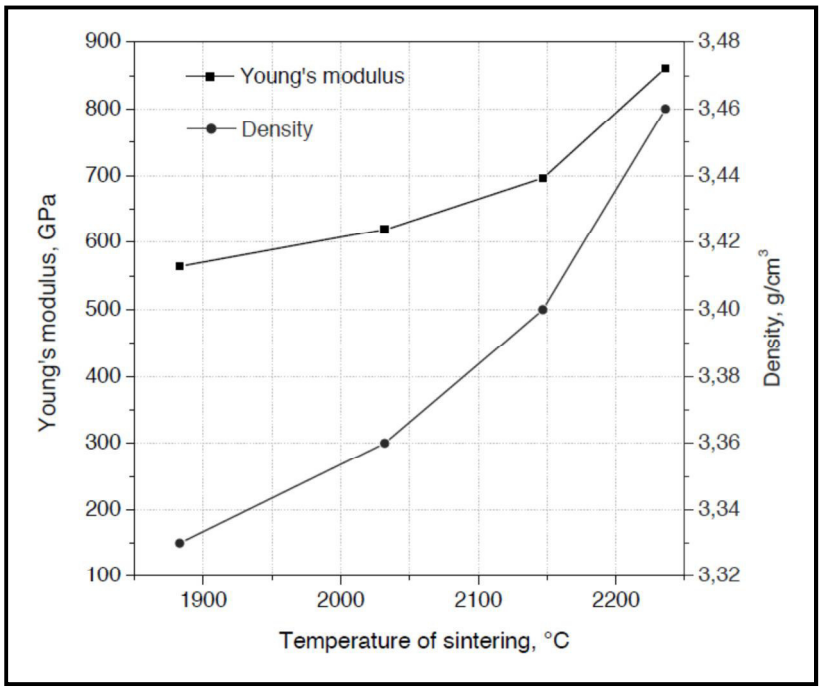


Figure 2.29: Young's modulus and density of cBN-Si_3N_4 (I) composites sintered at different temperatures under high pressure. Taken from Klimczyk et al., 2011 [75].

When sintering the cBN-Si_3N_4 composites at 2240°C, densities close to their theoretical values were obtained. Furthermore the addition of the cBN nanopowder (cBN-Si_3N_4 II) results in a small increase in hardness at the expense of the Young's modulus seen in Table 2.13, where a commercial material, BZN7000s (General Electric), was used as a reference material.

Table 2.13: A comparison of the density and mechanical properties of cBN-Si_3N_4 (3 vol. %) composites (I) and (II) sintered at 2240°C and 7.7 GPa pressure with BZN7000s as a reference material. Taken from Klimczyk et al., 2011 [75].

Properties	cBN-Si_3N_4 I	cBN-Si_3N_4 II	BZN7000s
Density (g/cm^3)	3.46 ± 0.02	3.45 ± 0.02	3.38 ± 0.02
Young's modulus (GPa)	842 ± 9	812 ± 17	714 ± 3
Vickers hardness (H_{v10})	4750 ± 580	4855 ± 630	3820 ± 83
Fracture toughness ($MPa.m^{1/2}$)	10.3 ± 0.8	10.9 ± 1.3	12.2 ± 1.2

Ye et al., 2010 [58] investigated cBN/β-sialon composites and consolidated the composites through a SPS technique. From Equation 2.3 a z-value of 3 was selected and thus the composition of the β-sialon used as the matrix is $Si_3Al_3O_3N_5$. The cBN content (2-4 μm) was varied from 0-30 vol. % and the composites were sintered in a nitrogen atmosphere utilizing a heating rate of 100°C/min, a dwell time of 5 minutes and an applied pressure of 50 MPa. However, as expected, the relative densities of the sintered composites decrease with increasing cBN content due to the negative effect of cBN on densification shown in Figure 2.30

.

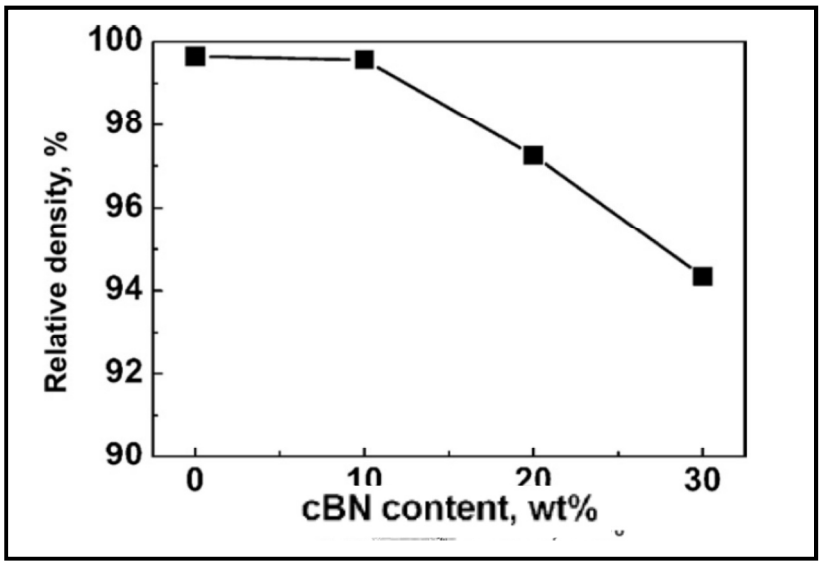


Figure 2.30: Negative effect of cBN content on the densification of cBN / β-sialon composites sintered at 1500°C for a dwell time of 5 minutes. Taken from Ye et al., 2010 [58].

Furthermore cBN addition to the β-sialon matrix results in an increase in the Vickers hardness (Figure 2.31, a) as well as significant improvements in the flexural strength and fracture toughness (Figure 2.31, b). The increase in hardness for the 10 vol. % cBN composite is due to high density and no transformation of cBN to the softer hBN phase. However it must be noted that when increasing the cBN content from 10 -30 vol. % the mechanical properties deteriorate due to the reduction in relative density. The strengths attained in these β-sialon/cBN composites are too low to allow these materials to be used as a cutting tool since strengths greater than 700 MPa are required.

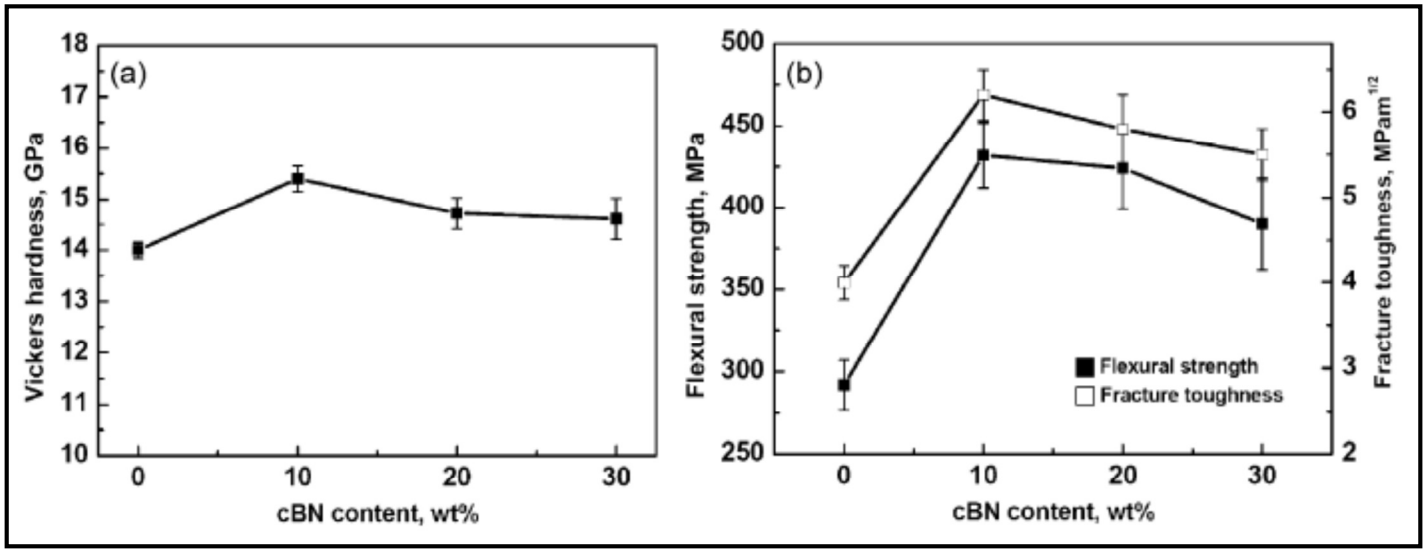


Figure 2.31: Effects of cBN content on the mechanical properties of cBN/β-sialon. a) Vickers hardness and b) flexural strength and fracture toughness. Taken from Ye et al., 2010 [58].

3. Experimental Procedure

This section pertains to the description of the various experimental procedures carried out in this scope of work. These methods include characterization and mechanical properties measurement techniques used to analyze the starting powders obtained from the specified suppliers (Table 3.1) and the sintered sialon and sialon-cBN composites. Two grades of cBN grains were used to investigate the reinforcing effects attributed to the size of these hard particulates and their interaction with the sialon matrix (see section 4.4.3 for more detail).

3.1. Starting powder characterisation

The various methods used to characterize the starting powders will be described in detail in the relevant sub-sections below. The details of the starting powders used in this work can be found in Table 3.1 and those of all other chemicals or consumables used can be found in Table 3.2.

Table 3.1: Details of the respective starting powders used in obtaining sialon based composites.

Starting powder	**Chemical composition**	**Product name**	**Supplier**
Silicon Nitride	Si_3N_4	SNE-10	UBE, Japan
Aluminium nitride	AlN	Grade H	Tokuyama Industries
Aluminium oxide	Al_2O_3	AKP-50	Sumitomo-Chemical Co. Ltd.
Yttria	Y_2O_3	Grade C	H. C. Starck
Cubic boron nitride	BN	Grade 1	Element 6 (Pty) Ltd.
Cubic boron nitride	BN	Grade 9	Element 6 (Pty) Ltd.

Table 3.2: Supplier information for other chemicals and consumables used in this scope of work.

Chemical/consumable	Supplier
Iso-proponal	Merck Chemicals
Sodium hexametaphosphate	Sigma-Aldrich (Pty) Ltd.
Hexagonal boron nitride	H. C. Starck
SPS graphite assembly	SGL Carbon
Grinding/polishing /lubricant/diamond suspensions	Struers
Diamond cut off wheel	Struers

The starting powders were analysed in terms of their particle size distribution, crystal structure and morphology of the respective phases.

3.1.1. Particle size analysis

The particle size distribution of the various starting powders was measured through the use of a Malvern Zetasizer Nano ZS. This instrument utilizes dynamic light scattering. This is carried out by laser illumination of the sample powder suspension where fluctuations in light intensity are attributed to the movement of the particles in the liquid they are in, through Brownian motion. The intensity fluctuations are then processed through the Zetasizer and through the use of built-in correlation functions it is possible to obtain the particle size distributions of the respective powders [(78)].

Before the measurements were taken it was imperative that the particles were well dispersed in the solution order to obtain an accurate particle size distribution. This was achieved by ultra-sonicating (120 W) the powders in water with sodium hexametaphosphate as a dispersing agent. Once ultrasonication had been completed, the mixtures were planetary ball milled using 2 mm alumina milling balls and an agate milling bowl (250 ml).

3.1.2. XRD analysis

The analysis of the crystalline phases of the starting powders was carried out through the use of the Bruker D2 phaser XRD analysis equipment. The XRD technique utilizes the fact that crystalline materials diffract x-rays at different angles (according to Braggs law) due to their various crystal structures. The D2 uses Cu Kα radiation produced at 30 kV and 10 mA. Measurements were taken under the following conditions: 2θ values ranging from 10°- 60° with a step size of 0.02° at 0.2 steps per second. After completion of the XRD scan it was then required to identify the various phases present. For this purpose a program package named X'Pert Highscore® (produced by Philips) along with the ICDS (International Centre for Diffraction Data) database was used.

3.1.3. Scanning electron microscopy of starting powders

The morphology of the various starting powders was analysed through the use of a scanning electron microscope, FEI Quanta 400 FEG, located at the Microscopy Unit at the University of the Witwatersrand. This SEM has both secondary and back-scattered electron detection modes. Due to powders being non-conductive it was necessary to attach them to a stub through double sided carbon tape and carbon sputter coated in order to improve the conductivity of the samples.

3.2. Calculation of sialon matrices

From Section 2.3.1 it was shown that sialon ceramics can have a large range of compositions, however for this project the primary sialon composition being studied is designated as 'M1'. Two other sialon matrices will also be studied, these matrices are variations of M1 where the differences are a two weight percent reduction in aluminium nitride (M2) and a two weight percent increase in yttria (M3) from the base M1 composition.

The initial matrix was based on an n value of 2.5 and an m value of 1. This combination of values is preferred for the mechanical strength it confers on the resulting material. With the use of Equation 2.1 it was possible to calculate the composition of the matrix. However considering this formula on its own is inadequate as the non-oxides have a tendency to oxidise when stored and have an average oxygen content of 2.5% which needs to be accounted for. Table 3.3 shows the corrected compositions for the M1, M2, M3 sialon matrices where the additional oxygen content has been accounted for. The composition of M4 is similar to that presented by Ye et al., 2010 [58] however the location of the M4 sialon composition is within the sialon plane whereas the composition used by Ye et al., 2010 [58] is below the sialon plane and was used for the study of β-sialon/cBN composites. The cation ratio is defined by the amount of yttrium present in the sample in comparison to the amount of yttria that can be incorporated in to the α-sialon structure. This cation content in comparison to the ideal composition, as well as the m and n values are also given. The location of the various matrices on the sialon plane (Si_3N_4-4/3(AlN.Al_2O_3)-YN-3AlN) is represented in Figure 3.1.

Table 3.3: A summary of the composition, n and m values and cation ratio for the various sialon matrices.

SiAlON matrices	m	n	Si_3N_4 (Wt. %)	AlN (Wt. %)	Al_2O_3 (Wt. %)	Y_2O_3 (Wt. %)	Cation ratio
Matrix 1 (M1)	0.991	2.502	66.18	16.57	9.02	8.23	1.337
Matrix 2 (M2)	0.822	2.458	67.53	16.90	9.20	8.40	1.651
Matrix 3 (M3)	0.992	2.502	64.88	16.25	8.84	10.03	1.660
Matrix 4 (M4)	1.987	4.493	41.69	29.04	17.24	12.03	1.003

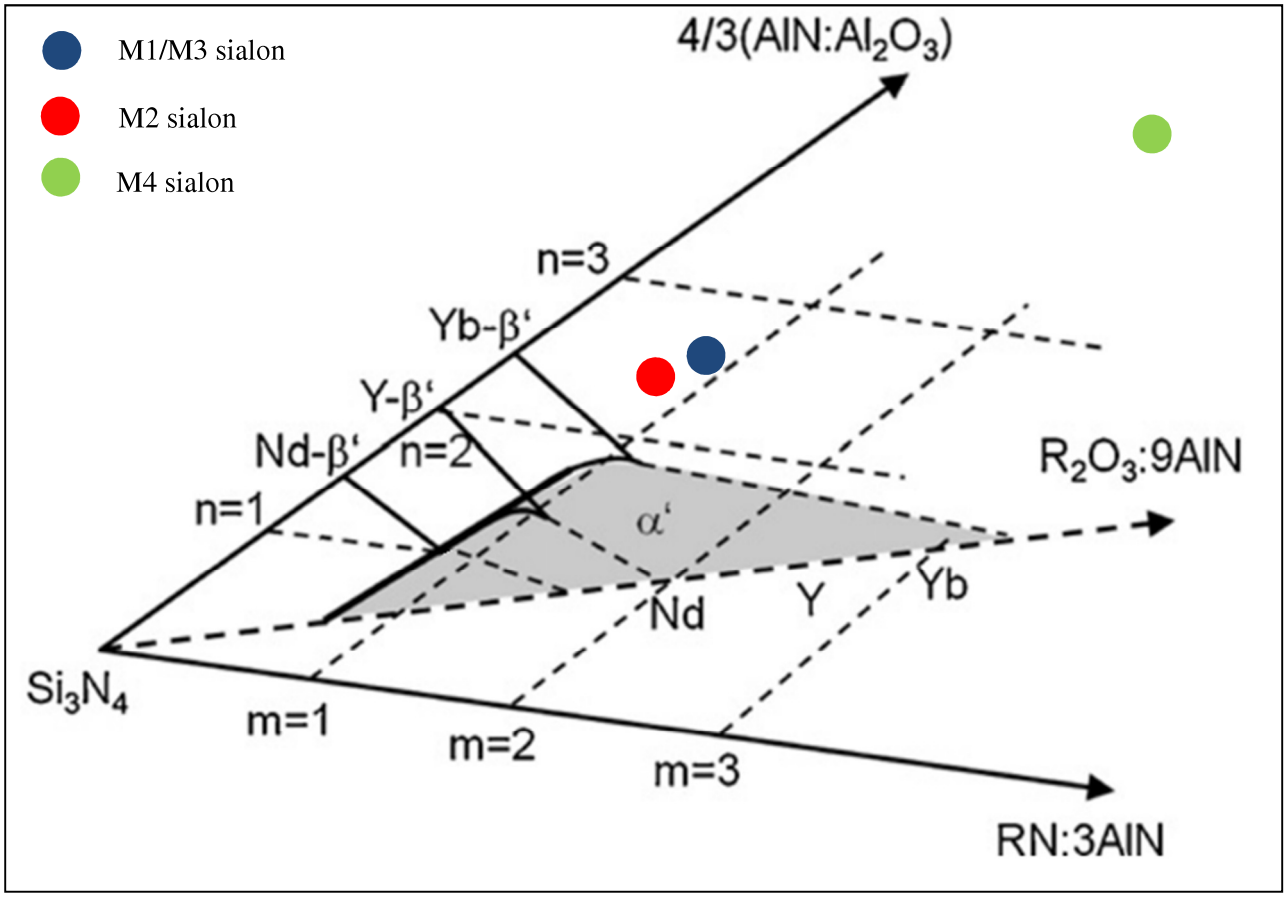


Figure 3.1: Location of sialon matrices on the sialon plane studied in this scope of work, showing the effect of compositional changes on the designing of sialon ceramics.

3.3. Mixing of composite powders

In order to obtain sintered composites that have consistent and reliable mechanical properties it is beneficial that a homogenous distribution of the constituents be obtained. When utilizing any of the mixing routes it is imperative that powders be weighed out carefully and accurately in accordance with the composition stated in Table 3.3.

3.3.1. Planetary ball mixing sialon constituents

The various sialon matrices were obtained by planetary ball milling the Si_3N_4, AlN, Al_2O_3 and Y_2O_3 starting powders. As recommended by Dr. M. Herrmann of IKTS, Dresden the matrices were milled in 50 gram powder batches, with 140 ml iso-propanol and 100 g of agate (10 mm) milling balls all contained in an agate milling bowl, 250 ml in size. The starting powders were mixed at a speed of 200 rpm for duration of 4 hours to ensure homogenous milling. The planetary ball mill used is a Fritsch Pulverisette 6 planetary mono mill capable of speeds from 100-650 rpm. The mixing/milling action is provided by the grinding bowl rotating around its own axis while orbiting (in planetary motion) around a central axis too, as shown in Figure 3.2.

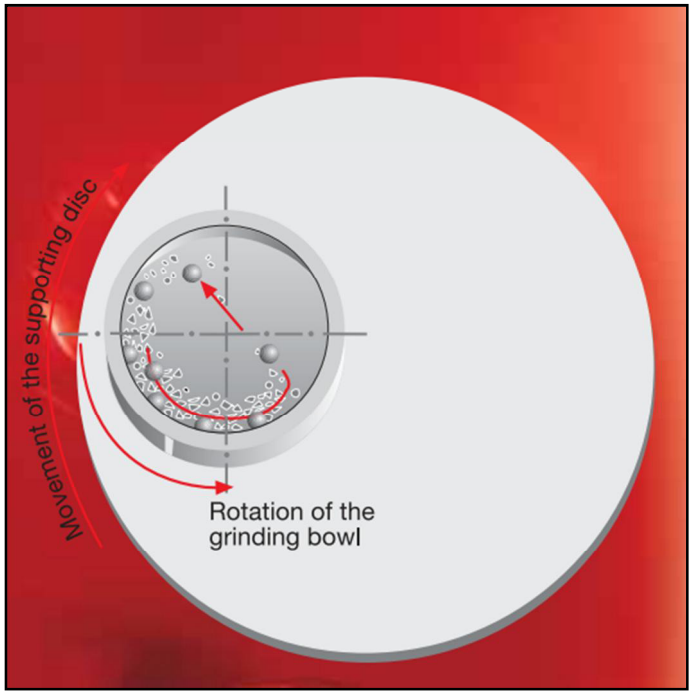


Figure 3.2: Milling action of the planetary ball mill [79].

3.3.2. Rotary evaporator

Once the planetary ball milling was completed the suspension was dried in a rotary evaporator (Heidolph Labrata 4010 digitial) where the bath temperature was set to 40°C and the rotation speed was 80 rpm whilst under a slight vacuum aiding the evaporation process.

3.3.3. Sieving powder

Once the powder is completely dried, it is taken from the round bottom flask and placed in a 400 µm Retsch® stainless steel sieve following by sieving through 200 and 150 µm sieves with the use of a Retsch® AS-200 control "G" sieve shaker. This sieving step is essential as it allows for better green compacts prior to the consolidation of the powders since these powders are able to flow better as well as larger agglomerates being broken up.

3.3.4. Turbula mixing of cBN grains

It was found that the cBN grains could be introduced into the sialon powder homogenously through a dry Turbula mixing route. The equipment used for this was the Turbula T2F from Willy A. Bachofen AG. This route utililized a 100 ml polyurethane container which was used to mix the cBN grains into the dried and sieved sialon matrix. The starting sialon and cBN powders mixed in 50 gram batches were rotated in the Turbula unit at a speed of 60 rpm for a duration of 2 hours where 10 agate milling balls (10cm sized) were used to aid in the homogenous mixing of the cBN.

3.4. Sintering of sialon based composites using the spark plasma technique

Consolidation of the various composite powders was completed through the use of the HP-D5 Spark Plasma Sintering furnace (FCT, Germany). The temperature in this furnace is measured by focusing an optical pyrometer through the centre of the upper punch which is 5 mm above the sample's surfaces. The composites were sintered under a constant vacuum. The pressure is applied through graphite punches in a graphite die assembly as seen in Figure 2.23. In order to preserve the life of the graphite dies a graphite foil is used as an interface between the graphite tool and sample. The graphite foils located on the surface of the graphite punches are coated with a layer of hexagonal boron nitride. This is done to limit interaction with carbon. The quantity of powder used to make each sintered composite was sufficient to obtain a dense sample approximately 5 mm thick and 20 mm in diameter. The sintered composites studied in this work were consolidated in a vacuum with a absolute gas pressure of 1hPa.

The sintering profile used for the SPS consolidation of sialon based composites allowed for an initial temperature upramp from 450°C to 1350°C at a heating rate of 250°C/min followed by a second upramp from 1350°C to the sintering temperature at a heating rate of 50°C/min. All compacts in this project were sintered at a pressure of 50 MPa where this pressure is applied at 450°C and is maintained throughout the sintering profile and only released at 450°C during cooling. The compacts dwell at the sintering temperature for 5 minutes after which they are cooled at 200°C/min. A typical sintering profile used for composites sintered at a temperature of 1550°C is illustrated in Figure 3.3. The isothermal heating temperatures used in this project ranged from 1500-1625°C. During heating of the graphite assembly a pulse time of 10 ms and a pause time of 5 ms were utilized.

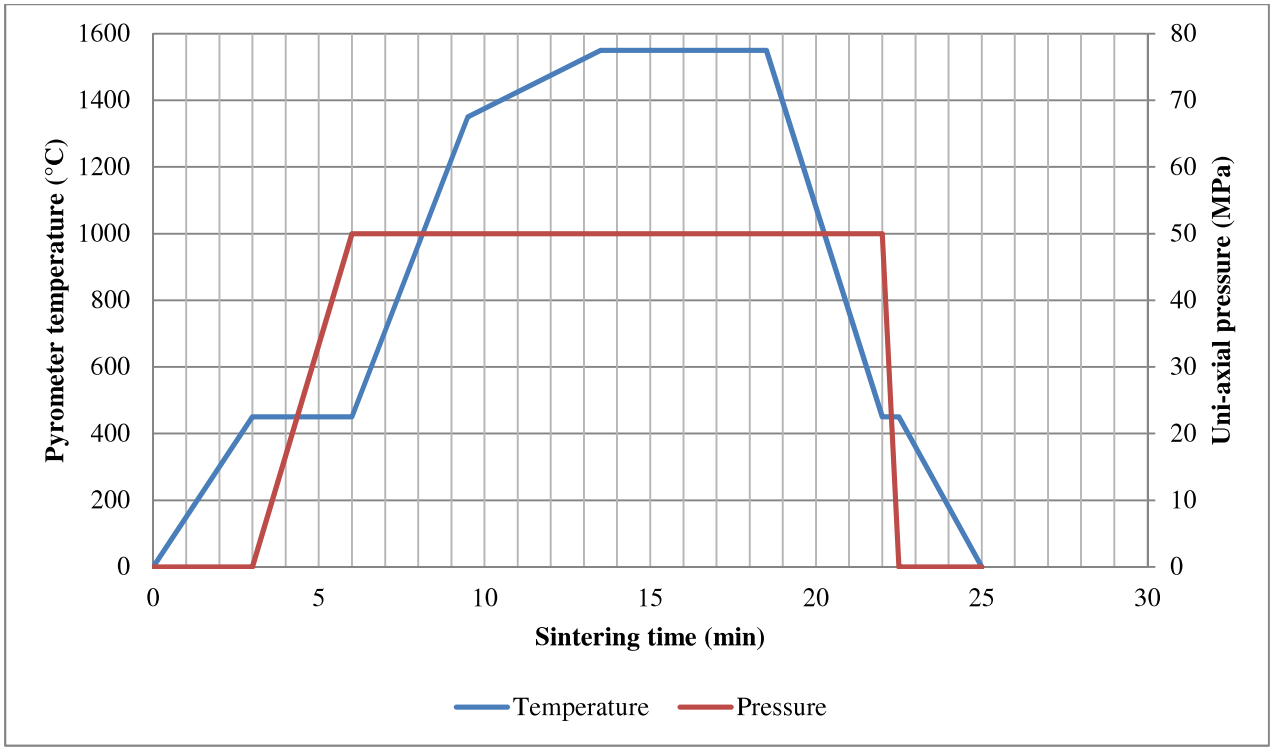


Figure 3.3: Sintering profile of composites sintered at 1550°C showing the schedule of the sintering temperature and applied pressure.

3.5. Characterization methods for sintered composites

This section describes the techniques used in preparing the composites for characterization. Once the composites had been sintered successfully it was necessary that the graphite foil adhering to the composite be removed. The most efficient way to do this is through silica sand blasting. Once the graphite foil has been removed the composites are placed in an ultrasonicating bath in order to dislodge any silica particles from the surface of the sintered composite.

3.5.1. Density measurements

Once the sample had been cleaned it was necessary to measure its density and open porosity. These were obtained through the use of the Archimedes method [80]. This technique required the

sample to be boiled in distilled water for five hours. This was done in order to remove any bubbles that were adhered to the surface as well as to fill the pores on the surface with water in order to obtain accurate measurements.

In order to calculate the density and open porosity it was required that the following mass measurements be taken: measure the suspended mass (M_S), water saturated mass (M_W) and the dry mass (M_D) on a 4 decimal point accurate scale. The suspended mass of the sample was measured by placing a small beaker on a supportive plate above the scale; the sintered sample was then lowered into a net submersed in distilled water and the mass weighed. The water saturated mass was measured by removing the sample out of a beaker filled with distilled water and lightly dry the surface using paper towel to remove excess water from the surface and placing the sample on the scale. The dried mass was measured by placing the sample in an oven at 80°C for 24 hours after which it is cooled and placed on the scale. Each measurement was repeated five times in order to calculate the mean and to obtain a standard deviation when these values were inserted into Equations 3.1 and 3.2.

Thus the measured density is calculated through Equation 3.1, taking the density of water to be 1g/cm^3.

$$\rho = \frac{M_D \times \rho_{Water}}{M_W - M_S} \qquad \textbf{Equation 3.1}$$

And the open porosity can be calculated through:

$$P_{Open} = \frac{M_W - M_D}{M_W - M_S} \qquad \textbf{Equation 3.2}$$

The theoretical densities of pure sialon ceramics were obtained through SEM analysis, however the theoretical densities for cBN containing sialon composites were calculated by taking into account the respective volume contents of sialon, cBN and hBN (if present) and their densities (Equation 3.3).

$$\rho_{Overall} = \left(\frac{x_{sialon}}{\rho_{sialon}} + \frac{x_{cBN}}{\rho_{cBN}} + \frac{x_{hBN}}{\rho_{hBN}} \right)^{-1}$$ **Equation 3.3**

Where x_i and ρ_i are the volume fraction and theoretical density of component i. The theoretical density of sialon is dependent on the initial compositions however the theoretical densities for cBN and hBN are 3.48 and 2.27 g/cm^3 respectively. The measured density (Equation 3.1) and theoretical density (Equation 3.3) were then used to calculate the percentage of the theoretical densities measured for sialon and sialon/cBN composites studies throughout this work.

3.5.2. Cutting the sintered composites

Once the density measurements had been obtained it was necessary to examine the cross section of the various composites. This was done through the use of a Struers Secotom-10 precision cut-off machine and a Struers diamond cut off wheel with a 12 cm diameter. The spindle speed used for cutting the now sintered compacts into two halves was 3500 rpm with a feed rate of 0.05 mm/s.

3.5.3. Mounting

The one half of the sintered compact was mounted in Bakelite (Struers polyfast) using a Struers Cito-Press 10 which can control pressure (250 bar) and temperature (180°C) independently. The bakelite was used because it would allow for SEM analysis to be conducted since the bakelite used was electrically conductive and therefore avoided excessive charging of the samples during SEM analysis.

3.5.4. Grinding and polishing techniques

After mounting it was necessary to grind the sample surface flat in order to expose the sialon based sintered compacts. Grinding with Struers 120, 220 and 1200 grit diamond grinding plates was used in order to obtain a flat surface with a minimal number of scratches. Once the grinding had been satisfactorily completed the polishing stage was entered. This was done with a Leco Spectrum System 2000 polishing instrument which had been programmed (i.e polishing time and speed) for surface grinding and polishing in several successive steps. The description of this polishing technique is summarised below in Table 3.4.

Table 3.4: Pre-programmed grinding and polishing cycle with the respect to the different wheel, lubricant, duration and rotation speed.

Step	Polishing/Grinding wheel	Lubricant	Time (min)	Speed (rpm)	Load (N)
1	MD-Piano 120	Water	15	300	30
2	MD-Piano 220	Water	15	300	30
3	MD-Piano 1200	Water	20	300	25
4	MD-Allegro	DP dispersion (9µm)	20	150	20
5	MD-Largo	DP dispersion (3µm)	20	150	15
6	MD-Dac	DP dispersion (3µm)	15	150	15
7	MD-Chem	OP-S/OP-U	3	150[a]	15

[a] The polishing head is rotated counter clockwise with respect to the clockwise rotation of the polishing disc.

3.5.5. XRD analysis

The phases of the sintered composites were identified by using a D2 Bruker XRD system, as discussed in Section 3.1.2.. The other half of the sintered compact which was cut as described in Section 3.5.1 was used for the XRD analysis and the cross sectional surface was ground flat with a 220 grit diamond grinding disc and the surface was used for the XRD analysis.

3.5.6. SEM of composites

The microstructure of the sintered compacts was investigated using SEM (same equipment as discussed in Section 3.1.3). In order to prevent any excessive charging of the sintered samples the polished surface was sputter coated with carbon to improve the electrical conductivity. This property was further improved through the use of double sided carbon tape to fix the sample in place on the specimen stub.

3.5.7. Mechanical properties

This section describes the techniques utilized in measuring the mechanical properties of the compact, specifically hardness and fracture toughness. Indentation and crack lengths required to calculate the hardness and fracture toughness were obtained with the use of a Leco V-100-A2 Vickers hardness tester.

3.5.7.1. Hardness

The hardness for each of the samples was measured through the use of a Vickers hardness tester. The indentations were created on the surface of the mounted sample with a diamond indenter, on

which a load of 5kg was applied for a period of 10s. The Vickers diamond indenter had a 136° angle between its opposite faces.

The mean of the two diagonals (illustrated in Figure 3.4), measured for a total of five indents, were then inserted into Equation 3.4.

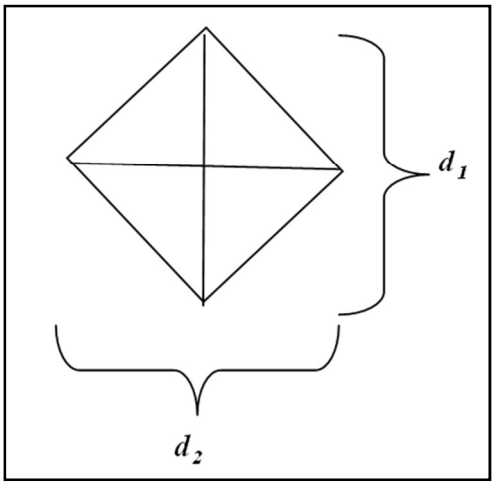


Figure 3.4: Illustration of the measurement of the indentation diagonals required for Vickers hardness measurement.

Vickers hardness is measured by using the following equation [81]:

$$H_V = \frac{F}{A} = \frac{2 \times F}{\frac{\bar{d}^2}{Sin\,\theta}} = \frac{2 \times F \times Sin\,\theta}{d^2} \qquad \textbf{Equation 3.4}$$

Where:

- $\mathbf{H_V}$ = Vickers hardness number (GPa)
- $\mathbf{F}$ = Applied test load (N)
- $\mathbf{A}$ = Surface area of indentation (μm^2)
- θ = Angle of opposite faces of indenter
- $\bar{d}$ = arithmetic diagonal mean of indentation (μm)

Since the angle between opposite faces of the diamond indenter is 136° it is possible to simplify the above expression to Equation 3. 5 [81]:

$$Hv = \frac{1854.4 \times F}{\bar{d}^2} \qquad \textbf{Equation 3.5}$$

3.5.7.2. Indentation fracture toughness

To measure a materials indentation fracture toughness the length of the crack produced from the indentation is required as can be seen in Figure 3.5.

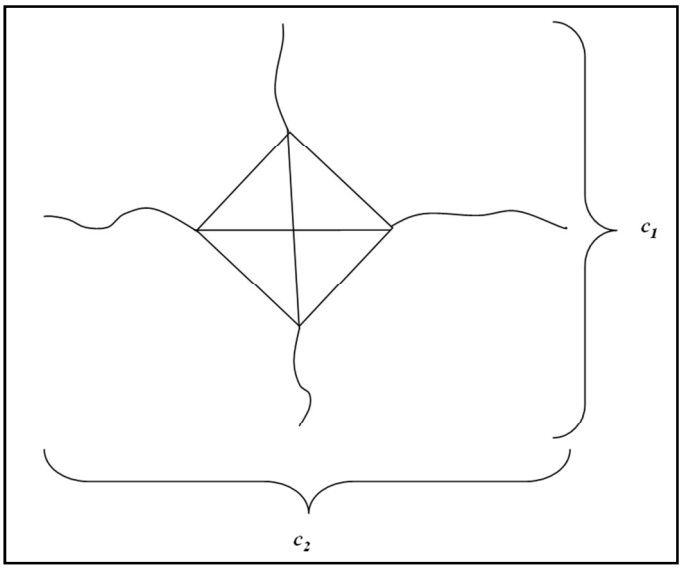


Figure 3.5: Crack length measurement for determination of the fracture toughness.

The arithmetic crack length mean is used in Equation 3.6 [82], to determine the fracture toughness (K_{1C}).

$$K_{1C} = \xi\left(\frac{E}{Hv}\right)^{1/2}\left(\frac{P}{\bar{c}^{3/2}}\right)$$ **Equation 3.6**

Where:

- K_{1C} = Fracture toughness of material (MPa.m$^{1/2}$)
- ξ = calibration constant (0.016)
- E = Young Modulus of Elasticity (GPa) = 300 GPa [83] [84]
- $\bar{c}$ = arithmetic radial crack length mean (μm)

4. Experimental Results

This section presents the experimental results obtained from the experiments described in Section 3; the results found in this section will cover the entire scope of work from starting powder to sintered compact analysis.

The notation used with respect to the different composites sintered utilized the following variables: matrix, cBN content and sintering temperature which were all varied. A uni-axial pressure of 50 MPa and sintering dwell time of 5 minutes remain constant throughout the sintering procedure. Below is an example of the notation used for a pure sialon compact and one with 30 vol. % cBN content sintered at 1600°C:

- Pure sialon: M1-1600
- Sialon matrix (M1) with 30 vol. % cBN: M1-30cBN-1600

4.1. Starting Powders

The starting powders used for the production of the sialon ceramics were analysed by measuring the particle size distribution, observing the morphology and identifying the crystalline phases present.

4.1.1. Particle size analysis

The particle size distribution was measured as per the described method in Section 3.1.1. The particle size analysis for the respective starting powders was found to be in agreement with what was described by the suppliers. The d_{10}, d_{50} and d_{90} for the various sialon starting powders obtained from the Zetasizer Nano ZS are shown in Table 4.1.

Table 4.1: d_{50} of the respective starting powders obtained from the particle size distributions.

Starting powder	Product name	Measured d_{10} (µm)	Measured d_{50} (µm)	Measured d_{90} (µm)
Silicon nitride	SNE-10	0.22	0.48	1.67
Aluminium nitride	Grade H	0.53	1.06	1.79
Alumina	AKP - 50	0.10	0.21	0.35
Yttria	Grade C	0.39	1.02	2.21
Cubic boron nitride	Grade 1	0.44	0.72	1.51
Cubic boron nitride	Grade 9	9.36	10.31	14.50

4.1.2. XRD Analysis

The crystalline phases were identified through the use of XRD analysis showing all starting sialon powders were mono-phased materials except from the silicon nitride starting powder which was found to contain 95% α and 5% β-Si_3N_4 as shown in Figure 4.1. XRD analysis additionally revealed that the grade 9 cBN consisted entirely of the cubic phase whereas the grade 1 cBN (Figure 4.2) consists of the cubic phase with trace amounts of the weaker hexagonal phase. The resultant crystalline phases for the various starting powders are shown in Table 4.2.

Table 4.2: XRD patterns used to identify the crystalline phases present in the starting powders.

Identified phases	Card number	Crystalline phase
α - Silicon nitride	01-076-1407	Hexagonal
β - Silicon nitride	01-076-1418	Hexagonal
Aluminium nitride	00-025-1133	Hexagonal
α - Alumina	01-075-1865	Hexagonal
Yttria	01-088-2162	Cubic
Boron nitride (Grade 1)	01-089-1499	Cubic
	01-073-2095	Hexagonal
Boron nitride (Grade 9)	01-089-1499	Cubic

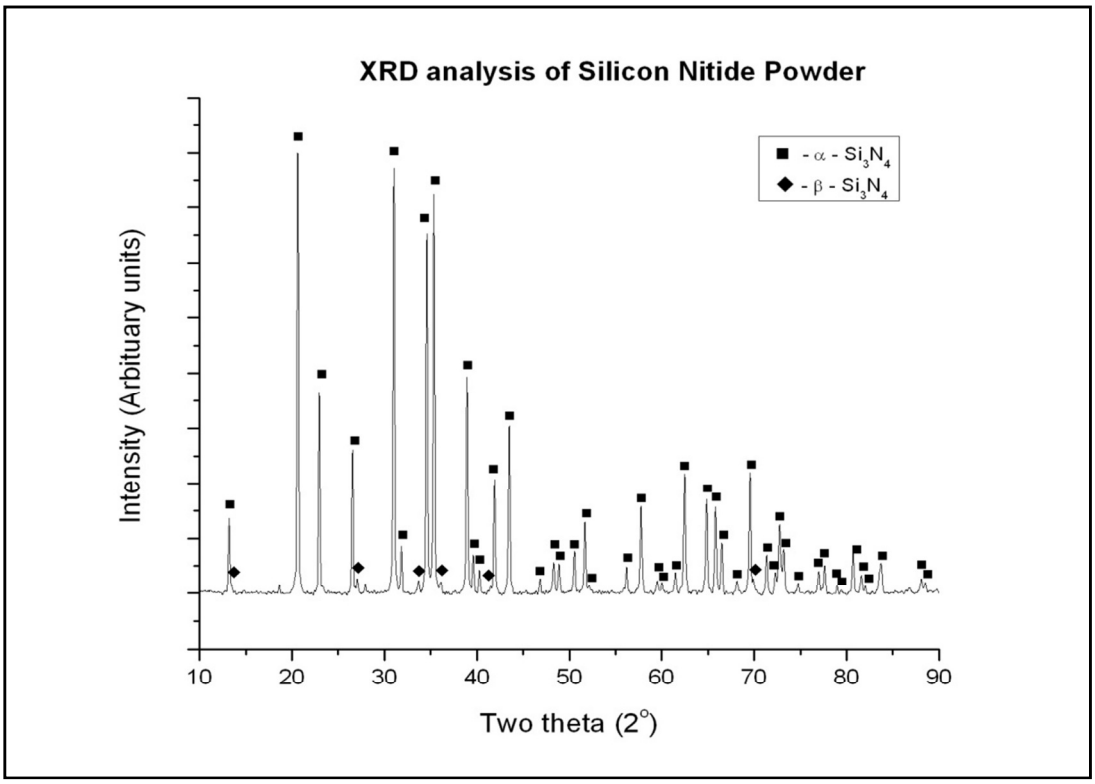


Figure 4.1: XRD pattern for UBE SNE-10 silicon nitride powder showing both phases α (■) and β (♦) are hexagonal.

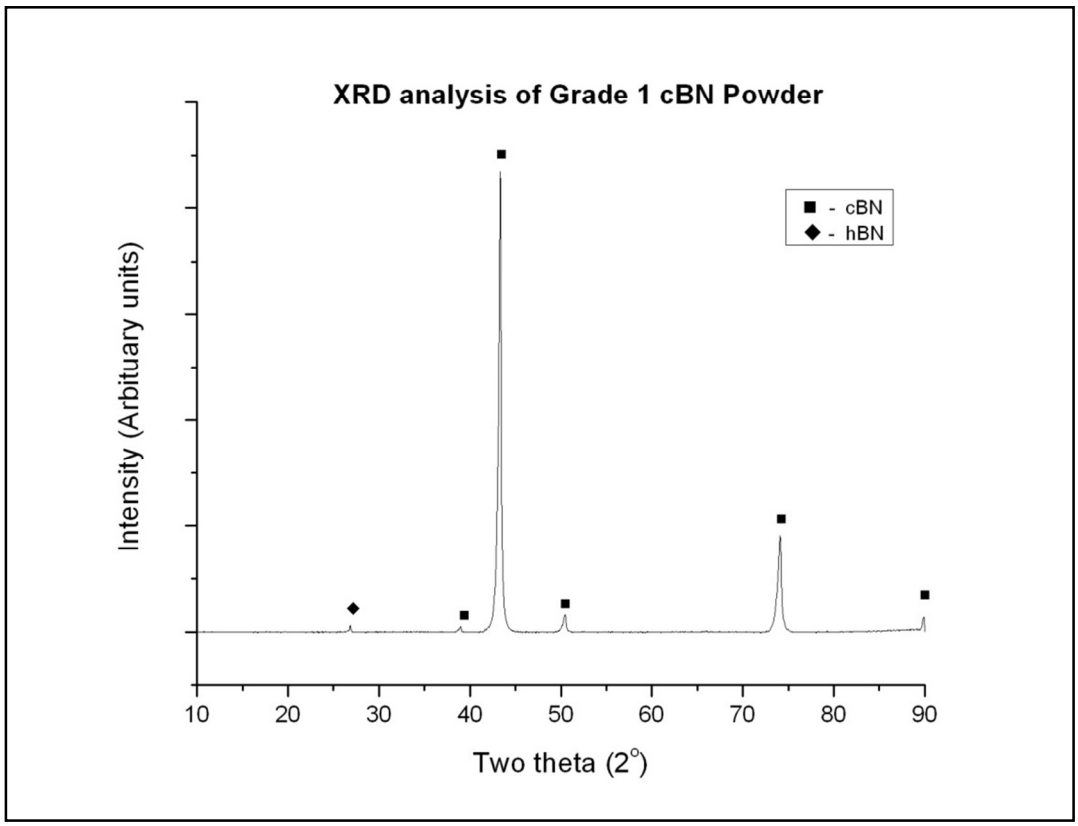


Figure 4.2: XRD pattern for grade 1 cBN powder showing the cubic (■) and hexagonal (♦) phases.

4.1.3. Scanning electron microscopy

High magnification micrographs were obtained for the respective starting powders through the use of a SEM in secondary electron mode, as described in Section 3.1.3. These SEM micrographs were also used to confirm the relative particle sizes of the starting powders as obtained from the particle size analysis. The images of the starting powders are shown in Figure 4.3 to 4.8:

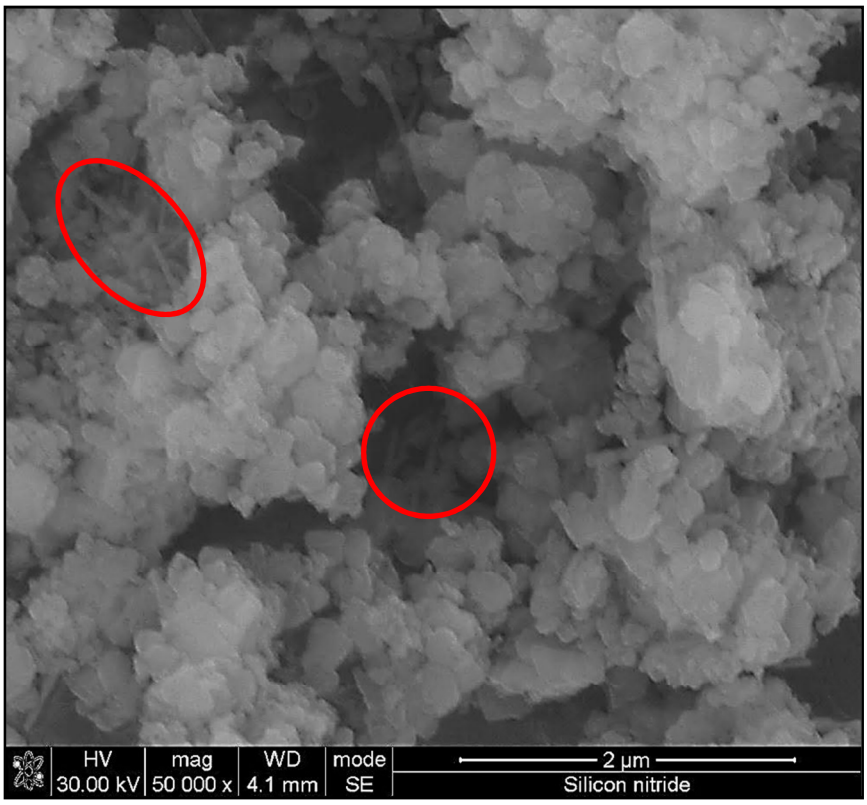


Figure 4.3: SEM imaging of alpha silicon nitride, SNE-10 starting powder from UBE Industries showing presence of beta silicon nitride whiskers (marked).

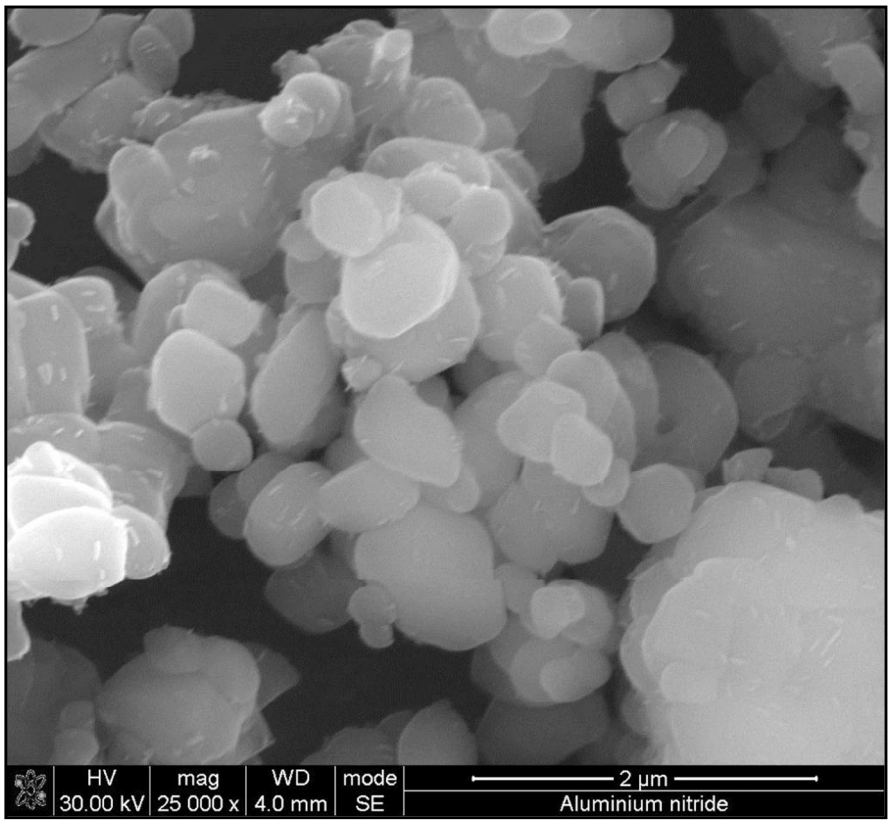


Figure 4.4: SEM imaging of Grade H aluminium nitride starting powder from Tokuyama Industries.

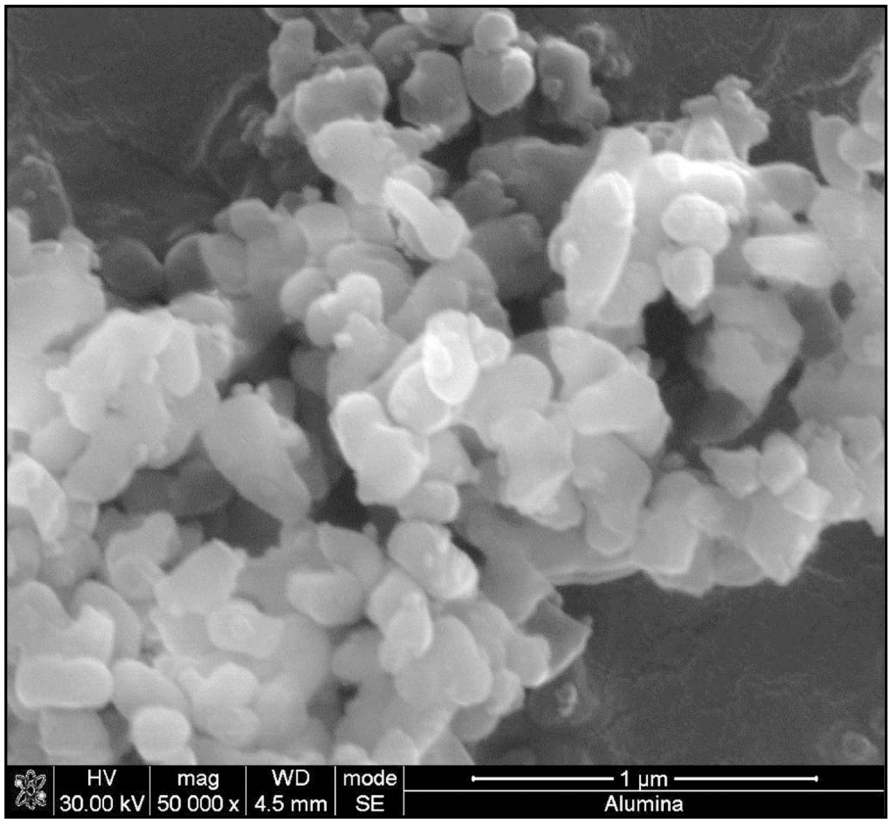


Figure 4.5: SEM imaging of AKP-50 alumina starting powder from Sumitomo.

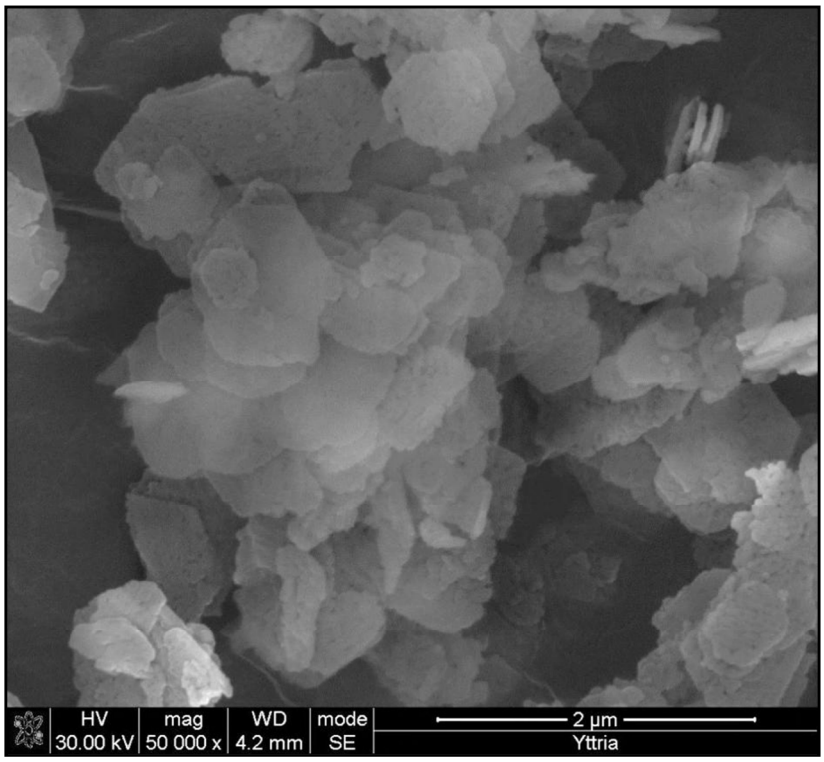


Figure 4.6: SEM imaging of fine grade yttria starting powder from H. C. Starck.

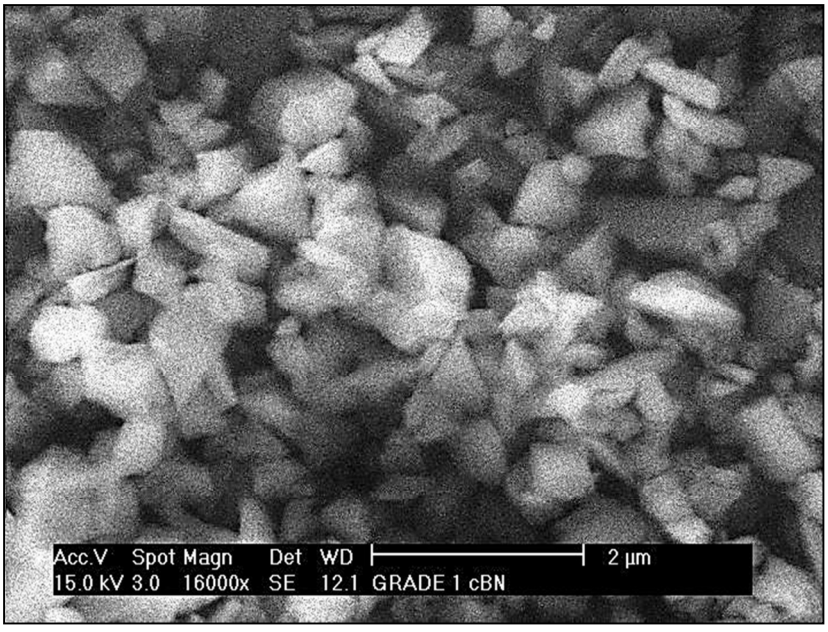


Figure 4.7: SEM imaging of Grade 1 cBN starting powder from Element 6 Pty Ltd.



Figure 4.8: SEM imaging of Grade 9 cBN starting powder from Element 6 Pty Ltd.

4.2. Distribution of sialon constituents

The planetary ball milling route for 4 hours at a rotating speed of 200 rpm proved to be an ideal technique for obtaining a homogenous mixture of the Si_3N_4, AlN, Al_2O_3 and Y_2O_3 starting powders required prior to the sintering of the sialon composites. Obtaining a homogenous mixture is an important step in obtaining a composite with reliable properties. The homogenous mixture can be seen in Figure 4.9, where the analysis was completed through SEM imaging in a back-scattered detection mode of a pure sialon composite (M1-1550).

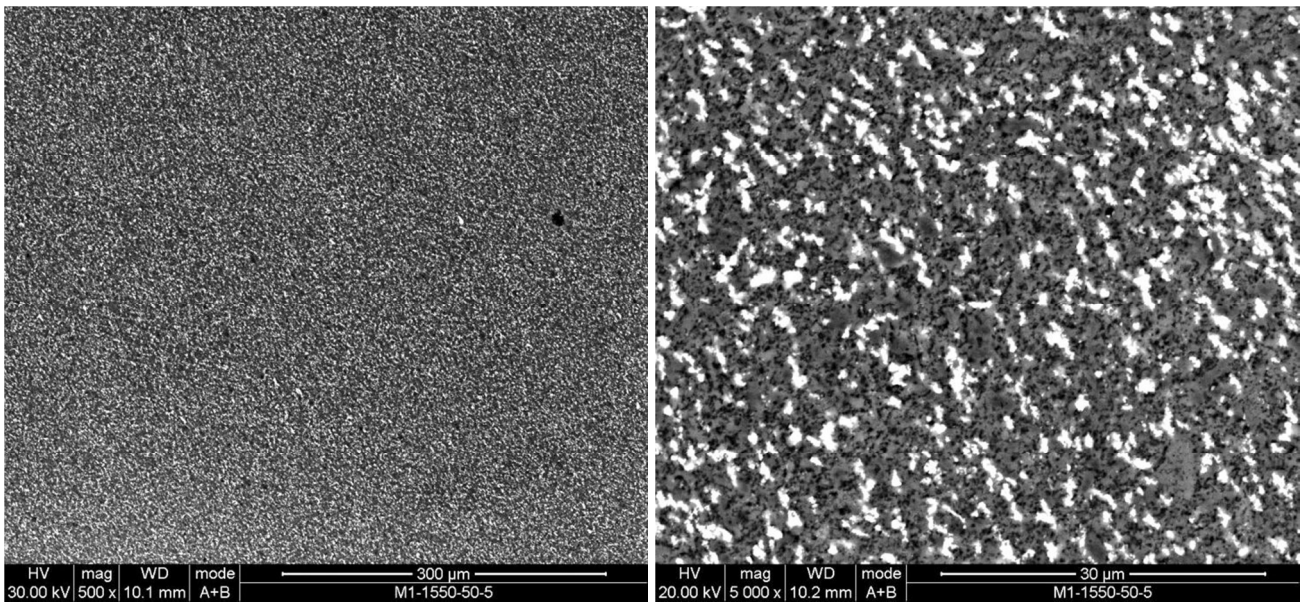


Figure 4.9: Back-scattered SEM imaging showing the distribution of the sialon constituents of M1-1550.

4.3. Distribution of cBN grains in the sialon matrices

The introduction of cBN into the starting sialon composite powders was completed through the use of a Turbula mixing route at 60 rpm for the 10, 20 and 30 vol. % cBN containing composites which can be seen in Figure 4.10. The M1 based samples were sintered at 1600°C with varying cBN content. The resulting samples were thereafter cross-sectioned, polished and analysed with the use of a SEM under a secondary electron detection mode where the distribution of the grade 9 cBN grains was found to be homogenous.

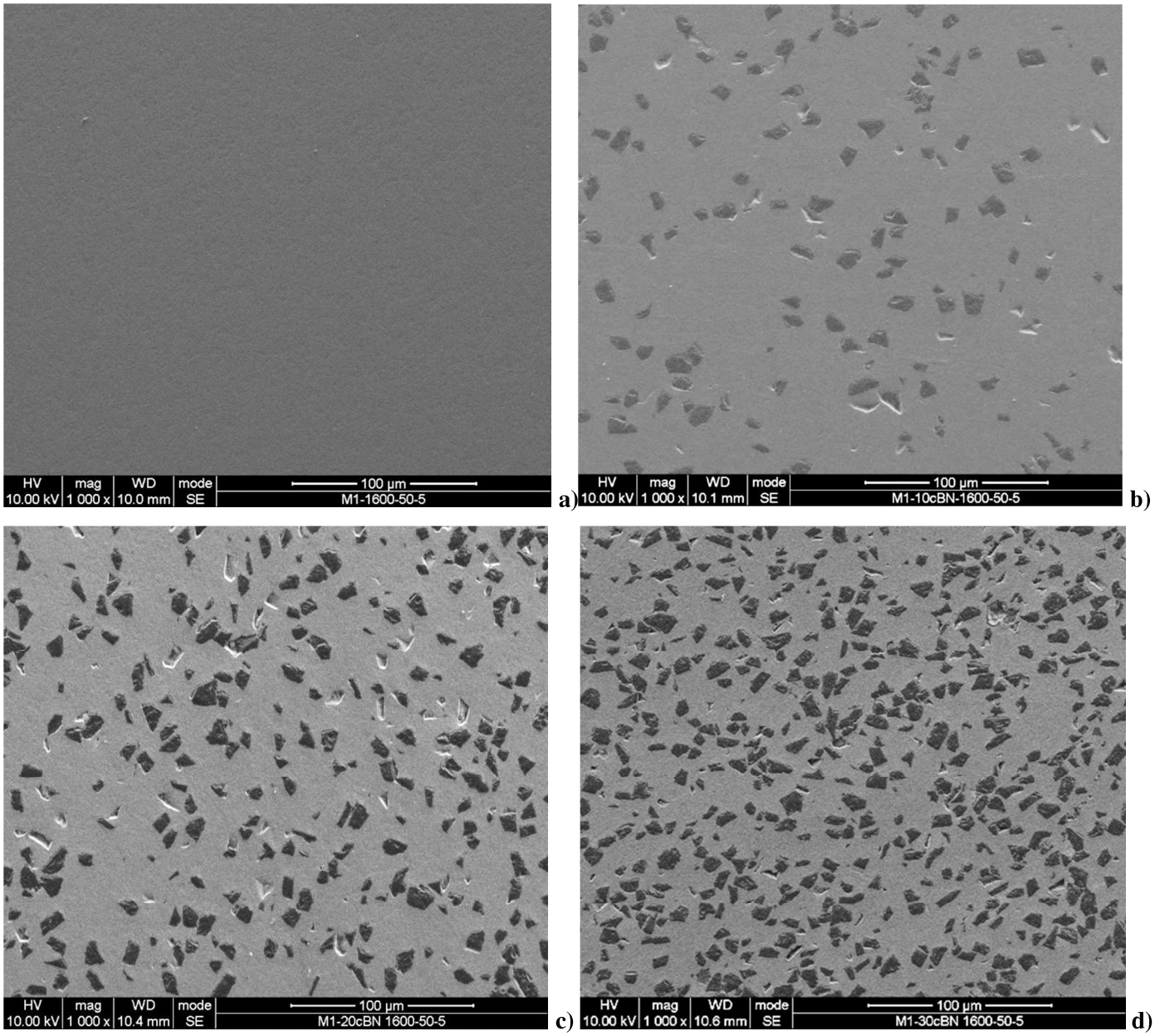


Figure 4.10: Secondary electron SEM imaging showing the grade 9 cBN grain distribution of M1 based composites sintered at 1600°C with varying cBN content: a) 0, b) 10, c) 20 and 30 vol, % cBN (d).

4.4. Densification of sintered sialon /cBN composites

Through the use of SPS as a consolidation technique, grain growth is limited because the sintered sialon materials are fully densified at lower temperatures and in significantly shorter times (faster heating and cooling rates, i.e. shorter sintering profiles) as compared to other sintering methods.

The various sialon ceramics produced were considered to be sufficiently dense when the sintered compacts had a percentage of its theoretical density higher than 97%.

4.4.1. Temperature measurements

Ye et al., 2010 [58] reported that 99.6% of the theoretical density could be obtained through consolidation of M4 at 1500°C, 50 MPa and a dwell time of 7 minutes. M4 is based on the composition used by Ye et al., 2010 [58] which was subsequently found to densify poorly when SPS sintering was attempted at 1500°C achieving only 79.97% of theoretical density. This is a clear indication that the temperature experienced by the sample is truly a function of the spot on which the optical pyrometer is focused when taking the temperature reading. When using the HP D5, the optical pyrometer is focused 5 mm from the upper surface of the sialon composites and the temperature recorded is very close to that experienced by the sintered sample. However when using the Dr. Sinter sintering furnace, where the optical pyrometer is focused on the outer surface of the die, a value lower to that experienced in the sample will be recorded. The temperature difference experienced by samples when using different machines was consistent with what was observed by Langer et al., 2010 [57] (oxide based materials) and Raethel et al., 2009 [85] (silicon nitride and tungsten carbide). Salamon et al., 2007 (86) experimentally verified that sialon samples sintered with the use of the Dr. Sinter systems experience higher sintering temperatures than that measured by an optical pyrometer out the outer surface of the die. Furthermore it was said that the sialon samples were exposed to an overshoot temperature ranging between 140-180°C when heating the sample and between 40-80°C for the isothermal dwell times. The density results for M1 and M4 sintered at 1500°C can be found in Table 4.3.

Table 4.3: Density and open porosity results for pure M1 and M4 sialon ceramics sintered at 1500°C

Sample name	Sintering Conditions	Density (g/cm^3)	Open porosity (%)	% Theoretical density
M1	1500, 50MPa, vacuum, 5 min	2.40 ± 0.07	17.72	70.00
M4	1500, 50MPa, vacuum, 5 min	2.81 ± 0.05	14.34	79.97

The density of the M1 sialon ceramic sintered at 1500°C had a considerably lower density (70.0%) when compared to M4 sialon sintered at the same temperature; however both the matrices show incomplete densification at that temperature.

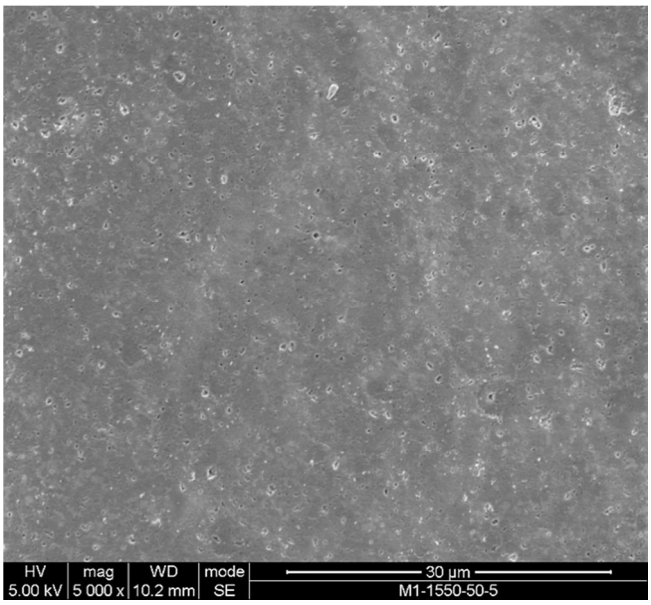
4.4.2. Pure sialon

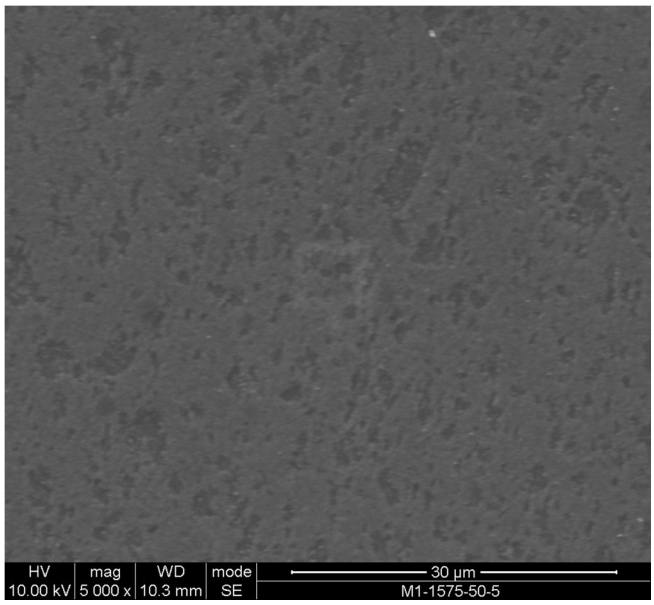
Initially a study was completed for α-sialon based ceramics (M1, M2 and M3), where M1 was used as the base matrix. Two compositional modifications were made to M1 in order to observe their effects on densification. Those included a 2 wt. % AlN reduction (M2) and a 2 wt. % excess of Y_2O_3 (M3). Lastly a composition based on that reported by Ye et al., 2010 [58], named M4 was used for comparison. The compositions of the various matrices are presented in Table 3.3.

Table 4.4: A summary of the composition, n and m values for the various sialon matrices.

SiAlON matrices	m	n	Si_3N_4 (Wt. %)	AlN (Wt. %)	Al_2O_3 (Wt. %)	Y_2O_3 (Wt. %)
Matrix 1 (M1)	0.991	2.502	66.18	16.57	9.02	8.23
Matrix 2 (M2)	0.822	2.458	67.53	14.87	9.20	8.40
Matrix 3 (M3)	0.992	2.502	64.88	16.25	8.84	10.03
Matrix 4 (M4)	1.987	4.493	41.69	29.04	17.24	12.03

In order to observe the effect of sintering temperature of the M1 based sialon composites, SPS sintering was completed using the method described in Section 3.4. The sintering temperatures used were 1550°C, 1575°C, 1600°C and 1625°C. A uni-axial pressure of 50 MPa was applied and a dwell time of 5 minutes was used. The densities of these samples were then measured as described in Section 3.5.1. The results obtained are shown in Table 4.5. The theoretical density of M1 sialon ceramics was obtained through SEM analysis of the cross-sectional surface of the sintered composites shown in Figure 4.11. It was found that full densification could be obtained at temperatures of 1575°C and above, thus the theoretical density was taken to be 3.33g/cm^3.



a)


b)

Figure 4.11: SEM images of the cross-sectional surface of pure M1 sialon sintered at: a) 1550°C showing porosity and b) 1575°C showing full densification.

From Figure 4.11 b) it can be seen that full densification can be achieved when sintering M1 sialon ceramics at 1575°C despite the appearance of grain pull out of the softer phases during the grinding and polishing steps. Figure 4.11 a) shows the lack of densification of M1 sialon sintered at 1550°C with pores being evident.

Table 4.5: The density results of pure M1, M2, M3 and M4 sialon ceramics sintered at various temperatures.

Sintering Temperature	M1		M2		M3		M4	
	ρ (g/cm^3)	ρ, %*	ρ (g/cm^3)	ρ, %*	ρ (g/cm^3)	ρ, %*	ρ (g/cm^3)	ρ, %*
1550°C	2.85 ± 0.03	85.6	2.74 ± 0.05	82.3	3.34 ± 0.01	100.0	2.73 ± 0.03	90.1
1575°C	3.33 ± 0.01	100.0	3.33 ± 0.01	100.0	3.34 ± 0.01	100.0	3.23 ± 0.01	94.4
1600°C	3.33 ± 0.01	100.0	3.30 ± 0.01	99.1	3.33 ± 0.01	99.7	3.39 ± 0.01	99.2
1625°C	3.32 ± 0.01	99.7	3.30 ± 0.01	99.1	3.32 ± 0.01	99.4	3.42 ± 0.01	100

* Theoretical density of M1 and M2 = 3.33 g/cm^3, M3 = 3.34 g/cm^3, M4 = 3.42 g/cm^3

The piston travel data presented in Figure 4.12 reveals that the densification of the various pure M1 sialon composites sintered increases with increasing sintering temperature, as expected. The initial decrease in the piston travel seen in Figure 4.12 is due to the thermal expansion of the graphite assembly. The incomplete densification of the sample sintered at 1550°C is also further confirmed (85.6% from Table 4.5) when compared to the other densification curves of the various M1 sialon sintered above 1550°C. There are two main peak regions when sintering M1 sialon ceramics; these will be discussed further in Section 5.1.

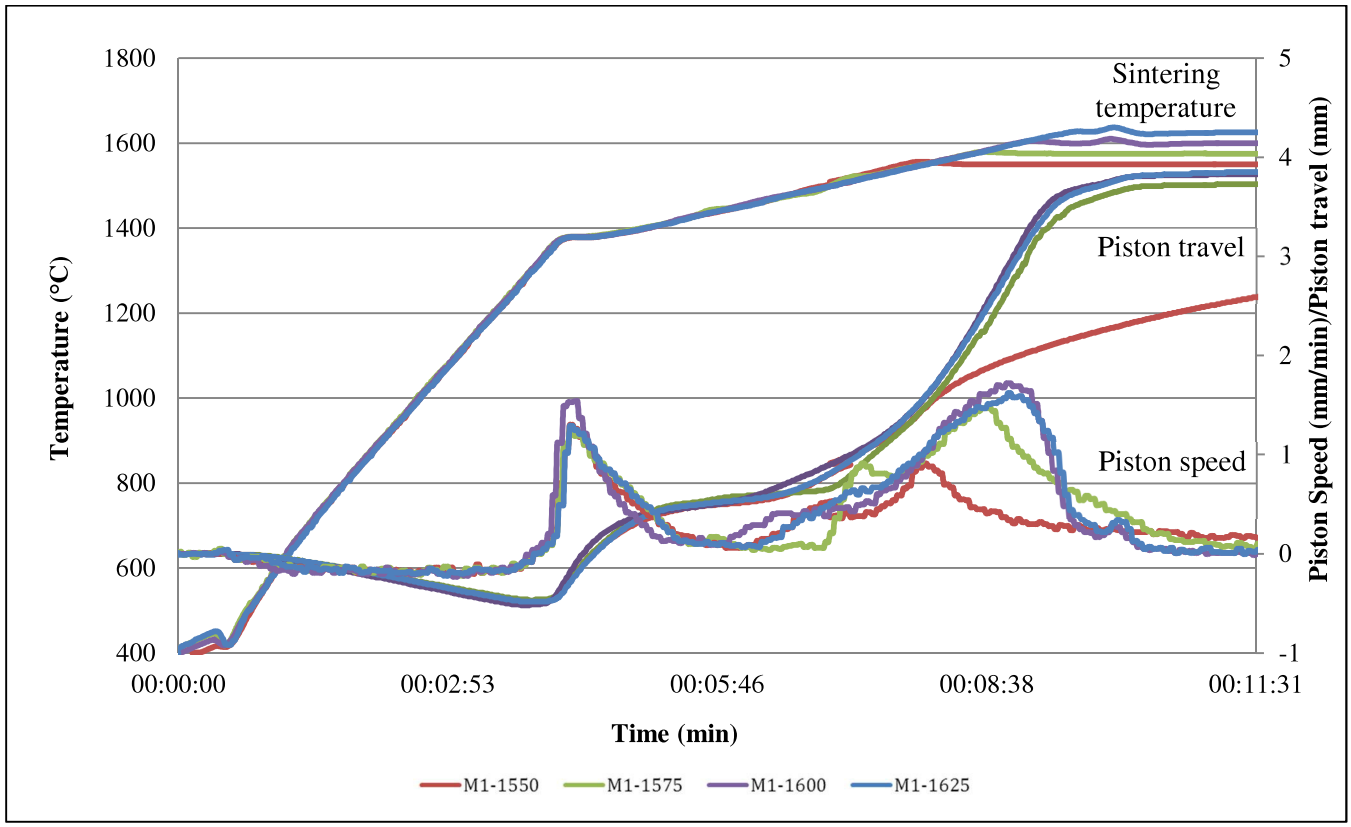


Figure 4.12: Comparative densification curves for M1 sialon ceramics sintered at various temperatures.

The M2 sialon matrix differs from the M1 by a 2 wt. % reduction of aluminium nitride in order to decrease the amount of polytype clusters present in M1 sialon (see black clusters Figure 4.18). The density and open porosity results can be found in Table 4.5. The theoretical density was determined to be 3.33 g/cm^3 through a similar approach used above for sintered M1 sialon ceramics. Full densification of M2 sialon could be achieved at 1575°C similar to that of M1

sialon; however the density of samples sintered at 1550°C is marginally higher for M1 sialon ceramics.

An investigation took place in order to observe the effects of excess yttria on the densification of sialon, thus M3 sialon was developed where the compositional change was a 2 wt. % excess of yttria based on the M1 sialon composition. The density and open porosity results for M3 sialon can be seen in Table 4.5. The theoretical density for M3 sialon was taken to be 3.34 g/cm^3. It was further found that through the excess amount of yttria it is possible to sinter M3 at a temperature of 1550°C, which is lower than that of both M1 and M2, which can sinter to full density only at temperatures greater than 1550°C.

Fully dense M4 sialon ceramics could only be obtained when sintered at 1625°C, which is significantly higher than that obtained for M1 (1575°C), M2 (1575°C) and M3 (1550°C). However it was possible to densify M4 sialon up to 99.2 % of the theoretical density at 1600°C which was found to be 3.42 g/cm^3.

4.4.3. Sialon /cBN composites

The effects of cBN addition on the densification of sialon were then investigated for the various sialon matrices by varying cBN content along with the sintering temperature whilst maintaining the uni-axial pressure of 50 MPa and a dwell time of 5 minutes.

For the reinforcing of the sialon matrix, two grades of cBN were used, namely grade 1 and grade 9 cBN (Element 6, Pty Ltd) with a mean particle size of 0.72 and 10.31 µm respectively (Table 4.1). Initially the use of grade 1 cBN as a reinforcing agent was investigated. It was found that the Turbula mixing route was not sufficient in dispersing the cBN grains homogenously throughout the sialon matrix. It can be seen in Figure 4.13 that an extensive porosity and poor distribution of the cBN grains was obtained. Therefore the grade 1 cBN had to be added through

a planetary ball mixing step for 30 minutes at a speed of 200 rpm. The mixing duration was low in order to reduce the excessive wear of the agate milling media. The pores at the location of the former cBN grain sites are depicted by the black colouration in the images whereas the lighter areas represent the M1 sialon matrix. The distribution through the planetary ball mixing step is improved; however porosity is still seen at the location of the former cBN grains (Figure 4.13b).

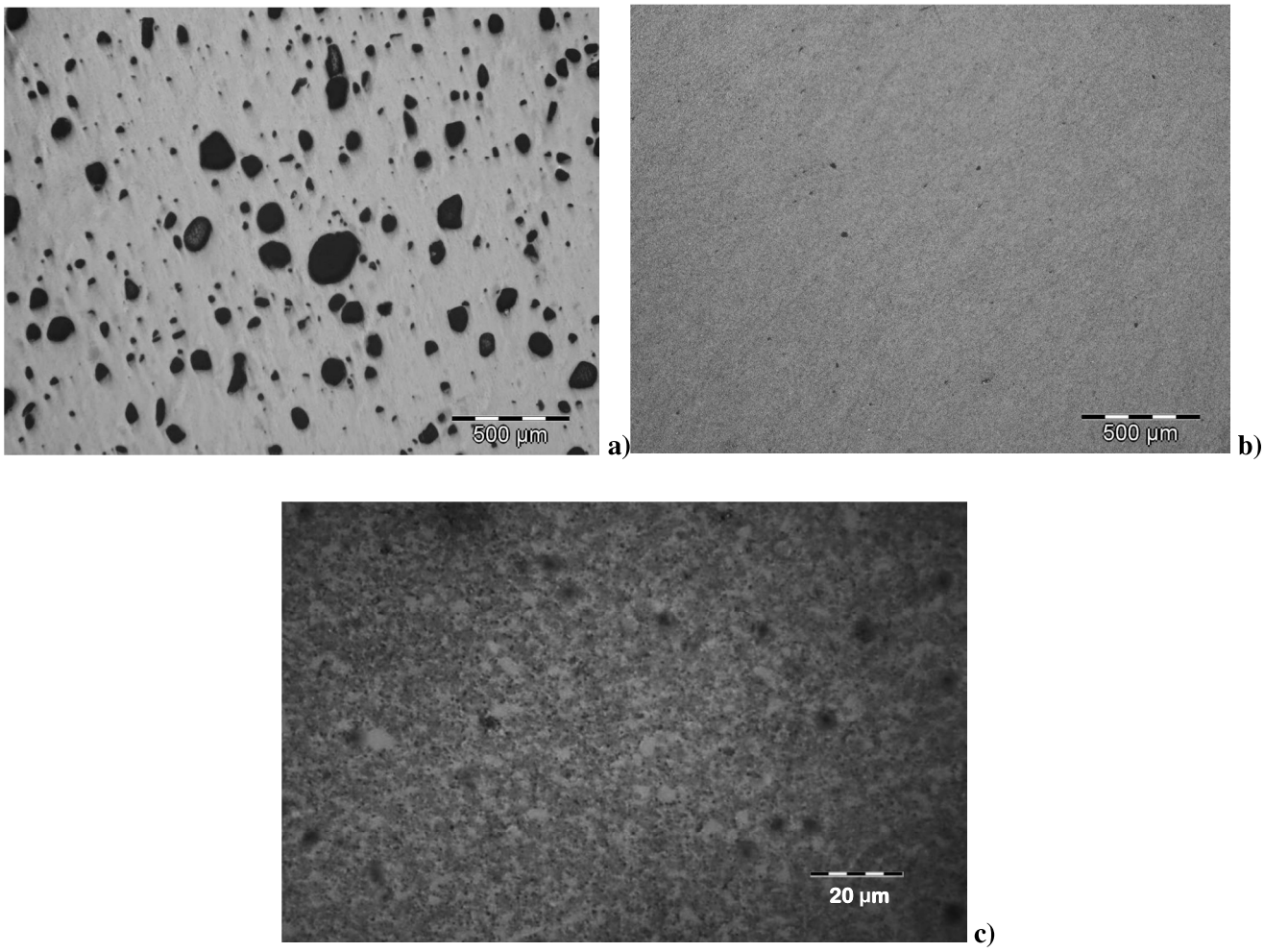


Figure 4.13: Optical microscopy of the dispersion of grade 1 cBN in the sialon matrix through the Turbula (a) and planetary ball milling (b and c) routes densified at 1575°C.

The porosity was attributed to the cBN grains undergoing hexagonalization when sintered at 1575°C with the addition of grade 1 cBN and as a result the transformation of cBN to the softer hBN phase promotes the pull out experienced during the grinding and polishing steps discussed further in Section 5.4. This hexagonalization of the cBN grains could not be confirmed through the use of XRD as majority of the hBN/cBN grains present had been pulled out during the grinding step. Sialon composites containing grade 1 cBN grains have significantly lower

densities than that of grade 9 cBN composites. The decrease in density (Table 4.6) was attributed to the transformation of cBN to hBN in grade 1 cBN sialon composites.

Table 4.6: The densities obtained for the sialon composites sintered with and without grade 1 and grade 9 cBN.

Sample	Grade cBN	Sintering temperature (°C)	Percentage of theoretical density (%)*	Density (g/cm^3)
Pure sialon	-	1575	100	3.33 ± 0.01
Turbula mixed (30 vol. % cBN)	1	1575	81.9	2.78 ± 0.04
Planetary ball mixed (30 vol. % cBN)	1	1575	83.4	2.83 ± 0.03
Turbula mixed (30 vol. % cBN)	9	1575	98.1	3.31 ± 0.01

* Theoretical density of M1 = 3.33 g/cm^3, M1-30cBN = 3.37 g/cm^3

Due to the extensive hexagonalization of the grade 1 cBN it was decided that a larger grain size of cBN had to be used, thus grade 9 cBN (Element 6, Pty. Ltd) was chosen. Through the addition of cBN to the sialon matrix a decrease in the sinterability and densification due to the expected retarding effect of cBN was experienced. The densities and open porosities for pure M1 sialon ceramics along with the values for the grade 9 cBN reinforced sialon composites are presented in Table 4.7.

Table 4.7: The density results of pure M1 and M1/cBN ceramics sintered at various temperatures.

Sintering Temperature	cBN content (vol. %)							
	0		10		20		30	
	ρ (g/cm^3)	ρ, %*	ρ (g/cm^3)	ρ, %*	ρ (g/cm^3)	ρ, %*	ρ (g/cm^3)	ρ, %*
1550°C	2.85 ± 0.03	85.6						
1575°C	3.33 ± 0.01	100.0	3.32 ± 0.01	99.3	3.31 ± 0.01	98.5	3.31 ± 0.01	98.1
1600°C	3.33 ± 0.01	100.0	3.32 ± 0.01	99.3	3.29 ± 0.01	97.9	3.29 ± 0.01	97.5
1625°C	3.32 ± 0.01	99.7	3.30 ± 0.01	98.7	3.28 ± 0.01	97.6	3.28 ± 0.01	97.2

* Theoretical density: M1 = 3.33, M1-10cBN = 3.34, M1-20cBN = 3.36 and M1-30cBN = 3.37 g/cm^3

Figure 4.14 shows the influence of the sintering temperature and cBN grain size on their respective relative densities of the M1 sialon composites, confirming that an increase in both the sintering temperature and the cBN content decrease the percentage of theoretical density. The reduction of density with increasing sintering temperature indicates the hexagonalization of the cBN grains since no porosity was observed through SEM.

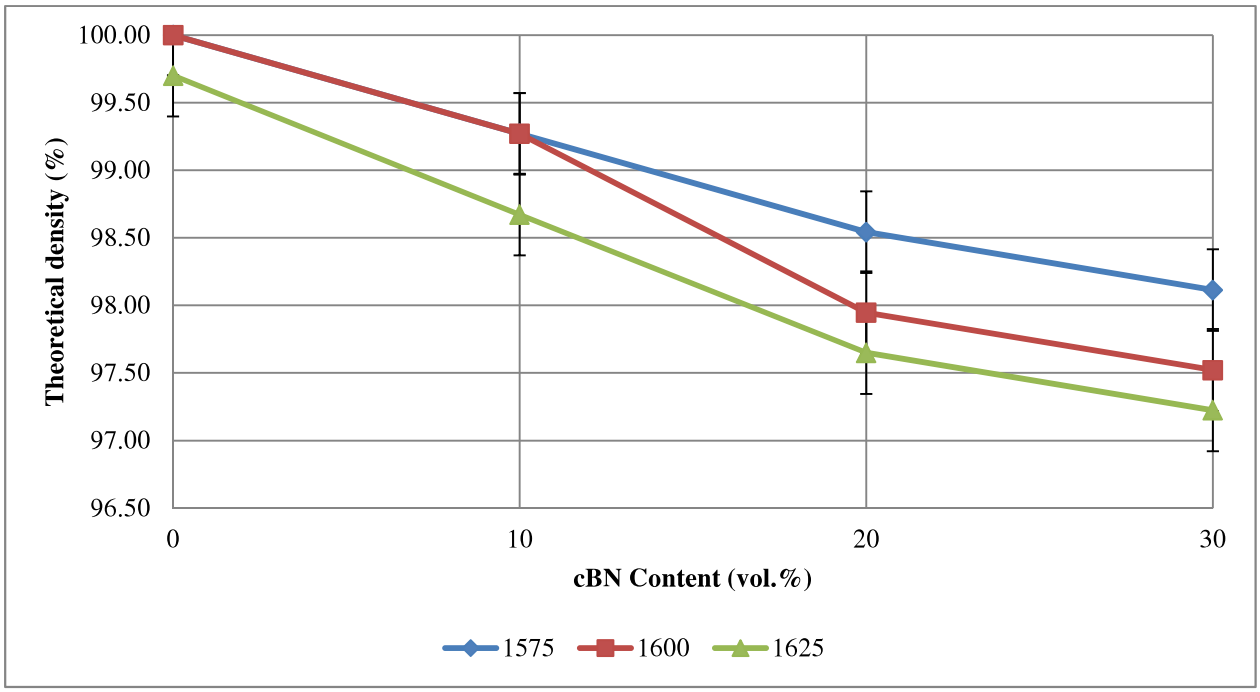


Figure 4.14: Influence of cBN content and sintering temperature on the percentage of the theoretical densities of M1 sialon ceramics.

The effect of grade 9 cBN on the aluminium nitride reduced matrix, M2, was then investigated by introducing 30 vol. % cBN to M2 sialon and sintering at 1575 and 1600°C. The results of the densities and open porosity are given in Table 4.8. Similar to M1/cBN composites, a decrease in the percentage of the respective theoretical densities of the composites is obtained with increasing cBN content and sintering temperature although for the remainder of the sialon matrices an addition of 30 vol.% cBN was studied (Table 4.8, 4.9 and 4.10).

Table 4.8: The density results of pure M2 and M2/cBN ceramics sintered at various temperatures.

Sintering Temperature	cBN content (vol. %)			
	0		30	
	ρ (g/cm^3)	ρ, %*	ρ (g/cm^3)	ρ, %*
1550°C	2.74 ± 0.05	82.3		
1575°C	3.33 ± 0.01	100.0	3.31 ± 0.01	98.1
1600°C	3.30 ± 0.01	99.1	3.29 ± 0.01	97.5
1625°C	3.30 ± 0.01	99.1		

* Theoretical density of M2 = 3.33 and M2-30cBN = 3.37 g/cm^3

The yttria rich matrix, M3, is expected to aid in the densification of the sialon/cBN composites since there is more liquid phase present as compared to M1 and M2 sialon matrices. The results of the density and open porosity for M3 sialon composites containing grade 9 cBN are summarised in Table 4.9.

Table 4.9: The density results of pure M3 and M3/cBN ceramics sintered at various temperatures.

Sintering Temperature	cBN content (vol. %)			
	0		30	
	ρ (g/cm^3)	ρ, %*	ρ (g/cm^3)	ρ, %*
1550°C	3.34 ± 0.05	100		
1575°C	3.34 ± 0.01	100.0	3.33 ± 0.01	98.5
1600°C	3.33 ± 0.01	99.1	3.31 ± 0.01	98.2
1625°C	3.32 ± 0.01	99.1		

* Theoretical density of M3 = 3.34 and M3-30cBN = 3.38 g/cm^3

The effect of sintering temperature and cBN content on densification follows the same trend experienced for M1 and M2 sialon composites containing cBN (grade 9). An increase in the sintering temperature and cBN content negatively affect the percentage of theoretical densities attained for M3 sialon based ceramics, with the volume fraction of cBN being a more contributing factor. The effect of cBN content (grade 9) on the final densities obtained for M4 was obtained by adding 30 vol. % cBN followed by sintering at a temperature of 1600°C since M4 did not reach sufficient density when sintered at 1575°C. Due to the hexagonalization experienced by the grade 9 cBN grains in M1, M2 and M3 when the composites were sintered at 1625°C the M4/cBN composites were not investigated at this temperature. In the case of M4-30cBN-1600 the addition of 30 vol. % cBN results in a significant decrease in density (99.2 to 97.1% of theoretical).

Table 4.10: The density results of pure M4 and M4/cBN ceramics sintered at various temperatures.

Sintering Temperature	cBN content (vol. %)			
	0		30	
	ρ (g/cm^3)	ρ, %*	ρ (g/cm^3)	ρ, %*
1500°C	2.73 ± 0.03	79.9		
1575°C	3.23 ± 0.01	94.6		
1600°C	3.39 ± 0.01	99.1	3.34 ± 0.01	97.1
1625°C	3.42 ± 0.01	100		

* Theoretical density M4 = 3.42 and M4-30cBN = 3.44 g/cm^3

4.5. Microstructure and phase evolution of sialon /cBN composites

Qualitative XRD analysis was carried out on sintered sialon ceramics with different matrix composition, sintering temperature and additive content (vol. % cBN). This qualitative analysis helps to identify phases that are favoured at specific conditions and compositions by comparing the relative peaks corresponding to the different identified patterns.

Table 4.11: XRD pattern data used to analyse the x-ray diffractograms in this project.

Name of crystalline phases	Chemical Formula	Card No.	Structure	a	c
α- sialon	$Y_{0.54}(Si_{9.57}Al_{2.43})(O_{0.81}N_{15.19})$	00-042-0251	Hexagonal	7.829	5.708
M1				7.803	5.684
M2				7.796	5.701
M3				7.813	5.686
M4				7.829	5.708
β- sialon	Si_5AlON_7 ($Si_{6-z}Al_zO_zN_{8-z}$)	00-048-1615	Hexagonal	7.635	2.934
Polytype (12H)	$SiAl_5O_2N_5$	00-042-0161	Hexagonal	3.030	32.730
α-Si_3N_4	Si_3N_4	01-076-1407	Hexagonal	7.752	5.620
YAG	$Y_3Al_2(AlO_4)_3$	01-082-0575	Cubic	12.024	-
cBN	cBN	01-089-1499	Cubic	3.616	-
hBN	hBN	01-073-2095	Hexagonal	2.504	6.661

The details of the patterns used for the qualitative XRD analysis can be found in Table 4.11 however it must be noted that the lattice parameters for α- sialon differ for Matrix 1, 2, 3 and 4 since the lattice parameters of both α and β-sialon depend on the composition of the matrix [19]. The various crystalline phases analysed for different sialon matrices sintered at 1600°C are presented in Figure 4.15. The intensities of the various phases in their respective sialon matrices are presented in Table 4.12.

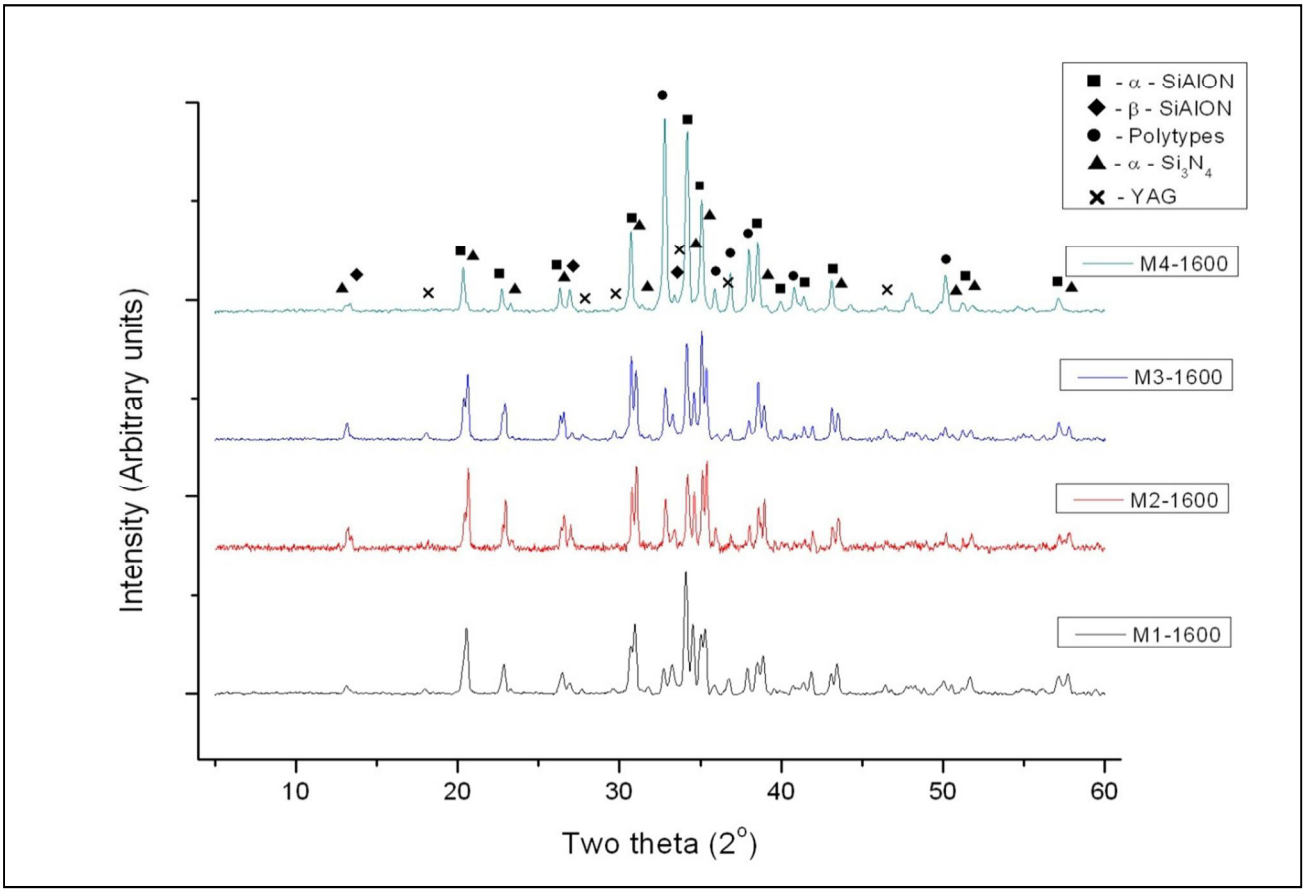


Figure 4.15: Comparison of the X-Ray Diffractograms of pure sialon ceramics sintered at 1600°C.

Table 4.12: Intensities of the various formations of crystalline phases for pure sialon ceramics sintered at 1600°C.

Sialon	X-ray peak intensity*				
	α - Si_3N_4	**α - sialon**	**β - sialon**	**Polytype (12H)**	**YAG**
M1-1600	m	s	vw	w	vw
M2-1600	s	m	w	vw	vw
M3-1600	m	s	vw	vw	w
M4-1600	vw	s	w	s	-

* The symbols used for intensity of the x-ray peaks were s (strong), m (medium), w (weak) and vw (very weak)

4.5.1. M1/cBN composites

4.5.1.1. Sialon materials without cBN

Initially a comparison of the x-ray diffractograms obtained for M1 sialon ceramics sintered at 1550, 1575, 1600 and 1625°C were used to observe the effect of sintering temperature on the formation of the different crystalline phases present.

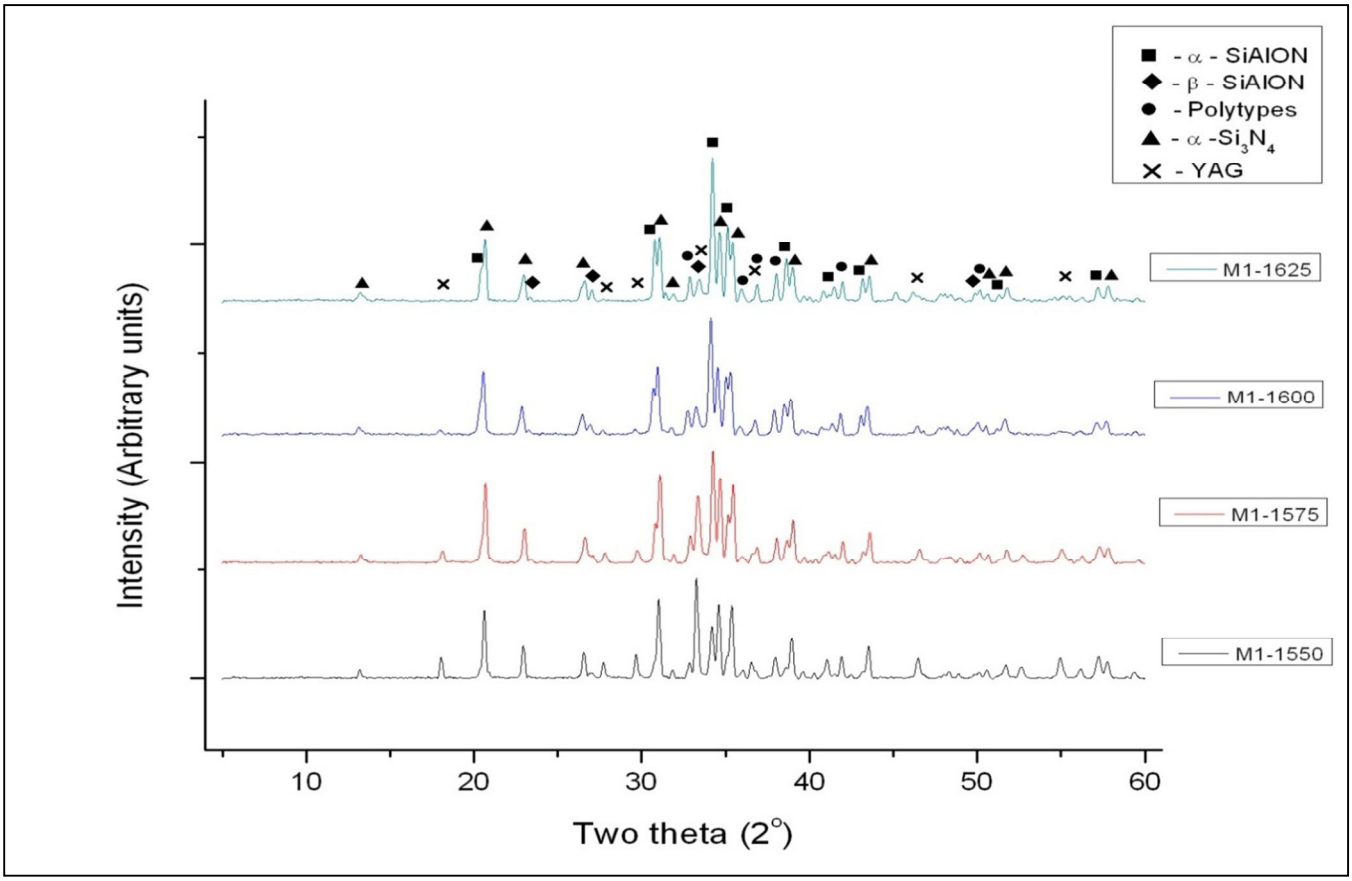


Figure 4.16: Comparison of the X-Ray Diffractograms of pure M1- sialon sintered at different temperatures (1550-1625°C).

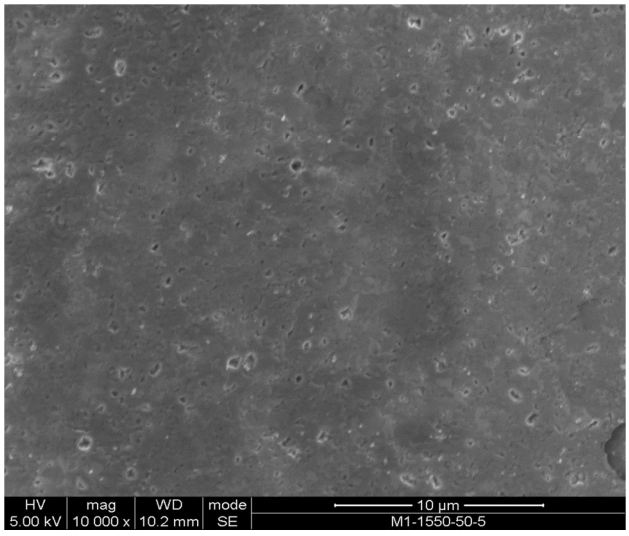
As shown in Figure 4.16 it was possible to identify phases that were present and to establish increasing or decreasing trends for the various phases present. Such increasing or decreasing trends are denoted by a '↑' or '↓' in Table 4.13. If the respective peak intensities of the various phases remain the same as compared to the standard, the trend is denoted as '–'.

Table 4.13: Identification of phases present and their respective trends for pure M1- sialon sintered at varying temperatures (x-phase present and ↑↓-trend).

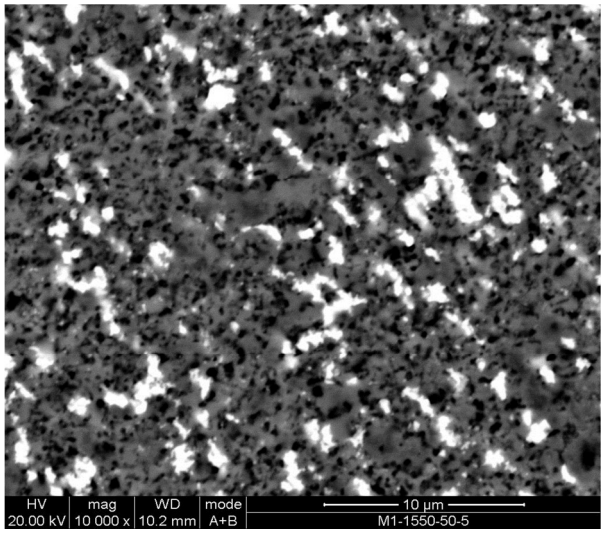
Sample	α- sialon		β- sialon		Polytype (12H)		Si_3N_4		YAG	
	ID	Trend	ID	Trend	ID	Trend	ID	Trend	ID	Trend
M1-1550 (Base)	x	-	x	-	x	-	x	-	x	-
M1-1575	x	↑	x	-	x	small ↑	x	↓	x	↓
M1-1600	x	↑	x	small ↑	x	small ↑	x	↓	x	↓
M1-1625	x	↑	x	small ↑		small ↑		↓		↓

Therefore as the temperature is increased an increase in the formation of the α-sialon phase is dominant with very little increase in the β-SiAlON phase. It was found that there was also a slight increase in polytype formation in the range of (1550-1625°C). Furthermore an increase in temperature decreases the content of Si_3N_4 and YAG phases; thisis expected due to the formation of the α-SiAlON phase as seen in Figure 4.16. The SEM micrographs are in agreement with the analysis derived from XRD as can be seen from Figure 4.17 - Figure 4.20 for M1 sialon sintered at different temperatures.

Figure 4.17 shows the microstructure of pure M1 sialon sintered at 1550°C. As can be seen, there was incomplete densification (black phase is porosity). The grey phase represents the mixture of α / β sialon with 12 H polytype and finally the light phase represents the yttria-rich grain boundary phase. Due to insufficient grain growth experienced at the sintering condition the densification of this sample was found to be poor (85.6%).



a)



b)

Figure 4.17: SEM micrographs of M1-sialon sintered at 1550°C showing porosity as well as poor grain growth in a) secondary electron and b) back-scattered detection modes.

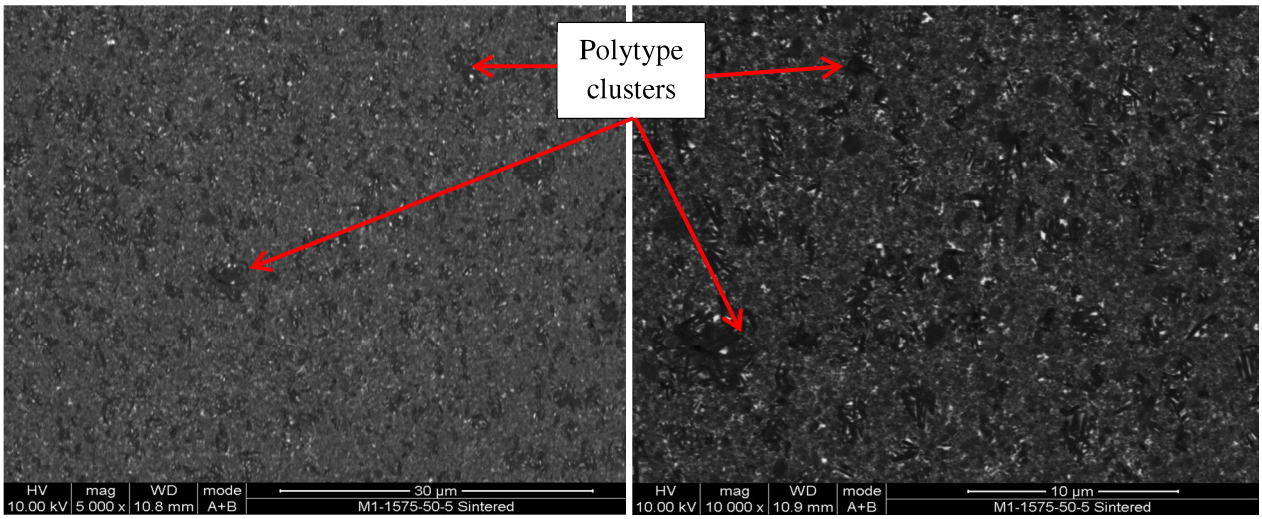


Figure 4.18: SEM micrographs of M1-sialon showing that a fully dense sample can be obtained at 1575°C.

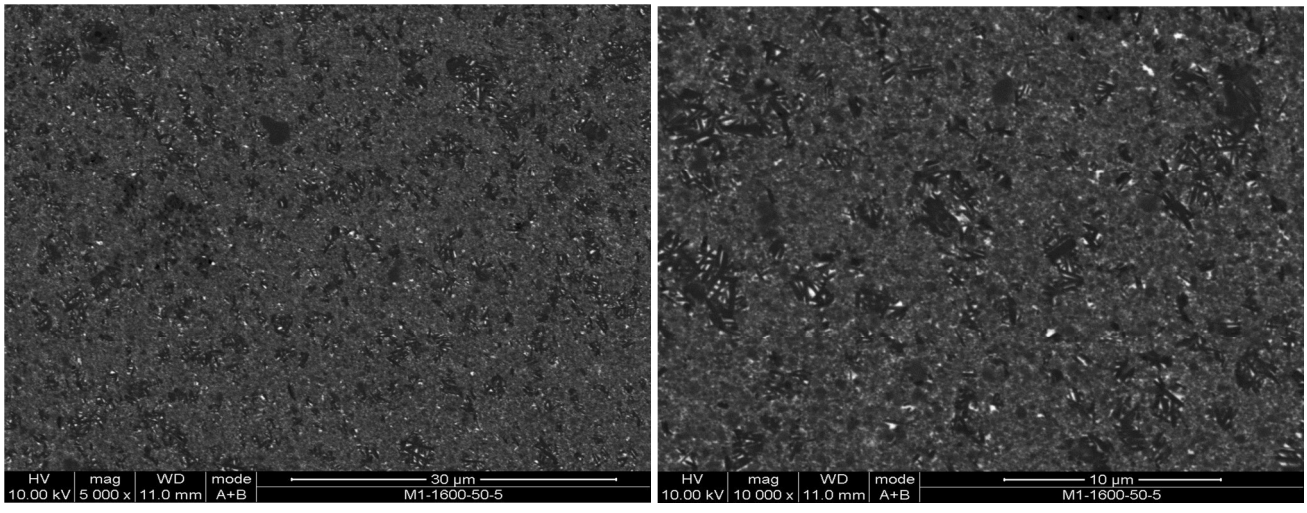


Figure 4.19: SEM micrographs of M1-sialon sintered at 1600°C in back-scattered detection mode.

Fully dense pure M1 sialon can be obtained at temperatures as low as 1575°C since the microstructure was observed to have no porosity (see Figure 4.18). As the sintering temperature is raised, the increased formation of the polytype (dark) cluster can be observed in back-scattered SEM imaging though Figure 4.18, Figure 4.19 and Figure 4.20. This is consistent with the XRD qualitative analysis given in Table 4.13. Furthermore, as the temperature increases the quantity of YAG pools is seen to decrease. This phase is located primarily at the grain boundaries for M1 sialon sintered at 1625°C. This decrease is due to the formation of the α-sialon phase since the structure incorporates yttrium in it.

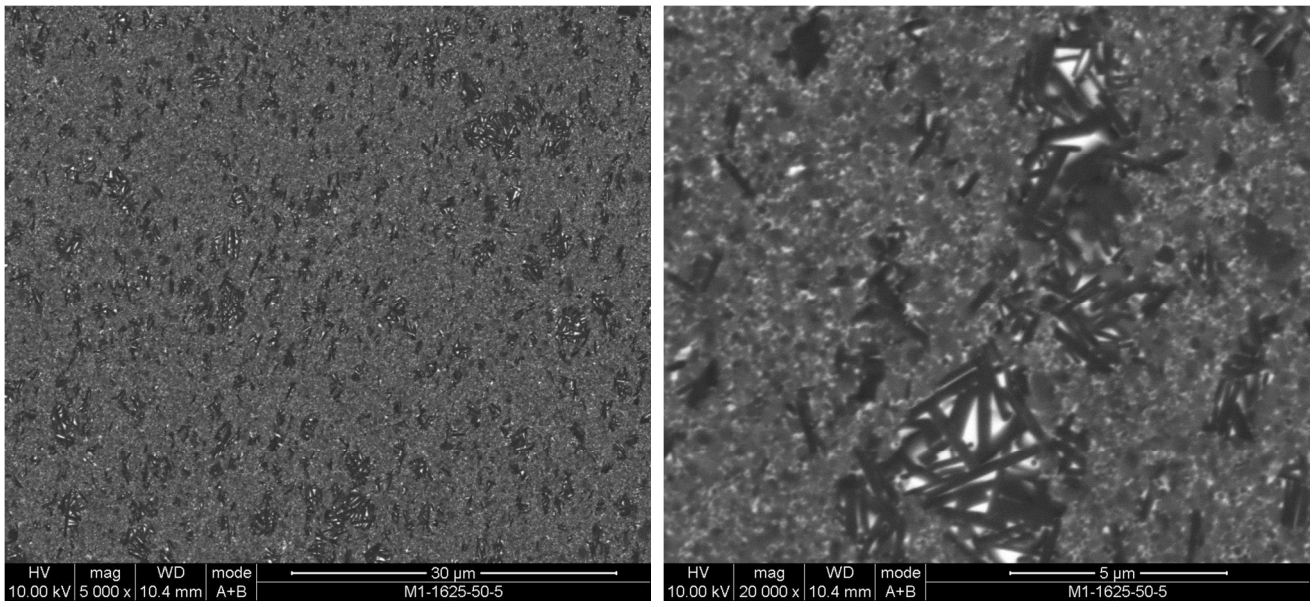


Figure 4.20: SEM micrographs of M1-sialon sintered at 1625°C in back-scattered detection mode.

4.5.1.2. M1 sialon containing cBN additive

In order to observe the effect of grade 9 cBN content on the phase formation of M1 sialon ceramics a single temperature (1575°C) was selected and the cBN content (0-30 vol. % cBN) was varied (Figure 4.21).

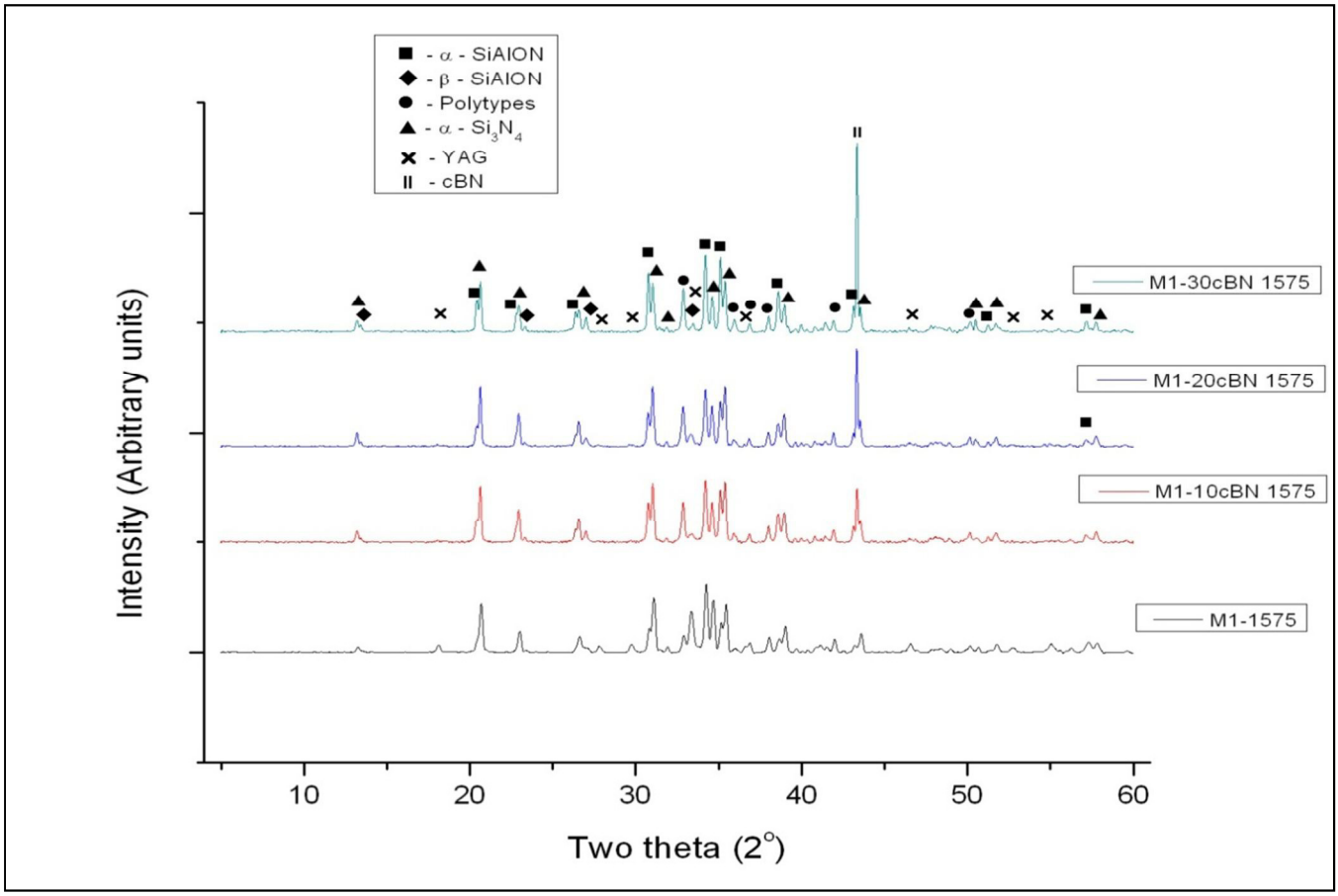


Figure 4.21: Comparison of the X-Ray Difftactograms of M1-sialon/cBN composites sintered at 1575°C with varying grade 9 cBN content (0-30 vol. %).

It was observed that an increase in the cBN content results in a significant increase of the α-sialon and very little increase in the β-sialon phase (Figure 4.21). Increasing the cBN content from 0 vol. % to 10 vol. % also increases the polytypoid phase formation; however an increase above 10 vol. % results in negligible change. Moreover the increase from 0 vol. % to 10 vol. % results in the elimination of YAG phase.

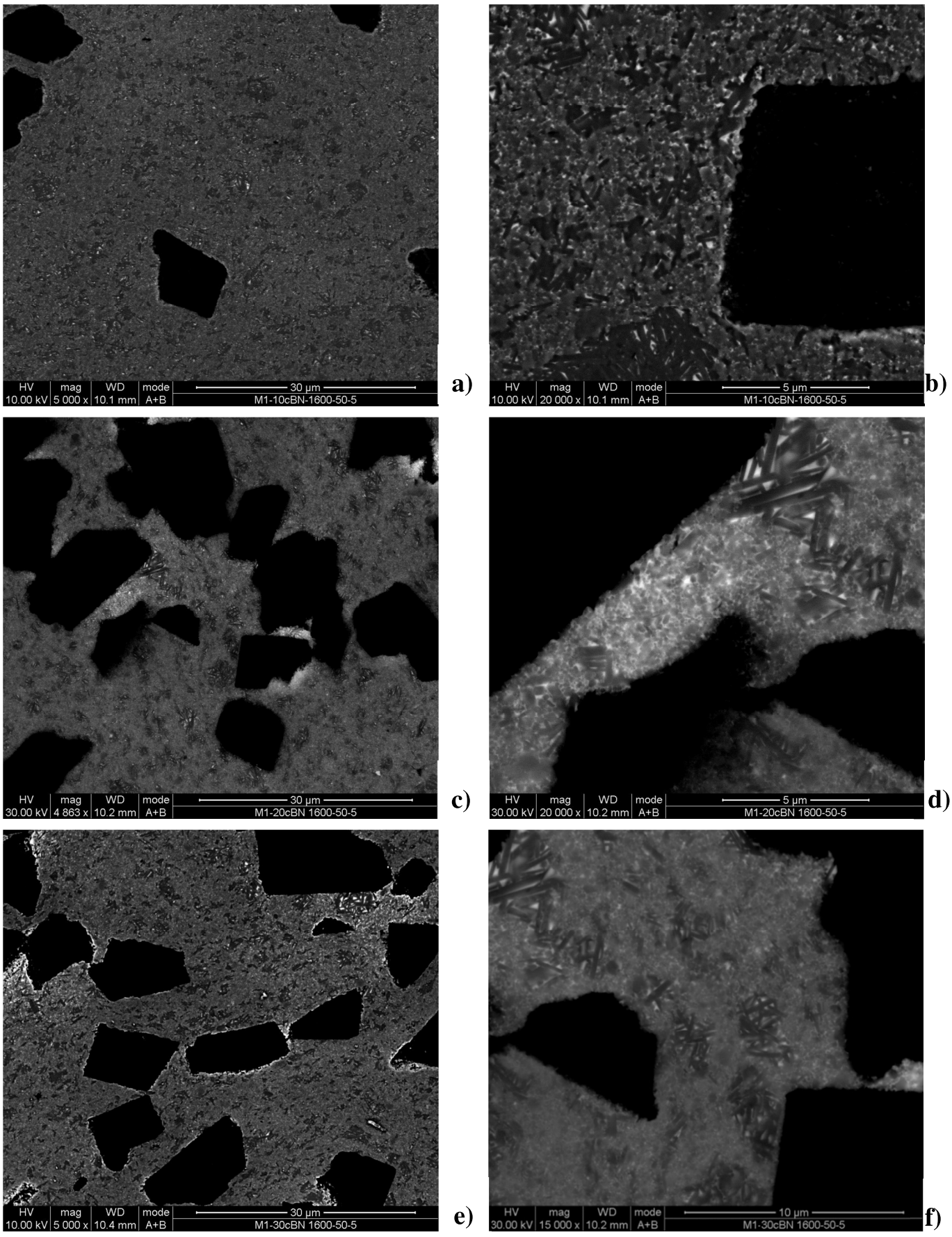


Figure 4.22: SEM micrographs of M1-Sialon/cBN composites sintered at 1600°C with varying cBN content: 10 (a, b), 20 (c, d) and 30 (e, f) vol. % cBN.

During SPS sintering the liquid/glassy phase-rich in in yttrium is expected to be present in the sialon matrix however when cBN grains are added to the matrix this yttria-rich phase is seen to be present in higher amounts between cBN grains (for composites with > 10 vol. % cBN additive) as shown in Figure 4.22. This liquid phase pooling was observed to increase with increasing cBN content. A similar analysis was completed for ceramics based on Matrix 2, 3 and 4 in order to observe the effects of sintering temperature and cBN content on the various phases present.

4.5.2. M2 /cBN composites

To observe the effects of sintering temperature and cBN content on the phase formation of M2-sialon ceramics pure M2-sialon and M2-30 vol. % cBN composites were sintered at 1575 and 1600°C (Figure 4.23).

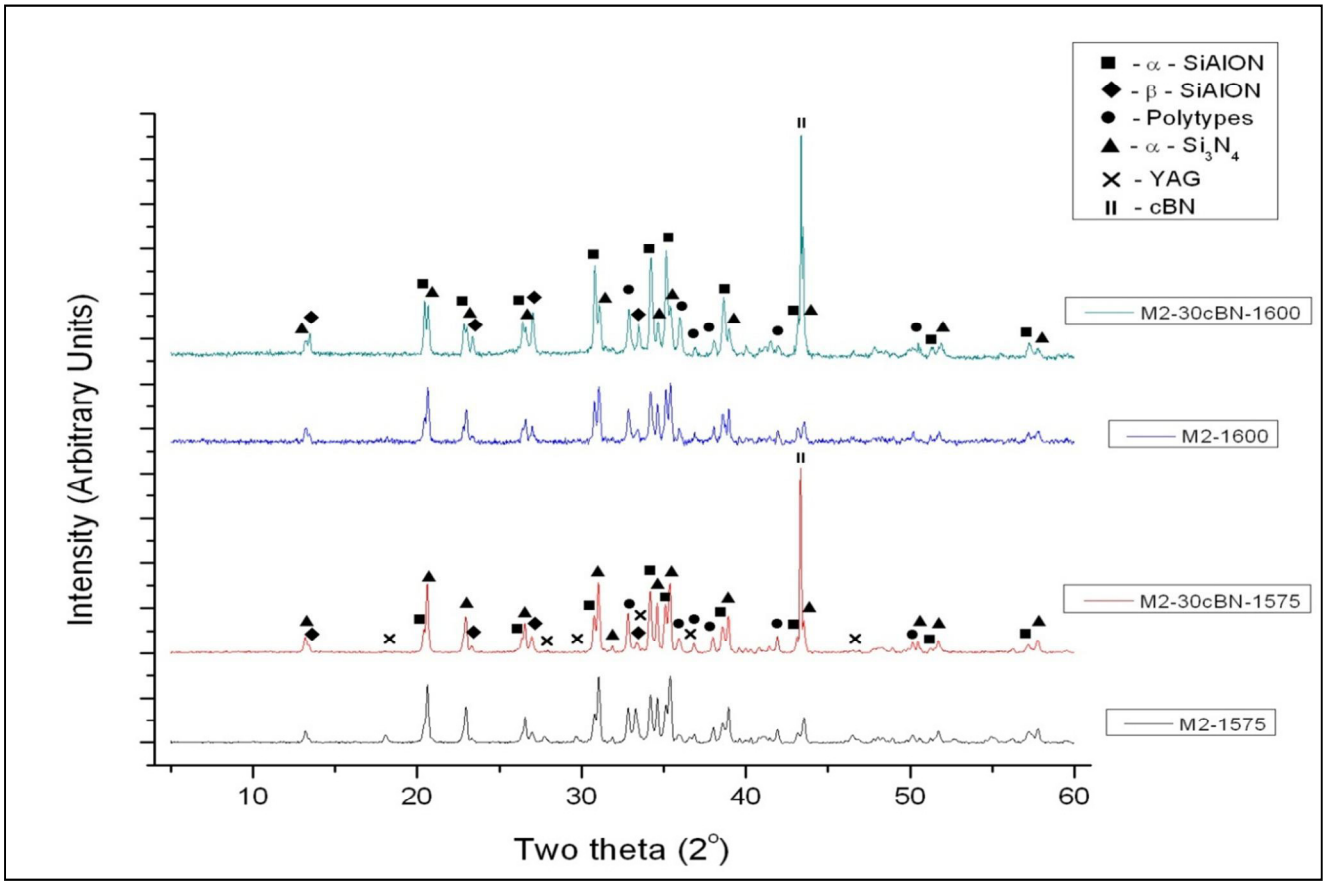


Figure 4.23: X-ray diffractograms of M2- sialon /cBN composites sintered with varying temperature (1575-1600°C) and cBN content (0 and 30 vol. %)

An increase in the sintering temperature and cBN content promote the formation of the α-sialon and β-sialon phases which consequently results in a decrease of the Si_3N_4 and YAG phases (eliminated at 1575° with 30 vol. % cBN). However the polytype formation is not affected by an increase in temperature although there is a slight increase with respect to increasing cBN content. The XRD analysis (Figure 4.23) was confirmed with the microstructural analysis of pure M2 sialon (Figure 4.24a,c,e) and that of a 30 vol. % cBN containing M2 sialon composite (Figure 4.24b,d,f). The differences in the microstructure are visible by comparing the secondary and back-scattered electron images.

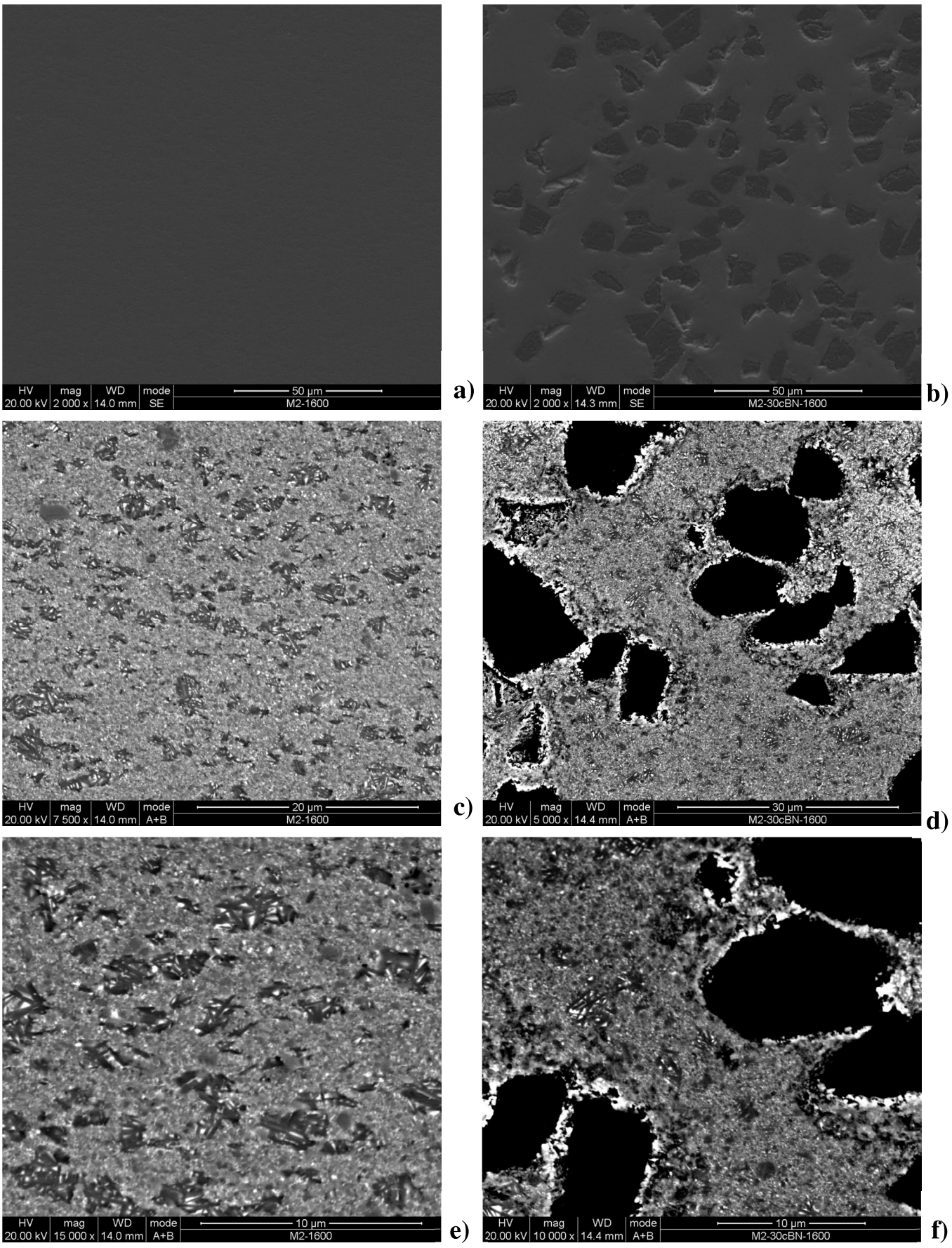


Figure 4.24: SEM micrographs comparing pure M2-sialon with M2-sialon sintered with 30 vol. % cBN at 1600°C: a, c and e) pure M2 and b, d and f) M2 with 30 vol. %cBN.

4.5.3. M3 /cBN composites

The same approach as discussed above was used for analysing the M3-sialon based ceramics and the respective comparative x-ray diffractograms can be found in Figure 4.25 for the composites sintered at 1575 and 1600°C.

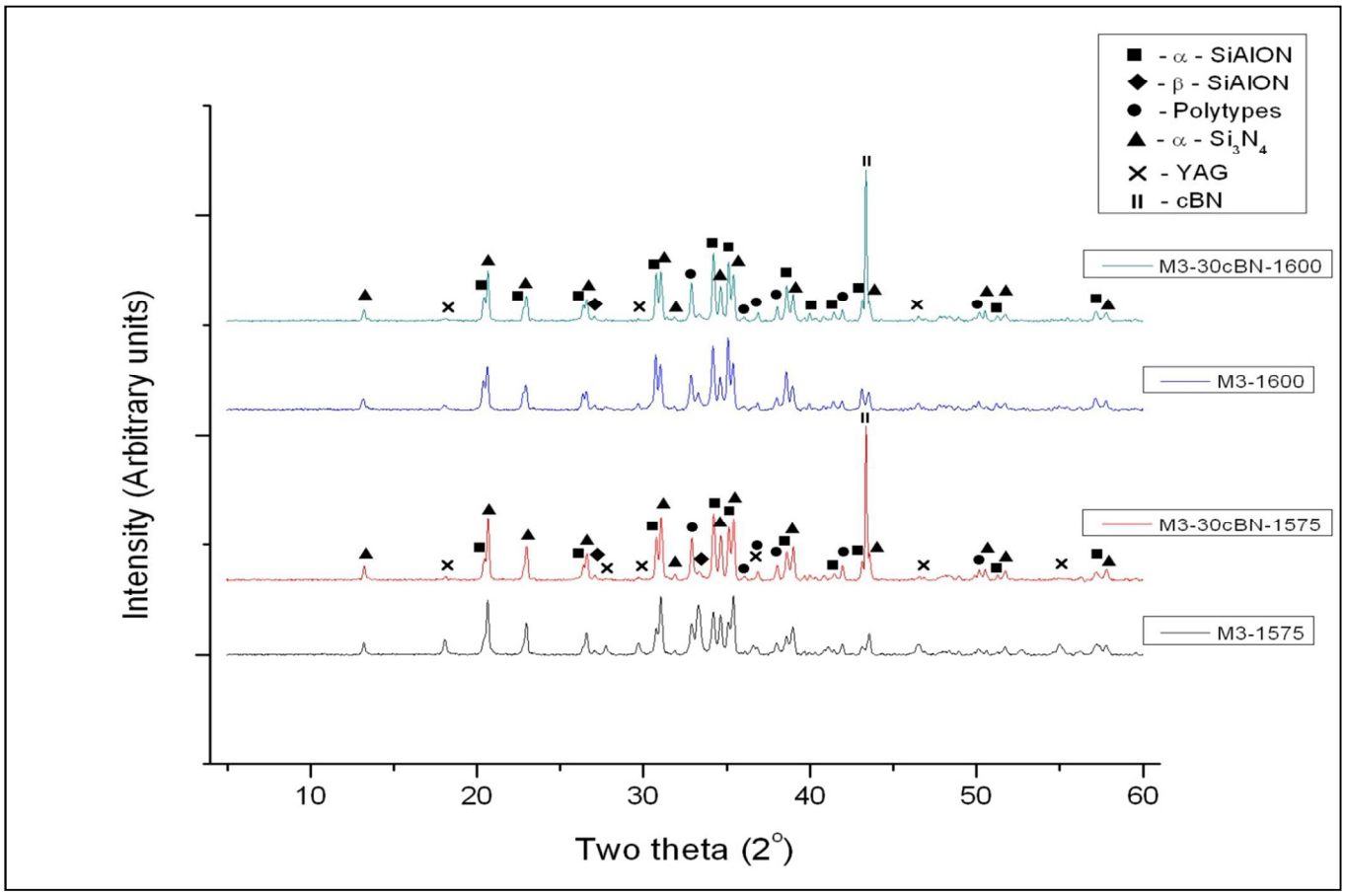


Figure 4.25: X-ray diffractograms of M3- sialon /cBN composites sintered with varying temperature (1575-1600°C) and cBN content (0 and 30 vol. %)

The yttria rich M3-sialon ceramic has a significantly higher amount of the YAG phase present as compared to Matrix 1 and 2. This phase decreases with increasing sintering temperature and cBN content. With increasing temperature an increase in the α-sialon phase is observed at the expense of the α-Si_3N_4 phase. However an increase in the cBN content slightly affects the α-sialon formation. When sintered at 1575°C there is a small increase and when sintered at 1600°C a

decrease in the α-sialon formation (compared to that of pure sintered sialon at their respective sintering temperatures), which consequently results in a decrease and increase of the α-Si_3N_4 phase respectively for the 1575 and 1600°C sintered samples. Lastly, the polytypoid formation increases with increasing cBN content however sintering temperature has no effect between 1575-1600°C. If M3-sialon sintered at 1550°C (Figure 4.26) is compared with that sintered at 1625°C (Figure 4.27) a difference in the yttrium-rich glassy phase (light) and polytype cluster formation (dark) can easily be seen.

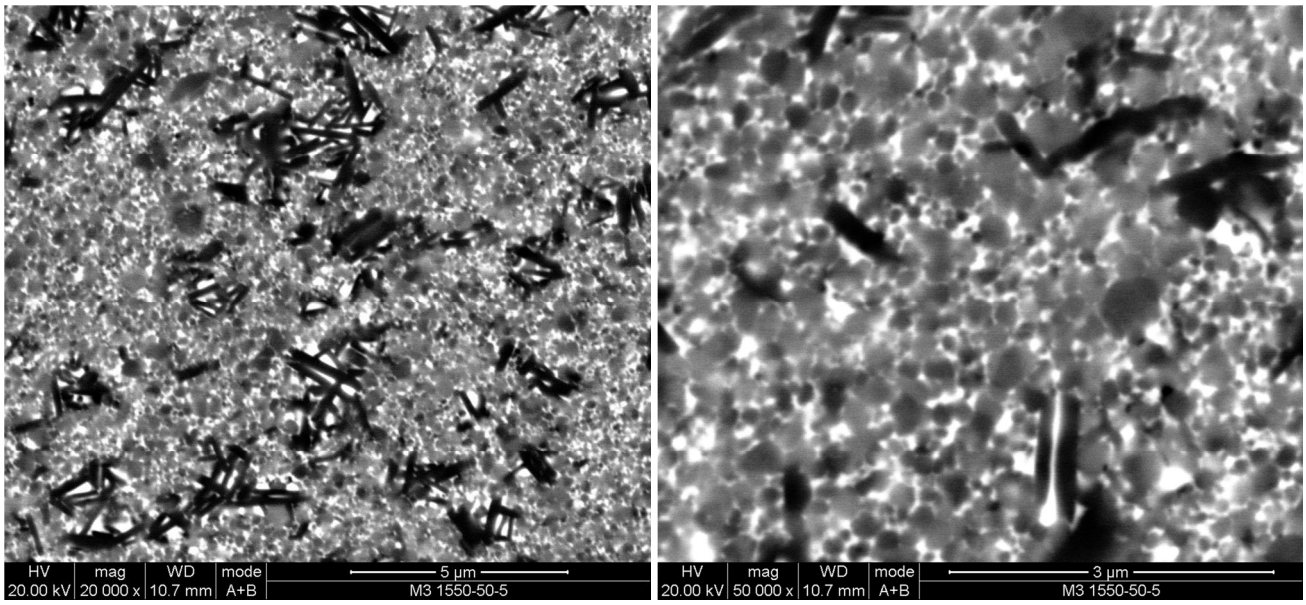


Figure 4.26: SEM micrograph of M3-sialon sintered at 1550°C showing high yttria-rich glassy phase (YAG) and a considerable amount of the polytype phase.

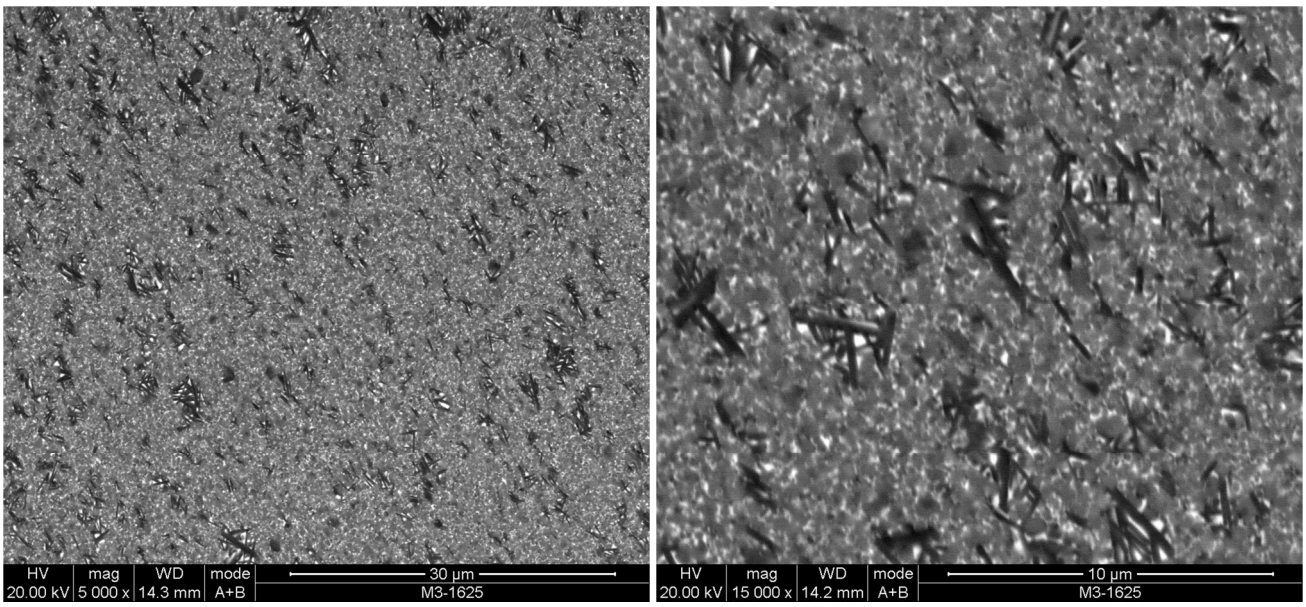


Figure 4.27: SEM micrograph of M3-sialon sintered at 1625°C showing lower amount of glassy phase and smaller polytype clusters as compared than that sintered at 1550°C.

In Figure 4.28 it is seen that the excess yttria causes higher amount of glassy phase near and around the cBN grains. Furthermore, it is also seen that the localised yttria-rich liquid pooling is not seen in sintered pure M3 (Figure 4.28a,b) when compared to M3 with 30 vol.% cBN (Figure 4.28c,d). The amount of glassy phase pooling observed in the M3/cBN composites is higher than what is experienced in M1/cBN (Figure 4.22) and M2/cBN (Figure 4.24).

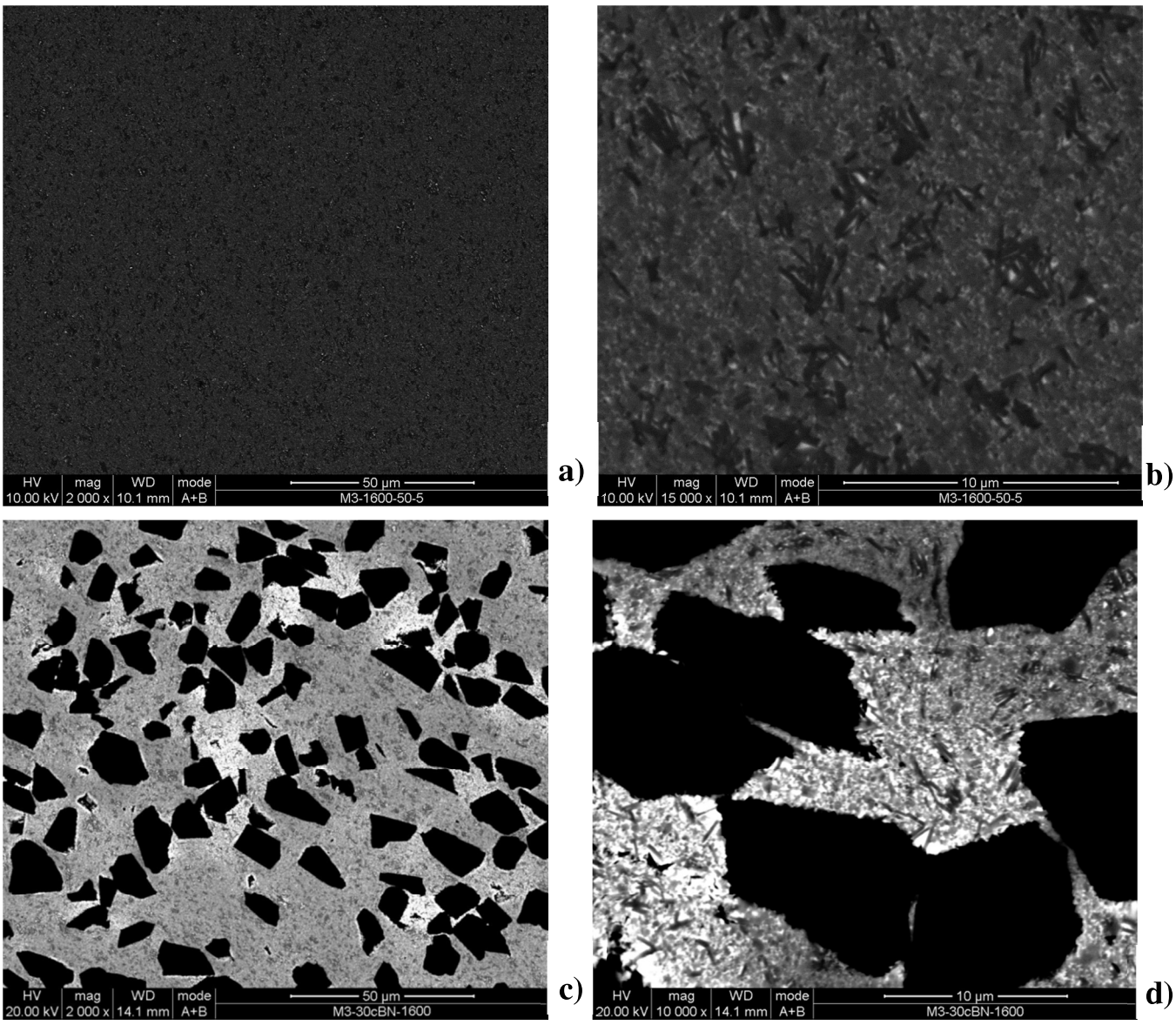


Figure 4.28: SEM micrographs comparing pure M3-sialon with M3-sialon sintered with 30 vol. % cBN at 1600°C: a, b) pure M3 and c, d) M3 with 30 vol. % cBN.

4.5.4. M4 /cBN composites

The effect of grade 9 cBN addition of the phase formation of M4 sintered at 1600°C can be achieved qualitatively by analysing at the respective peak intensities of the XRD traces (Figure 4.29).

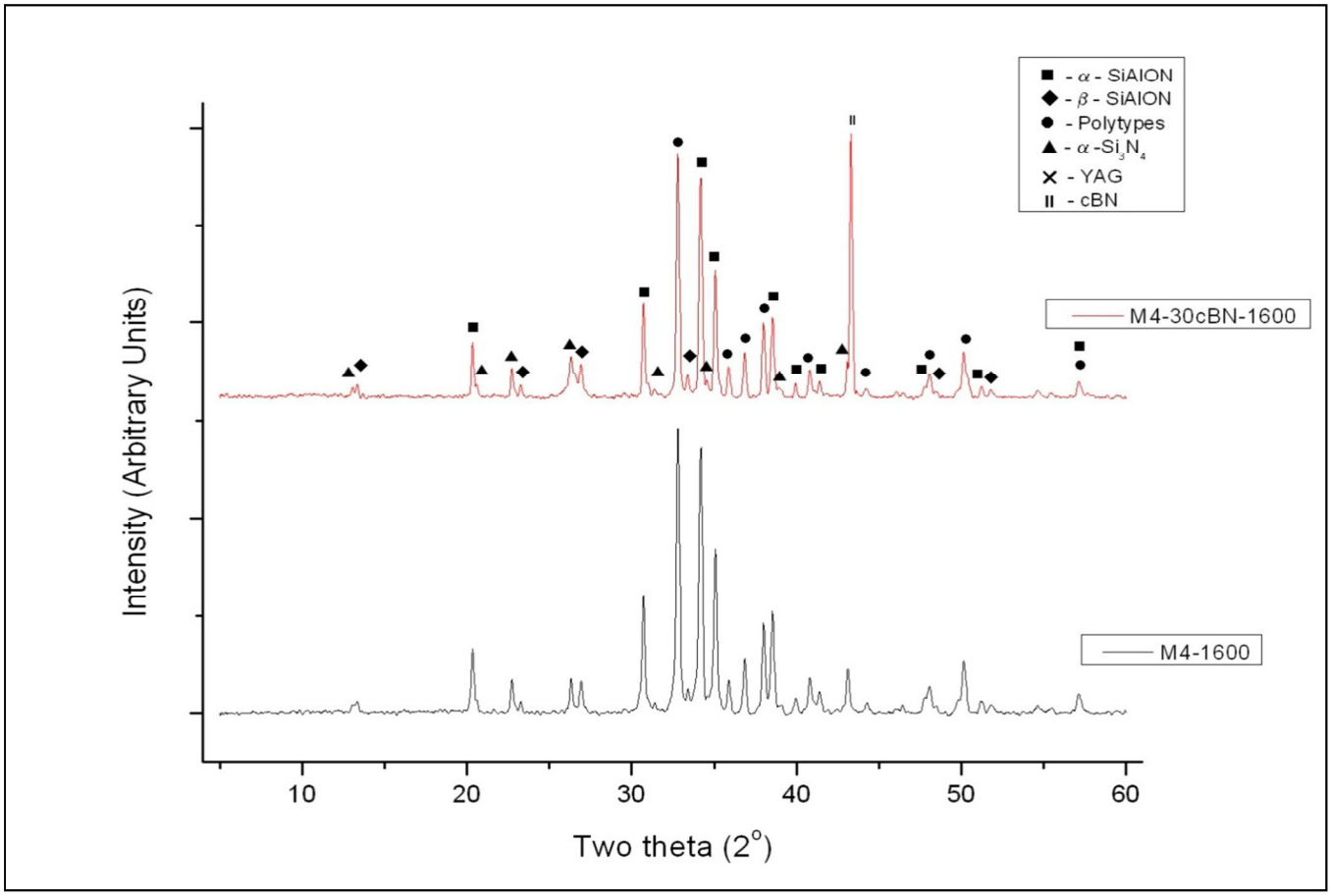


Figure 4.29: X-ray diffractograms of M4 sialon /cBN composites sintered with at 1600°C with varying grade 9 cBN content (0 and 30 vol. %).

Figure 4.29 shows that following the introduction of cBN to M4, no significant variation in the respective phase formation occurs when that composite was sintered at 1600°C.Furthermore it is also observed that the main constituent phase present at 1600°C for M4 sialon is the polytype phase as well as the α-sialon phase. There is a higher amount of β-sialon in M4 as compared to the other three sialon matrices. Figure 4.30a illustrates the yttria pooling existing in M4-30cBN-1600. The main phases present are the 12 H polytype and α-sialon, as seen in Figure 4.30b.

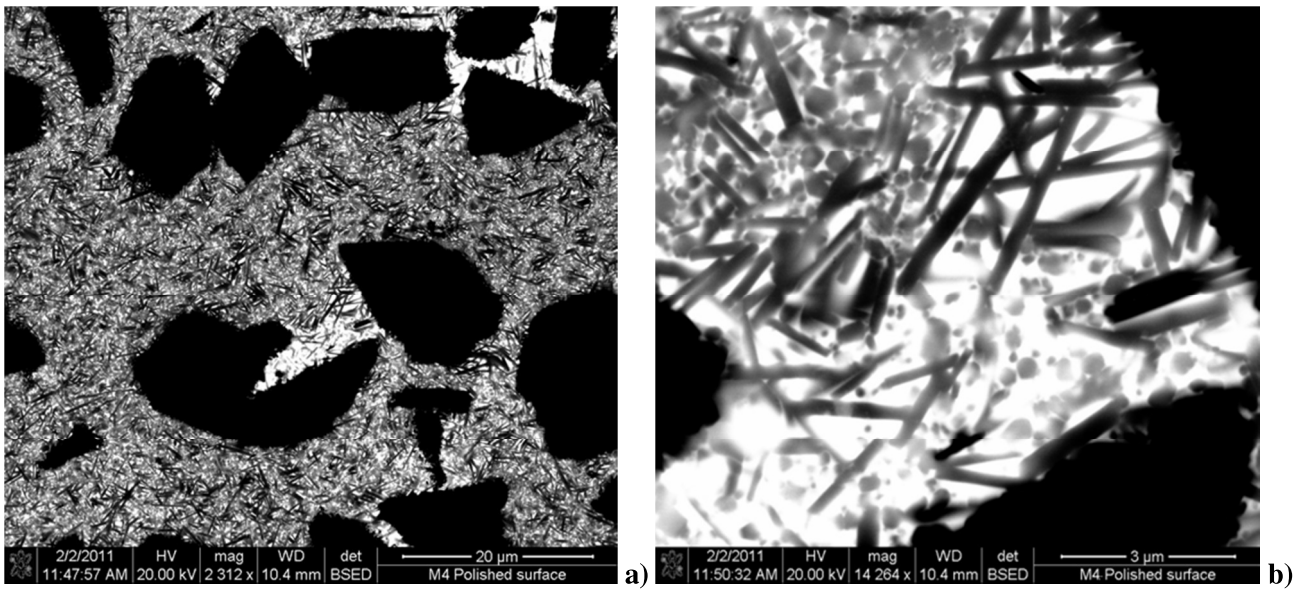


Figure 4.30: SEM micrograph showing the existence of the yttria rich pooling behaviour (a) and the α-sialon (equiaxed) and polytype (elongated clusters) phases that are present in M4 sialon sintered at 1600°C.

4.6. Mechanical Properties

The hardness and fracture toughness was measured through the use of a 5 kg load Vickers hardness indentation technique where the load was applied for 10 seconds as described in Section 3.5.7.1.

4.6.1. Pure sialon

Initially a study of the mechanical properties of the various pure sialon matrices sintered at different temperatures was completed. The sintering temperatures used were 1550, 1575, 1600 and 1625°C. However only samples with a measured density greater than 97 % of their theoretical density were tested for their mechanical properties (Table 4.14).

Table 4.14: Hardness and fracture toughness results for pure M1, M2, M3 and M4 sialons sintered at various temperatures.

Material	Hardness (Hv_5) GPa				Fracture toughness ($MPa.m^{0.5}$)			
	Sintering Temperature (°C)				Sintering Temperature (°C)			
	1550	1575	1600	1625	1550	1575	1600	1625
M1		18.2 ± 0.4	19.2 ± 0.3	19.6 ± 0.5		3.6 ± 0.3	3.7 ± 0.2	3.7 ± 0.2
M2		16.9 ± 0.4	17.2 ± 0.3	17.3 ± 0.3		4.0 ± 0.2	4.1 ± 0.1	4.3 ± 0.1
M3	17.7 ± 0.3	18.8 ± 0.3	19.0 ± 0.4	19.1 ± 0.3	3.7 ± 0.1	3.4 ± 0.2	3.3 ± 0.1	3.2 ± 0.1
M4			15.5 ± 0.3	16.3 ± 0.3			4.6 ± 0.2	5.2 ± 0.2

It was found that M3 could achieve sufficient density (> 97 % of the theoretical density) throughout the temperature range used in this work. This high density could only be obtained at 1575°C for M1 and M2 whereas M4 could only be densified sufficiently at 1600°C.

The measured hardness values obtained for pure M1 sialon were observed to increase with increasing sintering temperature; however no effect on the fracture toughness was observed. Like M1, pure M3 sialon sintered ceramics attained an increase in the hardness with increasing sintering temperature; however M2 sialon ceramics attained a marginal increase in the hardness. The fracture toughness values obtained for M1, M2 and M3 were observed to show no significant effect with increasing sintering temperature. Lastly, it was observed that increasing the sintering temperature of M4 sialon showed significant improvements in both the hardness and fracture toughness values measured.

4.6.2. Effects of cBN addition on the mechanical properties

The reinforcing effect of cBN when added as a secondary phase to the various sialon matrices was investigated by measuring the hardness and fracture toughness values of the various composites, in a way similar to the one used to measure the mechanical properties of pure sialon. Good bonding of the faceted cBN grains with the various sialon matrices is expected to benefit the mechanical properties of sialon-cBN composites.

The effect of cBN addition to M1 sialon composites was evaluated by measuring the mechanical properties for M1/cBN composites containing 10, 20 and 30 vol. % cBN. The results of this analysis are given in Table 4.15 where mechanical properties of pure M1 sialon are added for comparison.

Table 4.15: The hardness and fracture toughness results pertaining to sintered M1/cBN composites.

Sample name	Percentage of theoretical density (%)	Hardness (H_{v5}) GPa	Fracture toughness (MPa.m$^{0.5}$)
M1-1575	100.0	18.2 ± 0.4	3.6 ± 0.3
M1-10cBN-1575	99.3	20.9 ± 0.5	5.2 ± 0.2
M1-20cBN-1575	98.5	20.2 ± 0.8	5.2 ± 0.2
M1-30cBN-1575	98.1	19.7 ± 0.2	5.4 ± 0.3
M1-1600	100.0	19.1 ± 0.3	3.7 ± 0.2
M1-10cBN-1600	99.3	21.3 ± 0.8	4.6 ± 0.4
M1-20cBN-1600	97.9	19.5 ± 0.8	5.9 ± 0.4
M1-30cBN-1600	97.5	16.8 ± 0.9	7.3 ± 0.3
M1-1625	99.7	19.7 ± 0.5	3.7 ± 0.2
M1-10cBN-1625	98.7	20.7 ± 0.3	4.7 ± 0.2
M1-20cBN-1625	97.6	16.2 ± 0.4	7.0 ± 0.8
M1-30cBN-1625	97.2	15.9 ± 0.3	7.8 ± 0.7

The main reinforcing effect of the secondary phase cBN is that of improving the fracture toughness of sialon ceramics. This is achieved in all sialon composites containing additions of cBN as seen in Table 4.15. This relationship shows that an increase in the cBN content increases the fracture toughness, again particularly with increasing sintering temperature. The fracture toughness of the M1/cBN composites sintered at 1575° increases considerably with the addition of 10 vol. % cBN after which further addition only produces a slight increase as shown in Figure 4.31.

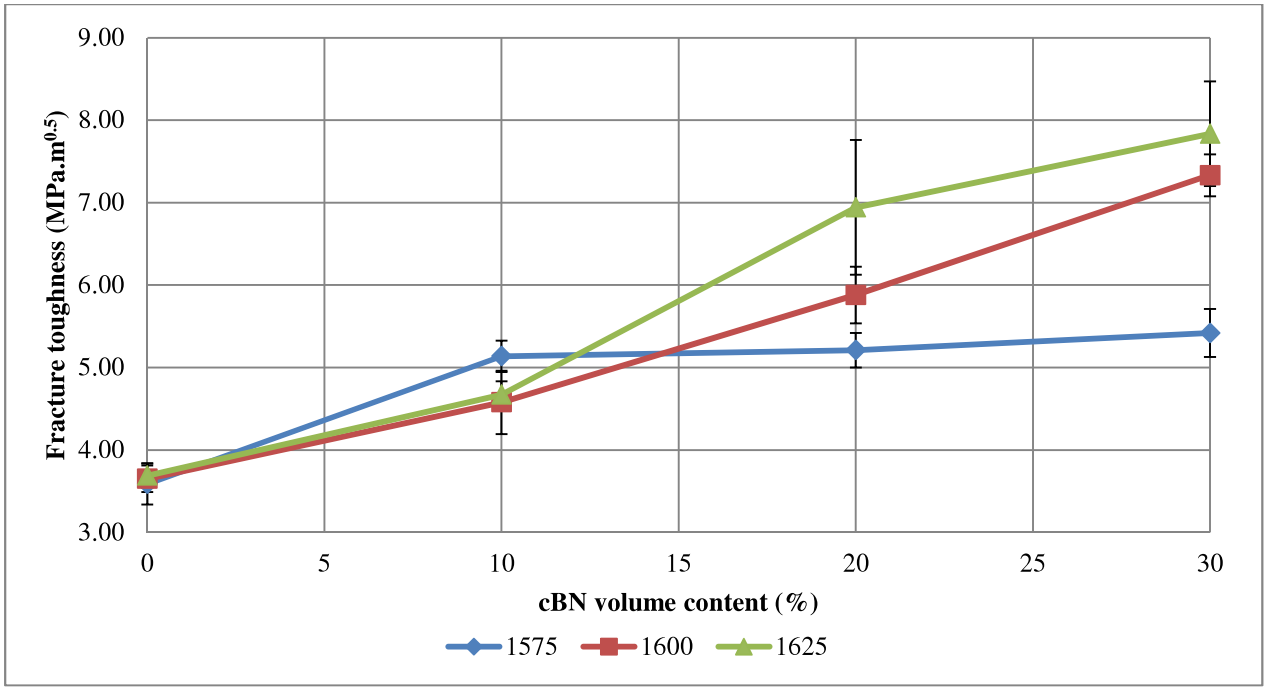


Figure 4.31: The effect of temperature and cBN content on the fracture toughness of M1/cBN composites.

The effect of cBN addition to the M2 sialon matrix was observed by sintering the M2/cBN composites containing 30 vol. % cBN at 1575 and 1600°C. M2/cBN composites were not sintered at 1625°C due to the significant deterioration in hardness as also observed for M1-cBN composites (Table 4.15). The mechanical properties of the M2/cBN composites are provided along with the results of the pure M2 sialon ceramics in Table 4.16.

Table 4.16: The hardness and fracture toughness results pertaining to sintered M2/cBN composites.

Sample name	Percentage Theoretical density (%)	Hardness (H_{v5}) GPa	Fracture toughness (MPa.m$^{0.5}$)
M2-1575	100.0	17.0 ± 0.4	4.0 ± 0.2
M2-30cBN-1575	98.1	18.6 ± 0.7	6.5 ± 0.1
M2-1600	99.1	17.3 ± 0.3	4.1 ± 0.1
M2-30cBN-1600	97.5	16.4 ± 0.6	7.9 ± 0.3
M2-1625	99.1	17.3 ± 0.3	4.4 ± 0.1

The fracture toughness of M2/cBN and M3/cBN composites is observed to increase with increasing cBN content and sintering temperature (Table 4.16 and Table 4.17). These results show similar trends to those obtained in M1/cBN composites (Figure 4.31).

Table 4.17: The hardness and fracture toughness results relating to sintered M3/cBN composites.

Sample name	Percentage Theoretical density (%)	Hardness (H_{v5}) GPa	Fracture toughness (MPa.m$^{0.5}$)
M3-1550	100.0	17.7 ± 0.3	3.7 ± 0.1
M3-1575	100.0	18.9 ± 0.3	3.4 ± 0.2
M3-30cBN-1575	98.5	18.0 ± 0.4	6.3 ± 0.1
M3-1600	99.7	19.0 ± 0.3	3.3 ± 0.1
M3-30cBN-1600	97.9	16.9 ± 0.3	6.8 ± 0.4
M3-1625	99.4	19.1 ± 0.3	3.3 ± 0.1

The addition of 30 vol. % cBN to M3-sialon results in a significant decrease in the hardness, this decrease in hardness is further promoted by an increase in the sintering temperature as presented in Table 4.17. The addition of cBN to the M3-sialon matrix results in a significant improvement in the fracture toughness, this increase in fracture toughness is also promoted when the sintering temperature is increased.

Due to the insufficient densification of M4 at a sintering temperature of 1575°C and below, only one M4/cBN composite was produced and sintered at 1600°C (Table 4.18). At higher sintering temperatures the transformation of the cBN grains to the hexagonal phase is expected. The mechanical properties obtained for M4 and M4/cBN composites are given in Table 4.18 where it is seen that through the addition of 30 vol. % cBN an increase in the hardness and fracture toughness is achieved when sintering at a temperature of 1600°C.

Table 4.18: The hardness and fracture toughness results relating to sintered M4/cBN composites.

Sample name	Percentage theoretical density	Hardness (H_{v5}) GPa	Fracture toughness (MPa.m$^{0.5}$)
M4-1600	99.2	15.5 ± 0.30	4.17 ± 0.12
M4-30cBN-1600	97.1	16.1 ± 0.42	6.89 ± 0.23
M4-1625	100.0	16.3 ± 0.24	5.21 ± 0.19

5. Discussion

5.1. Densification mechanism experienced in pure sialon ceramics

The densification mechanisms for sialon ceramics differ depending on composition and sintering conditions. Since M1, M2 and M3 differ only slightly in their composition the densification behaviour of these sialons are reasonably similar. The densification mechanisms experienced in M4, (Ye et al., 2010 [58]) composition, were somewhat different to those used to produce M1, M2 and M3. A comparison of the densification curves for different sialon matrices sintered at 1600°C is given in Figure 5.1.

When looking at the respective piston travel speeds for the various sialon matrices distinct peaks in densification curves can be identified. From Figure 5.1 it was revealed that for the densification of M1, M2 and M3, two major peaks were observed during consolidation whereas the M4 sialon trace consisted of three major peaks. The first peak is attributable to the formation of the lowest temperature eutectic oxide-based liquid in the Y_2O_3-SiO_2-Al_2O_3 system. This low temperature melt is essential for the particle rearrangement process in liquid phase sintering allowing particles to move over one another easier. The initial formation of this liquid melt and its amount results in slightly different onset temperatures for each sialon matrix (Table 5.1). The intensity of the shrinkage (related to magnitude of piston speed) pertaining to the formation of the oxide based eutectic melt (first peak in piston speed in Figure 5.1) was highest for M4, M3, M1 and M2 in decreasing order. This was found to be consistent with what was predicted on the basis of the estimate of the amount of liquid phase expected for each composition. Lower amounts of liquid phase were said to decrease the rate of the α-sialon formation, which is due to the reduction in the transport for the solid-liquid-solid mechanism [86].

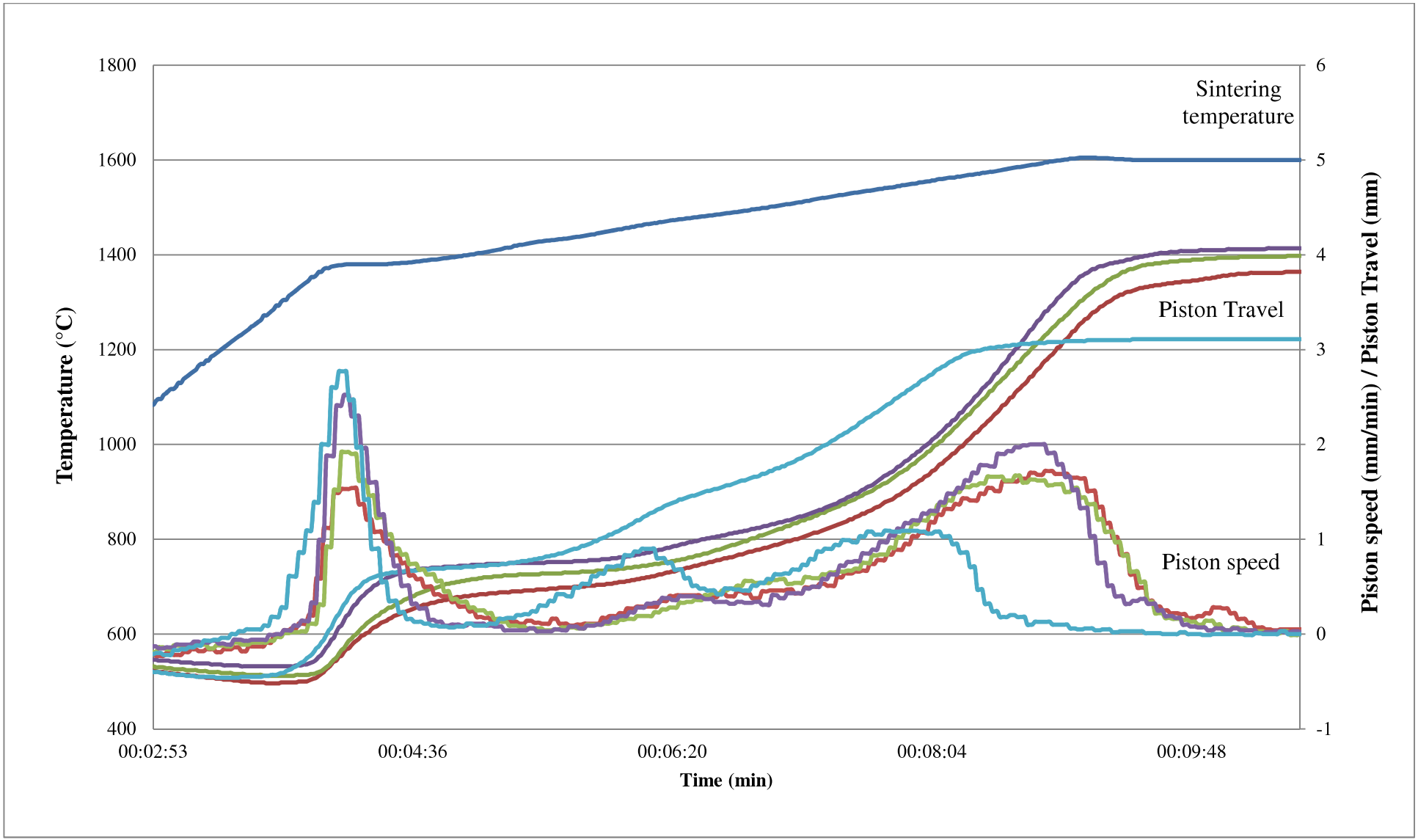


Figure 5.1: Comparison of densification behaviour of M1, M2, M3 and M4 sialons sintered at 1600°C with 50 MPa uni-axial pressure applied at 450°C and kept constant throughout sintering.

Table 5.1: Comparison of the onset temperature of eutectic liquid formation for the various sialon matrices.

Sialon Matrix	Onset temperature of the eutectic melt (°C)
M1	≈ 1275
M2	≈ 1300
M3	≈ 1250
M4	≈ 1210

The other main peak for M1, M2 and M3 and the third peak observed in M4 sialon is a result of the increased amount of nitrogen in the Y-Si-Al-O-N system. This nitrogen containing liquid is responsible for the solution/precipitation process of sialon phases. The intensive formation of the nitrogen-containing melt occurs around 1400-1450°C for M4 whereas for the other sialon compositions studied in this work this formation begins around 1500°C. This is in accordance with the findings pertaining to yttrium sialons produced by Peng, 2004 [19]; this melt was observed to exist at temperatures of 1350-1500°C for α-sialon spark plasma sintered (Dr. Sinter 2050) with a heating rate 200°C/min (m = 1.05 and n = 1.2) and a uni-axial pressure of 50 MPa. The dissolution of α-Si_3N_4 in the solution precipitation step for M1, M2 and M3 predominantly forms α-sialon with small amounts of β-sialon and the 12 H polytype phase. The formation of the nitrogen rich liquid phase is caused by dissolution of AlN and α-Si_3N_4 within the oxide liquid which subsequently becomes richer in nitrogen and results in the precipitation of the various sialon phases. The densification of M4 sialon is different to that of M1, M2 and M3 due to the distinct difference in composition (M4 is richer in oxygen compared to the other sialon matrices revealed in Figure 5.2), the reduced densification for M4 sialon ceramics is attributed to intermediate crystallisation of a phase not investigated in this work however will be researched at a later stage. The intermediate crystallization is represented by the second intensive peak for M4 (Figure 5.1). This crystallization results in the retardation of the densification, thus aiding in the formation of the minimum peak between the maximums (Figure 5.1).

The excess yttria contributes to liquid phase formation resulting in the full densification of M3 sialon at 1550°C, lower than M1 (1575°C), M2 (1575°C) and M4 (1600°C) sialon. The

theoretical density of M3 sialon is higher than M1 and M2 due to the increase in the yttria content which has the highest density; however it is not higher than M4. When comparing the matrices used to create the α-sialon ceramics it was revealed that since M3 has the most glassy phase present when compared to M1 and M2, this results in the marginal decrease of the eutectic melting temperature as well as obtaining fully dense compacts faster than the M1 and M2 sialon. It must be noted that M4 is the most oxygen-rich sialon composition which in turn results in the highest amount of the liquid phase being present thus secondary rearrangement and solution precipitation begins earlier than the other sialon matrices as shown in Figure 5.1. However these densification mechanisms are interrupted in M4 sialon due to the generation of additional crystalline phases above 1500°C which consequently retard the densification process. It was observed that sialons with lower m and n values in this work can be densified at lower temperatures then those with higher values. The location of the various sialon matrices on the sialon plane is presented in Figure 5.2.

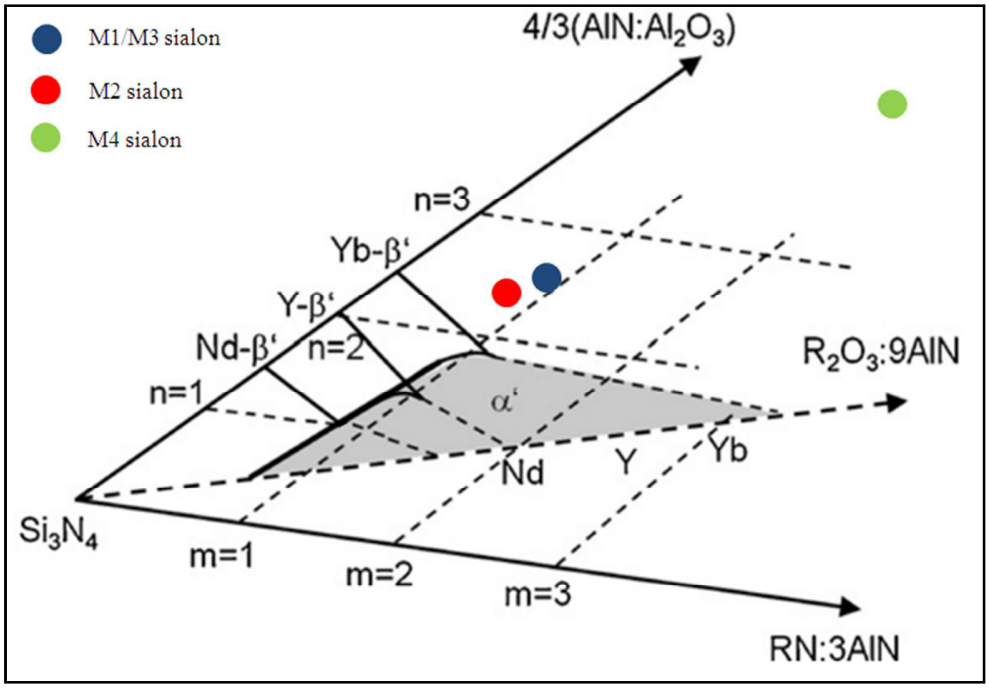


Figure 5.2: Compositions of the various sialon matrices on the sialon plane.

From Figure 5.3 the effect of temperature on the final density can be derived. Initial increases in the sintering temperature result in increased density, as expected. When comparing the percentage of the theoretical densities for M1, M2 and M3 pure sialons sintered above 1575°C the apparent decrease is attributed to the formation of phases with lower densities since no porosity was observed through SEM analysis. Due to the excess liquid phase it was possible to obtain densified M3 sialon at sintering temperatures as low as 1550°C. This was seen as an advantage over the other two matrices. M4 on the other hand showed an increase in final densities with increase in the sintering temperature since full densification was only attained at 1625°C.

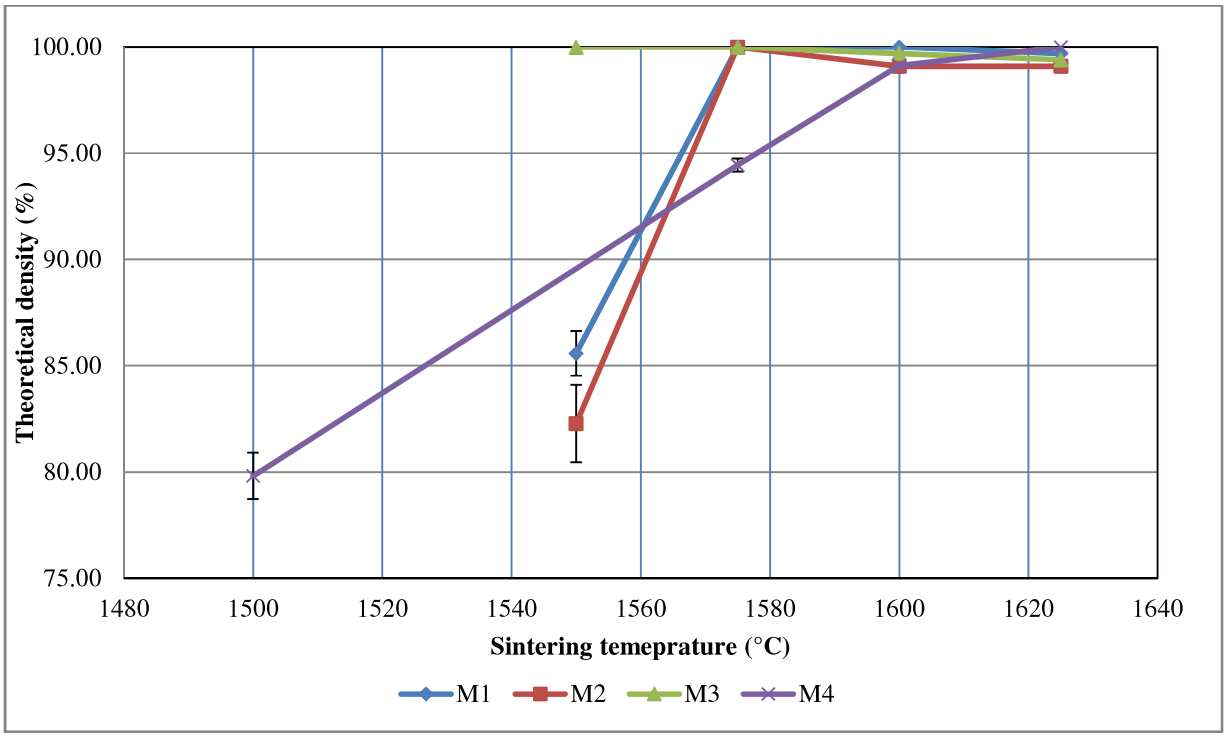
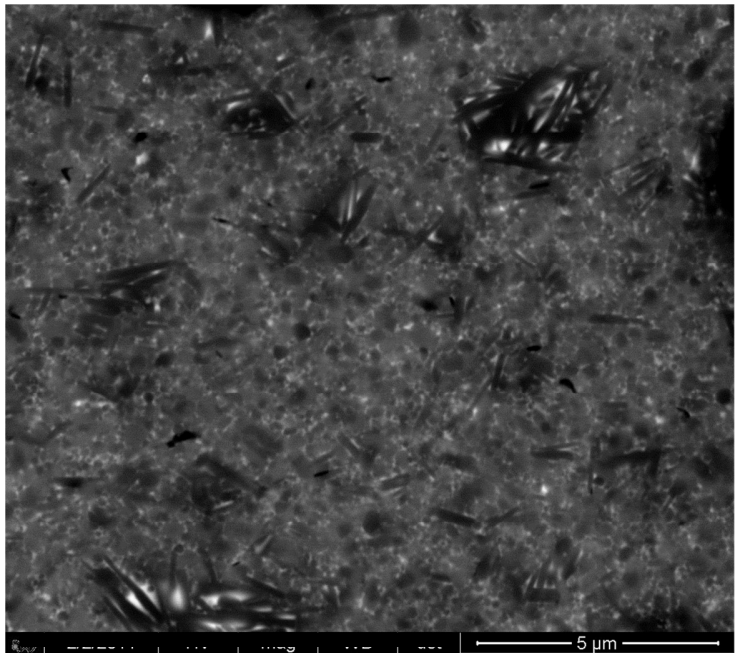


Figure 5.3: Graphical representation of the percentage of the theoretical densities for pure sialon ceramics sintered at various temperatures.

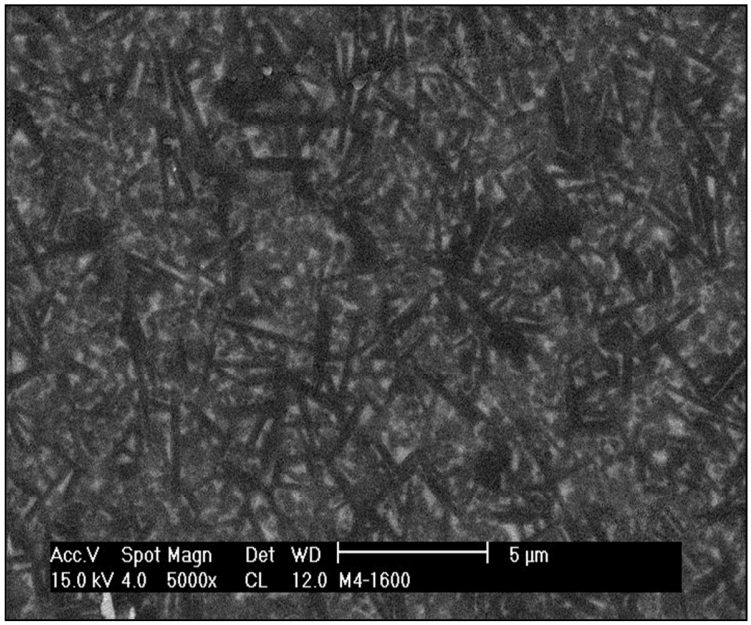
5.2. Effect of sintering temperature on the microstructure and mechanical properties of sialon ceramics

The difference in mechanical properties obtained for equiaxed and elongated grain morphologies were found to be in agreement with literature (Table 2.3) where equiaxed grains give rise to lower fracture toughness when compared to elongated grains. Hardness values correlate to the amount of α-Si_3N_4 and α-sialon content present in the sialon ceramic. The difference in the sialon grain morphologies obtained for the M1 and M4 sialon is represented in Figure 5.4. Subsequently it was revealed that the more uniaxial grains of M1 sialon have significantly higher hardness than M4 sialon; however the fracture toughness was observed to be inferior in comparison (Table 4.14). The effects of the mechanical properties of the varying pure sialons with increasing sintering temperature were investigated and the relationship with the Vickers hardness and fracture toughness is illustrated in Figure 5.5 and Figure 5.6 respectively.

The highest hardness for each of the pure sialon matrices was obtained at a sintering temperature of 1625°C. The highest hardness was measured for M1 followed by M3, M2 and M4 in decreasing order. Since M1, M2 and M3 were designed to be predominantly α-sialon composites, their hardness vales were expected to be higher than that of the M4. this is due to the higher amount of β-sialon and secondary phases present. The hardness values obtained for M4 sialon were found to increase with sintering temperature due to the formation of α-sialon; the fracture toughness was also improved. This was attributed to the formation of large β-sialon grains. It is also seen that the fracture toughness of M1 sialon is not affected by an increase in temperature whereas an increase in temperature promotes the formation of β-sialon in M2 and M4 sialons.



a)



b)

Figure 5.4: SEM micrographs showing the different grain morphologies of a) M1 sialon and b) M4 sialon sintered at 1600°C and analysed under back-scattered detection mode.

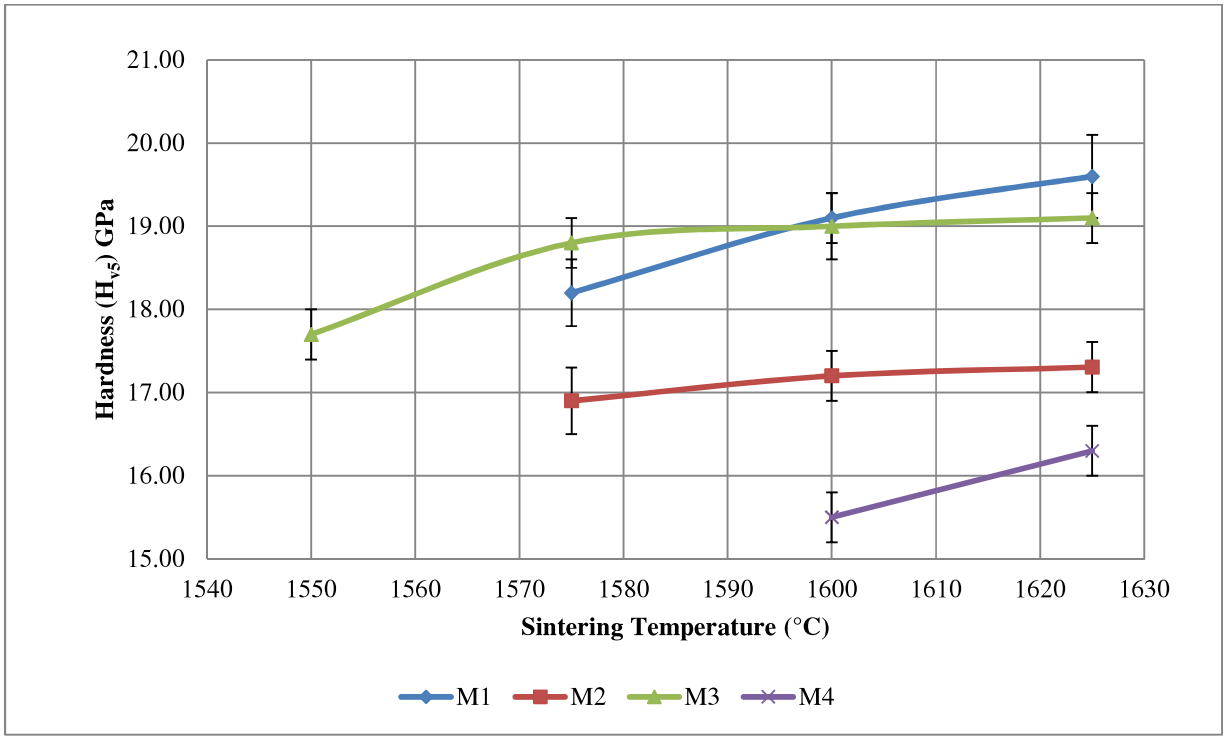


Figure 5.5: Effect of sintering temperature on the Vickers hardness of the varying sialon compositions.

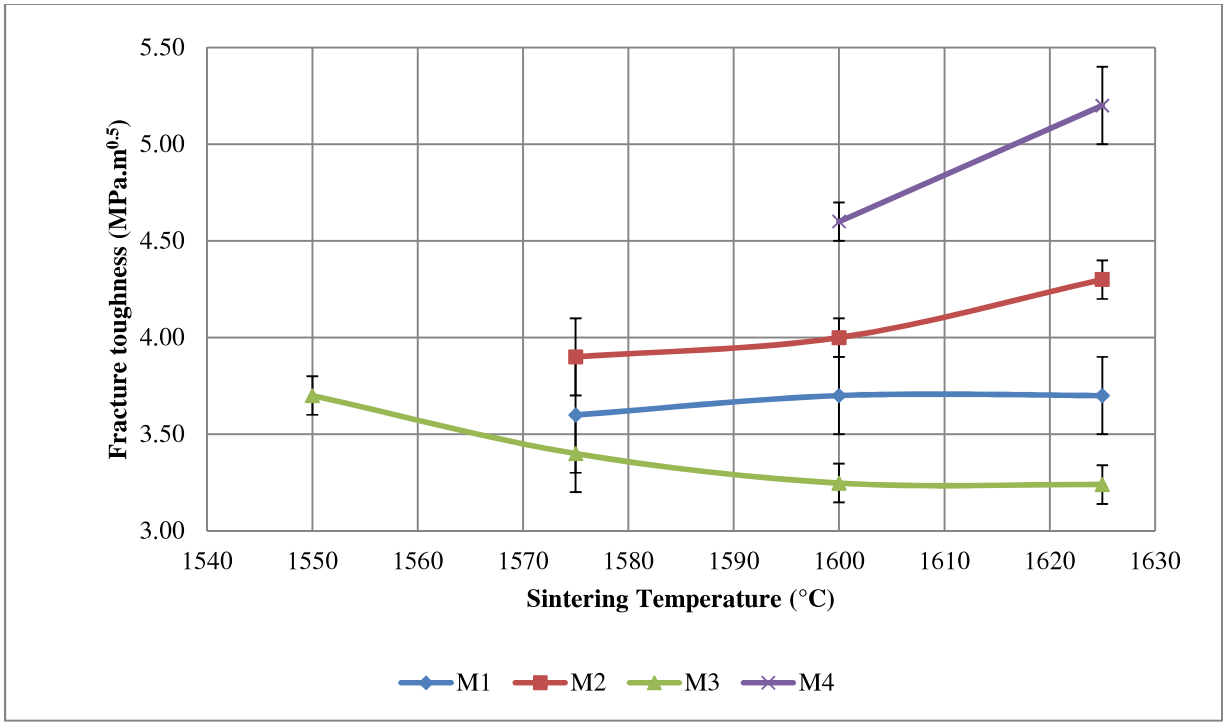


Figure 5.6: Effect of sintering temperature on the fracture toughness of the varying sialon compositions.

5.3. Effect on cBN addition on densification of sialon ceramics

It is expected that with increasing secondary phase content, the relative density will decrease due to the retarding effect of cBN addition. This was indeed seen to be the case as depicted by the percentage of the theoretical densities for cBN containing M1 sialon composites (Figure 4.14) where the effects on the relative densities are compared for increasing sintering temperature and cBN content. The cBN grains affect the rearrangement process due to the formation of a rigid 3-D network, thus with increasing cBN content the densification is expected to decrease. This was found to correspond with literature with respect to β-sialon/cBN[(2)], Al_2O_3/cBN [(87)] and WC/cBN [(88)] composites. This is further confirmed in the densification curves obtained for the varying cBN additions to M1 sialon sintered at 1600°C (Figure 5.7) where the addition of cBN to M1 sialon showed a retarding effect on the sintering process.

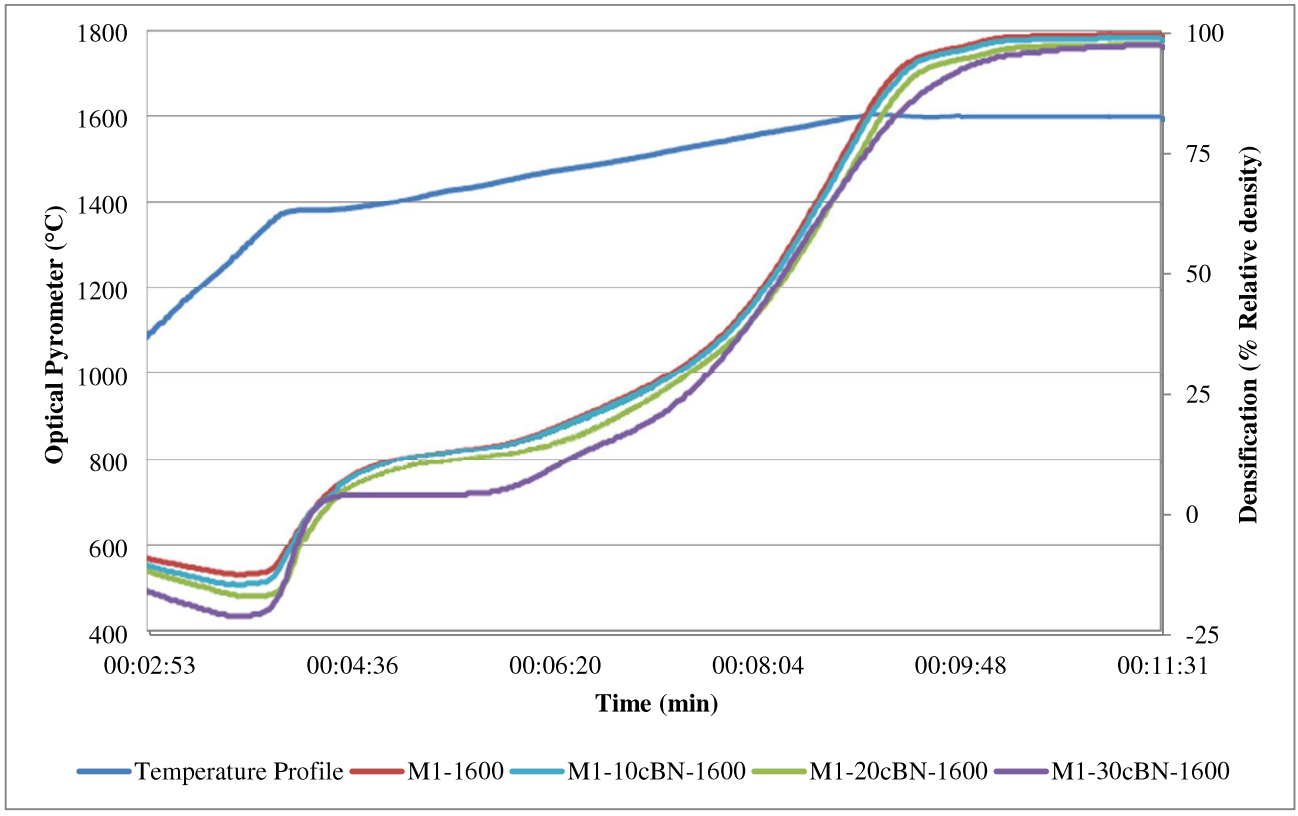


Figure 5.7: Comparative densification curves for M1 sialon ceramics sintered at 1600°C with varying grade 9 cBN content.

It can be seen in Figure 5.7 that the addition of the cBN to the M1 sialon matrix did not influence the densification of the composite at temperatures lower than ≈ 1380°C. Furthermore as the temperature is increased it is observed that additions of 10 and 20 vol. % cBN to the sialon matrix do not significantly affect the densification. However when 30 vol. % cBN is added to the sialon matrix a strong reduction in the particle rearrangement process is observed, likely due to the percolation limit being exceeded preventing effective distribution of the liquid oxide phase throughout the composites resulting in reduced densification. The Si_3N_4 and AlN grains have higher solubility in the liquid melt as opposed to the cBN grains; a lower wetting angle is expected for the Si_3N_4 and AlN. Moreover with lowering the wetting angle higher grain rearrangement, solution precipitation and densification is expected [89], thus with an increase in the amount of less wettable components (cBN) a decrease in the sinterability is promoted. However the fact that the cBN grains do not take part significantly in the solution precipitation sintering process is the main contributing factor to the retardation of the densification of the composites (Figure 5.7, Figure 5.8 and Figure 5.9).

This result is in accordance with increasing cBN volume fraction which in turn promotes the localised pooling of the yttria-rich phase between cBN grains due to the forced penetration of the liquid phase in amongst the cBN skeleton network when an external pressure is applied. This localised pooling results in an increased interaction with the cBN grains resulting in their surface hexagonalization dependent on the crystallographic orientation of the grain surfaces. The hexagonalization of the cBN grains was witnessed to increase with increasing sintering temperature. This is illustrated by comparing M1-30cBN sintered at 1600 (Figure 5.12) and 1625°C (Figure 5.13). The lower sintering temperature results in partial hexagonalization on certain surfaces of the cBN grains present in the sintered composite however samples sintered at 1625°C exhibit some grains which have been extensively hexagonalized. A significant reduction in the solution precipitation sintering mechanism is also witnessed with increasing cBN content by comparing pure M1 with sialons with increasing cBN content. Despite the slight hexagonalization of the cBN grains all M1 sialon/cBN composites studied at these temperatures were found to have densities greater than 97% of theoretical except for the sample sintered at 1550°C.

The negative effects of cBN addition on sinterability were also exhibited in M4/cBN composites; this relationship is presented in Section 5.4 where a comparison of the percentage of the theoretical densities obtained for M4-1600 (99.2 %) and M4-30cBN-1600 (97.1%) composites is given.

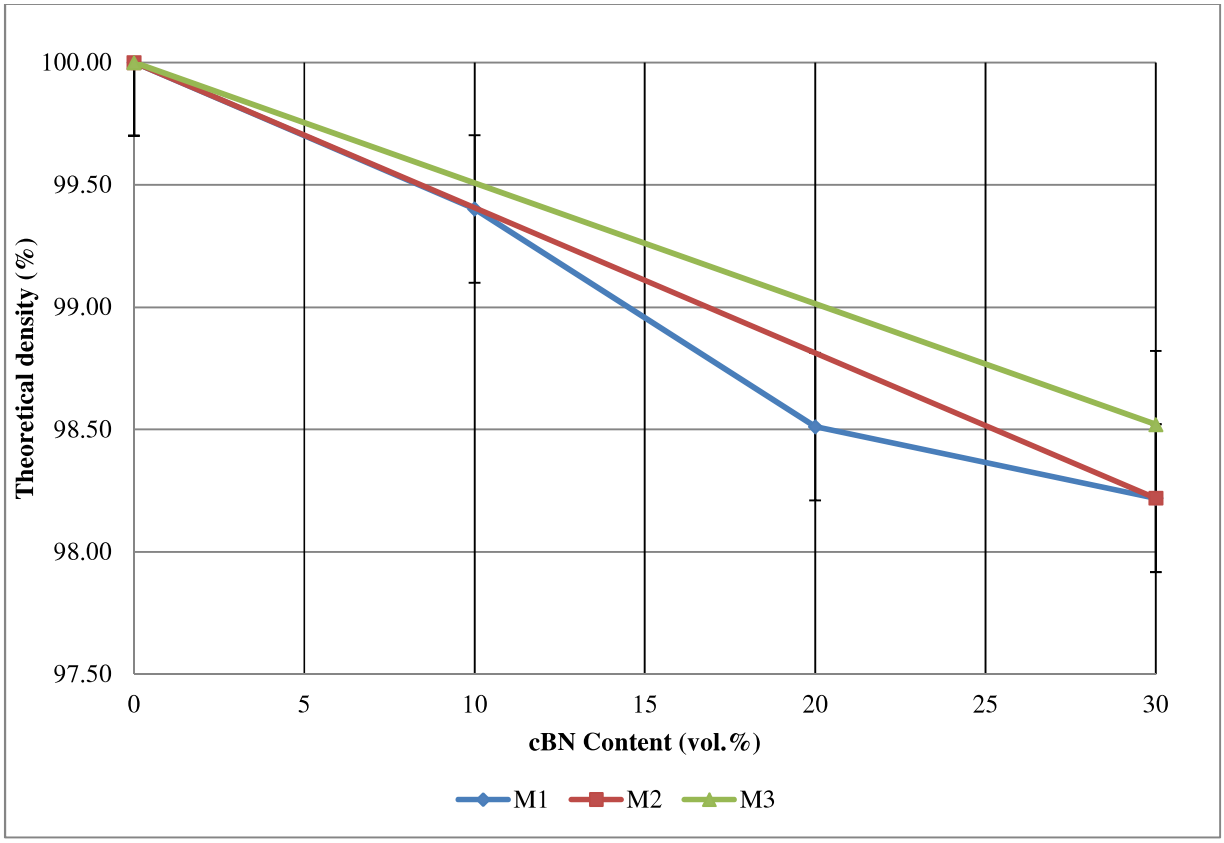


Figure 5.8: Effect of grade 9 cBN on the percentage of the theoretical density of sialon matrices sintered at 1575°C.

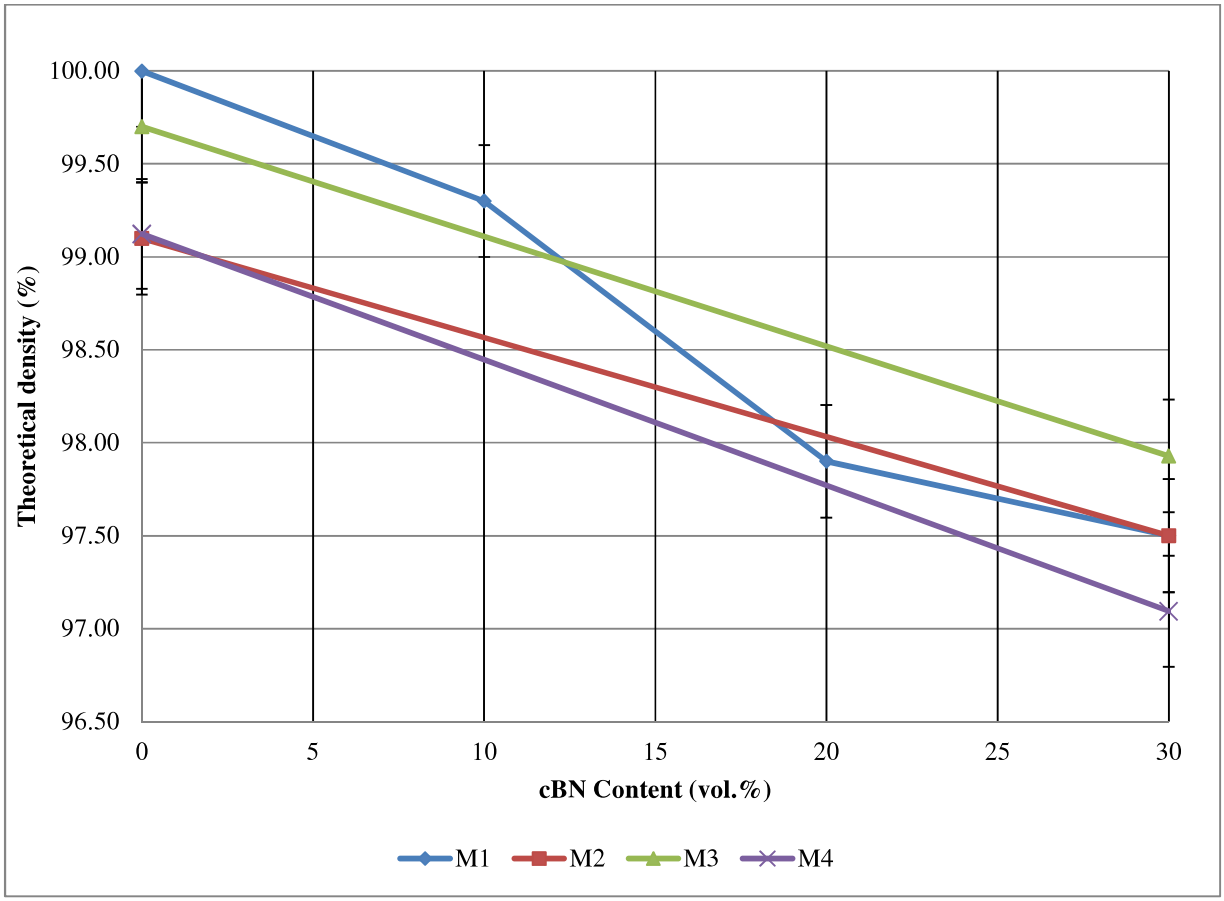


Figure 5.9: Effect of grade 9 cBN on the percentage of the theoretical density of sialon matrices sintered at 1600°C.

The effect of increasing cBN content in sialon ceramics sintered at 1575°C and 1600°C is illustrated in Figure 5.8 and Figure 5.9 respectively. Similar to the negative effects observed in M1/cBN composite are experienced in M2/cBN, M3/cBN and M4/cBN composites. From Figure 5.10 and Figure 5.11 a comparison of the densification curves obtained for pure sialons and 30 vol. % cBN containing composites is obtained where it is depicted that the effect of cBN content is similar for M1, M2 and M3 whereas the M4 sialon experienced significant decrease in the densification with 30 vol. % cBN additive. M3 sialon composites achieve the highest densification which is a result of the additional yttria in the composition when compared to the other sialon composites.

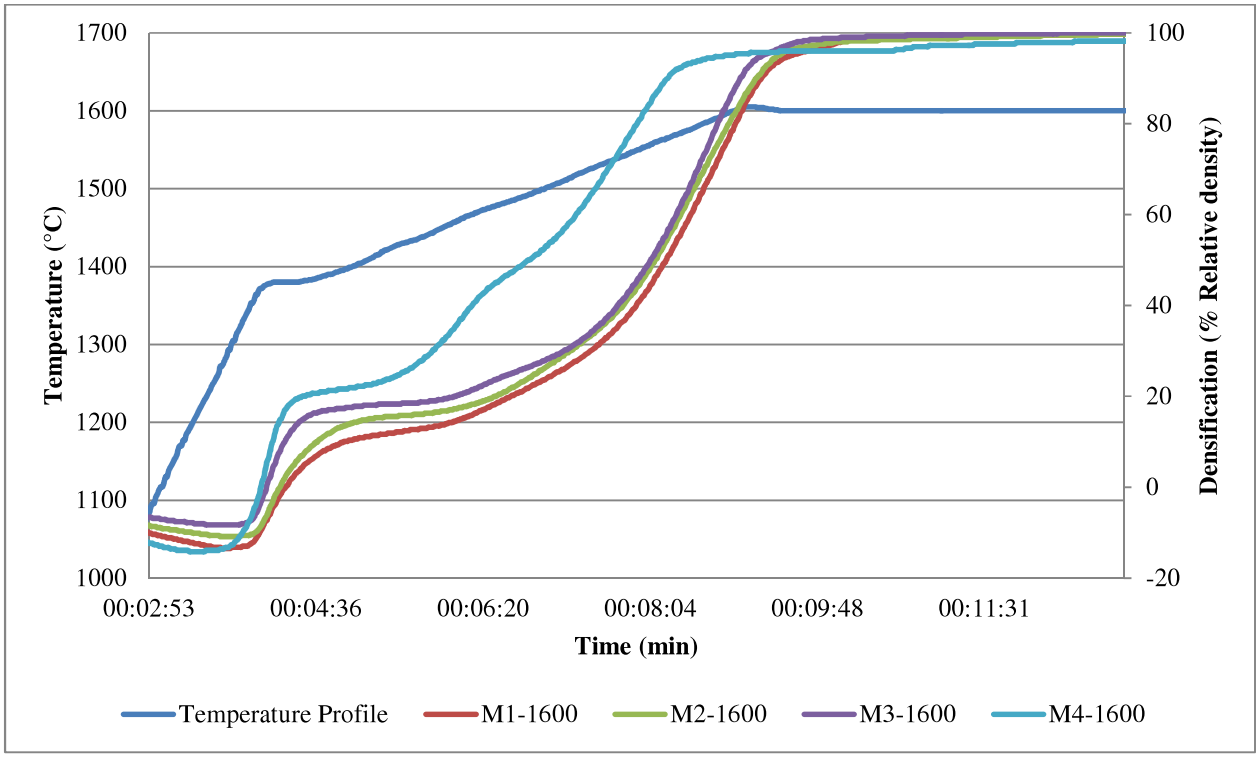


Figure 5.10: Comparative densification curves for sialon ceramics sintered at 1600°C.

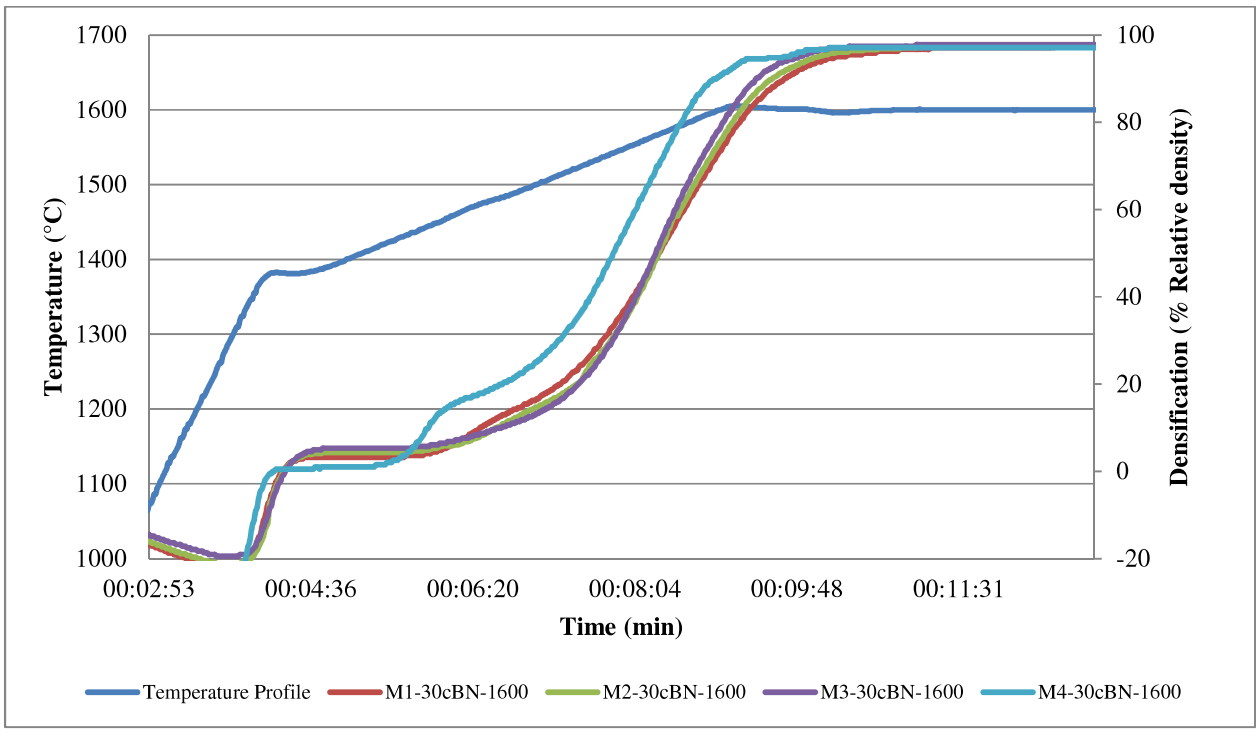


Figure 5.11: Comparative densification curves for sialon ceramics sintered at 1600°C with 30 vol. % grade 9 cBN content.

5.4. Hexagonalization of cBN grains

Deterioration of some cBN grains was witnessed in sialon matrices sintered at temperatures of 1600 and 1625°C, the latter having a larger effect. The interfacial energies of crystal surfaces and the wetting liquid depend on composition as well as the orientation of the crystal interface. From Figure 5.12 and Figure 5.13 it was observed that some cBN grains exhibited surfaces that appeared to have been reacted. This apparent reaction is due to the hexagonalization of the cBN grains. The yttrium rich glassy phase interacts with non-faceted interfaces and causes the hexagonalization of cBN. The hexagonalization of the cBN grains increases with increasing temperature. This is illustrated by comparing M1-30cBN sintered at 1600 (Figure 5.12) and 1625°C (Figure 5.13). The lower sintering temperature reveals that there is only partial hexagonalization on certain surfaces of the cBN grains present in the sintered composite however samples sintered at 1625°C exhibit some grains which have been extensively hexagonalized.

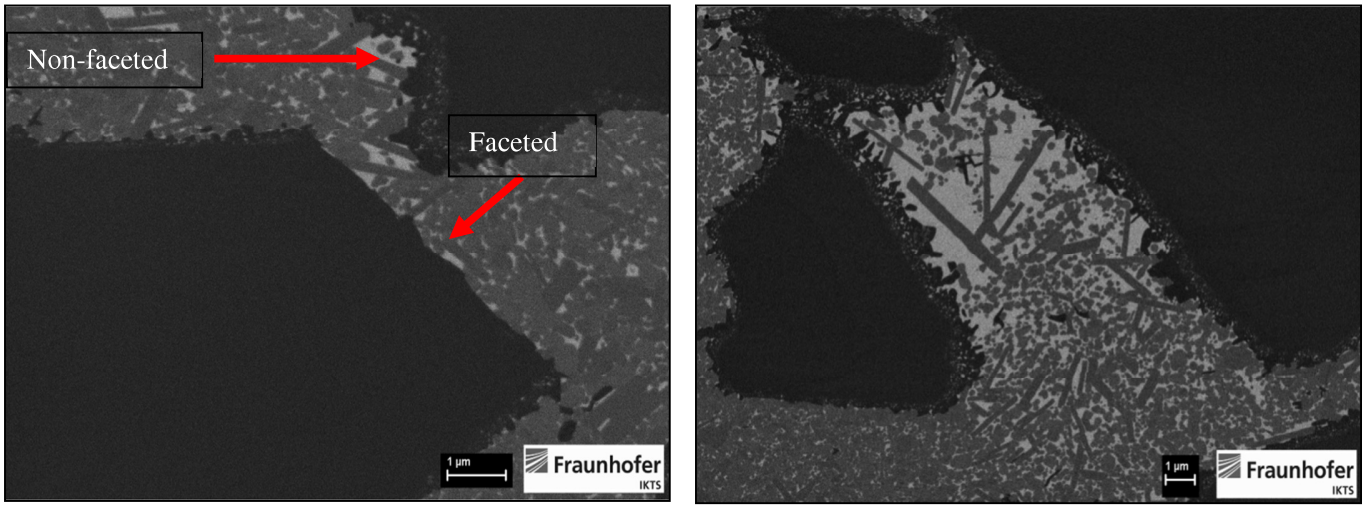


Figure 5.12 : SEM micrographs showing surface hexagonalization of some cBN grains in M1-sialon composite containing 30 vol. % cBN and sintered at 1600°C. Samples prepared by broad ion beam polishing courtesy of M. Herrmann of IKTS Fraunhofer.

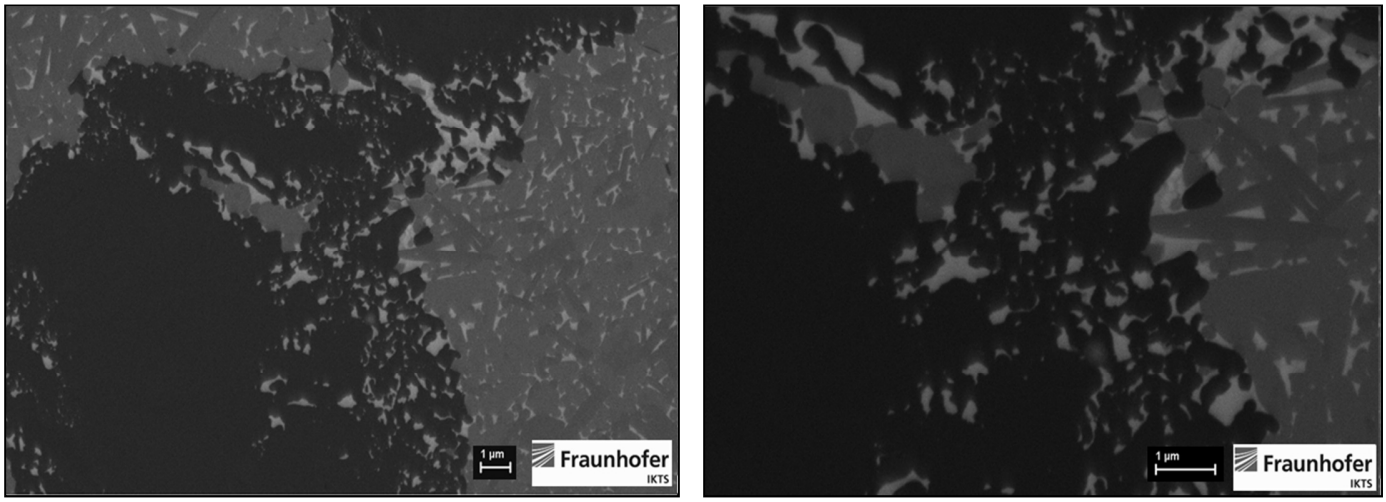


Figure 5.13: SEM micrograph showing considerable degradation of random cBN grains of the M1-sialon composite containing 30 vol. %cBN and sintered at 1625°C.

The liquid phase is found between the cBN grains as they form a skeleton (with increasing cBN content). The liquid is forced by the external pressure to penetrate between the cBN grains (through the uni-axial pressure of 50 MPa). This negative effect is expected to increase with increasing liquid phase present as well as with cBN content. Furthermore the penetration is dependent on the size of the matrix grains with respect to the secondary phase addition. The matrix grains, if small enough, can be forced between the cBN grains (Grade 9 cBN grains which are larger in size) with the applied external pressure. This process is enhanced with smaller matrix grains. The liquid phase reacts with the cBN causing hexagonalization of some surfaces of cBN grains. This shows that this reaction is dependent on the crystallographic orientation; not all grains exhibited this hexagonalization and not all sides of the cBN grains were affected equally as depicted in Figure 5.14, Figure 5.12 and Figure 5.14. Moreover it was seen that the increased presence of the liquid phase promotes the transformation of cBN to its hexagonal phase.

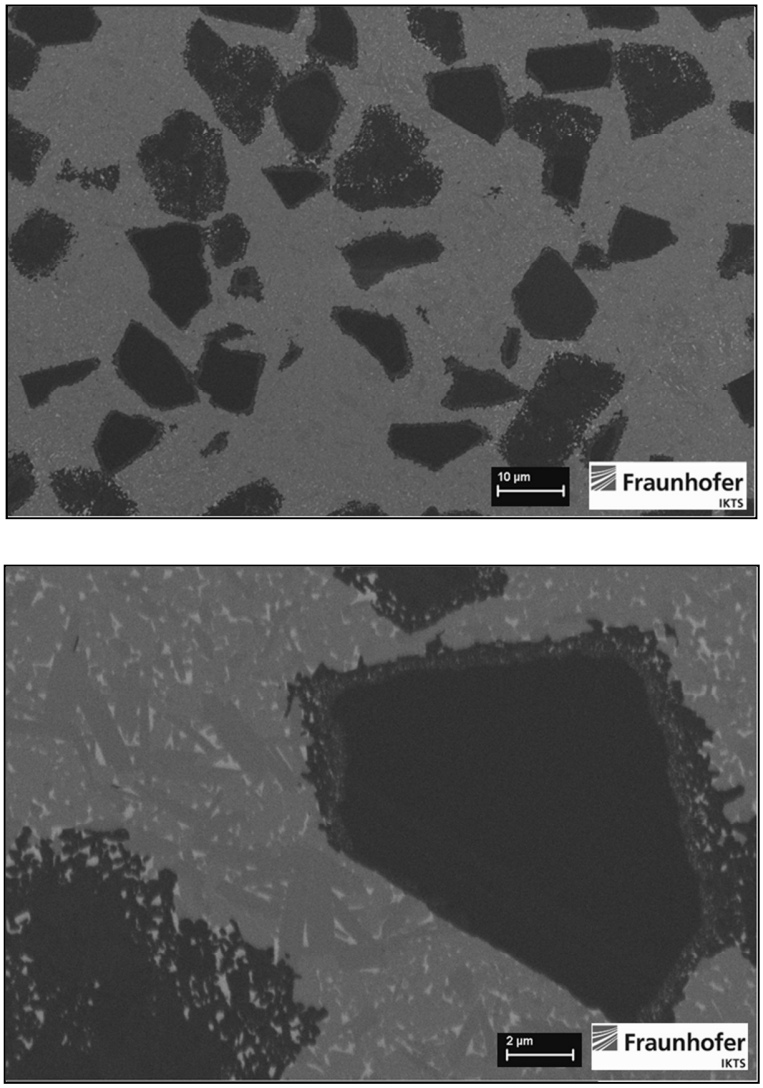


Figure 5.14: SEM micrograph showing inhomogenous hexagonalization of cBN grains within the M1-sialon matrix when sintered at 1625°C. Samples prepared by broad ion beam polishing courtesy of M. Herrmann of IKTS Fraunhofer.

This hexagonalization was observed through SEM analysis since XRD requires approximately > 5 vol. % of hBN for it to be detected accurately due to the fact that the principal peak for hBN is ≈ 26.6° which is between peaks relating to α-Si_3N_4 and β-sialon. Observation of a distinct peak for hBN in the XRD patterns would signify an extensive transformation to the hBN phase from the cBN one. This hexagonalization is predominantly seen in composites sintered at 1625°C (Figure 5.13). This justifies the poor hardness obtained for M1-20cBN and M1-30cBN sintered at 1625°C (Table 4.15). Whereas the sialon/cBN composites sintered at 1600°C only exhibit

slight hexagonalization of the non-faceted cBN grains or irregular surfaces (Figure 5.12). The interaction between sialon and cBN was observed to promote the hexagonalization of cBN grains particularly with increasing sintering temperature as compared to pure cBN sintered using SPS at 100MPa pressure; as reported by Hotta et al., 2010 [90] and shown in Figure 5.15.

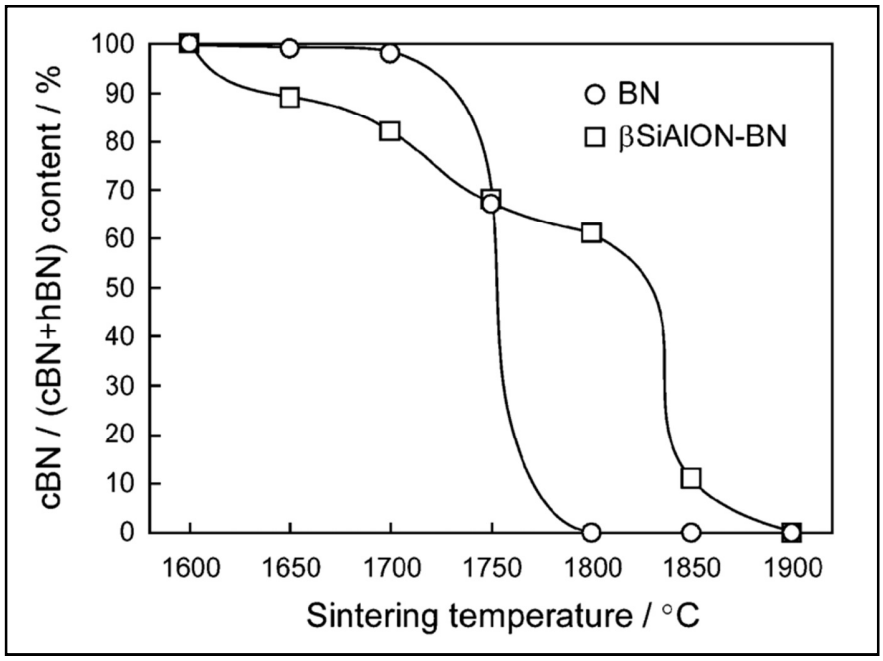


Figure 5.15: Comparison of the transformation of cBN grains with increasing sintering temperature, for pure cBN and β-sialon containing 20 vol. % cBN. Taken from Hotta et al., 2010 [90] .

These findings were in agreement with those obtained by Ye et al, 2010 [58] where it was claimed that the cBN grains only begin to hexagonalize at 1600°C. However the consolidation was completed through the use of Dr. Sinter equipment (Sumitomo Coal Mining Co.). The temperature measured through this machine leads to an under-estimated value since the optical pyrometer is focused on the outer surface of the graphite die and thus the temperature measured is lower as compared to the HP D5 (FCT, Germany) as explained in Section 4.4.1. This is due to the identification of the hBN phase through x-ray diffraction [58] [90], it was shown in this work that only highly hexagonalised cBN grains (> 20 vol. % of initial cBN) would be identified through this technique. This accounts for the difference in temperature readings of the two SPS machines, since the ceramics processed with Dr. Sinter SPS equipment experienced higher temperatures than that of the HP D5 and thus higher transformation from the cubic to hexagonal

phase. The decrease in cBN particle size results in an increase in the surface area which is then available for reaction. This hexagonalization is further promoted since cBN is only a metastable phase at the sintering conditions (low pressure) used in this work and thus a slight solubility of the boron nitride in the liquid phase will result in the partial dissolution of the cubic phase and precipitation of the hexagonal. Furthermore it is seen that a decrease in the percentage of the theoretical density occurs with increasing sintering temperature although no porosity was observed through SEM image analysis. This decrease is therefore attributed to the change in the theoretical density through the hexagonalization of cBN (3.48 g/cm^3) to hBN (2.27 g/cm^3). The promotion of the hexagonalization of cBN grains results in a decrease in the Vickers hardness of the sialon/cBN composites. Estimating the amount of hexagonalized cBN was achieved by calculating new theoretical densities whereby 10, 15 and 20 vol. % of the cBN additive was assumed to have been hexagonalized. The percentage of the theoretical densities assuming no hexagonalization of the cBN grains is presented in Table 5.2 as a comparison.

Table 5.2: Estimation of hBN content in the M1 sialon/cBN composites using 0, 10, 15 and 20 vol. % cBN to hBN formation.

Sample Name	Density (g/cm3)	Percentage of theoretical density (%)			
		0 vol. % hBN /cBN [a]	10 vol. % hBN /cBN [b]	15 vol. % hBN /cBN [c]	20 vol. % hBN /cBN [d]
M1-1575	3.33 ± 0.01	100.0	100.0	100.0	100.0
M1-10cBN-1575	3.32 ± 0.01	99.3	99.7	100.3	100.3
M1-20cBN-1575	3.31 ± 0.01	98.5	99.7	100.0	100.9
M1-30cBN-1575	3.31 ± 0.01	98.1	99.7	100.6	101.2
M1-1600	3.33 ± 0.01	100.0	100.0	100.0	100.0
M1-10cBN-1600	3.32 ± 0.01	99.3	99.7	100.3	100.3
M1-20cBN-1600	3.29 ± 0.01	97.9	99.1	99.4	100.0
M1-30cBN-1600	3.29 ± 0.01	97.5	99.1	100.0	100.6
M1-1625	3.32 ± 0.01	100.0	100.0	100.0	100.0
M1-10cBN-1625	3.30 ± 0.01	98.7	99.1	99.7	100.0
M1-20cBN-1625	3.28 ± 0.01	97.6	98.8	99.4	100.0
M1-30cBN-1625	3.28 ± 0.01	97.2	98.8	99.7	100.3

[a] Theoretical density: M1 = 3.33, M1-10cBN = 3.34, M1-20cBN = 3.36 and M1-30cBN = 3.37 g/cm^3

[b] Theoretical density: M1 = 3.33, M1-10cBN = 3.33, M1-20cBN = 3.32 and M1-30cBN = 3.32 g/cm^3

[c] Theoretical density: M1 = 3.33, M1-10cBN = 3.32, M1-20cBN = 3.31 and M1-30cBN = 3.30 g/cm^3

[d] Theoretical density: M1 = 3.33, M1-10cBN = 3.31, M1-20cBN = 3.29 and M1-30cBN = 3.27 g/cm^3

Taking the sialon/cBN composites to be fully dense it was found that M1/cBN composites sintered at 1575°C had approximately 10-15 vol. % cBN hexagonalized whereas the composites sintered at 1600°C and 1625°C had approximately 15-20 and 20 respectively; this is in agreement when observing the thickness of the hexagonalized layer of the cBN grains represented in Figure 5.14 and Figure 5.14

5.5. Comparison of mechanical properties sialon/cBN composites

The highest values of hardness (19.6 GPa) for pure sialon ceramics was obtained for M1 sialon sintered at a temperature of 1625°C. As the sintering temperature is increased the promotion of α-sialon formation is expected (Section 4.5.1.1.). Therefore the increase in α-sialon results in an increase in hardness from 18.2 GPa when sintered at 1575°C and 19.6 GPa when sintered at 1625°C. There was no effect on the fracture toughness with increasing sintering temperature, 3.6 ± 0.3 and 3.7 ± 0.2 MPa.m$^{0.5}$ for 1575°C and 1625°C respectively.

A 10 vol. % cBN addition to M1 sialon sintered at 1575 and 1600°C results in considerable increase in the hardness of the composites from 18.2 → 20.9 GPa and 19.1 → 21.3 GPa respectively. However this is not as high as expected from the introduction of these superhard cBN grains. Further addition of cBN results in the decrease in the hardness as compared to M1-10cBN composites. This decrease in hardness after addition of > 10 vol. % cBN is furthermore affected by increasing sintering temperature. However it is noted that the cBN containing composites sintered at 1575°C maintain hardness greater than that of pure M1 sialon with increasing cBN content up until 30 vol. % cBN. The cBN containing M1 composites experienced significant deterioration in the hardness when sintered at 1625°C with a cBN content of 20 and 30 vol. %. The hardness of the M1/cBN composites is thus seen to be affected by the sintering temperature due to the promotion of the surface hexagonalization of the cBN grains as discussed in Section 5.4.

From Figure 5.16 the fracture toughness is observed to improve with increasing sintering temperatures due to the reinforcing effect of cBN and partially due to the hexagonalization of cBN at higher volume contents. The composites sintered at 1575°C show an increase in the fracture toughness from 0 to 10 vol. % cBN (3.6 → 5.2 MPa.m$^{0.5}$) after which the fracture toughness is not significantly affected by the increasing cBN content (5.2 → 5.4 MPa.m$^{0.5}$) for composites containing 10 and 30 vol. % cBN respectively).

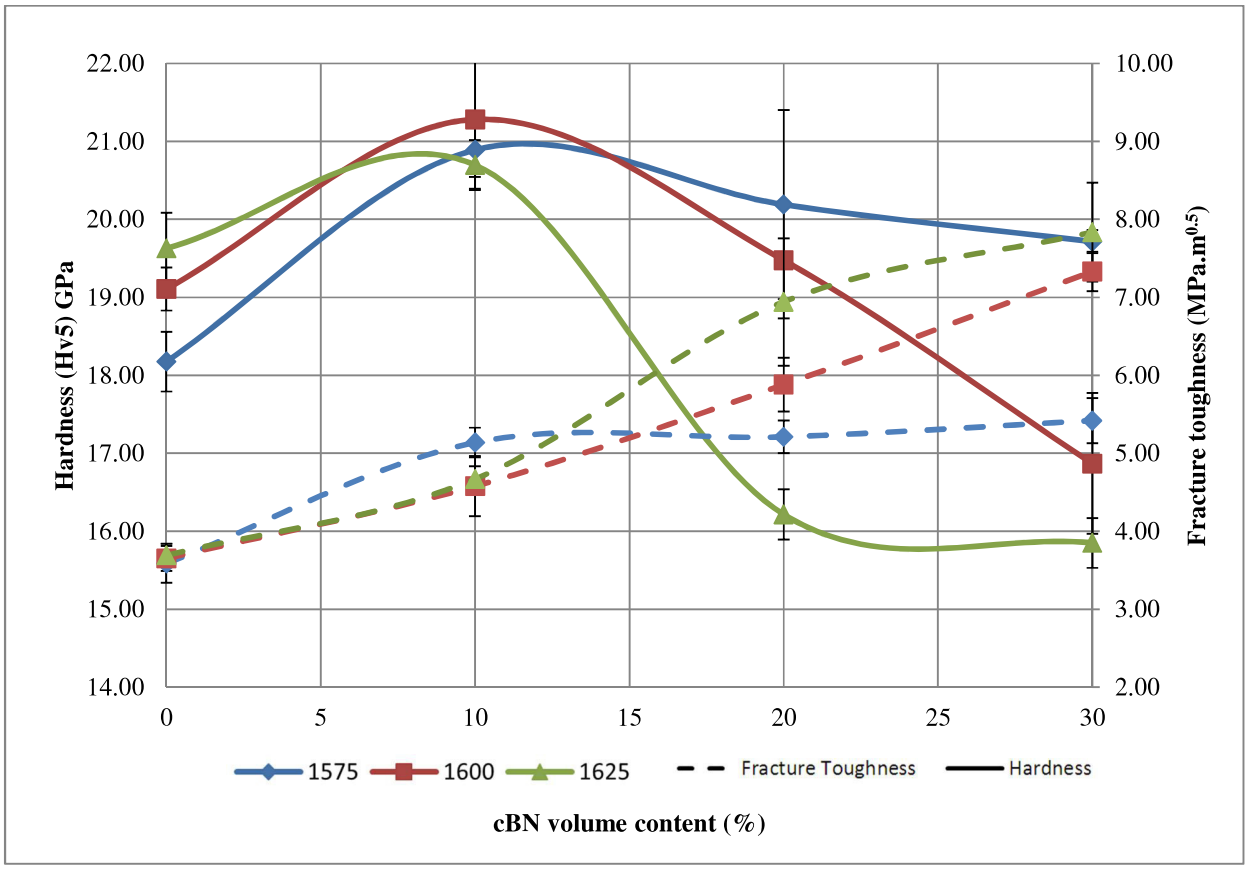


Figure 5.16: Effect of grade 9 cBN content on the mechanical properties of M1 sialon ceramics sintered with increasing temperature.

The hardness of pure M2 sialon increases only marginally with increase in the sintering temperature. It was found in Section 4.5.2 that an increase in temperature increases both the formation of α and β-sialon. Moreover the slight increase in hardness is due to the combination of the formations of the softer (β-sialon) and harder (α-sialon) phases. Also, due to the formation

of the β-sialon an increase in the fracture toughness from 4.0 to 4.33 MPa.m$^{0.5}$ is observed with increasing temperature. An increase in the β-sialon formation experienced when sintering M2 sialon as compared to M1 sialon results in a material that is not as hard however the fracture toughness is superior. This can be seen when comparing samples sintered at 1625°C for the respective pure sialon matrices where the hardness and fracture values for M1 are 19.6 GPa and 3.7 MPa.m$^{0.5}$, M2 - 17.3 GPa and 4.4 MPa.m$^{0.5}$, M3 - 19.1 GPa and 3.2 MPa.m$^{0.5}$ and M4 – 16.3 GPa and 5.2 MPa.m$^{0.5}$.

This is a similar result to that obtained for the M1/cBN composites where the hardness of composites sintered with 30 vol. % cBN and at 1575°C maintain a higher hardness than that of the pure matrix (16.9 → 18.6 GPa). For M2/cBN composites sintered at 1600°C with 30 vol. % cBN a lower hardness than the pure matrix is observed (17.3 → 16.4 GPa). The addition of cBN to M2 sialon results in an increase in the fracture toughness of composites with 30 vol. % cBN sintered at 1575 and 1600°C from pure M2 sialon. The improvements of the fracture toughness of 30 vol. % cBN reinforced sialon from pure sialon is 4.0 → 6.5 MPa.m$^{0.5}$ when sintered at 1575°C and 4.1 → 7.9 MPa.m$^{0.5}$ when sintered at 1600°C.

The hardness and fracture toughness were observed to significantly increase and decrease respectively for M3 sialon sintered at 1550 up until 1600°C, after which an increase in sintering temperature has little effect on the mechanical properties. This is due to the YAG phase being present in samples sintered at temperatures of below 1600°C. The elimination of the YAG phase results in the formation of the α-sialon phase and subsequently an increase in the hardness and decrease in the fracture toughness is observed.

The addition of 30 vol. % cBN to M3 sialon composites results in a negative effect with regards to the hardness as seen in Figure 5.16. Increasing the sintering temperature also has this effect. The hardness decreases with increasing cBN content (30 vol. % cBN) from the pure M3 sialon, when sintered at 1575°C (18.9 → 18.0 GPa) and 1600°C (19.0 → 16.9 GPa).

This is due to the increased ytrria-rich glassy phase aiding the hexagonalization of cBN as described in Section 5.4. The same relationship between cBN content and the sintering temperature is observed when examining the fracture toughness of sialon/cBN composites. This trend is again observed in M3/cBN composites as it was in M1/cBN and M2/cBN composites (Figure 5.16). The M3/cBN composites sintered with 30 vol. % cBN show improved fracture toughness as compared to the pure M3 sialon when sintered at 1575°C (3.4 → 6.3 MPa.m$^{0.5}$) and 1600°C (3.3 → 6.8 MPa.m$^{0.5}$).

Even though the improvements in the hardness weren't as high as expected for increasing cBN addition to sialon, it must be noted that the hardness obtained for M1, M2 and M3 are significantly higher than that obtained for β-sialon/cBN composites produced by Ye et al., 2010 [58] through SPS sintering at 1500°C, 7 minutes dwell time and pressure of 50 MPa (Figure 5.17). It was observed that the relationship of hardness with increasing cBN content of M1 sialon sintered at 1575°C was found to be similar to that of α-sialon/WC composites (WC d_{50} of 1.5µm) sintered through a two-step gas pressure sintering technique by Bitterlich et al., 2008. The consolidation of these sialon/WC composites was achieved through a two-step gas pressure sintering technique at 1930°C at an argon pressure of 20 and 80 bar respectively for 3 hours.

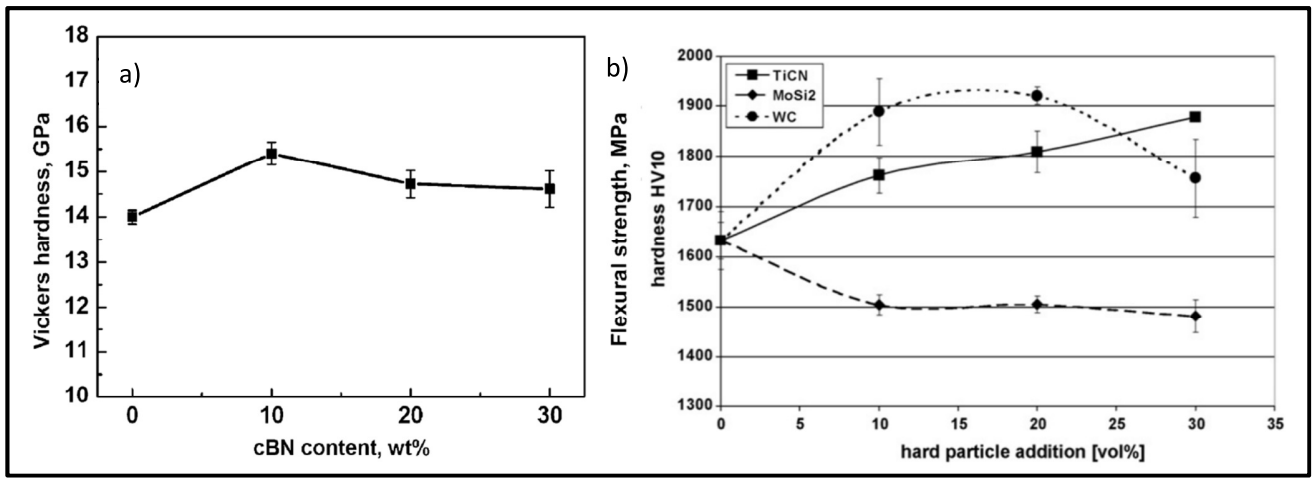


Figure 5.17: Effect of hardness with increasing secondary phase addition, a) SPS at 1500°C measured with 5 kg load Ye et al., 2010 [58], b) gas pressure sintered at 1930°C measured with a load of 10 kg.

Since M4 sialon is based on the composition used by Ye et al., 2010 [58] where the composition of M4 is located in the α-sialon plane whereas for Ye et al., 2010 [58] it is located below the sialon plane. A comparison of the mechanical properties of M4 sialon (sintered at 1600°C – HP D5 FCT) with the sialon ceramic produced by Ye et al., 2010 [58] (sintered at 1500°C - Dr. Sinter) it was revealed that M4 sialons have higher hardness and fracture toughness than that of the ceramics produced by those authors with and without cBN additions. These results are presented in Table 5.3. However it must be noted that the phase formation for M4 is somewhat different to that of Ye et al., 2010 [58] (Section 4.5.4).

Table 5.3: Comparison of the mechanical properties obtained for M4 sialon based composite with that sintered by Ye et al., 2010 [58].

Sialon composites	cBN content (vol. %)	Hardness (H_{v5})	Fracture toughness (MPa.m$^{0.5}$)
M4-1600	0	15.5 ± 0.3	4.2 ± 0.1
M4-30cBN-1600	30	16.1 ± 0.4	6.9 ± 0.3
Ye - 1500	0	14.0	4
Ye – 30cBN - 1500	30	14.5	6.3

The increase in hardness for M4 as compared to Ye et al., 2010 [58] presented in Table 5.3 is attributed to the fact that the M4 sialon consists mostly of α-sialon (which is the hardest phase in the sialon system given in Table 2.3) and 12 H polytypes as well as β-sialon wheras the composition used by Ye et al., 2010 [58] consists predominantly of β-sialon. Furthermore, in Table 5.3 it is shown that an increase in 30 vol. % cBN to M4 sialon composites results in a significant improvement in the fracture toughness (4.2 → 6.9 MPa.m$^{0.5}$) and a moderate increase in the hardness (15.5 →16.1 GPa).

5.6. Fracture toughening mechanisms

Since fracture toughness can be defined as the resistance to crack propagation [91], having a material with high fracture toughness will be beneficial for improving tool life and performance particularly for interrupted cutting applications. Since plastic deformation is very limited in ceramic materials, the predominant relief of stresses is obtained through the propagation of cracks through the material.

It was found that when adding cBN to sialon ceramics, the primary reinforcing effect is that of improving the fracture toughness of the cBN containing sialon matrices [58]. Toughening mechanisms such as crack branching, crack deflection and grain pull out improve the fracture toughness of a material [92]. Crack branching (Figure 5.18) occurs when a crack subdivides into multiple crack propagation fronts. Crack deflection (Figure 5.19) can be classified as the generation of out of plane components by a tilting or twisting of a crack plane around grains and secondary phases. These fracture mechanisms are exhibited in sialon/sialon and sialon/cBN interactions.

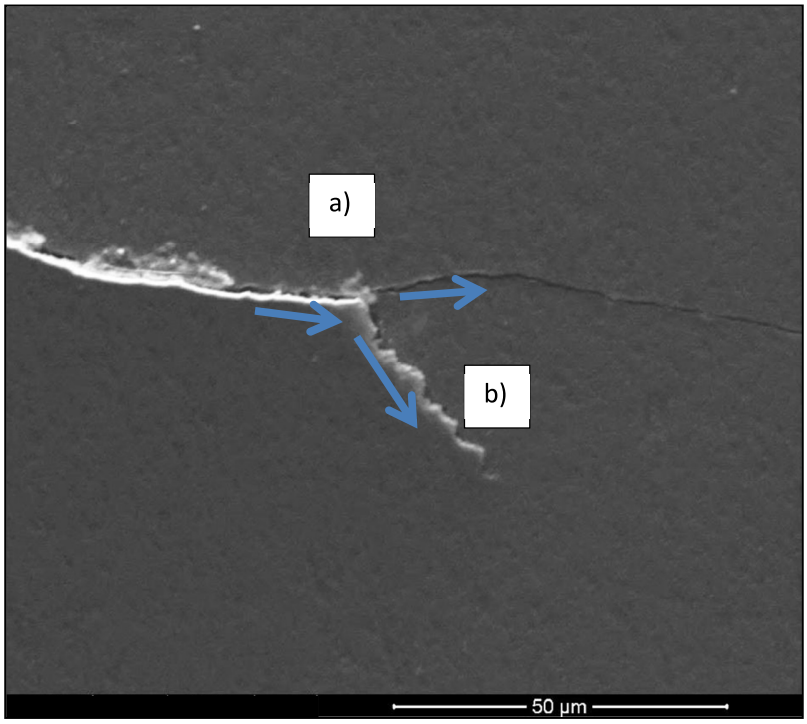


Figure 5.18: Fracture mechanisms experienced in pure sialon ceramics, a) crack branching and b) crack deflection for M1-1600.

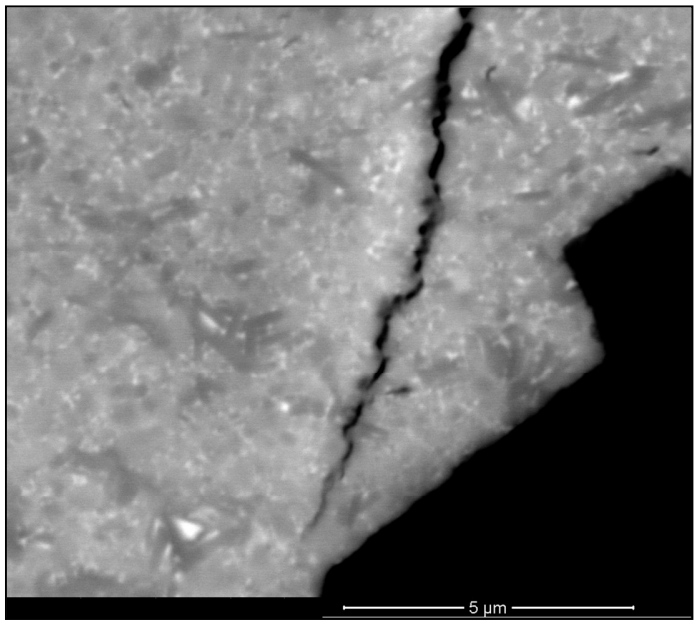


Figure 5.19: Typical back-scattered SEM image showing crack deflection in sialon M1-1600-10cBN.

Both of these mechanisms take place when a propagating crack adopts a less resistant crack path which could be due to remaining residual stress in the sintered composite or even difference in the mechanical properties of sintering aids which form along the grain boundaries. The grain boundary phase, usually the weakest, promotes inter-granular crack propagation in the sintered sialon ceramic [92]. cBN reinforced sialon composites exhibit both intergranular and transgranular crack propagation, contributing to the increase in fracture toughness as shown in Figure 5.20 and Figure 5.21.

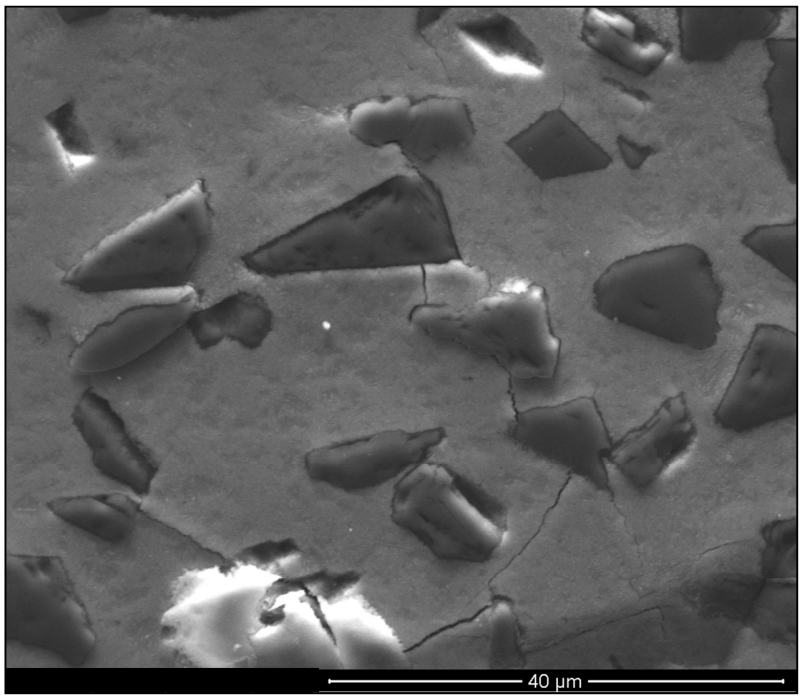


Figure 5.20: Intergranular crack propagation of cBN grains reinforcing sialon by improving fracture toughness M1-30cBN-1600.

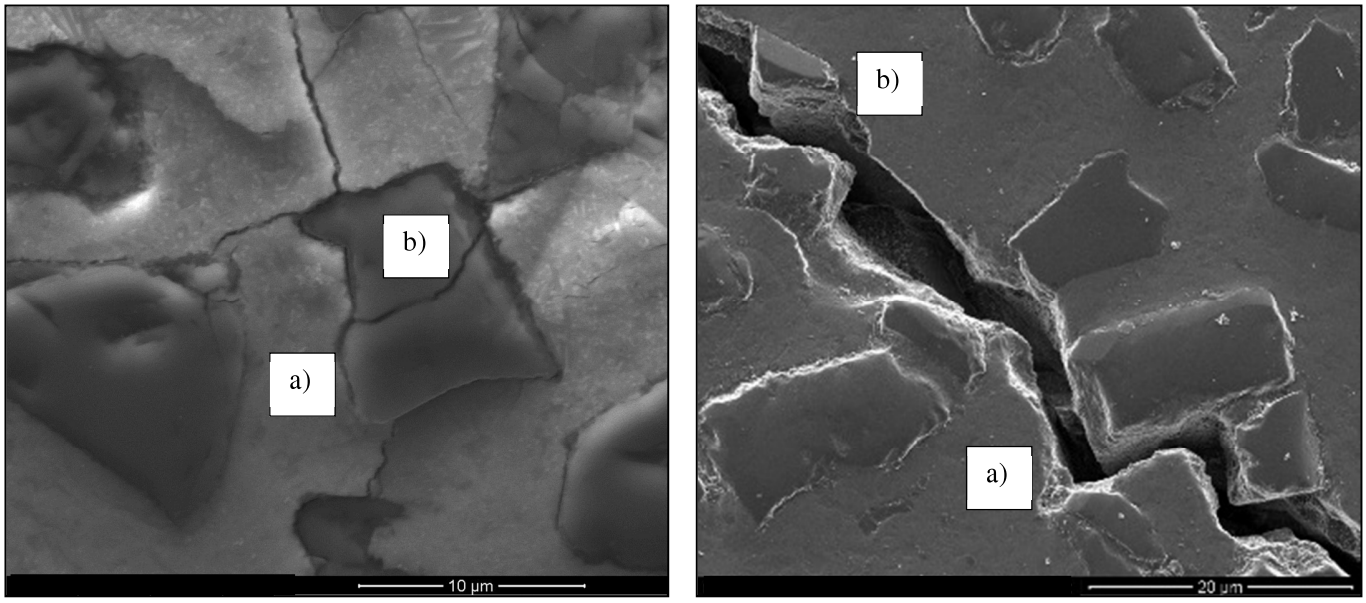
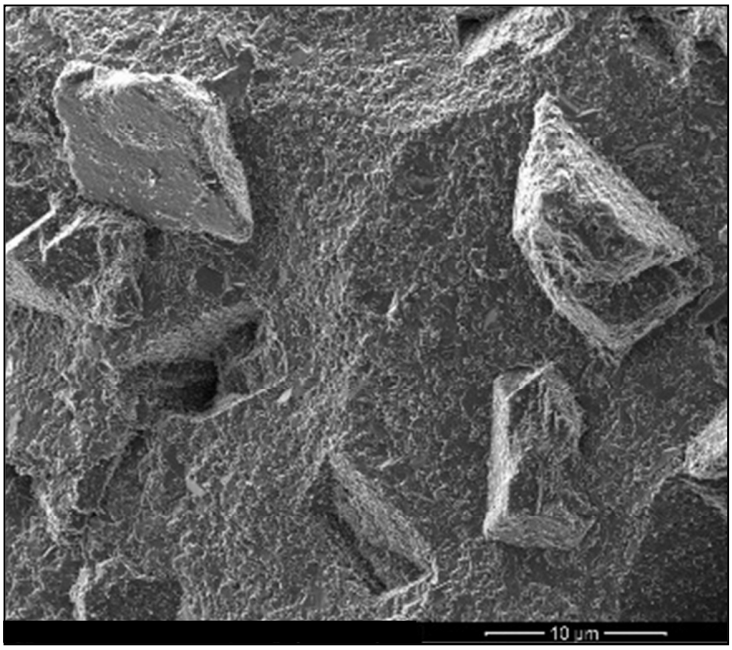


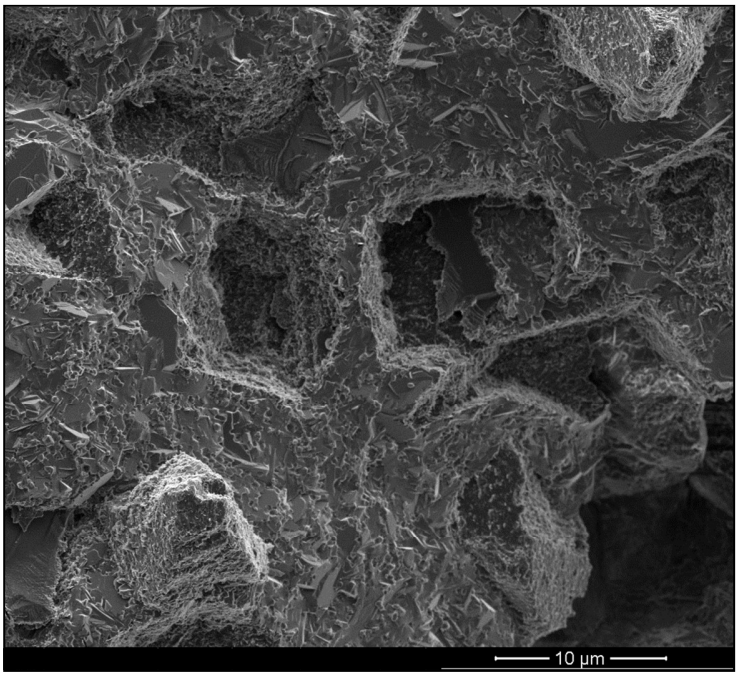
Figure 5.21: Intergranular (a) crack propagation around cBN grains and transgranular (b) crack propagation through cBN grains for M1-30cBN-1625.

The main fracture mechanism present in cBN containing sialon composites is through intergranular crack propagation since the interfacial bonding between the cBN grains and the matrix is significantly reduced with the hexagonalization of the cBN grains. The hexagonalization of cBN grains leads to weak sialon/cBN interfaces which in turn increase the fracture toughness and decreases the hardness values. The hexagonalization is promoted though increases in the cBN content and sintering temperature. Transgranular crack propagation of cBN grains in the sialon matrix are attributed mainly to the damage of cBN grains during sintering.

The fracture surface of cBN containing sialons consists primarily of crack deflection and cBN grain pull-out as the fracture mechanisms, presented in Figure 5.22. The intergranular fracture mechanisms are dependent on the grain morphology and since M1 and M4 sialons consist of considerably different compositions and microstructures as shown in Figure 5.4. The different compositions result in M1, M2 and M3 sialon having predominantly equiaxed grains while M4 sialon consists mainly of the elongated morphology this can be seen by the fracture surfaces of the respective composites (Figure 5.22).



a)



b)

Figure 5.22: Fracture surface of sialon/cBN composites showing cBN grain pull out as well as intergranular fracture of M1-30cBN (a) and M4-30cBN (b) sialon composites sintered at 1600°C.

6. Conclusion

Dense sialon materials with a cBN content of up to 30 vol. % could be produced through SPS densification of the respective starting powders. The composition of the α-sialon matrices can be expressed by their respective m and n values in the following formula:

$Y_{m/3}Si_{12-(m+n)}Al_{(m+n)}O_nN_{16-n}$.

Two main matrices were used, the first being more nitrogen-rich with m = 0.99 and n = 2.50 and the second being more oxygen-rich with m = 1.99 and n = 4.49. The composition of the second matrix was selected for comparison with the results of Ye et al., 2010 [58]. Investigations were also completed on two different sialon variants whose composition was changed, through the addition and reduction by 2wt. % of aluminium nitride and yttria respectively. The materials showed an increase in the fracture toughness, however only a slight increase in the hardness was realized. In detail, the following results were achieved and conclusions drawn:

Full densification of the sialon ceramics with lower values of m and n was obtained at a sintering temperature of 1575°C, which is lower than that of the more oxygen-rich (1625°C) sialon matrix. The temperature of formation for the eutectic oxide phase (yttria-rich) is lowest for the oxygen-rich sialon matrix as expected. Both sialon matrices show intensive piston-speed peaks relating to particle rearrangement and solution-precipitation; however the densification of the second sialon matrix is interrupted due to intermediate crystallization of oxide phases forming at the grain boundaries. Because it was possible to obtain fully dense sialon with the more nitrogen-rich matrix at lower temperatures the more nitrogen-rich matrix was the focus of the investigations. A 2 wt. % reduction of aluminium nitride was observed not to affect the temperature required for full densification however the increase of the yttria content by 2 wt.% resulted in a decrease of the oxide eutectic onset temperature. Moreover the temperature required for full densification also decreases (1550°C). This is attributable to the excess liquid phase.

It was found that the reinforcing ≈ 10 μm cBN grains could be homogenously distributed throughout the sialon matrix through the use of dry Turbula mixing of the cBN and the premixed sialon powders. Through additions of cBN grains to the various sialon matrices it was observed that the primary mechanisms of liquid phase sintering, namely particle rearrangement and solution-precipitation, were negatively affected. This negative effect on the densification was observed to be more prominent with the oxide-rich sialon as compared to the other sialon matrices. Increasing cBN grain content resulted in the localized pooling of the yttria-rich phase between cBN grains due to the forced penetration of the liquid phase between the cBN adjacent grains through the applied 50 MPa external pressure. The yttria-rich liquid phase was observed to react with non-faceted interfaces and irregular surfaces of the cBN grains. It was additionally observed that not all cBN grains experienced the same level of hexagonalization. The transformation of particular cBN grains in the cBN containing sialon composites were only observed at temperatures of 1600°C (partial) and 1625 °C (high). The hexagonalization was observed to decrease the final densities due to the large volume increase associated with the BN phase transformation from cubic to hexagonal. Additionally the effects of using smaller cBN grains to reinforce sialon was investigated. It was also found that ≈ 0.7 μm cBN grains did not survive sintering temperatures as low as 1575°C due to the increased surface area available for hexagonalization when in contact with the sialon constituents. The degree of hexagonalization of the cBN grains was found to increase with increasing sintering temperature and concentration of the yttria-rich liquid phase. Despite hexagonalization of the cBN grains in some cBN containing sialon composites, high percentages of the theoretical densities were still obtained (> 97%). Although fully dense sialon ceramics are obtained, it would be preferred that higher sintering temperatures were employed in order to aid the α-sialon formation. However the sintering temperature is limited due to the threat of hexagonalization of the cBN grains. Furthermore the densification of pure sialon as well as that of the cBN containing composites was found to depend strongly on the composition of the matrix.

The dissolution of α-Si_3N_4 in the solution-precipitation step for sialons with low m and n values produces primarily α-sialon with small amounts of β-sialon and the 12 H polytype phase whereas sialon with higher m and n values consists mainly of α-sialon and polytypes, with trace amounts

of β-sialon. The grain morphology of the first sialon ceramic is predominantly equiaxed (α-sialon) which is known to have a higher hardness compared to the elongated grain microstructure of M4, which has superior fracture toughness. The highest hardness was obtained at a sintering temperature of 1625°C for both sialon compositions, the Vickers hardness and fracture toughness values for the first sialon are 19.6 ± 0.05 GPa and 3.7 ± 0.2 MPa.$m^{1/2}$ whereas the second sialon had 16.3 ± 0.24 GPa and 5.21 ± 0.19 MPa.$m^{1/2}$. An increase in the sintering temperature promotes the α-sialon transformation in the presence of yttrium as the stabilizing cation and thus the Vickers hardness is increased for both sialon ceramics. The fracture toughness is only increased for the second sialon matrix since it was observed that increasing the sintering temperature promotes the formation of 12H polytype. The 2 wt. % compositional changes made to the first sialon matrix had no significant effect on the microstructure. However reducing the aluminium nitride content resulted in a decrease in the Vickers hardness and improvement of the fracture toughness whereas increasing the yttria content decreases the fracture toughness, with no effect on the Vickers hardness being observed. This has likely been caused by the increased amount of glassy phase present.

It was expected that due to the high hardness of cBN the incorporation of cBN into the sialon matrices would result in significant improvements in the hardness of these materials. It was found that this was not the case. Furthermore the hexagonalization of part of or the whole cBN grains results in a decrease in the Vickers hardness. Thus the primary reinforcing property of the cBN grains within the parent sialon ceramic was improving the fracture toughness. The optimum addition of the cBN grains was found to be 10 vol. % since significant improvements in the hardness and fracture toughness of the resulting reinforced materials were obtained. The materials thus produced were nitrogen-rich sialon composites sintered at temperatures of 1575 (18.2 → 20.9 GPa), 1600 (19.1 → 21.3 GPa) and 1625°C (19.7 → 20.7 GPa) as compared to the pure sialon ceramic. cBN containing sialon composites sintered at 1575°C maintain hardness greater than that of pure sialon with increasing cBN content up to 30 vol. % cBN, however at higher sintering temperatures considerable deterioration of the cBN grains occurred due to hexagonalization; this results in composites which have lower hardness than that of the pure sialon. However this is only noted when the cBN content is higher than 10 vol. %. The

hexagonalization promotes weak interfaces between the sialon matrix and the cBN grains which in turn decrease the hardness and increase the fracture toughness since this weak interface offers an easier crack propagation route.

The fracture toughness of cBN containing sialon composites was observed to improve with increasing amount of hexagonalization of the cBN grains, which was further promoted by an increase in sintering temperature. The fracture toughness was seen to improve significantly with 10 vol. % cBN addition to the nitrogen-rich sialon matrix (3.6 → 5.2 MPa.$m^{0.5}$) when sintered at 1575°C however further addition of cBN does not result in an improvement of the fracture toughness. cBN containing composites sintered at high temperatures with 30 vol. % cBN exhibit fracture toughness values as high as 7.8 MPa.$m^{0.5}$ due to excessive hexagonalization. The main fracture mechanism present in cBN containing sialon composites is intergranular crack propagation since the interfacial bonding between the cBN grains and the matrix is significantly reduced with the hexagonalization of the former. However transgranular crack propagation through cBN grains was also present in the sialon composites and is attributed mainly to the damage of cBN grains during sintering.

Lastly when comparing the mechanical properties of pure oxide-rich sialon ceramic and its cBN containing composites with that of the composites produced by Ye et al., 2010 [58] it is revealed that the α-sialon ceramics have better hardness and fracture toughness than those of the cBN composites based on β-sialon.

7. Further work

Although the mechanical properties of sialon materials were improved with the addition of cBN as a reinforcing agent, the improvement in properties was limited to a 10 vol. % cBN addition as well as a sintering temperature of 1575°C. Increasing the sintering temperature promotes the formation of α-sialon but it also aids the phase transformation for boron nitride from the metastable superhard cubic structure to the soft hexagonal one. More work is required for the better understanding of the densification mechanisms present in the formation of sialon ceramics and for the interaction between the sialon matrix and the reinforcing cBN grains. The possible future work is summarized below:

- Investigate more extensive sialon compositions in order to eliminate phases such as the soft 12H polytype phase completely from the sialon matrix and increase the formation of α-sialon.
- Understanding the mechanisms which lead to the hexagonalization of preferential surfaces of the added cBN grains in the sialon matrix, which can be achieved through TEM analysis.
- Prevent the hexagonalization of cBN grains through a reduction in the interaction of the liquid phases present in the formation of sialon with that of the cBN grains through the use of coated cBN grains, such as cBN with titanium carbonitride deposition.

8. Reference list

1. S. Hampshire, "Silicon nitride ceramics - review of structure, processing and properties", Journal of Achievements in Materials and Manufacturing Engineering", Vol. 24, 2007, pp. 43-50.

2. M. Herrmann, S. Hohn and A. Bales, "Kinetics of rare earth incorporation and its role in densification and microstructure formation of alpha-Sialon", Journal of the European Ceramic Society, Vol. 32, 2012, pp. 1313-1319.

3. G. Petzow and M. Herrmann, "Silicon nitride ceramics", Structure and Bonding, Vol. 102, Springer-Verlag Berlin Heidelberg, 2002, pp. 47-167.

4. I.-W. Chen, R. Shuba and M. Zenotchkine, "Development of tough alpha-sialon", Key Engineering Materials, Vol. 237, 2003, pp. 65-78.

5. M. Kutz, "Handbook of material selection", John Wiley & Sons, 200.

6. P. K. Trent and E. M. Wright, "Metal Cutting", Butterworths, 2000.

7. A. V. Smith and D. D. L. Chung, "Titanium diboride particle-reinforced aluminium with high wear resistance", Journal of Materials Science, Vol. 31, 1996, pp. 5961-5973.

8. B. Yaman and H. Mandal, “Spark plasma sintering of Co-WC cubic boron nitride composites”, Materials Letters, Vol. 63, 2009, pp. 1041-1043.

9. H. S. C. Deville and F. Wohler, "Erstamalige Erwahnung von Si_3N_4", Liebigs Ann. Chem, Vol. 104, 1857, pp.256.

10. B. C. Carter and G. M. Norton, "Ceramic Materials/Science and Engineering", Springer, 2007.

11. J. F. Collins and R. W. Gerby, "New Refractory Uses for Silicon Nitride Reported", Journal of Metallurgy, Vol. 7, 1955, pp. 612-615.

12. G. G. Deeley, L. M. Herbert and D. C. Moore, "Dense silicon nitride", Powder Metallurgy, Vol. 8, 1961, pp. 145-151.

13. R. Heinmann, "Classic and Advanced Ceramics", Wiley-VCH Verlag, 2010.

14. K. Berroth, T. Prescher and J. Schubert, "Silicon nitride based ceramics for foundry applications", 3rd DRACHE-Seminar - Casting Techniques, 2005.

15. C. R. Zhou, Z. B. Yu and V. D. Krstic, "Pressureless sintered self reinforced Y-α-SiAlON ceramics", Journal of the European Ceramic Society, Vol. 27, 2007, pp. 437-443.

16. E. F. Hockings, "Handbook of Inorganic and Organometallic Chemistry", 8th Edition, Springer-Verlag, Berlin, 1994, pp. 238-277.

17. M. N. Rahaman, "Ceramic processing and sintering", 2nd Edition, New York: Marcel Dekker, 2003.

18. M. Kitayam, K. Hirao, A. Tsuge, M. Toriyama and S. Kanzaki, "Oxygen Content in β-Si_3N_4 Crystal Lattice", Journal of the American Society, Vol. 82, 1999, pp. 3263-3265.

19. H. Peng, "Spark Plasma Sintering of Si_3N_4-Based Cermaics", Doctoral dissertation, Stockholm University, 2004.

20. L. Chen. E. Kny and G. Groboth, "Sialon ceramic with gradient microstructures", Surface and Coatings Technology, Vol. 100-101, 1998, pp. 320-323.

21. K. Kijima and S. Shirasaki, "Nitrogen self-diffusion in silicon nitride", Journal of Chemical Physics, Vol. 65, 1976, pp. 2688-2671.

22. A. Zerr, G. Miehe, G. Serghiou, M. Schwarz, E. Kroke, R. Riedel, H. Fue, P. Kroll and R. Boehler, “Synthesis of cubic boron nitride”, Nature, Vol. 400, 1999, pp. 340-342.

23. E. Kroke, “High-Pressure Sytheses of Novel Binary Nitrogen Compounds of Main Group Elements”, Angewandte Chemie International Edition, Vol. 41, 2002, pp. 77-82.

24. T. Sekine, "Shock synthesis of cubic silicon nitride", Journal of the American Ceramic Society, Vol. 85, 2002, pp. 113-116.

25. F.F. Lange, "The sophistication of ceramic science through silicon nitride studies", Journal of Ceramic Science Society Japan, Vol. 115, 2006, pp. 873-879.

26. K. H. Jack and W. I. Wilson, "Ceramics based on the Si-Al-O-N and Related Systems'", Nature Physical Science, Vol. 238, 1972, pp. 28-29.

27. S. Hampshire, H. K. Park, D. P. Thompson and K. H. Jack, "α'-sialons", Nature, Vol. 274, 1978, pp. 880-882.

28. A. Rosenflanz and I. W. Chen, "Phase relationships and stability of α'-SiAlON ", Journal of the American Ceramic Society, Vol. 82, 1999, pp. 1025-1036.

29. A. Rosenflanz and I. -W Chen, " Kinetics of Phase Transfromations in SiAlON Ceramics: I. Effects of Cation Size, Composition and Tempearture", Journal of the European Ceramic Society, Vol. 19, 1999, pp. 2324-2335.

30. K. H. Jack, "Review: SiAlONs and Related Nitrogen Ceramics", Journal of Material Science, Vol. 11, 1976, pp. 1135-1158.

31. M. H. Lewis, B. D. Powell, P. Drew, R. J. Lumby, B. North and A. J. Taylor, "The formation of single-phase Si-Al-O-N Ceramics", Journal of Materials Science, Vol. 12, 1977, pp. 61-74.

32. L. O. Nordberg and T. Eckstrom, "Hot-pressed MoSi2-particulate-reinforced α-SiAlON composites", Journal of the Amrican Ceramic Society, Vol. 78, 1995, pp. 797-800.

33. Z. J. Shen, L. O. Nordberg, M. Nygren and T. Eckstrom, "α-Sialon grains with high aspect ratio-Utopia or reality?", NATO ASI Series, Series 3: High Technology, Vol. 25, 1997, pp. 169-178.

34. L. O. Nordberg, Z. She, M. Nygren and T. Ekstrom, "On the extension of α-Sialon solid solution range and anisotropic grain growth in Sm-doped α-Sialon ceramics", Journal of the European Ceramic Society, Vol. 17, 1997, pp. 575-580.

35. H. Mandal, "New developments in α-SiAlON ceramics", Journal of the European Ceramic Society, Vol. 19, 1999, pp. 2349-2357.

36. M. H. Lewis, A. R. Bhatti, R. J. Lumby and B. North, "The microstructure of sintered silicon-aluminium-oxygen-nitrogen ceramics", Journal of Material Science, Vol. 15, 1980, pp. 103-113.

37. S. Hampshire and K. H. Jack, "Densification and transformation mechanisms in nitrogen ceramics", NATO ASI Series, Series E: Applied Sciences, Vol. 65, 1983, pp. 225-230.

38. L. J. Bowen, T. G. Carruthers and R. J. Brook, "Hot-pressing of silicon nitride with yttrium oxide and lithium oxide as additives", Journal of the American Ceramic Society, Vol. 61, 1978, pp. 335-339.

39. W. D. Kingerey, "Sintering in the Prescence of a Liquid Phase", Journal of Applied Physics, Vol. 30, 1959, pp. 301-306.

40. S. Kurama, M. Herrmann and H. Mandal, "The effect of processing conditions, amounts of additives and composition on the microstructures and mechanical properties of α-SiAlON ceramics", Journal of the European Ceramic Society, Vol. 22, 2002, pp. 109-119.

41. M. W. Barsoum, "Fundamentals of Ceramics", McGraw-Hill, 1997.

42. R. Reidel, A. Zerr and S. Vepřek, "Handbook of Ceramic Hard Materials", Wiley, Weinheim, 2000.

43. S. -L. Hwang and I. -W. Chen, "Reaction hot pressing of α'- and β'-SiAlON ceramics", Journal of the American Ceramic Society, Vol. 77, 1994, pp. 165-171.

44. A. Rosenflanz and I. -W Chen, " Kinetics of Phase Transfromations in SiAlON Ceramics: II. Reaction Paths", Journal of the European Ceramic Society, Vol. 19, 1999, pp. 2337-2348.

45. S. Hampshire, "Silicon nitride ceramics - review of structure, processing and properties", Vol. 24, 2007, pp. 43-49.

46. I. M. Lifshitz and V. V. Slyzov, "The Kinetics of Precipitation from Supersaturated Solid Solutions", Journal of Physical Chemistry Solids, Vol. 19, 1961, pp. 35-50.

47. J. E. Shelby and J. Kohli, "Rare-earth aluminosilicate glasses", Journal of American Ceramic Society, Vol. 73, 1990, pp. 39-42.

48. G. Ziegler, G. Heinrichad G. Wotting, "Review: Relationships between processing, microstructure and properties of dense reaction-bonded silicon nitride", Journal of Material Science, Vol. 22, 1987, pp. 3041-3086.

49. Z. Shen, Z. Zhao, H. Peng and M. Nygren, "Formation of tough interlocking microstructures in silicon nitride ceramics by dynamic ripening", Nature, Vol. 417, 2002, pp. 266-269.

50. S. Bandyopadhyay, "The In Situ Formation of Sialon Composite Phases", (PII: S0955-2219(96)00120-3), 1996, pp. 929-934.

51. H. Miao, L. Qi and G. Cui, “Silicon Nitride Ceramic Cutting-tool and their applications”, Key Engineering Materials, Vol. 114, 1996, pp. 135-172.

52. M. Hoffmann, G. Schneider and G. Petzow, "The potential of silicon nitride for thermal shock applications", NATO ASI Series, Series E: Applied Sciences, Vol. 241, 1993, pp. 49-58.

53. F. Ye, M. J. Hoffmann, S. Holzer and M. Iwasa, "Microstructural development of Y-α/(β)-sialons after post heat-treatment and its effect on mechanical properties", Ceramics International, Vol. 30, 2004, pp. 229-238.

54. P. O. Olsson and T. Ekstrom, "HIP-sintered β- and mixed α -β-sialons densified with Y_2O_3 and La2O3 additions", Journal of Materials Science, Vol. 25, 1990, pp. 1824-1832.

55. M. H. Bocanegra-Bernal and B. Matovic, "Mechanical properties of silicon nitride-based ceramics and its use in structural applications at high temperatures", Materials Science and Engineering A, Vol. 527, 2010, pp. 1314-1338.

56. R. S. Mishra, S. H. Risbud and A. K. Mukhurjee, "Influence of initial crystal structure and electrical pulsing on densification of nanocrystalline alumina", Journal of Materials Research, Vol. 13, 1998, pp. 86-89.

57. J. Langer, D. Quach, J. Groza and O. Guillon, "A comparison between FAST and SPS apparatuses based on the sintering of oxide ceramics", International Journal of Applied Ceramic Technology, 2010, pp. 1-9.

58. F. Ye, Z. Hou, H. Zhang, L. Liu and Y. Zhou, " Spark plasma sintering of cBN/β-SiAlON composites", Materials Science and Engineering A, Vol. 527, 2010, pp. 4723-4726.

59. M. Tokita, "Sumitomo Review- Mechanism of Spark Plasma Sintering", Sumitomo Coal Mining Company Ltd, pp. 1-13.

60. J. Räthel, M. Herrmann, W. Beckert and R. Holke, “Temperature Distribution during Spark Plasma Sintering (SPS/FAST)”, Journal of the European Ceramic Society, Vol. 29, 2009, pp. 1419-1425.

61. K. L. Smirnov, "Spark plasma sintering of SiAlON ceramics", International Journal of Self-Propogating High Temperature Synthesis, Vol. 18, 2009, pp. 92-96.

62. R. H. Wentorf, “Cubic form of boron nitride”, Journal of Chemical Physics, Vol.26, 1957, pp. 956.

63. J. Haines, J. M. Léger and G. Bocquillon, "Synthesis and Design of Superhard Materials", Annual Review of Material Research, Vol. 31, 2001, pp. 1-23.

64. T. Yano and X. Z. Rong, "TEM investigation of high-pressure reaction-sintered cBN-Al composites", Journal of. Material Science, Vol. 39, 2004, pp. 4705-4710.

65. R. H. Wentorf, R. C. DeVries, and F. P. Bundy, "Sintered Superhard Materials", Science, Vol. 208, 1980, pp. 873.

66. D. He, Y. Zhao, L. Daemen, J. Qian, T.D. Shen and T.W. Zerda "Boron suboxide: As hard as cubic boron nitride", Applied Physics Letters, Vol. 81, 2002, pp. 643-645.

67. P. F. McMillan, H. Hubert, A. Chizmeshya, W. T. Petuskey, L. A. J. Garvie and B. Devouard “Nucleation and Growth of Icosahedral Boron Suboxide Clusters at High Pressure”, Journal of solid state chemistry, 147, 1999, pp. 281-290.

68. E. Benko, J. Morgiel and T. Czeppe, "BN Sintered with Al: Microstructure and Hardness", Ceramics International, Vol. 23, 1997, pp. 89-91.

69. I.D. Marinescu, M. Hitchiner, E. Uhlmann, W.B. Rowe and I. Inasaki, "Handbook of Machining with Grinding Wheels", Taylor & Francis Group, 2006.

70. R. F. Bunshah, "Handbook of hard coatings - Deposition technologies, properties and applications", Noyes Publications, Park Ridge, New Jersey, USA, 2001.

71. J. Hosoi, T. Oikawa and M. Inoue, "Study of boron nitride by electron energy-loss spectroscopy", Journal of Electron Spectroscopy Related Phenomena, 27, 1982, pp. 243-254.

72. J. Haines, J. M. Leger and G. Bocquillon, "Synthesis and design of superhard materials", Annual Review of Materials Research, Vol. 31, 2001, pp. 1-23.

73. A. Stoyanova, L. Hozoi, P. Fulde and H. Stoll, "Correlation-induced corrections to the band structure of boron nitride: A wave-function-based approach", Journal of Chemical and Physics, 131, 2009, pp. 1-20.

74. S. Ozbayraktar, "Polycrystalline diamond and cubic boron nitride", Handbook of ceramic hard materials. Ed. R. Riedel, Wiley-VCH, Vol. 2, 2001, pp. 512-520.

75. P. Klimczyk, P. Figiel, I. Petrusha and A. Olszyna, "Cubic boron nitride based composites for cutting applications", Journal of Achievements in Materials and Manufacturing Engineering, Vol. 44, 2011, pp. 198-204.

76. A. R. Lang and J. C. Walnsley, "A transmission electron microscope study of a cubic boron nitride-based compact material with AlN and AlB_2 binder phases", Journal of Material Science, Vol. 87, 1987, pp. 4903.

77. O. Fukunaga and X. Z. Rong, "High-pressure sintering of cBN-TiN-Al composite for cutting tool application", Diamond and Related Materials, Vol. 11, 2002, pp. 280-286.

78. Malvern Zetasizer nano series user manual (MAN0317-5.0), Malvern Instruments Ltd., 2010.

79. Fritsch product brochure, planetary micro mill Pulverisette 7 premium line, 2010.

80. American Society for Testing and Materials (ASTM C373-88 2006) obtained from http://www.astm.org/Standards/C373.htm.

81. A. K. Mukhopadhyay, S. K. Datta and D. Chakraborty, "On the microhardness of silicon nitride and sialon ceramics", Journal of the European Ceramic Society", Vol. 6, 1990, pp. 303-311.

82. G. R. Anstis, P.Chantikul, B. R. lawn and D. B. Marshall, "A critical evaluation of indentation techniques for measuring fracture toughness: I Direct crack measurements", Journal of the American Ceramic Society, Vol. 64, 1981, pp. 533-538.

83. X. Jiang, Y. -K. Baek, S. -M.. Lee and S. -J. L. Kang, "Formation of alpha-sialon layer on beta-sialon and its effect on mechanical properties", Journal of the American Ceramic Society, Vol. 81, 1998, pp 1907-1912.

84. L. Liu, F. Ye, Y. Zhou, Zhiguo Zhang and Q. Hou, "Fast bonding alpha-sialon ceramics by spark plasma sintering", Journal of the European Ceramic Society, Vol. 30, 2010, pp. 2683-2689.

85. J. Räthel, M. Herrmann and W. Beckert, "Temperature distribution for electrically conductive and non-conductive", Journal of the European Ceramic Society, Vol. 29. 2009, pp.1419-1425.

86. D. Salamon, Z. Shen and P. Sajgalik, "Rapid formation of -sialon during spark spark plasma sintering: Its origin and implications", Journal of the European Ceramic Society, Vol. 27, 2007, pp. 2541-2547.

87. M. Hotta and T. Goto, "Densification and microstructure of Al_2O_3-cBN composites prepared by spark plasma sintering", Journal of Ceramic Society Japan, Vol. 116, 2008, pp. 744-748.

88. V. Martinez and J. Echeberria, "Hot Isostatic Pressing of Cubic Boron Nitride–Tungsten Carbide/Cobalt (cBN–WC/Co) Composites: Effect of cBN Particle Size and Some Processing Parameters on their Microstructure and Properties", Journal of the American Ceramic Society, Vol. 90, 2007, pp. 415-424.

89. R. German, P. Suri and S. Jin Park, "Review: liquid phase sintering", Journal of Material Science, Vol. 44, 2009, pp. 1-39.

90. M. Hotta and T. Goto, "Densification and phase transformation of beta-sialon-cubic born nitride composites prepared by spark plasma sintering", Journal of the American Ceramic Society, Vol. 92, 2009, pp. 1684-1690.

91. R. Bradt, M. Sakai and D. Munz, "Fracture mechanics of ceramics: Active Materials, nanoscale Materials, Composites, Glass and Fundamentals", Springer Science + Business Media, Inc. 2005.

92. J. B. Wachtman, "Mechanical properties of ceramics", New York, John Wiley and Sons, 1996.